Transients Fault Analysis based on the Wavelet Transform for Fault Identification and Protection on Cycloconverter based High Voltage Low Frequency Transmission System

Thesis submitted for the degree of

Doctor of Philosophy

at the

University of Leicester

By

Dhrgham Mousa Jwad

Supervisor

Paul W. Lefley

DEPARTMENT OF ENGINEERING
UNIVERSITY OF LEICESTER
UNITED KINGDOM

December 2017

Transients Fault Analysis based on the Wavelet Transform for Fault Identification and Protection on Cycloconverter based High Voltage Low Frequency Transmission System

By: Dhrgham Mousa Jwad
University of Leicester

ABSTRACT

This thesis presents a study on HVLF AC transmission systems for a long distance Offshore Wind Farm (OWF) grid connection. A particular scheme highlights the use of a high voltage cycloconverter as a frequency changer at the sending end of the transmission system, in which the voltage is stepped up at 60 Hz before inputting to the cycloconverter. This eliminates the need for a high voltage low frequency transformer on the offshore platform, and also it allows the use of standard 50/60 Hz generating equipment in the wind turbines. A modelling study has been undertaken to validate the operation of the system, including with the presence of transmission line faults. The study shows the effects of the pre-fault harmonics generated by the cycloconverter on the fault generated transients. Thus, the need to develop a new frequency based fault protection system for HVLF transmission is addressed.

New transmission line fault detection and location algorithms for the HVLF system have been developed. Firstly, the frequency range of the post-fault generated transients were identified using Fast Fourier Transform (FFT) analysis. It was shown that these transient components, ranging from DC to high frequency, are distributed throughout the spectrum of the three-phase current signals. However, the FFT analysis provides the frequency information of these transients but without time information.

In this thesis, the Wavelet Packets Transform (WPT) is introduced for the fault identification. The fault generated transients were detected by monitoring wavelet coefficients over a time window. The performance of the protection system under all possible fault scenarios of the HVLF transmission line are investigated.

Finally, practical considerations, such as the impact of the fault inception angle and the switching and control of the cycloconverter on the fault detection and location algorithm's accuracy were also investigated.

Acknowledgement

First and foremost, I would like to express my sincere appreciation and gratitude to my supervisor Dr. Paul Lefley. His guidance, support, and encouragement have made this work accomplished.

I owe particular thanks to Prof. Mohan Kansara. His extensive experience and fatherly advice have helped me to overcome every challenge throughout the entire period of my study.

I would like also to take this opportunity to thank Dr. Stephen Dodd for his invaluable advices and suggestions during assessment sessions.

Also, I would like to thank the Ministry of Higher Education and Scientific Research-Republic of Iraq for granting a Ph.D. scholarship.

Last but not least, I would like to extend my deepest gratitude to my parents back home, for their patience and endless support during my Ph.D. studies.

Table of Contents

ABSTRACT .... **i**
Acknowledgement .... **ii**
List of Tables .... **vi**
List of Figures .... **vii**
List of Abbreviations .... **xii**
List of Publications .... **xiii**
Chapter 1 Introduction **1**
1.1 Overview 1
1.2 Research Motivation 9
1.3 Research Aims and Objectives 10
1.4 Thesis Outline 12
Chapter 2 Literature Survey **14**
2.1 Overview 14
2.2 Power Collection from Offshore Wind Farms 15
2.2.1 AC Collection with AC Transmission Configuration 15
2.2.2 AC Collection with DC Transmission Configuration 16
2.2.3 DC collection with DC transmission configuration 17
2.3 High Voltage Low Frequency (HVLF) Transmission 19
2.4 HVLF Transmission System Structure 22
2.4.1 AC-AC Frequency Converters 24
2.4.2 Cycloconverter Control 26
2.4.3 Sending End Transformer 31
2.4.4 HVLF Cables 33
2.4.5 HVLF protection and circuit breaker systems 35
2.4.6 HVLF Advantages and Disadvantages 36
Chapter 3 Wavelet Transform for Fault Transients Analysis **38**
3.1 Fourier Transform 38
3.2 Short Time Fourier Transform (STFT) 40
3.3 Wavelet Transform 43
3.3.1 Continuous Wavelet Transform 44
3.3.2 Discrete Wavelet Transform 45
3.3.3 Implementation of the Wavelet Transform 50
3.4 Wavelet Transform Application for Transmission Line Protection 52

3.4.1 Transmission line protection ... 52
3.4.2 Protection Based Wavelet Analysis ... 53
3.4.3 Selection of Mother Wavelet ... 54
3.4.4 The Wavelet Analysis Level Selection ... 55

Chapter 4 HVLF System Modelling and Simulation ... 58

4.1 Overview ... 58
4.2 HVLF System Modelling ... 60
4.2.1 AC-AC Frequency Conversion ... 61
4.2.2 Harmonics and Filtering System ... 64
4.3 HVLF System Steady-state Analysis ... 71
4.4 HVLF System under Line Fault Conditions ... 75
4.4.1 Single-Line to Ground Fault (LG) ... 76
4.4.2 Line to Line Fault (LL) ... 79
4.4.3 Double Line to Ground Fault (LLG) ... 81
4.4.4 Three-Lines Fault (LLL) ... 84
4.4.5 Three-Phase to Ground Fault (ABCG) ... 87
4.5 FFT Results Analysis ... 90

Chapter 5 The HVLF Transmission Line Protection System ... 92

5.1 Overview ... 92
5.2 Wavelet and Packet Wavelet Transform ... 93
5.3 Selection of the Mother Wavelet Function for Fault Algorithm ... 96
5.4 Modelling of the Wavelet Packets Transform ... 99
5.5 HVLF Fault Signals Analysis using WPT ... 104
5.5.1 Single Line to Ground Fault (LG) ... 106
5.5.2 Line to Line Fault (LL) ... 113
5.5.3 Double Line to Ground Fault (LLG) ... 118
5.5.4 Three Lines Fault (LLL) ... 123
5.5.5 Three Lines to Ground Fault (LLLG) ... 128
5.6 Selection of WPT coefficients for fault Algorithms ... 133
5.7 Ground Faults ... 133
5.8 Design of the Protection Algorithm ... 137
5.8.1 Fault Detection ... 137
5.8.2 Fault Location ... 142
5.9 Advantages of the Proposed Protection Algorithm ... 149

Chapter 6 Impact of the Fault Parameters and System Structure on the Protection Algorithm ... 152

6.1 Overview ... 152

6.2 Impact of the Fault Inception Angle 153
6.3 Impact of Cycloconverter Utilisation 168
Chapter 7 Conclusions and Future Research 173
7.1 Conclusions 173
7.2 Future Work 177
References 179
Appendices 186
Appendix-A: Matlab model of the cycloconverter control system. 186
Appendix-B: Voltage and Current Waveforms of Different Fault Types 187
Appendix-C: Ground Fault Calculations 189

List of Tables

Table 4.1: Parameters of the sending end Source 60

Table 4.2: Parameters of the receiving end source and load. 60

Table 4.3 Harmonics of the cycloconverter output current 66

Table 4.4: Multi-stage filters specification 70

Table 5.1: frequency range of the WPT coefficients obtained at the third analysis level. 101

Table 5.2: The frequency features of the WPT coefficient CW1 obtained from the three-phase current signals when an **LG** fault occurs. 145

Table 5.3: Frequency features obtained from the WPT coefficient from the three-phase current signals when a **LL** fault. 147

Table 5.4: WPT features of coefficient CW1 from the three-phase current signals when a **LLL** fault. 148

List of Figures

Figure 1.1: Percentage share of power generated from renewable sources to the total national consumption for years 2005 and 2014. 2
Figure 1.2: The electrical power generation by source in Europe 2016 (in %) [2]. 2
Figure 1.3: Renewable power capacity installations (MW) in Europe until 2015 [2]. 3
Figure 1.4: Offshore wind farm development in Europe toward 2020 [6]. 5
Figure 2.1: AC/AC offshore wind farm configuration. 16
Figure 2.2: AC/DC offshore wind farm configuration. 17
Figure 2.3: AC/DC offshore wind farm configuration. 18
Figure 2.4: HVLF system structure proposed in [16]. 20
Figure 2.5: Maximum power transmission capability of 60 Hz and 20 Hz systems. 21
Figure 2.6: The CIGRE HVDC benchmark [37]. 23
Figure 2.7: Circuit of single-phase to single phase cycloconverter [39]. 25
Figure 2.8: Single phase cycloconverter voltage output at $f_o = f_{in}/5$ [40]. 26
Figure 2.9: Three phase to single phase Cycloconverter structure. 27
Figure 2.10: Input and output waveforms of 60 Hz to 20 Hz cycloconverter. 27
Figure 2.11: The maximum output voltage of a cycloconverter [40]. 28
Figure 2.12: Control scheme of three phase to single phase cycloconverter [40]. 30
Figure 2.13: (a) 50Hz conventional transformer and (b) 16.7 (1/3 of 50 Hz) transformer [33]. 32
Figure 2.14: Maximum power transmission on HVAC cable at different frequencies [25]. 34
Figure 3.1: Example of Fourier Transform for a signal $x(t)$. 40
Figure 3.2: STFT for an input signal $x[n]$. 41
Figure 3.3: Different window sizes of STFT analysis. 42
Figure 3.4: Time and frequency resolution at different window sizes of the STFT. 42
Figure 3.5: Wavelet transform for the signal $x(t)$ [52]. 43
Figure 3.6: Different types of wavelet functions. 45
Figure 3.7: The DWT multi-resolution analysis. 46
Figure 3.8: frequency and time resolution from the wavelet analysis. 47
Figure 3.9: Highpass and lowpass filter frequency bands on each analysis level. 48
Figure 3.10: Highpass and lowpass filter coefficients applied in WT analysis. 48
Figure 3.11: Scaling and wavelet functions with associated filters coefficients (a) Haar (b) db2 (c) db4. 49
Figure 3.12: Frequency response characterises of the lowpass and highpass filters. 51
Figure 3.13: Four levels Wavelet Transform analysis of an input signal $x[n]$. 51
Figure 3.14: The Discrete Wavelet Packets Transform structure. 56
Figure 3.15: Highpass and lowpass filters frequency band of WPT on each analysis level. 57
Figure 4.1: The schematic diagram of the modelled HVLF system. 59
Figure 4.2: Three-phase cycloconverter simulated in Matlab Simulink. 61
Figure 4.3: Circuit diagram of three phase to single phase Cycloconverter. 62
Figure 4.4: Input control signals to the Pulse Generator. 63

Figure 4.5: The pulses generated to the positive converter of a three-phase bridge....... 63
Figure 4.6: The cycloconverter output voltage and current waveforms. 64
Figure 4.7: Harmonic spectrum of the six-pulse cycloconverter output voltage. 66
Figure 4.8: Types of AC harmonic filters. 68
Figure 4.9: Multi-stage filter banks. 70
Figure 4.10: Frequency response of the multi-stage filter banks. 70
Figure 4.11: Matlab simulation of the HVLF power system. 72
Figure 4.12: Voltage and current waveforms under normal conditions measured at busbar B3 and B4. 73
Figure 4.13: Harmonic spectrum of current and voltage signals at the sending and receiving ends. 74
Figure 4.14: Active power flow on the simulated HVLF system. 75
Figure 4.15: Single line diagram of HVLF system under line fault conditions. 76
Figure 4.16: The captured waveform at B3 when an LG fault occurs (a) voltage (b) current. 77
Figure 4.17: Harmonic spectrum of the faulty phase current signal for an LG fault at 20 km and 180 km distances. 79
Figure 4.18: The captured waveform at B3 when an AB fault occurs (a) voltage (b) current. 80
Figure 4.19: Harmonic spectrum of the faulty phases (Ia and Ib) signals of an LL fault, at 20 km and 180 km distances. 81
Figure 4.20: The captured waveform at B3 when an ABG fault occurs (a) voltage (b) current 82
Figure 4.21: Harmonic spectrum of the faulty phases (Ia and Ib) signals of an LLG fault, at 20 km and 180 km distances. 83
Figure 4.22: The captured waveform at B3 when a ABC fault occurs (a) voltage (b) current. 84
Figure 4.23: Harmonic spectrum of the faulty phases (Ia, Ib and Ic) signals of an LLL fault, at 20 km and 180 km distances. 86
Figure 4.24: The captured waveform at B3 when an ABCG fault occurs (a) voltage (b) current. 88
Figure 4.25: Harmonic spectrum of the faulty phases (Ia, Ib and Ic) signals of an LLLG fault, at 20 km and 180 km distances. 89
Figure 5.1: A three level wavelet transform MRA. 94
Figure 5.2: One level analysis of the Wavelet Packets Transform (WPT). 95
Figure 5.3: Haar, Daubechie's 1, 2 and 3 mother wavelet functions. 97
Figure 5.4: Faulty phase signal analysed with wavelet transform using Haar, db1, db2, and db4 mother wavelets respectively. 98
Figure 5.5: Wavelet packet transform tree (a) filters distribution (b) coefficients. 100
Figure 5.6: Wavelet Packets Transform with Matlab-Simulink. 102
Figure 5.7: The WPT analysis of phase-A current signal when an AG fault occurs at 60 km. 103
Figure 5.8: Wavelet Coefficients of the three-phase current signals of an LG fault at 20 km from sending end. 108

Figure 5.9: Wavelet Coefficients obtained from the three-phase current signals of an LG fault at 60 km from sending end. 109
Figure 5.10: Wavelet Coefficients obtained from the three-phase current signals of an LG fault at 120 km from sending end. 110
Figure 5.11: Wavelet Coefficients obtained from the three-phase current signals of an LG fault at 180 km from sending end. 111
Figure 5.12: Wavelet Coefficients obtained from the three-phase current signals of an LL fault at 20 km from sending end. 114
Figure 5.13: Wavelet Coefficients obtained from the three-phase current signals of an LL fault at 60 km from sending end. 115
Figure 5.14: Wavelet Coefficients obtained from the three-phase current signals of an LL fault at 120 km from sending end. 116
Figure 5.15: Wavelet Coefficients obtained from the three-phase current signals of an LL fault at 180 km from sending end. 117
Figure 5.16: Wavelet Coefficients obtained from the three-phase current signals of an LLG fault at 20 km from sending end. 119
Figure 5.17: Wavelet Coefficients obtained from the three-phase current signals of an LLG fault at 60 km from sending end. 120
Figure 5.18: Wavelet Coefficients obtained from the three-phase current signals of an LLG fault at 120 km from sending end. 121
Figure 5.19: Wavelet Coefficients obtained from the three-phase current signals of an LLG fault at 180 km from sending end. 122
Figure 5.20: Wavelet Coefficients obtained from the three-phase current signals of an LLL fault at 20 km from sending end. 124
Figure 5.21: Wavelet Coefficients obtained from the three-phase current signals of an LLL fault at 60 km from sending end. 125
Figure 5.22: Wavelet Coefficients obtained from the three-phase current signals of an LLL fault at 120 km from sending end. 126
Figure 5.23: Wavelet Coefficients obtained from the three-phase current signals of an LLL fault at 180 km from sending end. 127
Figure 5.24: Wavelet Coefficients obtained from the three-phase current signals of an LLLG fault at 20 km from sending end. 129
Figure 5.25: Wavelet Coefficients obtained from the three-phase current signals of an LLLG fault at 60 km from sending end. 130
Figure 5.26: Wavelet Coefficients obtained from the three-phase current signals of an LLLG fault at 120 km from sending end. 131
Figure 5.27: Wavelet Coefficients obtained from the three-phase current signals of an LLLG fault at 180 km from sending end. 132
Figure 5.28: WPT coefficients CW1 and CW3 of the zero sequence current of an LL fault at distances 20, 60, 120, and 180 km from the sending end of the HVLF transmission line. 135
Figure 5.29: WPT coefficients CW1 and CW3 obtained from the zero sequence current of an LLG fault at distances 20, 60, 120, and 180 km from the sending end of the HVLF line. 136

Figure 5.30: flow chart of the proposed protection algorithm 138
Figure 5.31: Samples of the WPT coefficients CW1 and CW3 obtained from the three-phase current signals when an **LG** fault occurs at distances of (a) 20 km (b) 180 km. 140
Figure 5.32: Samples of the WPT coefficients CW1 and CW3 obtained from the three-phase current signals when an **LL** fault occurs at distances of (a) 20 km (b) 180 km. 141
Figure 5.33: Samples of the WPT coefficients CW1 and CW3 obtained from the three-phase current signals when a **LLL** fault occurs at distances of (a) 20 km (b) 180 km. 142
Figure 5.34: The calculated fault location features of **LG** faults distributed over the transmission line. 145
Figure 5.35: The calculated fault location features of LL faults distributed over the transmission line. 147
Figure 5.36: The calculated fault location features of LLL faults distributed over the transmission line. 148
Figure 6.1: The three-phase current signals when an LG fault occurs at 20 km with fault inception angle = (a) 0, (b) 45, (c) 90, (d) 135 and (e) 225 154
Figure 6.2: The three-phase current signals when an LG fault occurs at 180 km with fault inception angle = (a) 0, (b) 45, (c) 90, (d) 135 and (e) 225. 155
Figure 6.3: The WPT coefficients obtained from an **LG** fault of different fault inception angle at location of **20** km. 157
Figure 6.4: The WPT coefficients obtained from an **LG** fault of different fault inception angle at location of **180** km. 158
Figure 6.5: The three-phase current signals when an LL fault occurs at 20 km with fault inception angle = (a) 0, (b) 45, (c) 90, (d) 135 and (e) 225. 160
Figure 6.6: The three-phase current signals when an LL fault occurs at 180 km with fault inception angle = (a) 0, (b) 45, (c) 90, (d) 135 and (e) 225. 161
Figure 6.7: The WPT coefficients obtained from an **LL** fault of different fault inception angle at location of **20** km. 162
Figure 6.8: The WPT coefficients obtained from an **LL** fault of different fault inception angle at location of **180** km. 163
Figure 6.9: The three-phase current signals when an LLL fault occurs at 20 km with fault inception angle = (a) 0, (b) 45, (c) 90, (d) 135 and (e) 225 164
Figure 6.10: The three-phase current signals when an LLL fault occurs at 180 km with fault inception angle = (a) 0, (b) 45, (c) 90, (d) 135 and (e) 225. 165
Figure 6.11: The WPT coefficients obtained from an **LLL** fault of different fault inception angle at location of **20** km. 166
Figure 6.12: The WPT coefficients obtained from an **LLL** fault of different fault inception angle at location of **180** km. 167
Figure 6.13: Matlab model of the HVLF system supplied with 20 Hz voltage source. 169
Figure 6.14: The three-phase current waveforms for an LG fault at 20, 60, 120 and 180 km, with the cycloconverter replaced. 169
Figure 6.15: Harmonic spectrum of the current signal when an LG fault occurs at 20, 180 km locations on the HVLF transmission line supplied by a 20 Hz sine wave voltage source. 170

Figure 6.16: Samples of the WPT coefficients CW1 and CW3 obtained from the three-phase current signals when an LG fault occurs at distances of (a) 20 km (b) 180 km, with the cycloconverter replaced. 171

List of Abbreviations

CWn	Coefficient of the WPT at level n
CCV	Cycloconverter
DWT	Discrete Wavelet Transform
EWEA	European Wind Energy Association
FFT	Fast Fourier Transform
Fs	Sampling Frequency
HVAC	High Voltage Alternating Current
HVDC	High Voltage Direct Current
HVLF	High Voltage Low Frequency
IGBT	Insulated-Gate Bipolar Transistor
IGR	Inter Group Reactor
OWF	Offshore Wind Farm
PLL	Phase Locked Loop
RMS	Root Mean Square
STFT	Short Time Fourier Transform
T_s	Sampling Time
VSCF	Variable Speed Constant Frequency
VVVF	Variable Voltage Variable Frequency
WPT	Wavelet Packets Transform
WT	Wavelet Transform
XLPE	Cross-linked Polyethylene

List of Publications

1. D. M. Jwad, and P. W. Lefley. "Evaluation studies of combined wavelet and neural network applications in high voltage transmission line protection." (2014), IET-12th International Conference: Developments in Power System Protection.

2. D. M. Jwad, P. W. Lefley and M. Kansara "High Voltage Low Frequency AC Transmission System for Long Distance Offshore Wind Farm Grid Connection" was submitted to the International Journal of Renewable Energy Elsevier on 22nd/Sep./2017.

Chapter 1

Introduction

1.1 Overview

The demand for electrical power is growing rapidly. The generation capacity needs to keep in pace with the growing demand through utilisation of renewable sources to achieve a more environmentally friendly and economically competitive and sustainable power system, instead of relying on high carbon footprint technologies. The world energy statistics show that the highest increase in the renewable power generating capacity of a total of 161 gigawatts occurred 2016 [1]. The ongoing trends show that wind energy and solar photovoltaics (PV) are the most emerging renewable energy sources utilised for electrical power generation [2]. Within Europe only, the renewable energy contribution to the total power generation from all sources was about 28.8% in 2015 [2, 3]. Figure 1.1 shows the percentage of the electrical power generated from renewable sources to the total consumption per country for the given years. Both Norway and Iceland have the maximum share of electrical power generated from renewable sources. Although, other countries such as Denmark, Germany, Portugal and United Kingdom are still depending on non-renewable energy sources; but these countries had the highest growth in power generation from renewables between 2005 and 2014. Most of these countries have set a future target to eliminate power generation from fossil fuels by increasing the installed capacity of renewable energy.

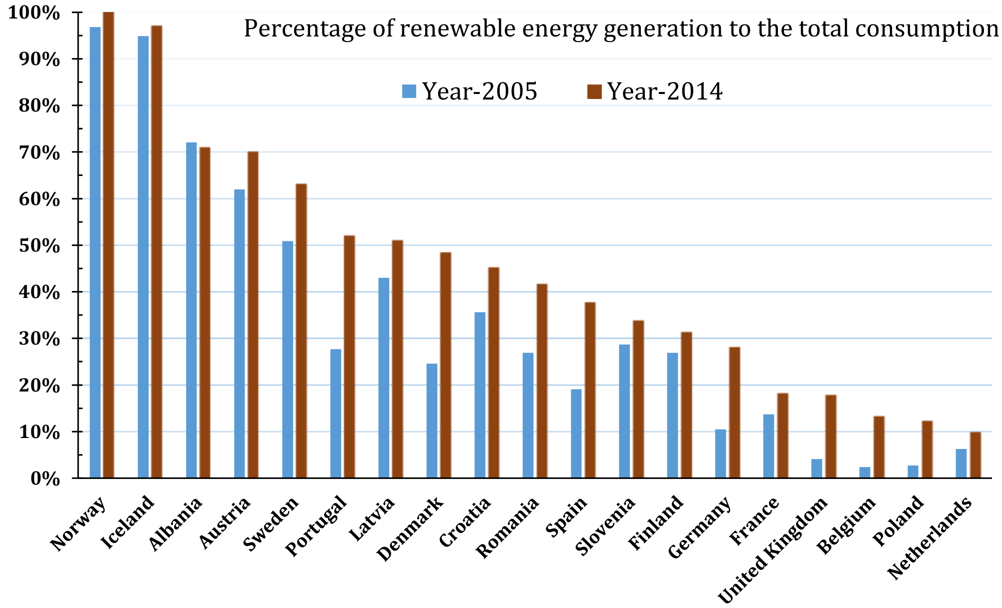

Figure 1.1: Percentage share of power generated from renewable sources to the total national consumption for years 2005 and 2014.

In Europe, the contribution from wind power generation was 10% in 2016, see figure 1.2. Wind power is catching up the contribution from hydro, although, hydro has been the basis of renewable energy with the maximum contribution for many years. The statistics show that in recent years wind was the fastest growing renewable power source [1].

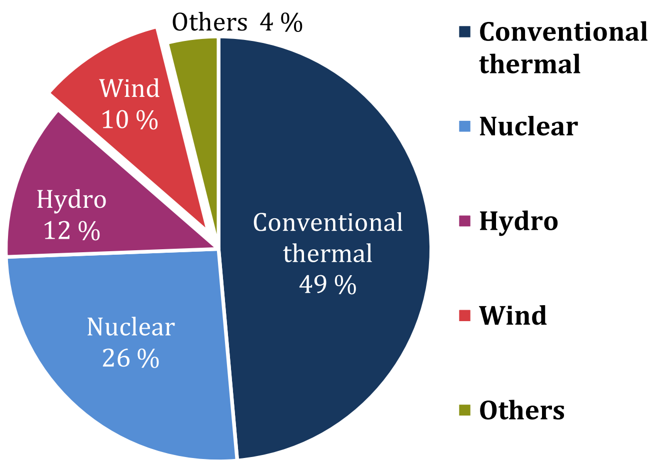

Figure 1.2: The electrical power generation by source in Europe 2016 (in %) [2].

In the last decade, the power sector in Europe has continued to increase its total installed generation capacity from wind power plants. The pie chart of figure 1.3 shows that contribution from wind is the highest among other sources due to many reasons such as, the relatively large quantity of power generated from a single wind turbine compared with a solar photovoltaic array for example [2].

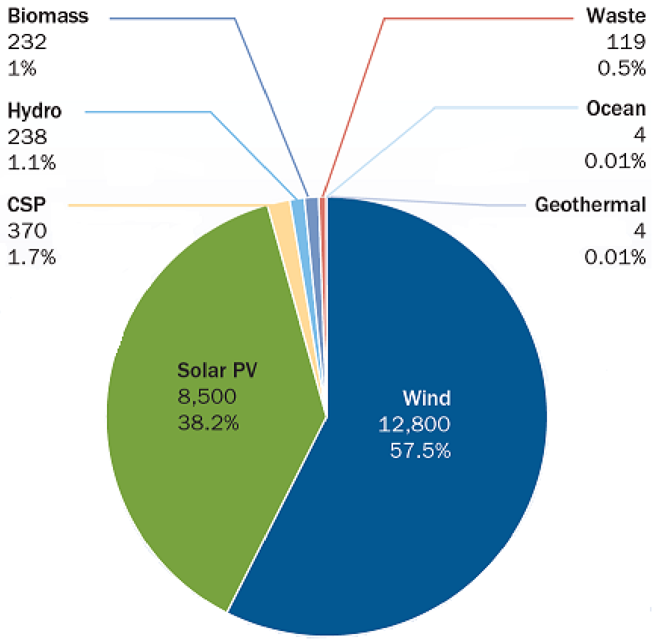

Figure 1.3: Renewable power capacity installations (MW) in Europe until 2015 [2].

Therefore, wind energy is expected to play an increasingly significant part in the future of power generation from renewable sources. The ongoing growth of wind power demand has led to an increased catchment through geographical expansion and enhancement of current technologies. Hence, the development of effective technologies applied to generation, transmission and integration to the grid are of relevance and interest.

There are a number of important issues affecting the power generation from wind energy such as, the size and location of wind farms, which results in an increase in the capital cost, and the unpredictability of wind speed which results in lower generation capacity. As the power generated from a single wind turbine can be calculated by [4]:

$$P = \frac{1}{2}\rho A v^3 \qquad (Watts) \qquad (1.1)$$

where A is the area of turbine blades (m^2), ρ is the air density (kg/m^3) and v is the wind velocity (m/s). From equation (1.1) the amount of power extracted from wind is proportional to the cube of the wind speed. Therefore, the selection of wind farm location has a major impact on improving the overall power generation efficiency and capacity. Locating wind farms onshore is a very cost effective technology, but it has many limitations due to the high population density and the required land usage. In addition, recent studies have shown that onshore wind is less effective i.e. less frequent and at lower speed in comparison to offshore wind [5]. This means that offshore wind farm (OWF) can generate more power than an equivalently sized onshore located wind farm. Hence, the realisation of OWFs are receiving much more attention, especially in the United Kingdom, Denmark, Germany, Sweden, and the Netherlands [2]. The European Wind Energy Association (EWEA) 2015 annual report has stated that:

"During 2015, 13,805.2 MW of wind power was installed across Europe, 5.4% more than in the previous year. 12,800.2 MW of it was in the European Union. Of the capacity installed in the EU, 9,765.7 MW was onshore and 3,034.5 MW offshore. In 2015, the annual onshore market decreased in the EU by 7.8 %, and offshore installations more than doubled compared to 2014" [2].

Additionally, the statistics show that OWFs of rating up to 160 MW are in operation and there are several plans for 340 MW farms [6]. Figure 1.4 shows that the next generation of OWFs will be expanded further out to sea to a distance of over 100 km.

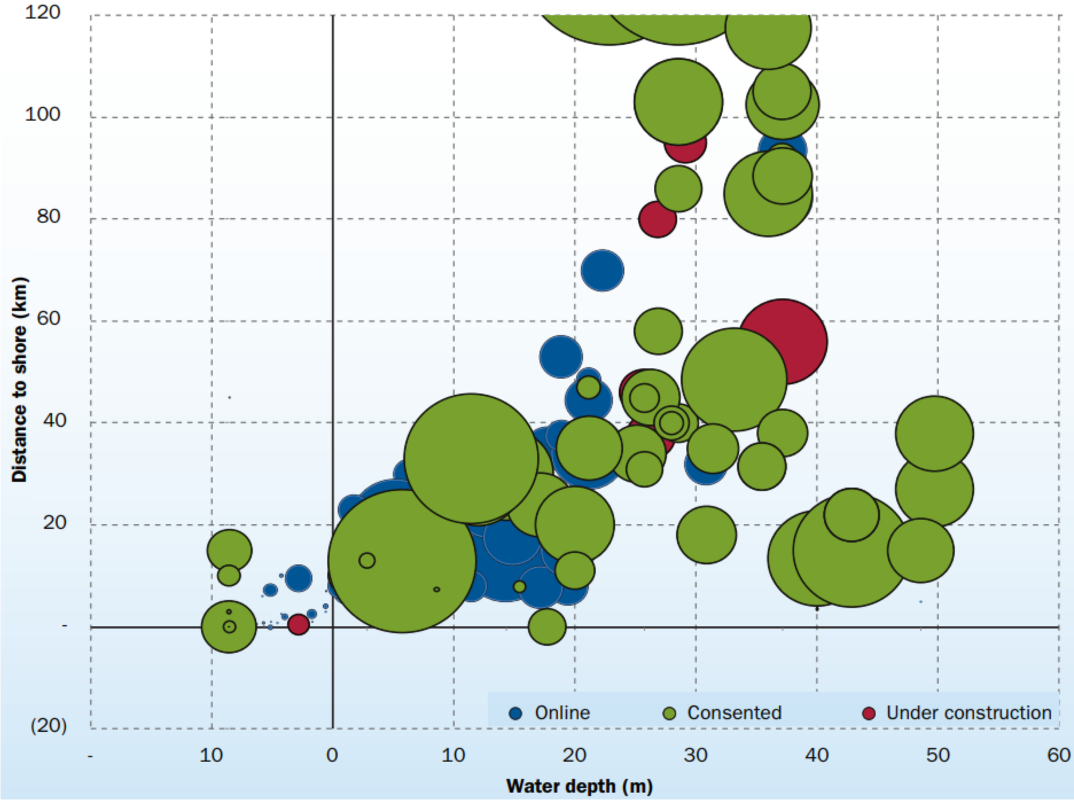

Figure 1.4: Offshore wind farm development in Europe toward 2020 [6].

The increase in size and distance of OWFs has led to new challenges in terms of power collection and transfer technologies. The demand on bulk power transmission over long distance from shore has grown considerably in recent years [5]. So far, High Voltage Alternating Current (HVAC) and High Voltage Direct Current (HVDC) power transmission technologies have been implemented depending on the transmission distance and capacity.

In the conventional HVAC systems, the power transmission capacity and distance were increased by raising the voltage level of the transmission line. Since the transmission lines have thermal and environmental limitations, the maximum voltage level of AC transmission is 750 kV [7]. However, for long distance offshore power transmission, HVAC submarine lines have high losses and excessive reactive power compensation is needed due to the high capacitance of the cables. This high capacitance causes a charging current that reduces the active power transmission capacity [7]. Therefore, HVAC can only be used for short distances, which is typically below 50 km. For example, London Array is the world's largest offshore wind farm located 20 km off the Kent coast in the United Kingdom that utilises HVAC system for power transfer [6]. A total capacity of 630 MW is generated by 175 wind turbines, and transferred at nominal voltage of 150 kV over a distance of 53 km via four XLPE cables. However, two offshore substations were constructed to accommodate transformers used to step up the voltage level from 33 kV to 150 kV. This example clarifies that the HVAC system utilised for offshore transmission requires multiple cables and offshore platforms to meet the required transmission capacity.

An HVDC transmission system has been implemented as an alternative to provide higher transmission capacities [7, 8]. In an HVDC system no reactive power is consumed or produced in the cables. Thus, the HVDC transmission system has the advantages of lower losses, longer transmission distance and higher power transmission capacities in comparison with the conventional HVAC system [9]. In the last few decades, the number of planned and installed HVDC systems has increased rapidly, and particularly for long distances offshore power transmission [7]. Recently, the DolWin1 transmission link in Germany was implemented to deliver 800 MW from windfarms in the North Sea via 167 km HVDC cable at a rated DC voltage of ± 320 kV [1].

However, an HVDC power network requires expensive converter stations at both ends of the transmission line. Additionally, most of the HVDC systems are point-to-point transmission due to a lack of DC circuit breaker technologies [10] as, an interconnected

HVDC grid requires circuit breakers able to interrupt the high level non-zero crossing DC fault current. High rating short-circuit current DC breakers are still under development [11]. Furthermore, HVDC network reliability is greatly affected by faults due to insulation breakdown [12]. One of the main reasons for insulation breakdown is the accumulation of space charge in the insulating material. In an HVDC system the electric field direction remains constant and consequently so does the injection of charges into the insulation. Hence, these electric charges will accumulate in the insulating material if there are non-homogeneities in the insulator [13]. The non-homogeneities are microscopic faults in the insulator, resulting in enhancing the electric field and leading to premature ageing and breakdown of the insulator [14]. Whereas, the space charge accumulation at the AC cable insulator could be neglected because the electric field direction reverses periodically causing the injection of charges to reverse as well [14].

A High Voltage Low Frequency (HVLF) transmission system has been recently proposed as an alternative solution for the above HVAC and HVDC systems and to overcome their limitations [15-17]. The HVLF system uses a lower fraction of the conventional transmission frequency, typically less than 1/3 of 50 or 60 Hz. Transmitting power at a lower frequency results in a reduction of the reactive power in the line, and hence an increase in the active power transmitted. In comparison with HVDC, HVLF has a cost advantage for transmission distances up to 90 km and for a typical 600 MW capacity [18]. This cost estimation is based on 16.7/20 Hz generating equipment, and a low frequency step-up transformer, but effects of the total life-time costing due to cable ageing were not considered.

Nevertheless, according to Papadopolous et al. [19] AC losses in an HVAC cable are significant at normal power frequencies. For example, a typical HVDC cable carrying

600 amps of current would have a cable loss of 20 watts/m due to only ohmic losses of the central conductor. For a similar rated HVAC cable carrying 600 amps RMS, the combined cable losses are slightly more than 40 watts/m due in part to the dielectric heating of the insulator. In addition the cable current will have a significant reactive component too depending on cable length. So, by applying a low frequency alternating field, the effects of protracted space charge injection and migration in the insulator, induced electro-thermal cable ageing, and loss due to the reactive cable charging current are significantly reduced.

Many power transmission companies in conjunction with university research departments are conducting research to mitigate the ageing effects of cable insulation as well as to improve high voltage transmission systems in terms of reliability, protection and cost. Low frequency power transmission is gaining interest and is a serious contender for submarine cable based HVDC systems. Once high current circuit breakers are developed, then the HVLF system will allow power grids of different frequencies to be interconnected. Another advantage of an AC system over HVDC is the presence of zero crossing current that will make interruption of the fault current by the circuit breaker easier. Yet, the alternating field albeit at a much lower frequency mitigates the space charge accumulation mechanism and thus reduces this ageing effects on the cable. Therefore, ongoing research is being conducted to improve HVLF transmission systems in terms of reliability, protection and cost.

1.2 Research Motivation

Extensive research has been carried out on the development of offshore bulk power transfer to the load centres. Much of this research is focused on overcoming limitations of the existing HVAC and HVDC systems by upgrading the utilised technologies. However, there are many medium and long transmission lines that can be upgraded to increase their capacity by transmitting power at a low frequency. This means the introduction of a High Voltage Low Frequency AC (HVLF) transmission system. This technique can be applied to the future projects as a solution to the HVAC and HVDC transmission limitations. A number of HVLF topologies have been proposed, and all with particular advantages and disadvantages [15, 20-23].

In an attempt to categorise these topologies it appears that there are no clear boundaries between one design and the next, but a spectrum of designs that lies between two extremes: systems based on a number of large low frequency magnetic components, and others based on power electronics frequency conversion with no or few large magnetic components. At one end of the spectrum, power is generated at low frequency and large magnetic systems are utilised as a frequency changer, such as the high power saturable transformer introduced by Wang [17]. This transformer exploit the high distorted core flux waveform to enhance a large magnitude third harmonic to convert power to three times the frequency [22]. At the other end of the spectrum, an HVLF system based power electronic converter topologies have been introduced [15, 20, 24, 25]. Various types of power electronic frequency step-down or -up changers are proposed at line ends, such as a cycloconverter and the multi-level matrix converters [20]. This topology seems to be more accepted, since it is of a similar structure to the HVDC system, and can be utilised with conventional transformers and wind turbines. However, up to date there is no optimum topology for the proposed HVLF transmission system.

Little research has been conducted to address the system behaviour under fault conditions, and the suitability of applied protection and fault location systems. Introducing a low operational frequency as well as the existence of pre-fault harmonics makes the conventional transients signal based protection methods encounter difficulties to detect and locate line faults. Therefore, analyses of the pre- and post-fault system transients of the proposed low power frequency system must be investigated thoroughly.

1.3 Research Aims and Objectives

This research introduces an alternative HVLF transmission system structure specifically applied to offshore wind power transmission using a cycloconverter as a frequency changer at the sending end of the transmission line. A literature survey was required to address the design challenges and limitations of the offshore converter station and the step-up transformer if power is generated at a frequency lower than 50/60 Hz. The impact of the cycloconverter generated harmonics during the pre- and post-fault conditions on the protection system of the HVLF transmission line was investigated thoroughly. The main aim of the research was to develop a transmission line protection scheme that is able to provide the required reliability level of protection for the proposed HVLF transmission system.

The main objectives of this research were as follows:

- To investigate the theories, design specifications, and topologies required to introduce the concept of a High Voltage Low Frequency (HVLF) system applied to offshore wind power transmission.
- To build a mock-up model of the proposed HVLF power system including the high voltage AC-AC frequency converter station (Cycloconverter) with Matlab-Simulink software [26]. Validate the HVLF system by verifying the voltage and current harmonics obtained during normal conditions and to implement the required filtering system, as well as investigate the power flow.
- To investigate and analyse system harmonic spectra during transmission line post-fault conditions and under various fault types and locations and identify their frequency range and magnitudes using the FFT analysis.
- To review theories of the wavelet transform and its applications to high voltage transmission line protection. Identify the limitations of the traditional Discrete Wavelet Transform (DWT)
- To propose an HVLF transmission line protection algorithm based on the Wavelet Packets Transform (WPT). Also, to develop fault detection and location models for the proposed HVLF transmission system based on the analysis of current signals obtained at the sending end of the line using the WPT.
- To optimise the Wavelet Packets Transform analysis and evaluate the results of the simulation.
- To test and evaluate the robustness of protection algorithms by investigating the impact of system parameter change as well as the system topology. These tests include changes to the fault inception angle of different fault types and locations.

Further tests include the change in network configuration. This test includes replacing the cycloconverter, and investigate the system behaviour during various fault types and locations.

1.4 Thesis Outline

Chapter 2 provides a literature survey of offshore wind farm configurations and the currently applied transmission technologies. In addition, this section reviews the development of the HVLF system proposed for long distance offshore wind power transmission. A detailed study on the HVLF system structure options are given. This chapter addresses design challenges and limitations of the offshore converter station and transformer in the HVLF system. The requirement for a suitable protection system based on the fault transients analysis of the HVLF transmission system is addressed in this chapter.

A brief review on the development in signal processing techniques applied to conventional HVAC and HVDC fault signals analysis is given in Chapter 3. The theory of traditional analysis tools such as Fourier Transform (FT) and Short Time Fourier Transform (STFT), and their limitations to the analysis of fault transients is explained. This chapter provides a detailed study on the wavelet transform theories and their current applications into power system protection. The selection of appropriate mother wavelet and analysis structure by means of introducing the Wavelet Packets Transform (WPT) is presented.

Chapter 4 of this thesis details the structure of the proposed HVLF transmission system. The HVLF power system simulation model used to investigate the system behaviour during pre- and post-fault conditions is presented in this chapter. This includes the modelling, operation and control of the cycloconverter and the filtering system. The harmonics introduced by the cycloconverter and the necessary filtering system are explained. Additionally, the system validation by means of monitoring the power flow and the three-phase voltage and current waveforms is demonstrated. Furthermore, an investigation of the frequency spectra of the three-phase current signals during pre- and post-fault conditions using the FFT analysis is given. This chapter clarifies the need for an analysis tool to precisely differentiate between cycloconverter harmonics and fault generated transients with its corresponding time signature presentation.

Chapter 5 describes the proposed fault detection and location algorithms based on the Wavelet Packets Transform (WPT) analysis. The analysis of the three-phase current signals obtained for various fault types and locations is given. In this chapter, the selection of the appropriate wavelet coefficients that contain the fault transients is illustrated. The fault detection and location algorithm results and analysis are also given.

Test and evaluation of the robustness of protection algorithms is investigated in chapter 6. These tests include changes in the HVLF transmission line fault parameters, particularly, fault inception angle at different fault types and locations. A comparative study to show the impact of the cycloconverter harmonics on fault signature is carried out by investigating the HVLF system behaviour under various fault types and locations with the cycloconverter being replaced by its inter-group reactance only. Finally, the thesis conclusions are drawn and future work recommendations are presented in chapter 7.

Chapter 2

Literature Survey

2.1 Overview

Presently, the total generating capacity of OWFs is continuously increasing [27]. The next generation of OWFs will be much larger and at a distance of more than 100 km from shore [6]. The increase in size and distance impose a number of challenges in terms of power collection and transmission to the shore. Nowadays, two main transmission solutions, HVAC and HVDC are the only two technologies implemented for this purpose. As mentioned previously, each one of these two technologies has its advantages and limitations when applied to offshore power collection. Therefore, the process of implementing a large scale wind energy requires a comprehensive analysis to be applied to the utilised technologies in order to ensure a high operation efficiency at the optimum cost. In these terms, offshore power grid planning requires the definition of several factors, such as the collection technology to be implemented with respect to the total number of installed turbines, and the transmission technology depending on the total generated capacity and distance to the shore. In this chapter, a review to the OWFs configuration and the currently applied transmission technologies is presented. This chapter discuss the key benefit of introducing an HVLF transmission system as an alternative to the HVAC and HVDC. In this regard, a detailed study on the HVLF system structure options, the design challenges and limitations are investigated. Additionally, the requirement for a compatible protection system for the HVLF transmission line is addressed in this chapter.

2.2 Power Collection from Offshore Wind Farms

The power system for a typical offshore wind farm can be divided into three main sections, namely the collection system, the offshore platform and the transmission and grid integration system [27]. The first section is the collection system, which includes the wind turbines, power collection network. In this section, the wind turbines are connected to each other with different topologies and the power is collected in AC or DC form. In most wind farm topologies the wind turbines generate electrical power in AC form and at a nominal frequency of 50 or 60 Hz. The second part is the offshore platform where the step-up transformer and switchgear are located. The third section is the transmission and grid integration system, where the generated power is transmitted at a higher voltage level and integrated to the onshore grid through a common connection point. In practical, these three sections of OWF are implemented with various configurations. In the next subsections, a brief description on each configuration with its advantages and limitations is given [4].

2.2.1 AC Collection with AC Transmission Configuration

The wind system layout of this configuration is given in figure 2.1. In this configuration, the power is generated in AC form and at the nominal frequency of 50 or 60 Hz. Taking into consideration that each wind turbine consist of turbine blades, speed gearbox, generator with a power electronic converter in order to control the power fluctuation, and a medium voltage transformer. Several wind turbines are connected to a common medium voltage feeder, and all feeders from turbines are connected to the collection point. The collection point in the case of an offshore wind system represents the offshore platform. A high voltage step-up transformer connected to the transmission cable on the platform is used to step up the transmission voltage.

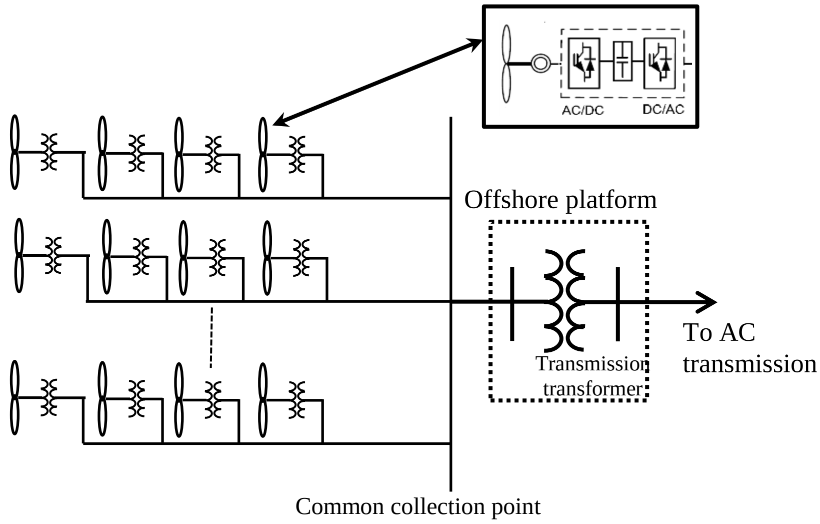

Figure 2.1: AC/AC offshore wind farm configuration.

This configuration is very cost effective since only one power transformer is required on the offshore side [4]. The main disadvantage of this configuration is the high power losses on the subsea feeders and transmission line due to the charging current on the AC cables. Also, several parallel transmission cables are required to transmit high generated capacities. Therefore, this configuration has been utilised for offshore wind farms located at a distance close the shore. This configuration has been implemented for power collection from the “Horns rev1” OWF in Denmark, with a total capacity of 160 MW generated by 80 turbines located at a distance of 18 km from the shore [28].

2.2.2 AC Collection with DC Transmission Configuration

This system configuration is preferred for large scale OWFs that are located far away from the shore (50 km and above) in order to avoid the HVAC cable current charging limitation [4]. This configuration requires a converter station on the offshore platform in order to convert AC power at the collection point into a high voltage DC for transmission, see figure 2.2. Another converter station is also required on the receiving end that converts DC voltage back to AC to integrate the power with the gird. An example of this configuration is the “BARD1” OWF in Germany with a capacity of 400 MW transmitted at ±150 kV via 125 km HVDC submarine cable [3].

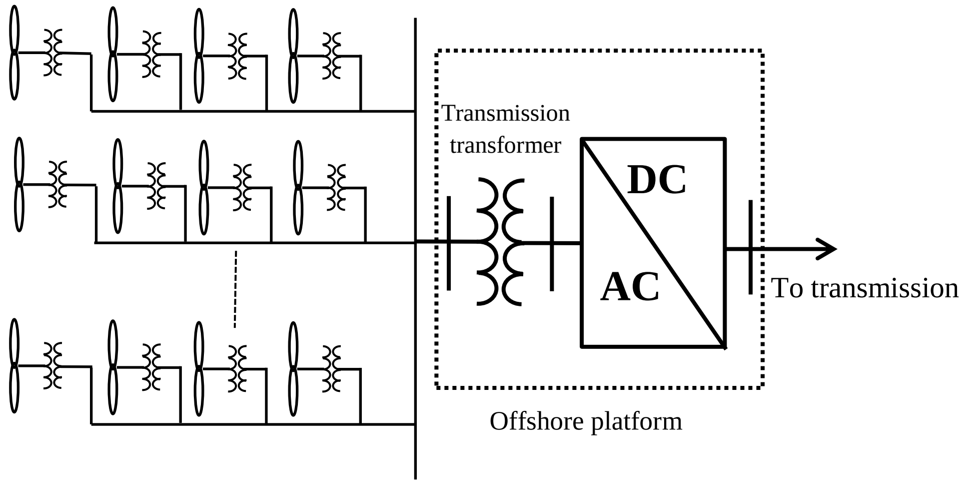

Figure 2.2: AC/DC offshore wind farm configuration.

This configuration has the advantages of high power transmission capability with lower cable losses in contrast to the HVAC system [28]. However, beside the high cost of the converter stations at each terminal the installation and maintenance cost of the offshore platform is also relatively high [4]. Moreover, another limitation of this configuration is the insulation breakdown of the submarine HVDC cables due the space charge accumulation [29]. Space charge accumulation is considered one of the main reasons for HVDC transmission line faults. Therefore, this transmission configuration has a relatively lower reliability even though the losses in the line are reduced.

2.2.3 DC collection with DC transmission configuration

In this configuration, each wind turbine is installed with an AC to DC medium voltage converter [30], see figure 2.3. Then, each converter is connected to the DC collection grid in either a series, parallel, or hybrid configuration. The DC-DC converter located on the platform is used to step up the voltage to a higher level for the transmission stage. This configuration has the advantage of reducing the capital cost by eliminating the large size power transformer on the platform used in the previous AC-DC configuration. However, this configuration still has the same limitation of the previous AC/DC configuration in terms of cable insulation breakdown. In addition, in case of any wind turbine failing to operate, the DC converters of other turbines will need to compensate by increasing their output voltage to match the DC bus voltage [4]. Therefore, these converters need to have the capability to handle very high voltage levels. So far, this configuration has been proposed in the research literature, but not yet implemented [4, 30].

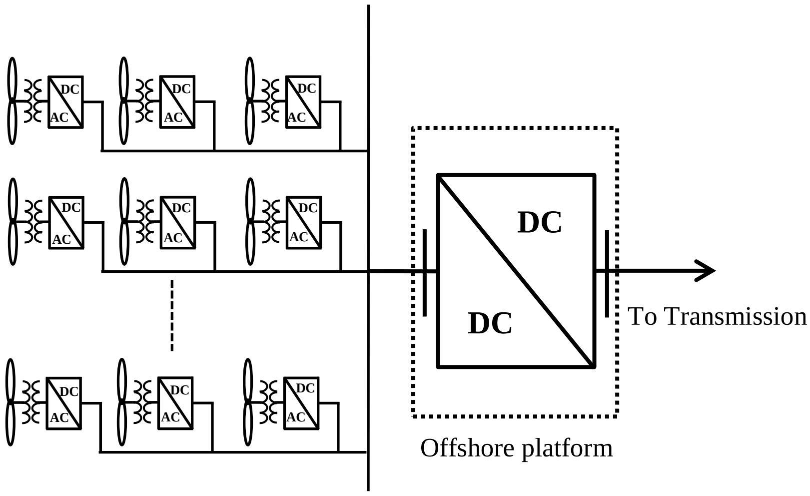

Figure 2.3: AC/DC offshore wind farm configuration.

By summarising the above configurations, it is clear that all configurations presented and compared above have technical and economic advantages and disadvantages. In general, configurations with HVDC technology have a relatively high capital cost, but less power losses in comparison to the conventional AC system. Nevertheless, the implementations of HVDC multi-terminal system is still a challenging task [10], where a reliable protection system and high current interruption DC circuit breakers located at each terminal are required to ensure stable operation of the system. For example, in case of a fault incident on the HVDC transmission line, the current reaches a high and steady magnitude, which makes it more difficult for the circuit breakers to isolate the fault line. In recent years, many researches have been focused on the analysis of DC fault currents, DC fault detection methods and the design of HVDC circuit breakers [10]. However, the proposed solutions of an HVDC protection system and DC circuit breakers are not advanced enough to enable fast fault clearing and system restoration.

This research described in this thesis is an investigation into the feasibility of an OWF configuration based on introducing a High Voltage Low Frequency (HVLF) transmission as an alternative solution to HVAC and HVDC and their limitations. A detailed survey and description of the HVLF transmission system is given in the following section.

2.3 High Voltage Low Frequency (HVLF) Transmission

The HVLF transmission or so-called Fractional Frequency Transmission System (FFTS) utilises a lower transmission frequency (fractions of 50 or 60 Hz) in order to reduce the total line reactance and increase the active power transfer capacity. This system was initially introduced by Xifan and Xiuli in 1994 [16, 17]. The authors proposed a transmission system with a lower frequency of 50/3 Hz and compared their results to the conventional 50 Hz system. The study suggested that electrical power could be generated at a low frequency (50/3 Hz) from hydro-power turbines and then stepping the voltage up to 500 kV before transmission. The theoretical results of this study have shown that a total power of 1700 MW can be transmitted over a distance of 1200 km. The structure of the HVLF transmission system proposed by the authors is given in figure 2.4. The system structure shows that at the sending end a high voltage low frequency transformer is required, as well as at the receiving end a high power tripler transformer is utilised as a static step-up frequency converter. The tripler transformer exploits the high distorted core flux waveform to enhance a large magnitude third harmonic to convert power to three times the frequency.

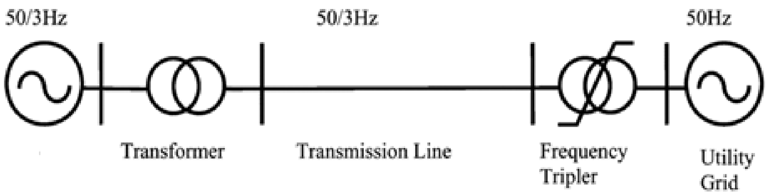

Figure 2.4: HVLF system structure proposed in [16].

The study is based on the theoretical analysis of a lossless line in which the active power transmitted is inversely proportional to the line reactance (and so the frequency) at any voltage level as given in equations (2.1, 2.2) [31].

$$P = \frac{V^2}{X}\ \sin\delta \qquad (Watts) \qquad (2.1)$$

and

$$X = 2\pi f L l \qquad (ohms) \qquad (2.2)$$

Where, P is the maximum active power that could be transmitted over an AC line, V is the transmitting and receiving voltage level (Volts), l is the line length (m), δ is the power angle (deg.), X is the line reactance, L is the total line inductance (H), and f is the system frequency. Figure 2.5 shows the power transmission capability of the conventional 60 Hz system and 20 (1/3 of 60 Hz) at the same voltage level and line length. The power curve illustrates that a 20 Hz transmission line can transmit power three times higher than the conventional 60 Hz line.

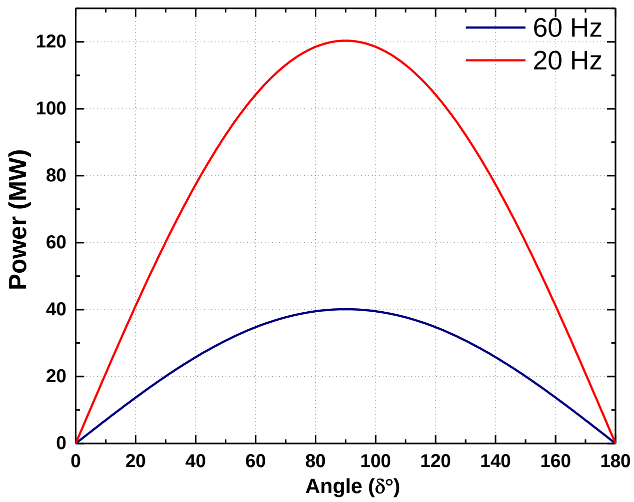

Figure 2.5: Maximum power transmission capability of 60 Hz and 20 Hz systems.

Later, Xifan et al. in 2006 [32] have demonstrated a laboratory experiment on the previously proposed fractional frequency transmission system (FFTS). The experimental results showed that with FFTS 2000 MW could be transmitted over 1200 km distance at 500 kV voltage level. In this experiment they have also verified that the FFTS can be used to transmit power that is three times higher than the conventional 50 Hz HVAC system of the same voltage level.

Furthermore, the HVLF transmission system has been recently proposed to transmit bulk power collected from OWFs located at far distance from the shore [15, 20-22, 24, 33, 34]. Qin et al. in [34] proposed an HVLF submarine transmission system to integrate large scale OWFs with the grid. The study investigated the possibility of generating power at low frequency (50/3) from the wind turbines. The results showed that for low frequency the operation the wind turbine needs to be redesigned in order to obtain maximum wind power capture. Chen et al. [21] presents an HVLF transmission scheme with a cycloconverter at the receiving end with a low frequency transformer at the sending end. The conclusion from these studies imply that a cost reduction can be achieved by generating power at lower frequency and thereby simplifying the offshore station. Nevertheless, the cost of redesigning wind turbines and the sending end transformer need to be considered. Up to date there are a number of technical challenges need to be considered before the implementing an HVLF system. The topology and components required to build up the HVLF system are still argued in the literature. In terms of frequency conversion, different converter types have been proposed [22]. Various studies have suggested the use of a cycloconverter, matrix converter or Back to Back Converter [20, 23, 35]. Each type of these converters has been chosen to reduce the effect of harmonics generated due to the frequency conversion from its nominal value (50 or 60 Hz) to lower frequency. As such still no one has come up with a satisfactory scheme to transmit power at low frequency over a long distance from the shore.

2.4 HVLF Transmission System Structure

The HVLF system was introduced to the offshore wind power transmission as an alternative option to the HVAC and HVDC systems in order to overcome the their limitations [17, 32]. However, it is still a new proposal and has not yet implemented. The HVAC system utilised for OWFs has been in industrial and domestic use for decades, and its structure and components are well standardised [7, 36]. As previously mentioned, for OWFs located at a distance less than 50 km the HVAC is a cost effective option. But, still for large generated capacities multiple cables are required. Numerous studies have been conducted on the development of the required HVAC system components such as the wind turbine generator, transformer, and the transmission cable. Additionally, these components have been modelled with computer simulation tools in order to investigate the system behaviour under steady-state and fault conditions. Hence, in order to ensure and maintain the stability of the power system, these components have to operate within certain standards such as IEEE, IEC etc. in order to meet a predefined grid code.

Similarly, these standards also applies to the HVDC system including limits to the harmonics introduced by converter stations. Therefore, the first well known CIGRE-HVDC benchmark introduced in 1991 by Szechtman et al. has been used as a standard benchmark for studying steady-state and fault conditions of the HVDC system [36-38], see figure 2.6.

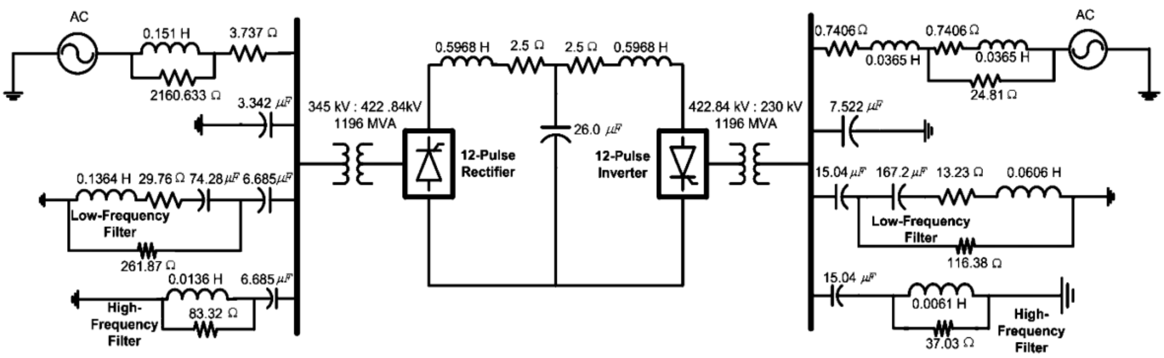

Figure 2.6: The CIGRE HVDC benchmark [37].

This model represents a mono polar 500 kV, 1000 MW HVDC transmission system with 12-pulse converters on both sides. The AC grid is represented by voltage sources, and AC filters are utilised to supress the harmonics introduced by the converter and to supply reactive power to the system as well.

In contrast, there have been various structures proposed for the HVLF system, and all with a particular advantage and disadvantage. So far, unlike the HVDC system there is no standard benchmark implemented for the HVLF studies. However, the HVLF structure can be very similar to the HVDC system, except the DC converter and inverter stations are replaced by frequency changers. Hence, this thesis proposes an HVLF system consisting of four main parts; frequency converters, power transformer, transmission cables and the harmonic filters. The design and limitation of each component are discussed in the next subsections. Additionally, the required control and protection subsystems in order to ensure a stable operation of the system are addressed.

2.4.1 AC-AC Frequency Converters

In the HVLF system, it is desirable that only the power cable operates at low frequency, and the generating and voltage transformation systems operate at the usual power frequency to maintain standard sizes in all the magnetic components. Therefore, the frequency converters located at each end of the power cable are key elements in the proposed HVLF system. A high voltage single phase output cycloconverter was developed for the 16.7 Hz European railway power transmission network, and in use for many decades [39]. So far, this application is one of the implemented low frequency power systems. However, still the voltage level applied for the electric trains that operates at 16.7 Hz is 15 kV. The large series-wound traction motors were designed to operate at low frequency in order to overcome the high inductive reactance of the motor windings. Recently, for the longest rail tunnel in the world (Gotthard Base Tunnel, opened in 2016 in Switzerland) a 15 kV, 16.7 Hz AC Electrification system was implemented.

The rapid development of HVDC systems has advanced power electronic converter technology. Nowadays, most HVDC converters utilise high rated power electronics switches such as thyristor or Insulated Gate Bipolar Transistors (IGBTs) which have the ability to control the transmitted power rapidly and efficiently [7]. A power electronic direct AC-AC frequency changer device called a cycloconverter has been used widely in many applications such as, large-power low-speed variable-voltage variable-frequency (VVVF) AC drives, large ore mining roles mills and variable-speed constant-frequency (VSCF) systems in aircraft and ships [40-42]. Unlike other types of frequency converters the cycloconverter is a direct frequency changer and no intermediate DC link or energy storage component is required. Additionally, the cycloconverter has the ability to allow bidirectional power flow between source and load [43]. Another important characteristic of the cycloconverter is the high power ratings that reaches to about 20 MW has made it preferable for high power applications such as grinding mill drives [41, 43].

The basic principle of the cycloconverter is to construct a lower frequency voltage waveform from a higher frequency AC supply by a consecutive switching operation of the power electronic switches [39, 42]. This can be described as two full wave bridge rectifiers with back to back connection, see figure 2.7 [39].

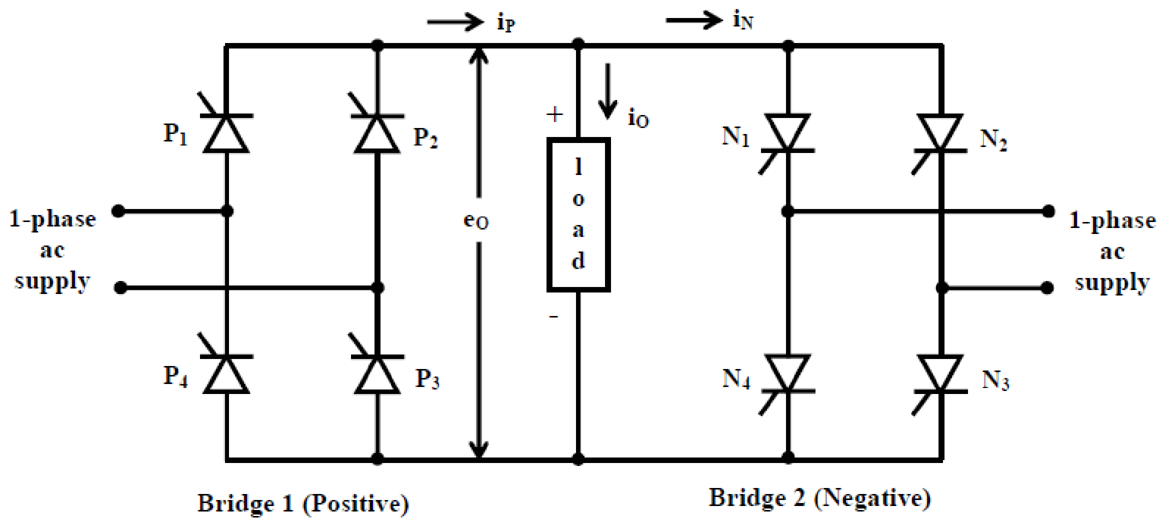

Figure 2.7: Circuit of single-phase to single phase cycloconverter [39].

For example, if an output frequency of one fifth of the input frequency is required, the positive converter (P group) only conducts for five positive half cycles supplying current to the load. The negative converter (N group) conducts for the next five cycles to supply negative half cycle to the load see figure 2.8 [40]. When one of the converters is conducting the other one is off in order to avoid current circulating between both groups. In case any of two thyristors in positive and negative conducting at the same time a short circuit will result on the supply terminals.

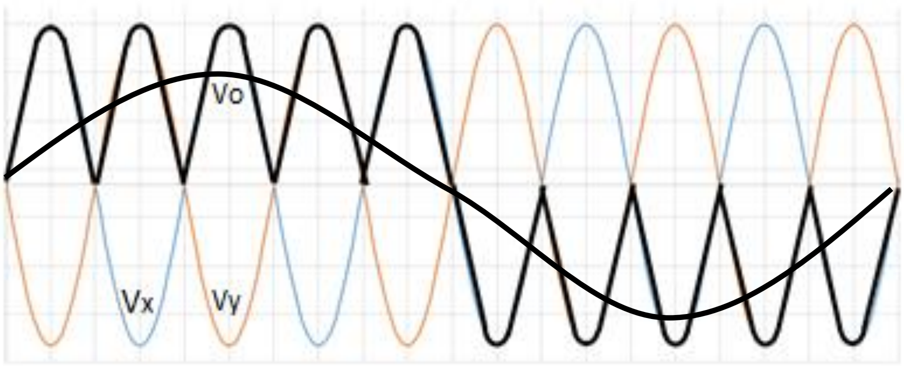

Figure 2.8: Single phase cycloconverter voltage output at $f_o = f_{in}/5$ [40].

Therefore, the firing pulses need to be controlled so that when one of the positive or negative group is conducting and the other one is off. This mode of operation of the cycloconverter is called a blocking operation mode. Another solution is connecting a centre tap reactor between the positive and negative groups so that the circulation current is limited [40]. Thus, in case of inductive load, any current lagging the voltage will be limited by the intergroup reactor (IGR). A brief description on cycloconverter control and modes of operation is given in next subsection.

2.4.2 Cycloconverter Control

The output voltage shown in figure 2.8 tends to be a square wave rather than a continuous sine waveform. This means the output voltage will contains a large low order harmonics. Hence, a firing angle delay (α) need to be introduced to each thyristor in order to shape the output waveform as closer as possible to the desired output sinewave. For example, the three phase to single phase cycloconverter given in figure 2.9 is used to supply single phase load at maximum output voltage.

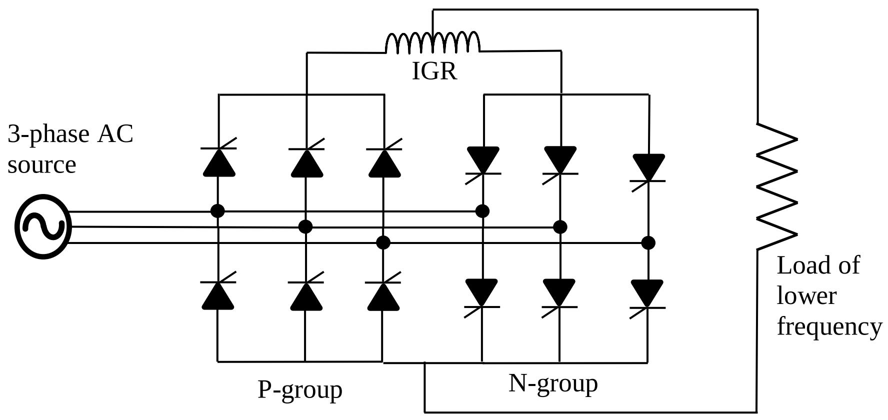

Figure 2.9: Three phase to single phase Cycloconverter structure.

The thyristor firing angle (α) is controlled to switch on each thyristor with a specified delay so that the constructed output voltage follow as closely as possible to the desired output waveform. Figure 2.10 shows the input and the output voltage waveforms of a 60 to 20 Hz single phase cycloconverter connected to a resistive load.

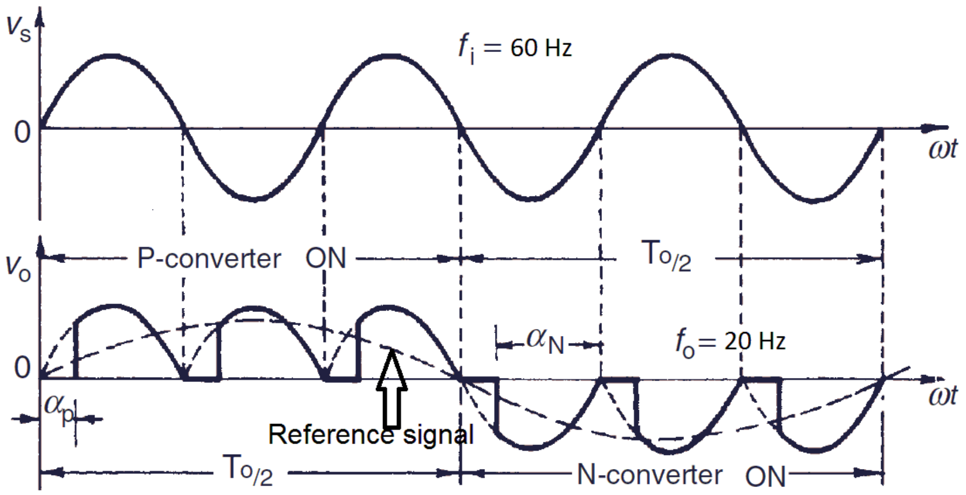

Figure 2.10: Input and output waveforms of 60 Hz to 20 Hz cycloconverter.

The fundamental output voltage of the positive and negative converters (V_P and V_N) of the cycloconverter are given by [39, 42]:

$$V_P = V_{do} \cos[\alpha_P(t)] \qquad (2.3)$$

$$V_N = -V_{do}\cos[\alpha_N(t)] \tag{2.4}$$

$$\alpha_P = \pi - \alpha_N \tag{2.5}$$

Where, V_{do} is the average dc output voltage when the firing angle delay is zero (as depicted in figure 2.8), and obtained as follows [42]:

$$V_{do} = V_{domax}\cos\alpha \tag{2.6}$$

$$V_{domax} = \sqrt{2}\,V_{ph}\frac{p}{\pi}\sin\frac{\pi}{p} \tag{2.7}$$

where, V_{ph} is the per-phase input voltage, p is the cycloconverter number of pulses, α_p is the firing angle of the positive converter, and α_n is the firing angle of the negative converter. Figure 2.11 shows the maximum voltage obtained from three phase cycloconverter by varying the firing angle (α) from 0 to π for all thyristors in each group. Therefore, the positive group or negative group thyristors receive firing pulses which are timed such that each group delivers the same mean terminal voltage. This is achieved by adjusting the firing angle limits of the two groups so that $\alpha_P = \pi - \alpha_N$; where α_P and α_n are the positive and negative groups firing angles respectively.

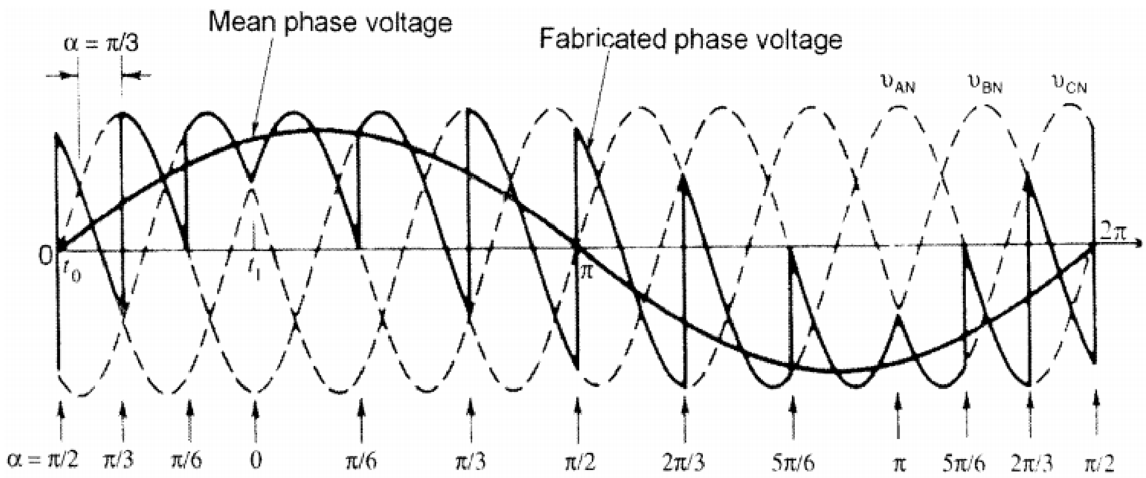

Figure 2.11: The maximum output voltage of a cycloconverter [40].

Thus, the average dc output voltage V_P of the positive or negative group in a 6-pulse cycloconverter that is controlled by adjusting the firing angle (α) can be given as follows [39]:

$$V_P = V_{domax}.\cos\alpha \tag{2.8}$$

and

$$V_{domax} = \frac{6\sqrt{2}}{2\pi} V_{ph} \tag{2.9}$$

where, V_{domax} is the dc output voltage with zero firing delay (given in figure 2.8), V_{ph} is the per-phase supply voltage. A common control method has been introduced to control the firing angle delay called cosine wave crossing control [40]. In this method, the firing angle delay is obtained by comparing the desired output waveform with a cosine reference of the input voltage. According to equations 2.3 and 2.4, the required variation of α to obtain a sinusoidal output can be given by [39]:

$$\alpha = \cos^{-1}\left[\frac{V_{oref}}{V_{domax}} \sin 2\pi f_o t\right] \tag{2.10}$$

where, V_{oref} is the maximum value of the desired cycloconverter output, and f_o is the output frequency. The term (V_{oref}/V_{domax}) is defined as the voltage magnitude control ratio (r) [39]. Figure 2.12 illustrates the basic layout of the cosine wave crossing control method applied for three-phase to single phase cycloconverter. In this method, a cosine timing signal is obtained from the supply input voltage using integrator. Then, a sinewave reference signal that has the desired output frequency is compared with the obtained cosine signal, in this case using a phase locked loop (PLL) given in figure 2.12. The intersection of the reference voltage with the corresponding cosine wave determines the trigger pulse for each thyristor in the cycloconverter group. Therefore, the amplitude and frequency of the output voltage can be controlled by controlling sinewave reference signal.

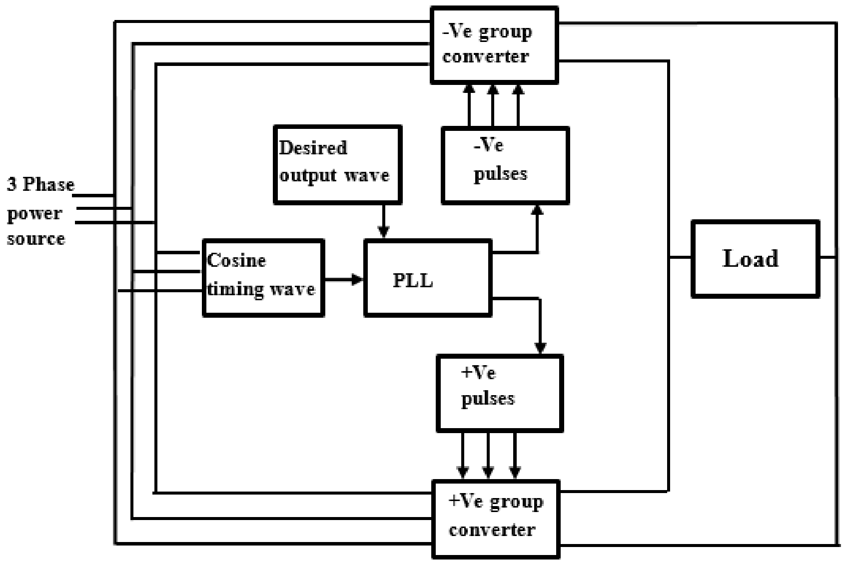

Figure 2.12: Control scheme of three phase to single phase cycloconverter [40].

The utilised control method tries to construct the output voltage of the cycloconverter as close as possible to a sinusoidal waveform, see figure 2.11. However, it is clear that the output voltage waveform of the cycloconverter contains other frequencies components, or so called harmonics, in addition to the desired output frequency as a results of the modulation of the firing angle. These harmonics are highly dependent on the several factors related to the design of the cycloconverter such as, the pulse number of the converter and the ratio of the output to input frequency. Numerous studies have been conducted on the minimisation of those harmonics by improving either the control method, the filtering system, or the cycloconverter topology [35, 41, 43, 44]. A recent study by Xu et al [44] has proposed a hybrid-cycloconverter that utilises additional auxiliary forced commutated inverter in order to improve the control of the cycloconverter and so the quality of the output voltage. A wide range of control methods have been proposed, but the cosine crossing method sill in wide use for cycloconverter applications [43]. Therefore, in this thesis it has been utilised for the control of the frequency stepdown cycloconverter applied to the HVLF system.

There have been a number of frequency changer types such as the multi-level matrix converter and the DC link (AC-DC-AC) converter that have been proposed in literature as well as practical applications[33, 34]. However, still theses configurations require large filtering systems in addition to the complexity of its configuration and control system. Nevertheless, the cycloconverter is preferred as a step-down frequency changer for high power ratings applications due to its mature technology and low cost. With the rapid development in the semiconductor devices technologies, a high power rating cycloconverter can be implemented using high rating thyristor switches (rated up to 5kv) [41]. In contrast, the utilisation of the cycloconverter as a step-up frequency changer, in which a higher frequency output is constructed from lower frequency input, still not an ideal choice. In addition to the force commutation control that the step-up cycloconverter requires, the output voltage and current waveform will have large unwanted low order harmonics which are very difficult to filter out. Hence, this thesis adopts a high voltage three-phase to three-phase cycloconverter as a step-down frequency changer located at the sending end for the HVLF system.

2.4.3 Sending End Transformer

The sending end transformer is used to step-up the voltage to a required level for transmission. As mentioned previously, several studies have proposed HVLF system structure that employs the generation of electrical power at lower frequency from renewable power plants with a low frequency step-up transformer [15-17, 22]. These studies did not take into account, when generating power at low frequency, the sending end step-up transformer needs to have a larger core cross-section area and a higher number of winding turns [33]. This is because, the induced voltage of a transformer is proportional to the operational frequency as given in equation (2.11) [33]:

$$E_{rms} = \frac{2\pi}{\sqrt{2}} f N_a \qquad (2.11)$$

Where, E_{rms} is the induced voltage of the transformer, N_a is the primary or secondary number of turns, B is the maximum flux in the core, and f is the operational frequency. So reducing the frequency by any factor will require a corresponding increase in the number of turns. Furthermore, the primary inductance must be increased to maintain the same magnetising current. This is achieved by also increasing the number of turns and/or the core-cross-sectional area. Increasing the core area and numbers of turns will result in increasing the weight and footprint of the transformer. A recent study in [33] shows that a transformer operating at low frequency of 16.7 Hz (1/3 of 50Hz) will be heavier and larger in size in comparison with 50 Hz transformer of the same rating. Figure 2.13 show a comparison between 50 Hz conventional transformer and 16.7 (1/3 of 50 Hz) transformer proposed in [33].

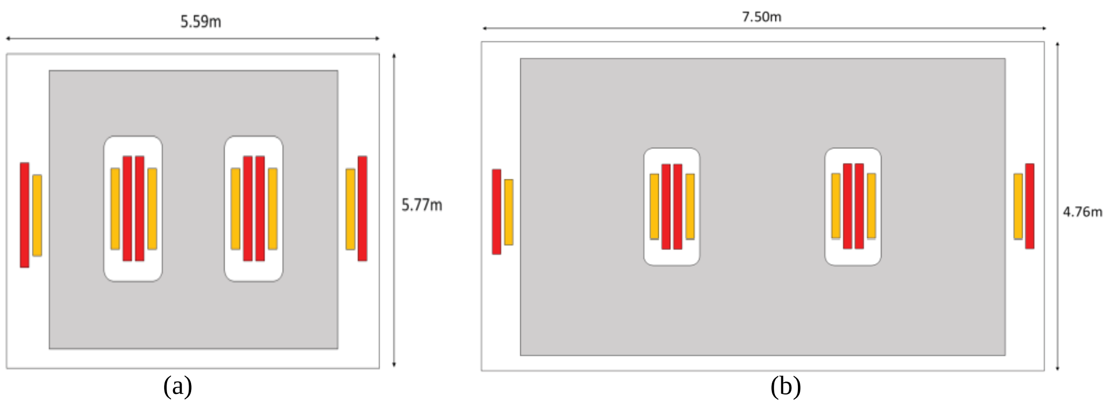

Figure 2.13: (a) 50Hz conventional transformer and (b) 16.7 (1/3 of 50 Hz) transformer [33].

Implementing this type of transformer for OWFs power collection is not preferred, as the offshore platform needs to be redesigned in order to accommodate the heavy weight and larger size transformer. In addition, the total cost of the transformer and the platform implementation will be relatively high. Although many researchers have been carrying out work on HVLF transmission, no single study adequately found an optimum design for the sending end transformer [22, 33]. As a solution to the limitation of the sending end transformer, a high voltage power electronic frequency changer is still required at the sending end [35].

2.4.4 HVLF Cables

The submarine power cable technologies used for power transmission in both HVAC and HVDC systems have developed rapidly in recent years [15, 22]. In the last several decades, submarine cables of high voltage level (up to 420 KV) have been implemented on offshore power transmission [22]. Nowadays, single core and multi core cross-linked polyethylene (XLPE) cables with low dielectric losses and lower mutual capacitance are in operation for HVAC and HVDC power transmission.

However, in high voltage long AC transmission cable, the reactive power flow will limit the maximum transmission distance due to the large cable capacitance. The reactive power (Q_c) generated in the transmission cable is given by [15]:

$$Q_c = 2\pi f C l V^2 \qquad (VAR) \qquad (2.12)$$

Where f is the frequency in Hz, C is the cable capacitance (F), l is the cable length (m), and V is the rated voltage (Volt). Therefore, the charging current of XLPE cables will increase as the line capacitance increases. Additionally, the charging current on power transmission cables is proportional to the voltage level and frequency as given in equation 2.13 [15]:

$$I_{ch} = 2\pi f C l V \qquad (2.13)$$

In contrast with HVDC, the limitation of charging current for long transmission cables does not exist. However, HVDC cables have the limitation of insulation aging and possible breakdown due to accumulation of space charge in the insulating material. The space charge accumulation in an AC cable insulator could be neglected, as the electric field direction reverses causing the flow of charges to reverse direction as well. Hence, an alternative solution to avoid these limitations, the HVLF transmission system is proposed. A test system presented by Mau et al in [25] has investigated the characteristics and the maximum transferable active power of an HVAC cable operating at various frequencies. The test cable was supplied with 220 kV AC voltage in order to deliver active power to a pure resistive load. The cable RLC parameters values were set to 0.0128 Ω/km, 0.437 mH/km and 233.0 nF/km, with a rated current of 2200 A. At each tested power frequency, the length of cable was increased until the current supplying the load reached approximately zero. The reduction in the load current is a result of increasing the cable length, and so increase the current flow through the capacitance of the cable. As shown in figure 2.14, it was found that the maximum active power can be transferred at frequencies of 50Hz, 16Hz, 15Hz, 10Hz, 5Hz and 1Hz when the cable length is 140km, 437km, 465km, 630km, 1280km and 14945km respectively.

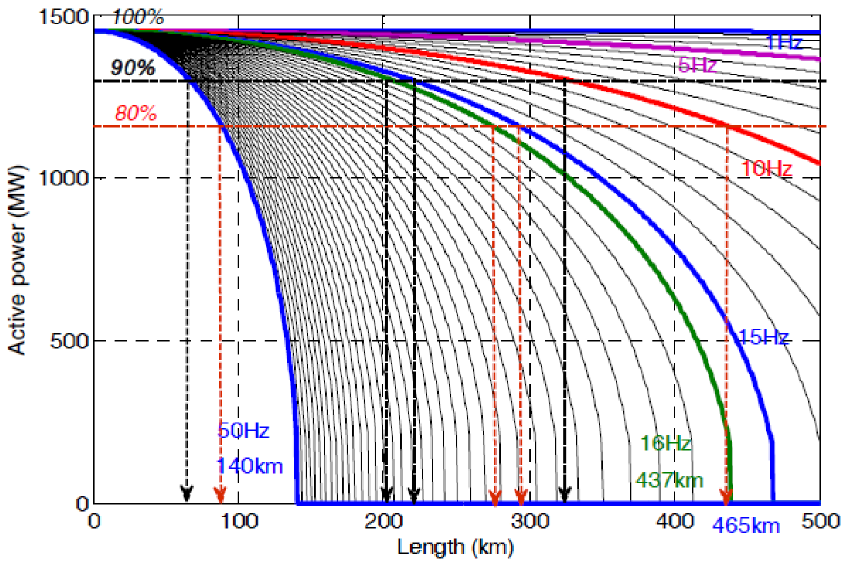

Figure 2.14: Maximum power transmission on HVAC cable at different frequencies [25].

2.4.5 HVLF protection and circuit breaker systems

In the literature, the HVLF system only has been proposed for point-to-point power transfer from remote generation stations [33]. This system could also be developed into an interconnected network comprising more terminals and links. As mentioned earlier, one of the limitations of an HVDC system is the design of the circuit breakers to interrupt high level fault currents with the absence of a zero-crossing. Although, a recently developed ABB HVDC hybrid breaker is able to break the constant high current level in very short time using combined mechanical and power electronics switching system, still the complexity and the cost of such device are high [45]. The zero current crossing exist in the HVLF system will makes the development of low frequency circuit breaker not a challenging task. Therefore, such a system only requires a full understanding of its operation and behaviour during normal and faulty conditions. Additionally, a protection and breaker systems need to be evaluated effectively in order to ensure the security and reliability of HVLF system.

In an HVLF system, the protection system of the frequency converters is a mature technology and has been implemented for several decades [22]. In general, the protection of frequency converters is based on pre-set limits for voltage and/or current levels. The HVLF transmission line protection is based on the analysis of transients occurring during fault conditions. These transients are highly influenced by several factors including the power frequency, system loading and transmission line lengths. With the high current level of the HVLF transmission line, a special attention is required for fault detection and clearing time. In addition, the existence of harmonics generated by the frequency changer that injected into the line makes the conventional transients based protection methods encounter difficulties in fault diagnosis.

This research has been focused on developing an HVLF transmission line protection system that is able to provide accurate and reliable protection performance. To achieve this, an analysis of the HVLF system including the control and operation of the frequency changer and the generated harmonics was carried out. The harmonics that exist in HVLF transmission line during normal and fault conditions has been captured and analysed. The selection of a suitable analysis tool in order to provide comprehensive details of those harmonics, in term of magnitude and time, has been investigated. This analysis was performed by simulating the system in the Matlab-Simulink software. Additionally, the study has investigated the system behaviour under different transmission line fault conditions.

2.4.6 HVLF Advantages and Disadvantages

It was shown in the previous sections that the HVLF systems have many advantages over the conventional HAVC and HVDC transmission systems. These advantages can be summarised as follows:

- The active power transfer capability of the transmission line is increased by reducing the operation frequency that results in reactive power reduction.
- Although the HVLF systems operates at high rated current, the presence of zero current crossing allows mature HVAC circuit breakers technology to be used with minor modification if necessary. Hence, the realisation of HVLF multi-terminal offshore grid becomes feasible.
- The service life of the subsea cable will increase as the alternating field mitigates the space charge accumulation mechanism and thus reduces the aging effects of the XLPE cable.

- The conventional wind turbine generators, offshore collection network, and conventional HVAC transformers can be retained by introducing a frequency changer at the sending end.

However, there are some disadvantages that need to be considered when implementing HVLF system like:

- The frequency changer at the sending end generates high frequency harmonics. Therefore, ac filters are required to supress harmonics and supply reactive power to the frequency changer.
- The HVLF system is highly dependent on the reliability of the frequency charger.
- The implementation of multi-terminal HVLF network need to meet the grid code in terms of voltage stability and frequency synchronisation.

Chapter 3
Wavelet Transform for Fault Transients Analysis

Recently, digital relays have been used to detect power system faults by analysing the high frequency transients associated with the fault [46, 47]. Since, in many cases when a fault occurs many transient components with multiple frequencies will be generated, these transient components could be utilised to obtain fault information such as fault type and location [46]. A fault identification algorithm based on the utilisation of the higher frequency contents of the transient signals was firstly proposed by Dommel et al in [48]. The authors used voltage and current waveforms at the relay point in order to detect the fault on the transmission line. Later, numerous algorithms have been proposed to improve the performance of digital relays by introducing several signal analysis tools such as Fourier Transform, Short Time Fourier Transform (STFT) and wavelet transform (WT) [49]. The aim of these signal processing tools is to provide a more understandable and accurate time or frequency representation of the analysed signals. This chapter presents a brief review on the development in signal processing techniques applied to the transient signals analysis.

3.1 Fourier Transform

The Fourier Transform has been widely applied as a signal processing tool to represent signals from the time domain into the frequency domain [50]. This is done by decomposing the signal into a sum of sine and cosine functions over the time window of interest. The Fourier transform *X(f)* of a continuous time signal *x(t)* is given by:

$$X(f) = \int_{-\infty}^{\infty} x(t)\, e^{-i2\pi f t} dt \tag{3.1}$$

The discrete Fourier Transform (DFT) is applied to convert a sampled signal $x[n]$ (where n is an integer) to another discrete sequence $X[k]$ of frequency coefficients. The DFT is defined as:

$$X(k) = \sum_{n=0}^{N-1} x[n]\, e^{-i2\pi kn/N} \tag{3.2}$$

or in terms of sine and cosine functions as:

$$X[k] = \sum_{n=0}^{N-1} x[n] \cos 2\pi kn - j\, x[n] \sin 2\pi kn \tag{3.3}$$

Where, N is the total number of samples in the input signal, and $k = 0, 1, 2, \dots . N-1$. Fourier analysis requires the input signal to be a complete cycle waveform and sampled according to the Nyquist sampling theorem [51]. An example of the output from the Fourier analysis of an input signal contains frequencies of 20, 100 and 313 Hz is shown in figure 3.1. The figure shows there are two frequency peaks at 20 and 100 Hz and there are frequency sidebands around 313 Hz. These sidebands are the result of the presence of non-periodic (not multiples of the fundamental 20 Hz) components in the analysed signal. The percentage magnitude of each frequency presents the existence of that frequency existence during the analysed period. Hence, it is clear that the Fourier transform has a limitation of obtaining transient frequencies that are not multiple of the fundamental. These frequencies are represented by a lower magnitude sidebands distributed around the actual frequency that exist in the signal as shown in figure 3.1. Therefore, another technique has been introduced to overcome the limitation of the Fourier transform, which is the Short Time Fourier Transform (STFT) or Windowed Fourier Transform [52].

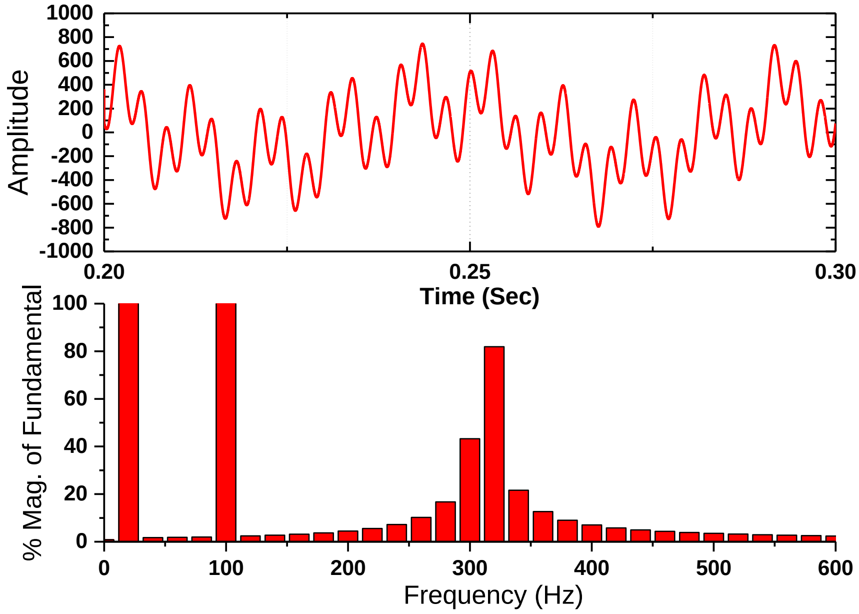

Figure 3.1: Example of Fourier Transform for a signal *x(t)*.

3.2 Short Time Fourier Transform (STFT)

In the STFT the analysis is performed over a sliding window translated in time. The part of the signal within the sliding window is assumed to be periodic. Therefore, for a discrete signal *x[n]* having *N* samples the STFT can be obtained by:

$$STFT(k,m) = \sum_{n=0}^{N-1} x[n]\, w[n-m] e^{-\frac{i2\pi kn}{N}} \tag{3.4}$$

where, $w\,[n]$ represents the window function in which the Fourier transform is being performed, $[n-m]$ is the width of the window and $k = 0,1,2,\dots.N-1$.

The analysis window function could be a rectangular, Gaussian or Hamming etc. depending on the application of the analysis. Figure 3.2 shows an example of the STFT performed on the signal *x[n]*, at every window function *w[n-m]*, shifted by time τ along the time axis. Subsequently, the Fourier Transform is performed on the entire signal through consecutive steps of the analysis window. Hence, the STFT decomposes a time domain signal into a two dimensional time-frequency representation.

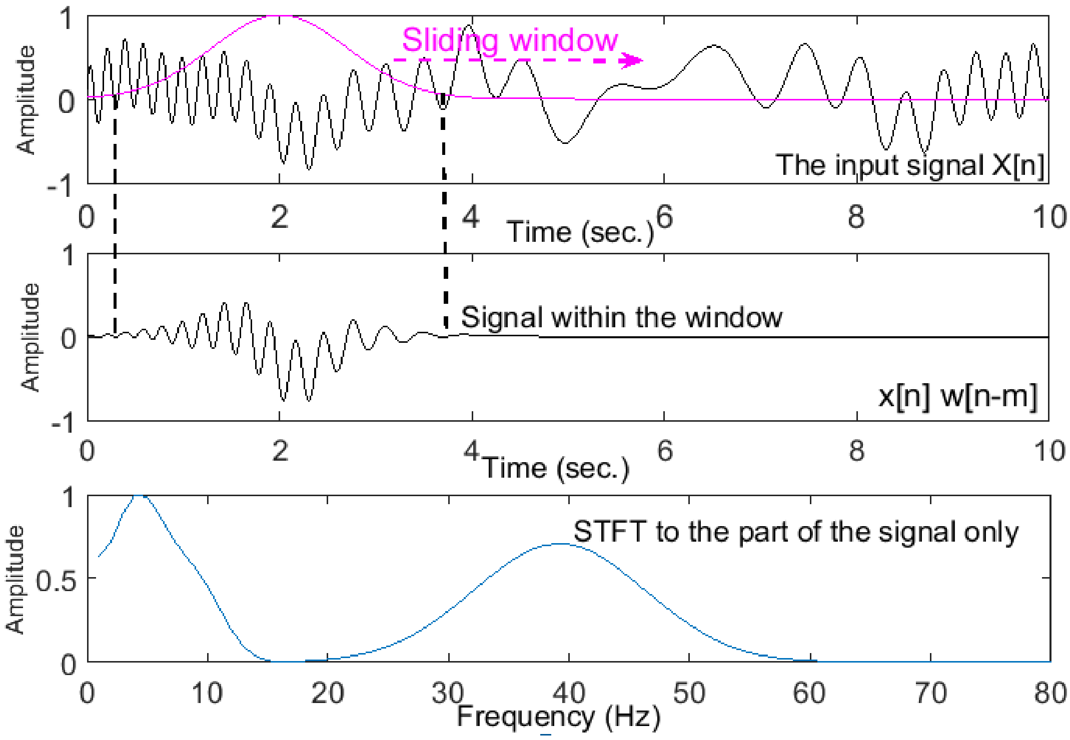

Figure 3.2: STFT for an input signal *x[n]*.

The STFT provides frequency information of the signal during a time range that is limited by the window function, see figure 3.2. This will show what particular frequencies exist in the signal at that time and a time-frequency localisation can be obtained. However, the accuracy of this time-frequency localisation is determined by the size of the analysis window. Figure 3.3 illustrates three analysis windows of different width applied to perform an STFT on a signal $x[n]$. It is obvious that selecting a narrow analysis window provides good time resolution but have poor frequency localisation, because only high frequencies can be detected. While, selecting wide analysis window results in good frequency localisation as the low and high frequencies can be obtained, but poor time resolution.

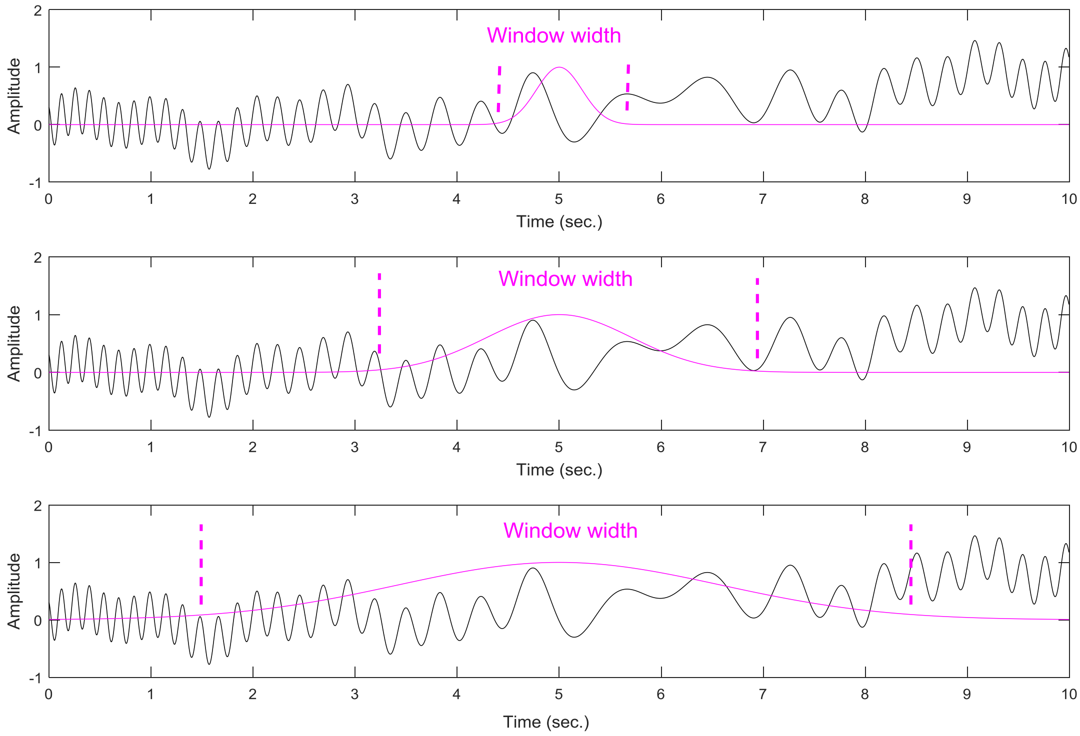

Figure 3.3: Different window sizes of STFT analysis.

Therefore, STFT analysis needs a compromise between the time and frequency localisation. Figure 3.4 shows how the fixed size of the analysis window is resulted in either a good time localisation or good frequency resolution but not both. Therefore, by using STFT in the analysis of non-stationary transient signals it is not possible to obtain the exact time-frequency representation of a signal. But it is possible to find what interval of frequencies exist during each time interval.

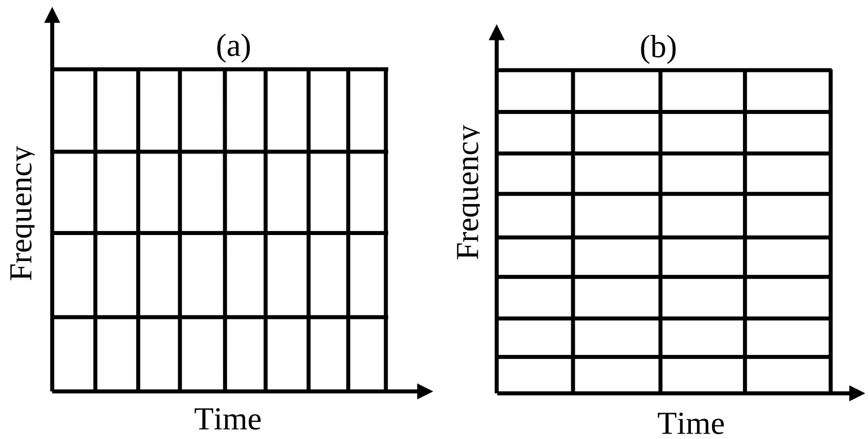

Figure 3.4: Time and frequency resolution at different window sizes of the STFT.

3.3 Wavelet Transform

For a solution to the fixed window size of the STFT, the Wavelet Transform has been introduced [53]. The fixed width window function of the STFT is replaced by a wavelet function or so called mother wavelet. The wavelet analysis is performed by comparing the input signal to scaling and translating versions of the wavelet. The scaling or dilation of the wavelet function refers to stretching or narrowing of the analysis function. While, the translation of the wavelet function is defined as the shift of the analysis function along the time axis of the input signal. Figure 3.5 illustrates an example of the Wavelet Transform analysis of the signal *x(t)* using a mother wavelet shifted by time, τ [52].

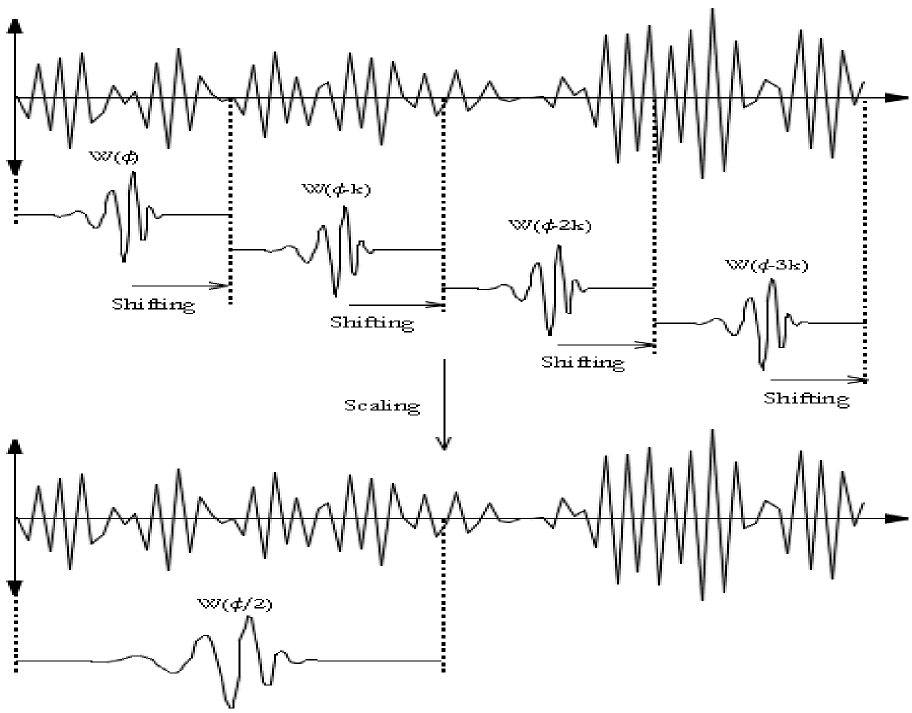

Figure 3.5: Wavelet transform for the signal *x(t)* [52].

The figure above shows how the Wavelet Transform function has the ability to adjust in width with high and low frequency components of the analysed signal. This gives the Wavelet Transform the ability to extract frequency components of fast transient signals. There are two main types of wavelet transforms; the Continuous Wavelet Transform

(CWT) and the Discrete Wavelet Transform (DWT). A brief description of these two types of Wavelet Transform is given in the next subsections.

3.3.1 Continuous Wavelet Transform

The continuous wavelet transform (CWT) of an input signal $x(t)$ is given by:

$$CWT(a,b) = \frac{1}{\sqrt{a}} \int_{-\infty}^{\infty} x(t)\, g^{*}\left(\frac{t-b}{a}\right) dt \tag{3.5}$$

where $x(t)$ is the input signal, the mother wavelet is $g^{*}(t)$, and the scale and translation factors are a and b respectively. The CWT analysis operates by varying the wavelet scaling parameter a and the shifting parameter b and compares it with the signal along the time axis. Starting with a low scale parameter (narrow wavelet), this obtains the high frequency components of the input signal; the higher the scale (stretching) then the lower frequency features can be extracted, see figure 3.5.

In the above equation, the applied mother wavelet $g^{*}(t)$ is a limited duration wave function that satisfies certain mathematical requirements. This function is normalised ($\| g^{*}(t) \|^2 = 1$) so that all wavelets at any analysis level have the same energy of the mother wavelet and have a zero average ($\int_{-\infty}^{\infty} g^{*}(t) dt = 0$). There are many types of mother wavelets and each have different characteristics that applies to various applications for example Haar, Daubechies, Symmlet, etc., see figure 3.6. Most of these wavelet functions are oscillating in time and the wavelet order (for example db4) determines its vanishing time. The selection of the mother wavelet has a major impact on the analysis of the decomposed signal. The wavelet type and order is determined by the nature of the application and the signal characteristics to provide optimum results.

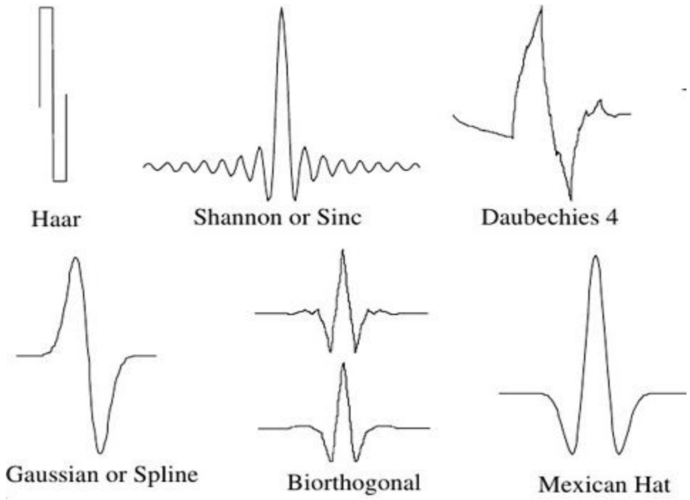

Figure 3.6: Different types of wavelet functions.

As given in equation 3.5, the result from the CWT at a particular scale and translation is a two dimensional time-frequency representation of the input signal. This results in a high redundancy, where the continuous wavelet transform produce a two dimensional representation of a one dimensional time series signal.

3.3.2 Discrete Wavelet Transform

The digital implementation of the CWT is the Discrete Wavelet Transform (DWT). The DWT applied for the analysis of a sampled input signal *x[n]* is given by:

$$DWT(m,k) = \frac{1}{\sqrt{a}} \sum_{n} x[n]\; g^{*}\left(\frac{k-b}{a}\right) \qquad (3.6)$$

Where *k* is a particular sample of the input signal.

For a discrete signal analysis, the DWT is applied to decompose the input signal into a series of scaled wavelet components. These components are obtained by the scaling and translation of the mother wavelet with the processed signal. This is achieved by passing the input signal into multiple stages of lowpass and highpass filter banks. When the input signal is passed through a lowpass filter the approximation coefficients are obtained, and when passed through a highpass filter the detail coefficients are obtained simultaneously, see figure 3.7.

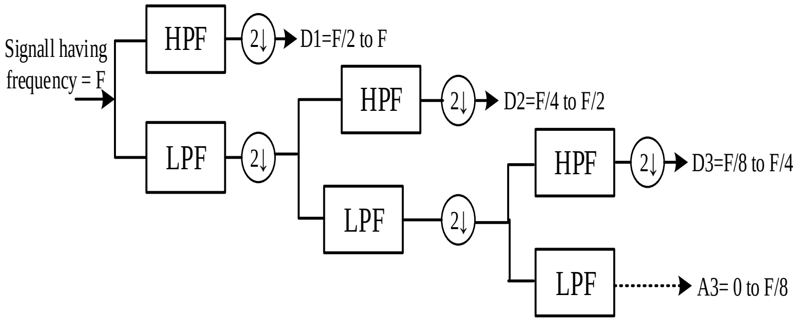

Figure 3.7: The DWT multi-resolution analysis.

The output of the lowpass filter (the approximation coefficients) is fed again into another set of highpass and lowpass filters for obtaining further detailed and approximation coefficients. This process is repeated until the original signal is decomposed to the required level. At each stage, the sampling frequency of the output signal is halved to overcome the redundancy. Since a different frequency resolution obtained on each analysis level, this type of analysis called multi-resolution wavelet analysis (MRA). Figure 3.8 illustrates time and frequency resolution obtained from the wavelet MRA. Each box represents a particular band of frequencies (scaled) that exist in the analysed signal during a particular time window. The dimensions of each box correspond to time-frequency resolution. Starting from low scale (top of the figure) narrow boxes provides good time representation with wide frequency range (poor frequency resolution). As the scale increases, the height of the boxes decreases providing a good frequency resolution over a wider time range (poor time representation). Thus, low frequency content of the signal is obtained at the final analysis level.

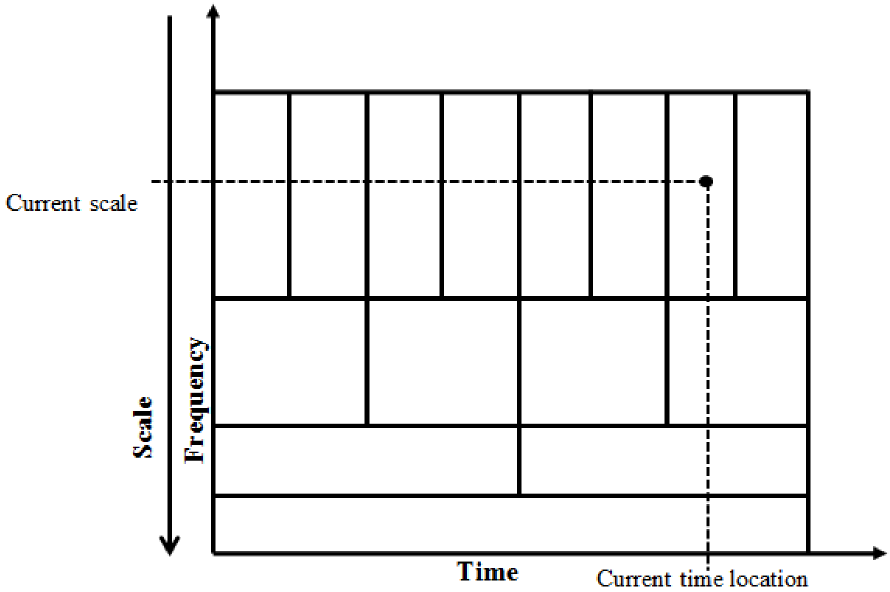

Figure 3.8: frequency and time resolution from the wavelet analysis.

In the Fourier Transform, the orthogonality relationship of the sine and cosine functions is employed in the analysis of periodic signals [51]. Similarly, the wavelet transform utilises two orthogonal scaling and wavelet functions for frequency analysis. At each level of the DWT the input signal convolutes the scaling function (LPF) and the wavelet function (HPF), see figure 3.7. These two functions determine the filters coefficients from the applied mother wavelet. As mentioned earlier the HPF and LPF divided the input signal into subsignals of high frequency components and low frequency components, see figure 3.9. It should be mentioned that the frequency response of the highpass and lowpass filters must be symmetric. This allows the wavelet MRA divided the signal into two symmetric halves of high frequency and low frequency components. Figure 3.9 illustrates how the signal spectrum has been spilt into two equal frequency bands by lowpass and highpass filters at each level of three level analyses. The symmetrical property of the highpass filter and lowpass filter is achieved by reversing and negating odd coefficients of each filters, see figure 3.10. For example if the lowpass filter have four coefficients (a, b, c, d) the highpass filter coefficients will be (d,-c, b, -a). This type of filter bank has been used widely in signal processing and they are known as Quadrature Mirror Filters [51].

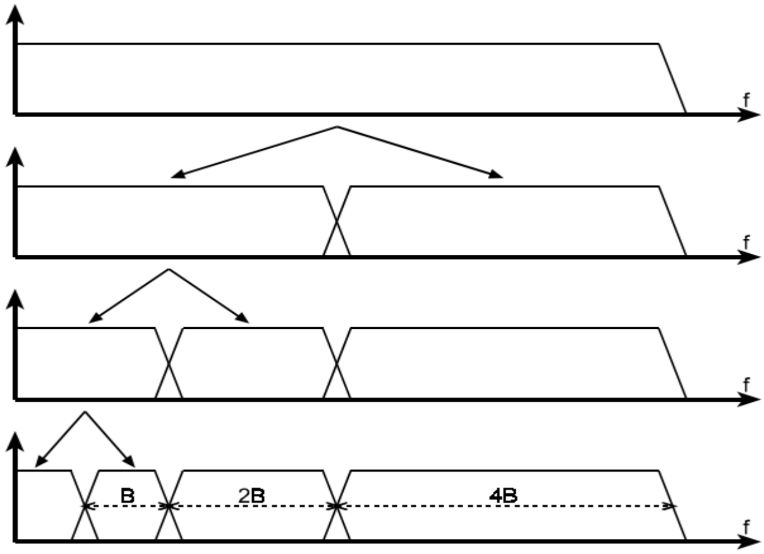

Figure 3.9: Highpass and lowpass filter frequency bands on each analysis level.

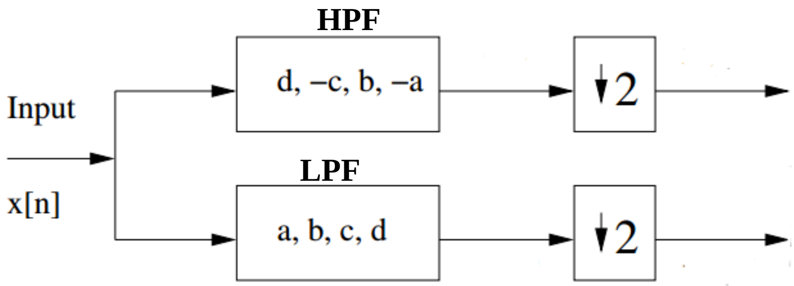

Figure 3.10: Highpass and lowpass filter coefficients applied in WT analysis.

As mentioned earlier, the filter coefficients are obtained from the scaling and wavelet functions that are derived from the applied mother wavelet. Figure 3.11 shows examples of scaling and wavelet functions with the associated filters coefficients for Haar, Daubechies 2, and Daubechies 4 mother wavelets.

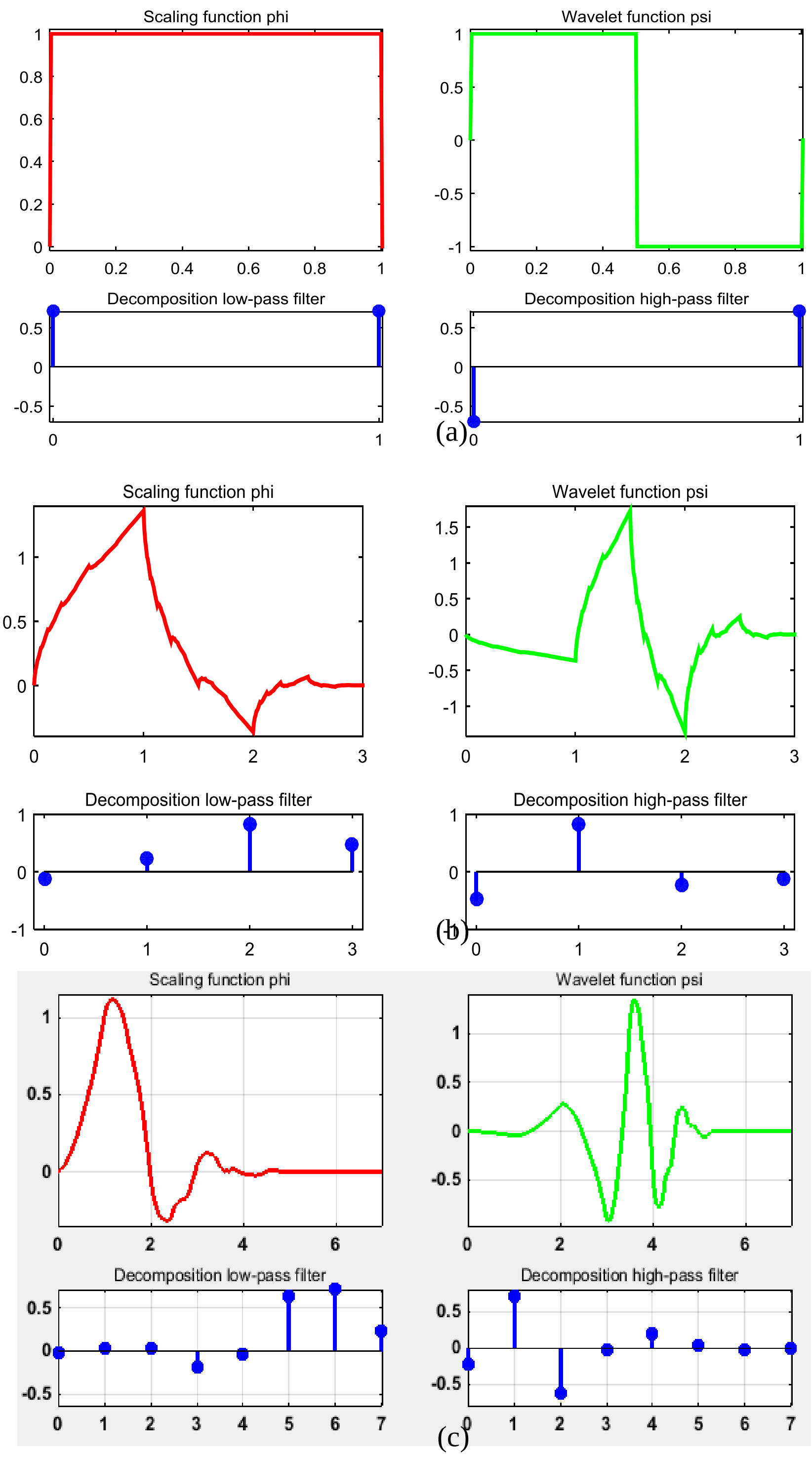

Figure 3.11: Scaling and wavelet functions with associated filters coefficients (a) Haar (b) db2 (c) db4.

3.3.3 Implementation of the Wavelet Transform

As previously illustrated, the Wavelet Transform convolves the input by the shifting and scaling of the wavelet (highpass) and the scaling (lowpass) functions obtained from the mother wavelet function. In this section a simple example is given to clarify the procedure of one level wavelet analysis into an input signal. Assuming that an input signal $x[n]$ having a number of samples equal to N is being decomposed with the Wavelet Transform using daubechies mother wavelet (db2). As shown in figure 3.11 (b), the db2 mother wavelet has four coefficients in each one of the wavelet and scaling functions. The values of these wavelet (highpass) and the scaling (lowpass) functions are given as follows:

$Wavelet\ function\ coefficients\ (h)$:

$$h1 = -0.129, \qquad h2 = 0.224, \qquad h3 = 0.836, \qquad h4 = \ 0.482$$

and according to figure 3.10 the scaling function coefficients can be given as:

$Scaling\ function\ coefficients\ (s)$:

$$s1 = -0.482, \qquad s2 = 0.836, \qquad h3 = -0.224, \qquad h4 = \ -0.129$$

Then, by applying equation 3.6, the wavelet analysis can be represented by the products of the matrices following:

$$W = \begin{bmatrix} s1 & s2 & s3 & s4 & 0 & 0 & 0 & 0 & \cdots \\ h1 & h2 & h3 & h4 & 0 & 0 & 0 & 0 & \cdots \\ 0 & 0 & s1 & s2 & s3 & s4 & 0 & 0 & \cdots \\ 0 & 0 & h1 & h2 & h3 & h4 & 0 & 0 & \cdots \\ 0 & 0 & 0 & 0 & s1 & s2 & s3 & s4 & \cdots \\ 0 & 0 & 0 & 0 & h1 & h2 & h3 & h4 & \cdots \\ 0 & 0 & 0 & 0 & 0 & 0 & s1 & s2 & \cdots \\ 0 & 0 & 0 & 0 & 0 & 0 & h1 & h2 & \cdots \end{bmatrix} . \begin{bmatrix} x_0 \\ x_1 \\ x_2 \\ x_3 \\ x_4 \\ x_5 \\ x_6 \\ x_7 \\ \vdots \\ x_N \end{bmatrix}$$

Note that, in the last iteration only two coefficients of the wavelet transform exist, because the following two elements of the input data will be processed. Figure 3.12 shows the frequency response of the lowpass and highpass filters obtained from the scaling and wavelet functions respectively. Figure 3.13 shows the analysis results of four levels Wavelet Transform. The high frequencies details were extracted during the four levels, and the final signal represents the input signal that have the fundamental frequency only.

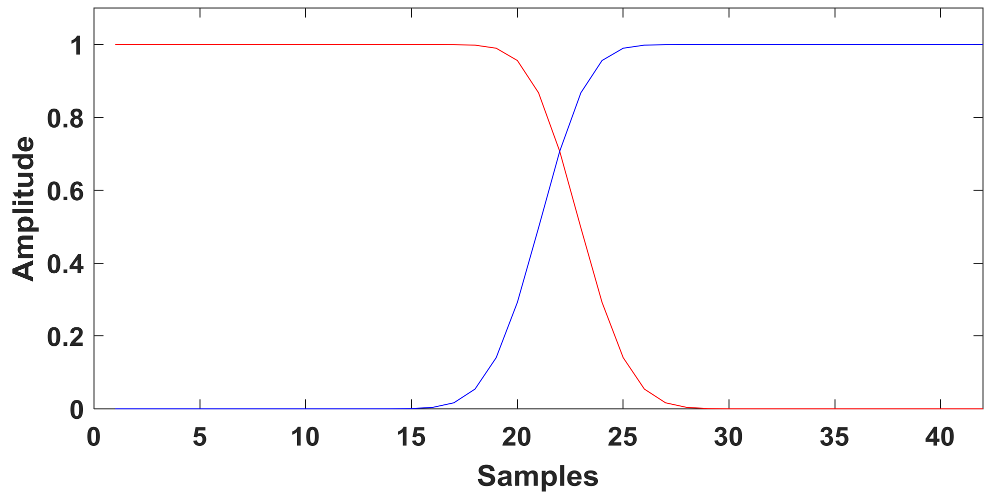

Figure 3.12: Frequency response characterises of the lowpass and highpass filters.

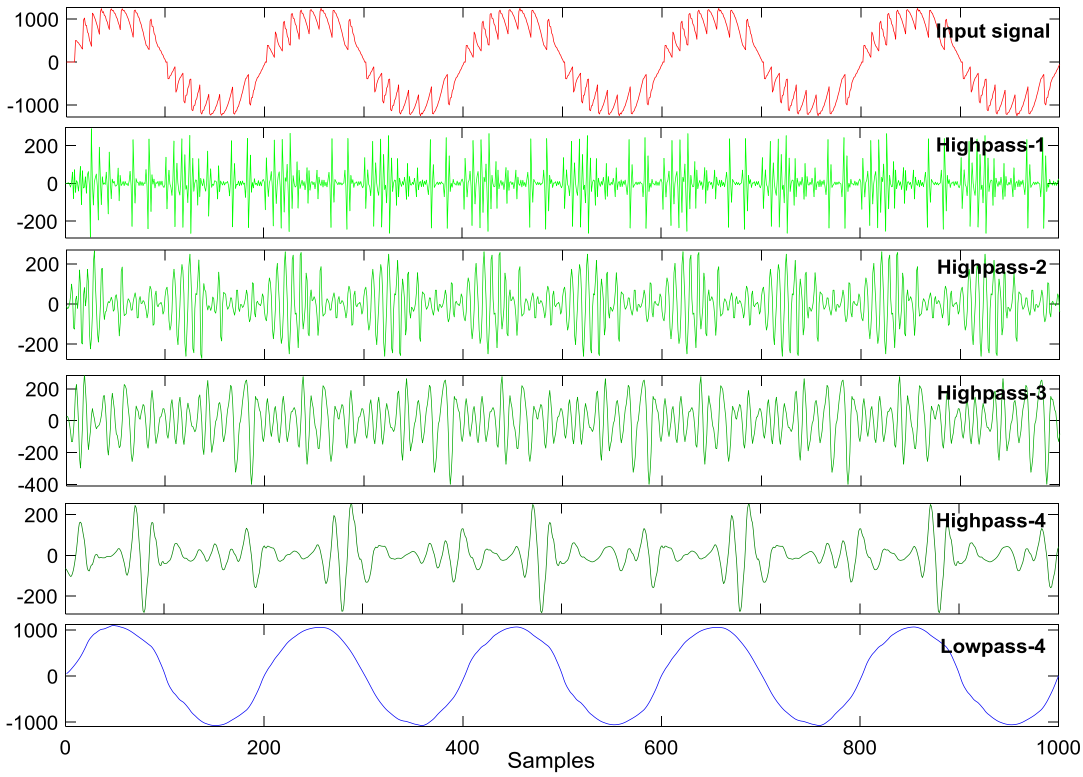

Figure 3.13: Four levels Wavelet Transform analysis of an input signal $x[n]$.

3.4 Wavelet Transform Application for Transmission Line Protection

3.4.1 Transmission line protection

Transmission line protection is an extremely important and very complex field. Protection relays that are designed to protect a transmission line should meet many different requirements in order to provide primary and backup protection, and at the same time ensure correct operation for different faults and other abnormal power system conditions. In any electrical power system when a fault occurs on a transmission line, it is essential to detect and discriminate its type accurately in order to make necessary maintenance and to recover the faulted line for power restoration. In many cases when a transmission line fault occurs, many transient components with multiple frequencies are produced. Fault information could be extracted from these transient components. Recently the transient components of fault signals have been used to predict the fault type or disturbances in power system equipment [54-56]. Improving the reliability and accuracy of the fault detection algorithms will greatly reduce the impact of the fault on the power system. Nowadays, new techniques based on utilisation of transient signals for fault diagnosis have been proposed. Therefore, to identify the fault and discriminate its type a powerful signal processing tool is required.

This thesis has discussed the HVLF system structure, and a cycloconverter at the sending end of the transmission line was proposed. By operating the transmission line at low fundamental frequency using a power electronic converter, it is expected that the fault generated transients will have different signature from those of the conventional HVAC systems. In addition, during the pre-fault condition some harmonics are exist in the system due to the utilisation of the cycloconverter. Therefore, the conventional transients based protection system may misjudge the occurrence of fault, if they applied to the

HVLF system. A high time-frequency localisation tool is therefore required to the analysis of HVLF fault signals.

3.4.2 Protection Based Wavelet Analysis

As illustrated above, the wavelet transform allows precise time and frequency localisation of transient signals. It is able to analyse a localised portion of a larger signal using its mother wavelet, and to focus on short durations where high frequency information is required; and on long durations where low frequency information is desired. Due to these properties, the wavelet transform has been successfully applied to power systems for analysing abnormal transient phenomena. Understanding these transient phenomena helps in detecting the fault within the power system.

The wavelet transform has been used widely as a mathematical tool for many applications in signal processing. It was first introduced into power systems by Riberio in 1993 [57]. The author introduced the concept of the wavelet transform for power system distortion analysis. Robertson et al [53] have presented a comparative study on fault detection using different signal analysis techniques including the Fourier transform (FT), Short Time Fourier transform (STFT) and the wavelet transform (WT). The study proved that wavelet transform provides relatively more accurate results in the analysis of non-stationary fault signals. Later, according to much literature wavelet transform for transmission line fault identification has been applied [58], including, classification [59], and fault location [60, 61].

Taking into consideration, the results from the wavelet analysis is highly dependent on the sampling frequency and the applied mother wavelet [62]. Kim and Aggarwal in [50, 63] applied the DWT analysis with different mother wavelets (Daubechies4, Symlet5 and Biorthogonal3) for fault detection on a 154 kV, 26 km long HVAC transmission line.

The fault information was extracted from the current signals with a 60 Hz fundamental power frequency and sampled at 64 samples per one cycle (3480 samples/sec.). The analysis was carried out for one level and the detailed coefficient, d1, was used for fault indication. The study showed that the DWT analysis provides an accurate fault detection decision and identify correctly the faulted phase. Also, it was shown that db4 mother wavelet has a better resolution analysis compared to the other mother wavelets.

3.4.3 Selection of Mother Wavelet

Numerous studies was carried out later applying wavelet transform analysis for fault detection and classification on transmission lines. These studies have tried to improve the detection algorithm by applying the same mother wavelet (Daubechies) with different mother wavelet orders and analysis levels. The order of the mother wavelet obtains the number of samples associated with that wavelet, for example the db2 mother wavelet has four samples while db4 has eight samples and so on, see figure 3.11 (b, c). The number of samples in these mother wavelets determines the size of the analysis window and hence the choice will depend on its application.

For transmission line fault detection, the Daubechies of order 4 mother wavelet (db4) has been used in [64-67]. In some of these studies the fault information was obtained from one level of analysis, whereas in other cases the analysis was carried out to several levels. The analysis level in all studies was obtained according to the frequency information required for fault identification. Therefore, the sampling frequency of the fault signals was varied in a range of 1–200 kHz. Additionally, other types of mother wavelets have been applied for fault detection for example, Bior2.2 in [68], Haar wavelet in [69] and Sym2 in [70]. Ekici et al tested in [71] different types of mother wavelet used in fault detection and location on a 380 kV, 360 km transmission line. By processing the three phase voltage and current signals at the sending end with five different mother wavelets (db5, bior5.5, coif5, sym5, and rbio5.5), the study proved that in multi-resolution analysis the Daubechies mother wavelet was the most effective choice for extraction of the frequency feature from the fault signal.

3.4.4 The Wavelet Analysis Level Selection

As mentioned above, the level of the wavelet analysis was varied from one level up to several levels depending on the frequency band required to capture the fault signature. Hence, the coefficients that obtained at the required level were processed for fault decision and classification. In many of the proposed protection algorithms, the spectral energy of the detail coefficient at the final analysis level was used as a fault indicator. If the spectral energy of any phase signal exceeded a pre-set threshold, a trip signal is sent to the circuit breakers, and the fault classification is carried out by comparing the spectral energy from all three phase signals.

The three phase current and voltage signals have been employed to enhance the reliability of the proposed algorithms [59, 72-74]. However, many studies have employed wavelet analysis to the current signals only in order to reduce the processing time and improve the detection speed [46, 61, 75]. In both cases these signals where obtained at either single end or at both ends of the transmission line. The studies in [55, 59] have applied the Wavelet Transform to the current signal only obtained at both ends of the line and synchronised with the help of GPS satellite to obtain the fault location. Other studies have used the current signals that was obtained at one end of the line in order to eliminate the need for the data transmission link [46, 67, 76].

All the above studies have proved that the Wavelet Transform analysis has the ability to extract fault information from the captured signals and provide an accurate fault detection decision. The wavelet analysis has been applied to different transmission lines with different configurations and power capacity. For HVAC systems wavelet analysis has been successfully able to detect and classify faults on the transmission line as given in [46, 55, 59, 64, 67, 68, 71, 73-75, 77]. In the HVDC transmission systems the transient current signals were analysed with the wavelet transform and many protection algorithms have been proposed [8-10, 78-80].

Barros et al in [56] and Perez et al in [61] proposed a Discrete Wavelet Packets Transform (WPT) for signal frequency decomposition in order to improve the overall performance. In the WPT both the detailed and approximation coefficients at any level of the analysis are decomposed again to produce new detailed and approximation coefficients [81]. Figure 3.14 illustrates a two levels WPT of an input signal having a sampling frequency equal to *F*. As a result, the wavelet packet analysis provides a better high frequency resolution of the decomposed signal. In this research, an investigation into the application of the WPT to transmission line protection was carried out in the past years. A paper was published by the author of this thesis in 2014 proposing an HVAC transmission line protection algorithm based on the analysis of fault transient signals [82]. In the summary, it has been shown that the Wavelet Transform is a powerful analysis tool for time-frequency localisation of transient signals.

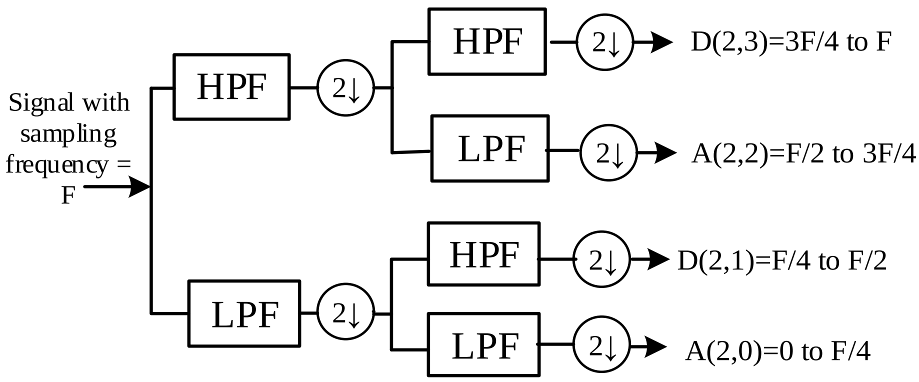

Figure 3.14: The Discrete Wavelet Packets Transform structure.

As previously mentioned, the HVLF system requires a high time-frequency resolution tool for the analysis of the fault signals. Therefore, in this research, the WPT is proposed for transmission line transient analysis of the proposed HVLF systems. The WPT provides higher frequency details by extracting frequency features from both the approximation and detailed coefficients, see figure 3.15. This allows the WPT to provide details on high frequencies within short analysis level, resulting in a high accuracy detection of faults.

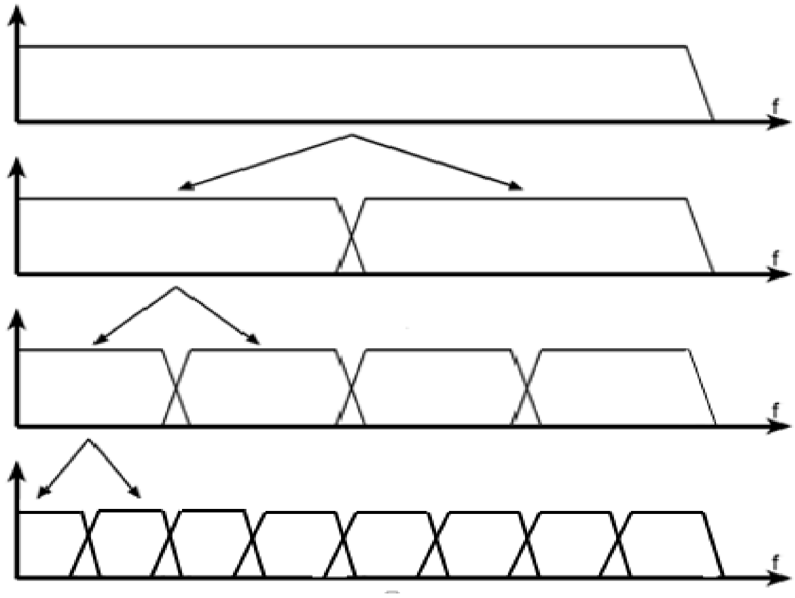

Figure 3.15: Highpass and lowpass filters frequency band of WPT on each analysis level.

Chapter 4
HVLF System Modelling and Simulation

4.1 Overview

This chapter presents the design details of the proposed High Voltage Low Frequency (HVLF) power system. Firstly, this system is designed to transfer 200 MW offshore generated power over a 200 km, 20 Hz HVLF transmission line. Figure 4.1 illustrates a schematic diagram of the HVLF system modelled with Matlab-Simulink software [26]. Matlab software has been chosen for this modelling due to its ability for both power systems simulation and signal analysis. As discussed in the literature survey of this thesis, unlike the HVAC or HVDC systems, to date there is no standard benchmark for steady-state or transient studies of the HVLF system. However, in this thesis the modelling of the HVLF system was built up using standard data provided by either IEEE standards or manufacturers. Hereby, the line parameters and transformer configurations etc. were set according to the practical electrical parameters [83]. This was carried out to ensure accurate results obtained from the model when performing various experiments.

In this model the power was generated and collected with the conventional topology. Hence, this study adopts a cycloconverter at the sending end in order to step down the transmission frequency. This design had the advantages of eliminating the need for the large size low frequency transformer.

Note that another frequency changer is required to step-up the frequency at the receiving end in order to inject the transmitted power to the utility grid. However, utilising a cycloconverter as a step-up frequency changer is not a suitable choice for the HVLF system application, due to its highly distorted output voltage waveform and the requirement for forced commutation control [22]. Furthermore, a complex filtering system is required in order to eliminate the switching generated harmonics. The selection and utilisation of the receiving end frequency changer is retained as part of the future work.

In this research, the step-up frequency changer was not considered, and it was replaced with a parallel connected load and a 20 Hz voltage source. This is because the main objective of this study was to investigate the effect of the sending end cycloconverter generated harmonics on the fault generated transients and the protection system as well. Additionally, the main objective was to investigate the system behaviour under transmission line fault conditions. This was achieved by applying short circuit faults on the line phases and monitor the voltage and current signals from a single line end. The measurement point is set near to the sending end at busbar 3 of the system. The captured signals were analysed initially with the Fast Fourier Transform (FFT) in Matlab. The FFT is used to identify the frequency range of these transients. This will help in developing a line protection scheme based on the utilisation of these transients.

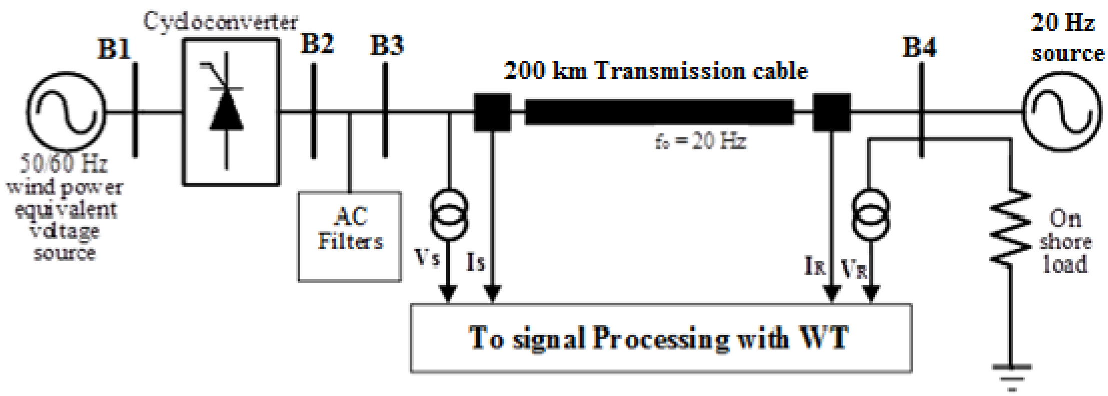

Figure 4.1: The schematic diagram of the modelled HVLF system.

4.2 HVLF System Modelling

The HVLF system modelled with Simulink is comprised of a power collection point at Bus1, a cycloconverter at the sending send, harmonic filters and the transmission line. The wind turbines connected to a 60 Hz step-up transformer and the collection network are represented by an equivalent three phase AC source in order to simplify the system. The AC sources at the sending of the model each had a resistance of 0.025Ω and a reactance of 1.85Ω at 60Hz frequency, this was based on a 230kV transmission system as shown in table 4.1[84].

Table 4.1: Parameters of the sending end Source

Base voltage/ V	**Resistance/ohms**	**Reactance/ohms**	**Frequency/** Hz
230e3 V	0.025	1.85	60 Hz

The cycloconverter is used to step down the 60 Hz frequency of the transmission voltage to 20 Hz. A 60 Hz frequency was chosen for the transmission voltage in order to obtain an integer number (20 Hz) when stepping down the frequency by 1/3 conversion factor of the cycloconverter. However, the cycloconverter control still can be modified to convert 50 Hz system to 16.7 Hz. The onshore end of the line was represented by a load connected at Bus 4 equivalent to the onshore station and the grid. The receiving end source and load details are shown in table 4.2.

Table 4.2: Parameters of the receiving end source and load.

	Base voltage/ V	**Resistance/ohms**	**Reactance/ohms**	**Frequency/** Hz
Source	230e3	1.02	0.25	20
Load	230e3	191.2	16.58e-3	20

In this chapter, the cycloconverter configuration, control and harmonics filtering are given in detail. Then, the frequency conversion and the power transfer have been validated by observing the power flow during normal operation.

4.2.1 AC-AC Frequency Conversion

As mentioned earlier, in the proposed HVLF system, the frequency converter located at the line sending ends is required in order to step-down the transmission frequency. Hence, this research adopts a high voltage three-phase to three-phase cycloconverter as a frequency changer. The cycloconverter model consists of three sets of three-phase to single-phase units as shown in figure 4.2.

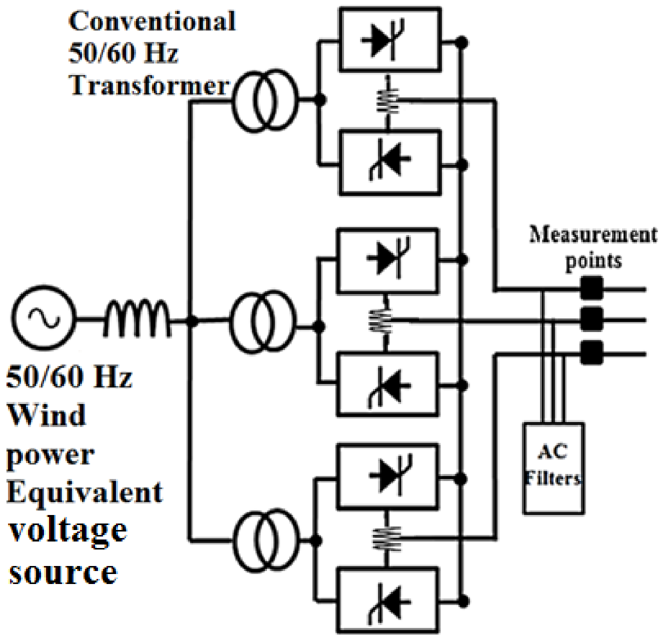

Figure 4.2: Three-phase cycloconverter simulated in Matlab Simulink.

A 6 pulse-36 thyristor, in which each 12 thyristors form a three phase to single phase cycloconverter, has been simulated using the Matlab Simulink software, see figure 4.3. The cosine wave crossing control method was used to control the firing delay angle [40]. In this method, the firing delay angle is obtained by comparing the desired output waveform with a cosine reference synchronised with the input voltage. The firing delay determines which individual thyristor is triggered so that the required output voltage waveform is constructed. The firing angles are adjusted so that the output voltage is kept close to a sinusoidal form. The cycloconverter given in figure 4.3 consists of two anti-parallel three phase bridges, in which one of the bridges carries the positive current while the other one carries the negative current. This allows the cycloconverter to operate in a four-quadrant operation providing a lagging or leading power factor output, and bi-directional power flow [42].

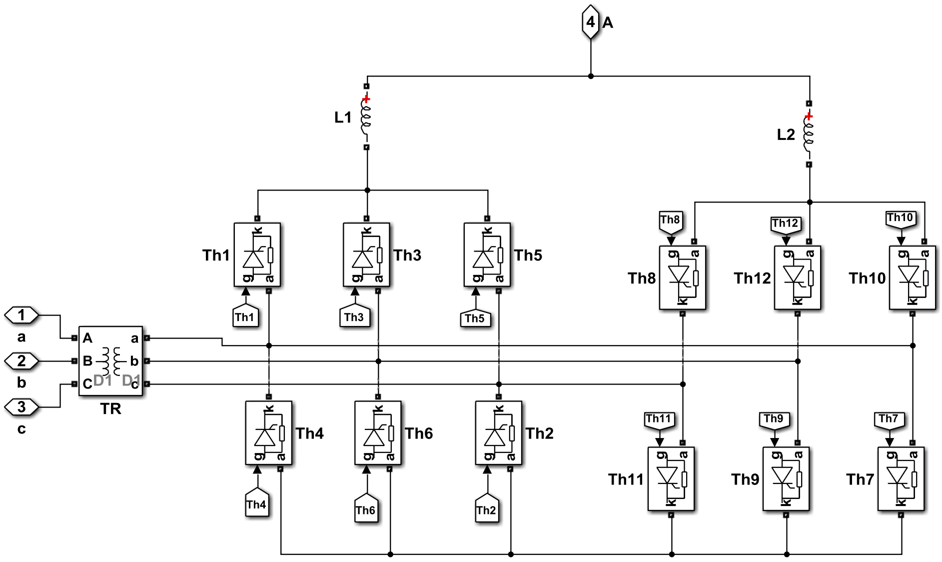

Figure 4.3: Circuit diagram of three phase to single phase Cycloconverter.

The cycloconverter control was designed so that thyristors of either positive converter or negative converter is firing at each half cycle of the output frequency, in order to produce a current in the required direction. Therefore, if the firing angle of the positive converter is α_p, then the negative converter firing angle will be $\pi - \alpha_p$. This means when one of the converters is in the ON period the other converter is blocked. Taking into consideration, when the current changes direction, both converters must be blocked for a short time.

The Pulse Generator provided by Matlab-Simulink is designed to generate a periodic pulse train to the positive and negative converters. This Pulse Generator is controlled by an angle obtained from the desired output signal and by a synchronisation signal (wt) obtained from the input voltage signal, see figure 4.4. The synchronisation signal (wt) is a ramp function synchronised with the zero crossing of phase-A voltage signal obtained using the phase locked loop (PLL) system. The pulses generated with the corresponding thyristor order on the positive converter of a three-phase bridge is shown in figure 4.5. The Matlab modelling of the control system details are given in appendix-A.

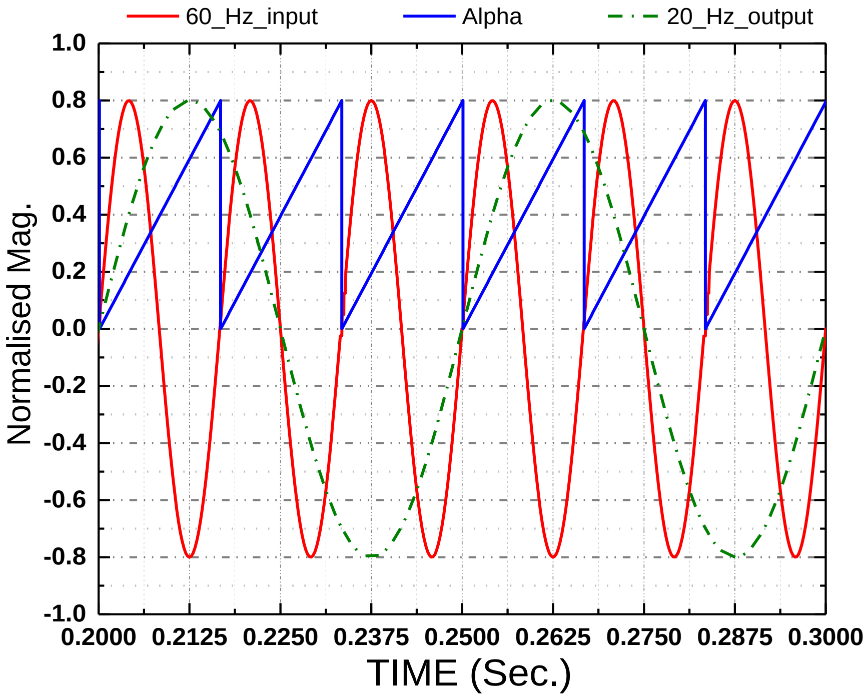

Figure 4.4: Input control signals to the Pulse Generator.

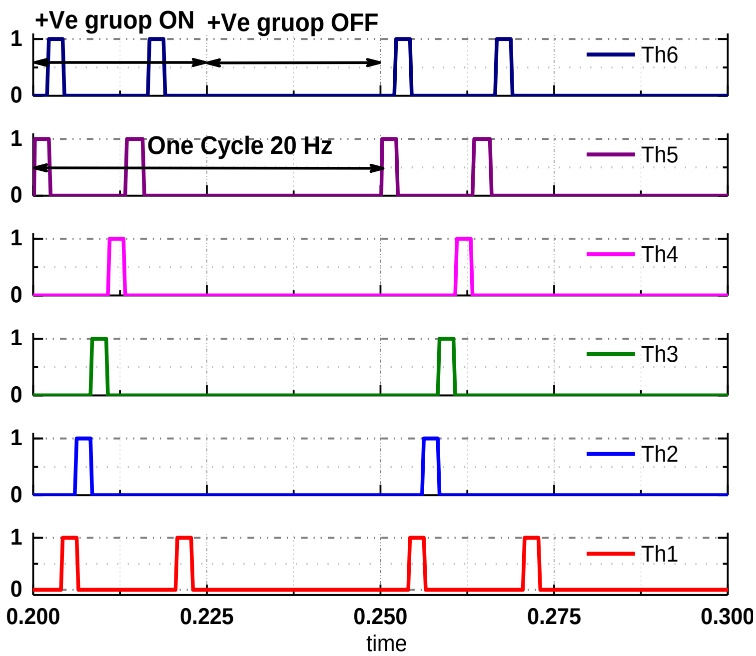

Figure 4.5: The pulses generated to the positive converter of a three-phase bridge.

The configuration and control of the cycloconverter have been tested by connecting an input voltage source at a frequency of 60 Hz, and a resistive load on the lower frequency side. As previously mentioned, the cycloconverter is designed to step down a 60 Hz input power to 20 Hz low frequency. The three phase output voltage and current waveforms obtained from the cycloconverter at a sampling frequency of 4 kHz are demonstrated in figure 4.6. It is clear that both voltage and current waveforms contain harmonics generated due to the cycloconverter switching. Hence, a number of filters need to be introduced in order to attenuate these harmonics.

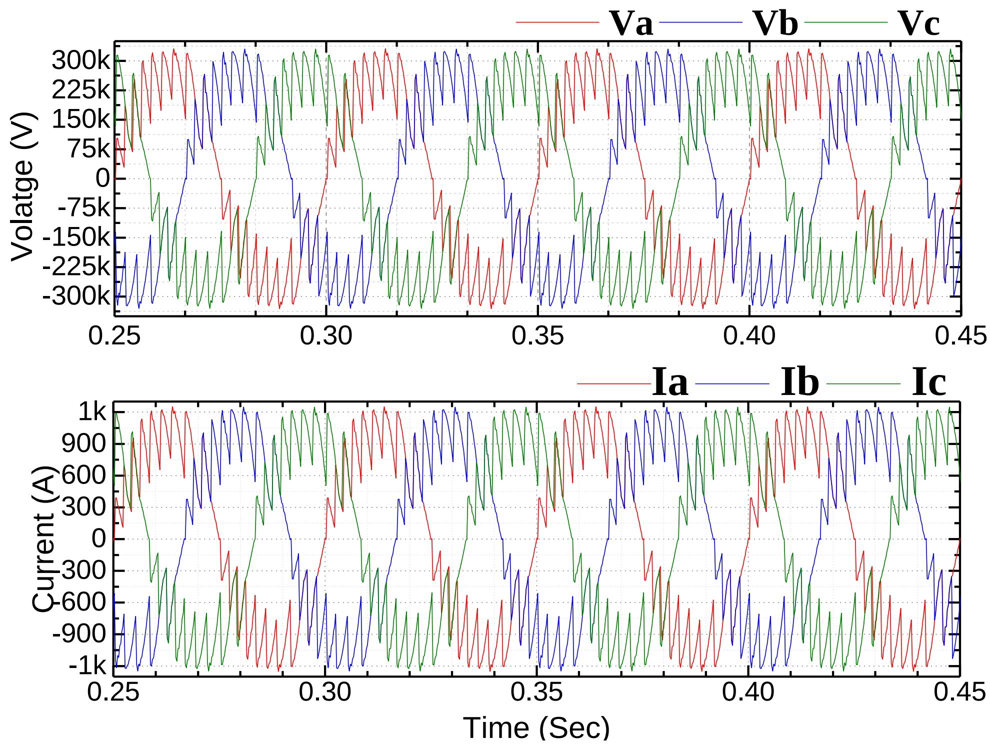

Figure 4.6: The cycloconverter output voltage and current waveforms.

4.2.2 Harmonics and Filtering System

It is clear that the cycloconverter current and voltage output waveforms contain harmonics. If these harmonics are injected directly into the transmission line, it will result in serious power quality problems. In the proposed HVLF system, these harmonics need to be suppressed in order to comply with the IEEE Standard-519 [85].

The harmonic content of the output voltage and current of the cycloconverter is affected by several factors such as, the number of pulses per output period, or the output to input frequency ratio [39]. A cycloconverter with a higher number of pulses generates fewer low order harmonics in the output waveform. In addition, if the output frequency is closer to the input frequency the output harmonics will increase. The applied six-pulse cycloconverter in the HVLF model produces harmonic frequencies (f_h) defined by [39]:

$$f_{h(k,n)} = 6kf_i \pm (2n+1)f_o \qquad (4.1)$$

Where k is an integer between 1 to infinity that represents the harmonic order, n is an integer between 0 to infinity, f_i the input frequency and f_o is the output frequency.

In this study, the harmonic content of the voltage and current waveforms was analysed by applying a Fast Fourier Transform (FFT) over a one cycle window based on a power frequency of 20 Hz having a sampling frequency of 4 kHz. The harmonic content of the output voltage from the simulated six-pulse cycloconverter with a resistive load and without any filtering is shown in figure 4.7. Table 4.3 shows harmonics with a magnitude above 3% of the fundamental frequency.

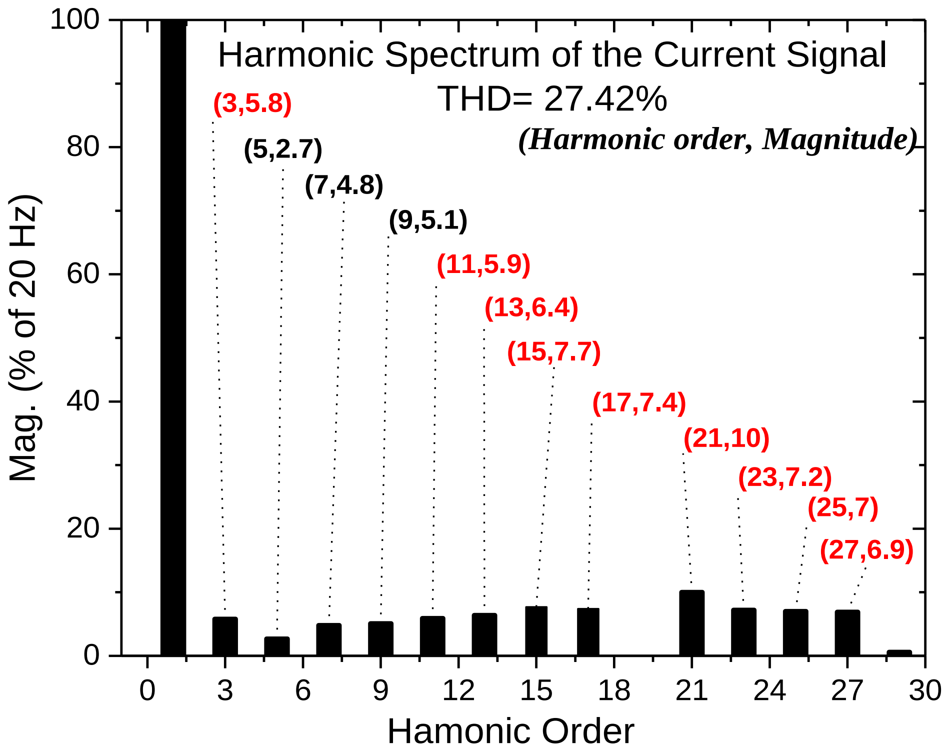

Figure 4.7: Harmonic spectrum of the six-pulse cycloconverter output voltage.

Table 4.3 Harmonics of the cycloconverter output current

Harmonic Order	Mag (%of 20Hz)
1	100
3	5.84
7	4.8
9	5.16
11	5.93
13	6.49
15	7.77
17	7.49
19	3.80
21	10.77
23	7.23
25	7.02
27	6.99
37	3.51
41	4.26
49	5.00
51	3.76
61	3.88
73	3.29
75	3.00

It is obvious that the cycloconverter generates harmonics with a total harmonic distortion of approximately 27%. Thus, suitable filters are required to be implemented in order to attenuate these harmonics and to improve the overall power quality of the network. The filters need to be designed so that all highlighted harmonics given in table 4.3 are eliminated. Therefore, a typical filter comprises of passive elements, such as resistance (R), inductance (L), and capacitance (C) passive filters were used to suppress these harmonics. The utilised passive filter are classified into; a tuned filter to suppress a specific harmonic frequency, and a highpass filter to suppress higher order harmonics. Both types are designed so that the filtered harmonics flow to the ground, rather than travelling to the power system. Numerous studies have been conducted on harmonic filter design for power electronic converters in the HVDC system applications [21, 86, 87]. CIGRE HVDC system benchmark given in figure 2.6 utilises multi-stage passive harmonic filters on both sides of the transmission line. These filters have been designed to attenuate harmonics generated by the HVDC converter stations.

The Band-pass filter is constructed by connecting an inductor in series with a capacitor, see figure 4.8. For harmonic suppression, this type of filter provides a low impedance at the designed resonant frequency. A high-pass filter is designed by connecting a resistor in parallel with the inductor in the bandpass filter. The introduction of the resistor will result in filtering all high frequency characteristics and higher filter losses at the fundamental frequency. Therefore, high-pass filters are usually used in combination with bandpass filters to eliminate the high frequencies bands of the harmonics spectrum only. Both types of filters have been widely applied in practice for high voltage power system applications. A practical example of these filters is the HVDC system filters manufactured by ABB in [88].

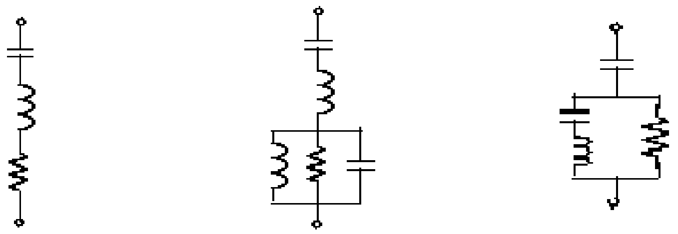

Band-pass filter (Single tuned) **Band-pass filter (Double tuned)** **High-pass filter (C-type)**

Figure 4.8: Types of AC harmonic filters.

For cycloconverter applications, AC multi-stage passive filters have been introduced to suppress the harmonics and supply reactive power [21, 43]. Matlab-Simulink provides several types of three-phase filter such as, single tuned, double tuned and C-type. The single tuned is a band-pass filter applied to suppress the lowest order harmonics such as 5th, 7th, and 9th individually. The double tuned filter is designed using a series LC circuit with a parallel RLC circuit in order to remove two consecutive harmonics. The C-type filter is an improved type of the highpass filter, in which the inductance L of the high-pass filter is replaced with series LC circuit. This LC circuit is tuned to resonate at the fundamental frequency, and therefore, the resistance is shorted at the fundamental frequency, resulting in lower filter losses.

All filter types are designed in Matlab-Simulink using the specified tuning frequency or band, quality factor *(Q)* and the required reactive power. The quality factor of the filter is determined by [89]:

$$Q = \frac{nX_L}{R}, \qquad = \frac{X_C}{nR} \tag{4.2}$$

Where, R is the filter resistor, X_L is the inductor reactance ($2\pi f_I L$), X_c is the capacitor reactance ($1/2\pi f_I C$), both at fundamental frequency (f_I), and n is suppressed harmonic order (f_n/f_I). The sharpness of the tuning frequency is determined by the filter bandwidth which is determined by:

$$B = \frac{f_n}{Q} \qquad (4.3)$$

where, f_n the tuned frequency and Q is the quality factor. Note that, for a double tuned filter the tuned frequency (f_n) is the geometric mean of both tuned frequencies (f_1, f_2), in which $f_n = \sqrt{f_1\, f_2}$.

The reactive power supplied by the designed filter is determined as follow [89]:

$$Q_c = \left(\frac{V^2}{X_C}\right) \cdot \frac{n^2}{n^2 - 1} \qquad (VAR) \qquad (4.4)$$

where, n is the suppressed harmonic order, V is the RMS value of line to line voltage.

As stated on the IEEE 519 standards, harmonic distortion in power systems should be limited to about 5.0% total harmonic distortion (THD) and on each individual harmonic is limited to about 3% [85]. Hence, the multi-stage filter applied in this study is tuned to attenuate the third and ninth harmonics as well as the higher frequency bands (the 23rd harmonic and above), see figure 4.9. Figure 4.10 shows the frequency response of the filters, in which each filter has a low impedance at the tuned frequency providing a flow path to ground. The specifications of the filters are given in table 4.4.

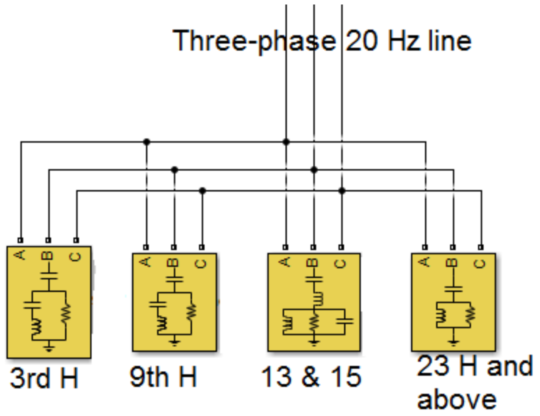

Figure 4.9: Multi-stage filter banks.

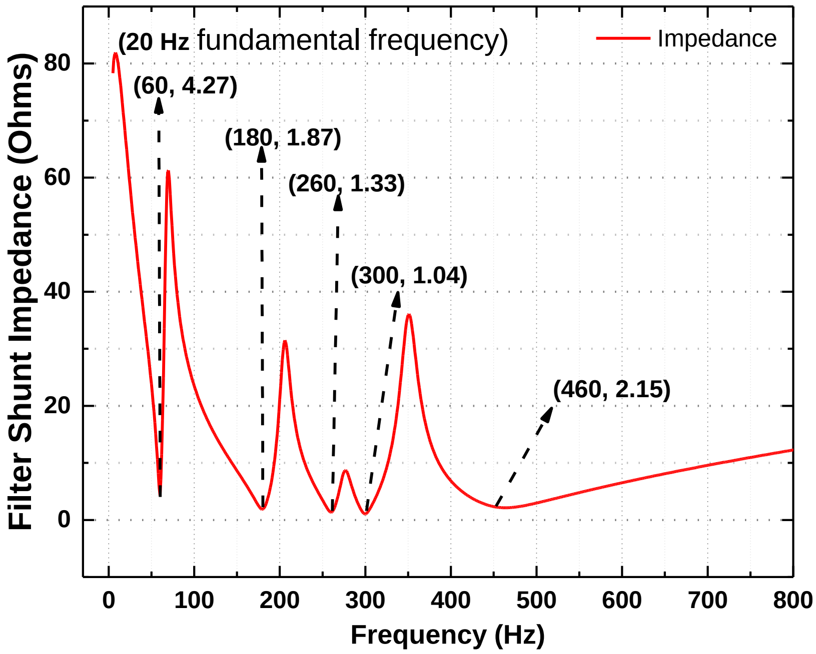

Figure 4.10: Frequency response of the multi-stage filter banks.

Table 4.4: Multi-stage filters specification

Filter type	Tuned frequency (Hz)	Reactive power supplied/ VAR
Single tuned	60 (third)	50e6
Single tuned	180 (ninth)	50e6
Double tuned	260 and 300	80e6
C-type	460 and above	80e6

4.3 HVLF System Steady-state Analysis

The simulated cycloconverter and the filter bank were integrated into the Matlab-Simulink model as shown in figure 4.11 with the following specifications: 230 kV, 60 Hz supply, 200 MW load via 200 km XLPE cable. The three phase AC source in figure 4.11 represents a collection of wind turbines connected to a 60 Hz step-up transformer. The cycloconverter is utilised as a step down frequency changer, in which 60 Hz supply frequency is converted to 20 Hz. The 200 km transmission cable was modelled as a three-phase transmission cable with parameters lumped in four PI sections. The resistance (R), inductance (L), and the capacitance (C) parameters of the line are uniformly distributed and were set by the positive, negative and zero sequence components given in table 4.5. The cable is characterised by the values of the surge impedance ($Z_c = \sqrt{L/C}$) and the wave propagation speed ($v = 1/\sqrt{LC}$). The self and mutual parameters of the resistance and the inductance as well as the ground capacitances are also taken into consideration in this model. All these parameter values are taken from the 230 kV rated cable specification manufactured by ABB [83].

Table 4.5: The transmission line parameters specification.

Parameter	Positive/Negative-sequence	Zero-sequence
Resistance	0.01273 Ω/km	0.3864 Ω/km
Inductance	0.9337 mH/km	4.1264 mH/km
Capacitance	12.74 nF/km	7.75 nF/km

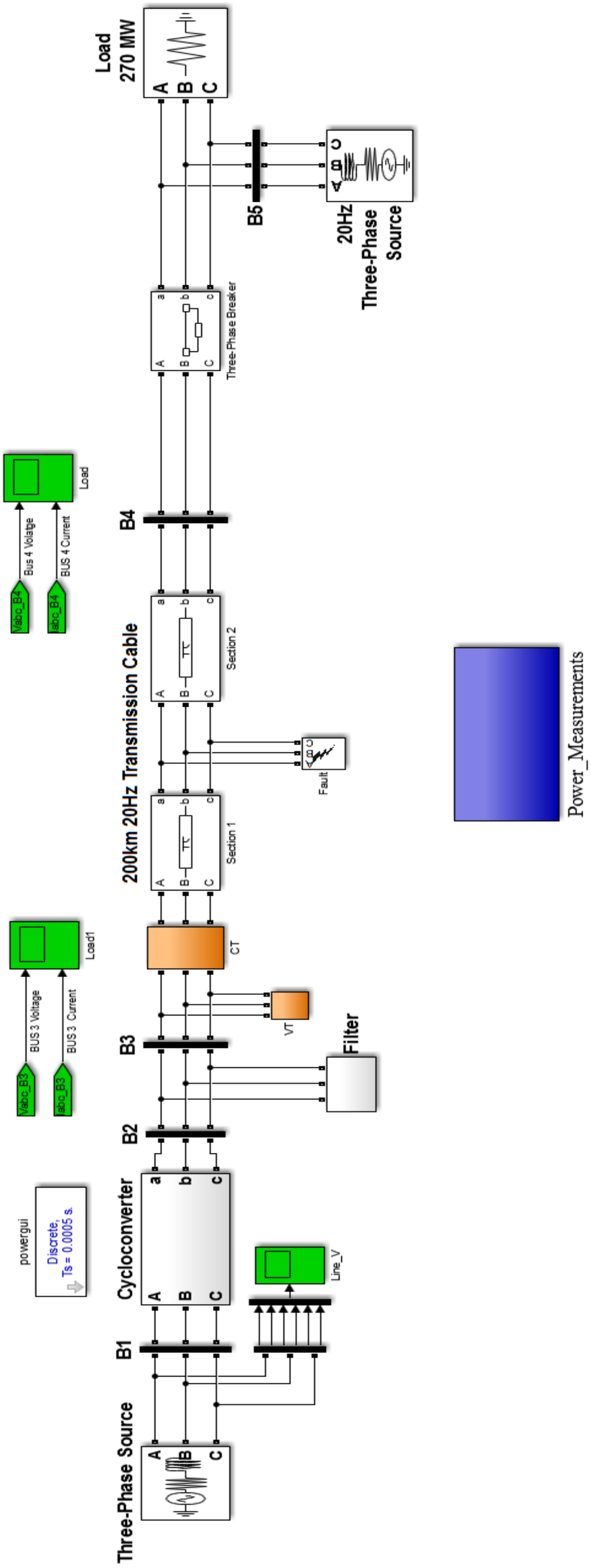

Figure 4.11: Matlab simulation of the HVLF power system.

Under normal conditions, the simulated voltage and current waveforms measured at the sending end (busbar B3) and the receiving end (busbar B4) are given in figure 4.12. These waveforms are obtained from the simulation output file based on a sampling frequency of 4 kHz. A sampling rate of 4 kHz is chosen in order to capture the higher frequency contained in transients according to Nyquist sampling criteria [51]. Whereas, applying a lower sampling rate will result in losing the high frequency information, and a higher sampling rate will increase the cost in real system. For harmonic measurements, the captured signals are analysed with Fast Fourier Transform (FFT) over a 0.05ms window, i.e. one cycle of 20 Hz. As a result of connecting the AC filters and the cable, the harmonics in the system have been suppressed and the THD is reduced to about 4.5% and 3.2% at busbars 3 and 4 respectively, see figure 4.13.

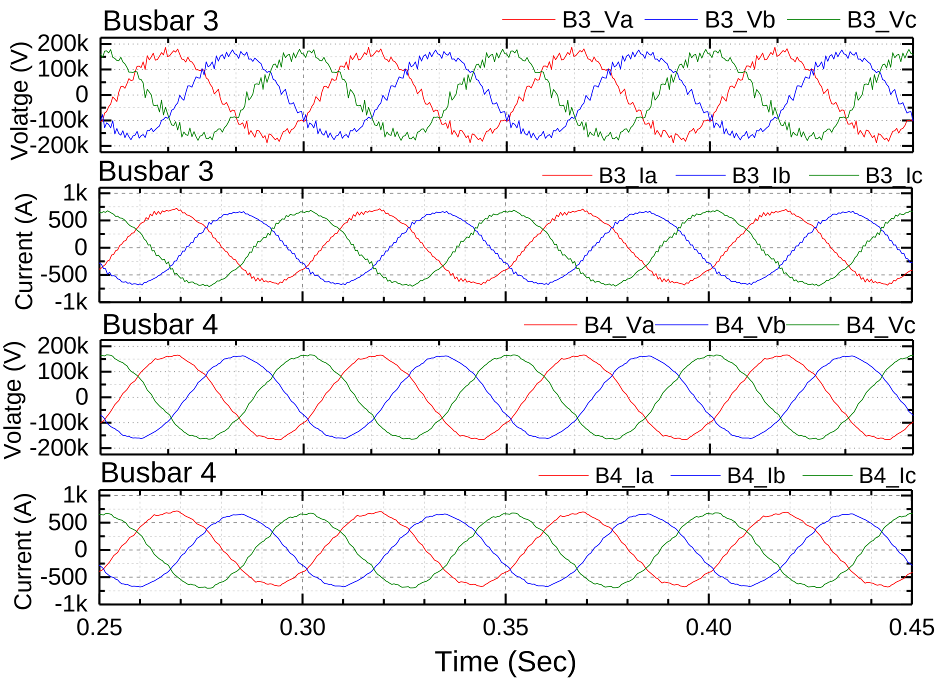

Figure 4.12: Voltage and current waveforms under normal conditions measured at busbar B3 and B4.

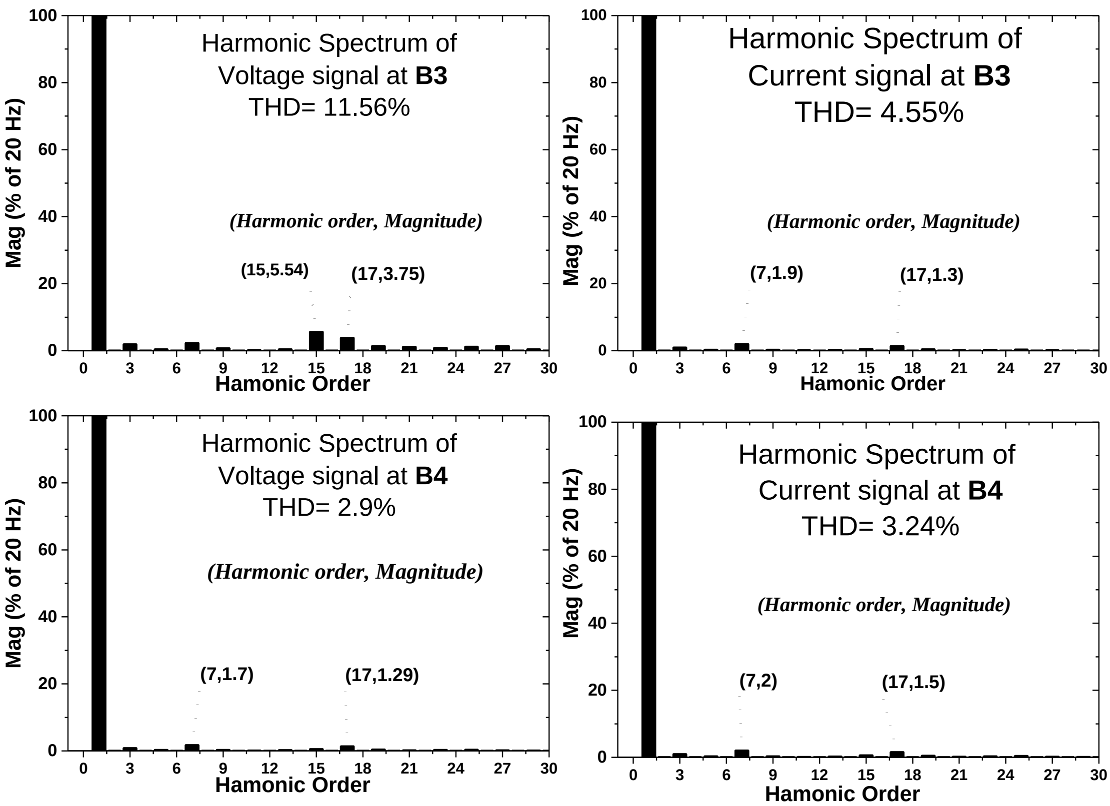

Figure 4.13: Harmonic spectrum of current and voltage signals at the sending and receiving ends.

The HVLF system is designed to have a unidirectional power flow from the OWFs to the load, the current flowing in the line can be seen to be around 750A peak phase current, see figure 4.13. The simulation validation was carried out by monitoring the power flow under the steady-state condition at the system busbars and the load as shown in figure 4.14. The real power received at the load point is about 200 MW.

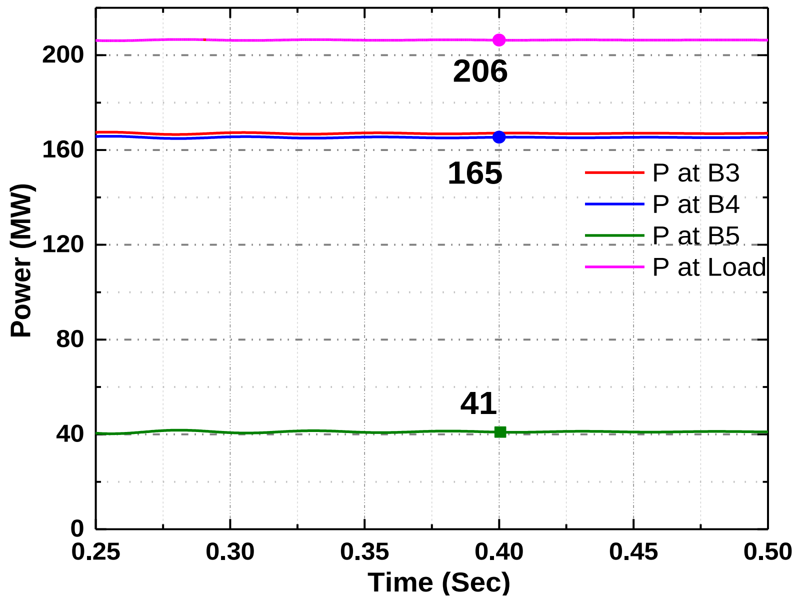

Figure 4.14: Active power flow on the simulated HVLF system.

4.4 HVLF System under Line Fault Conditions

The main objective of this modelling is to investigate thoroughly the HVLF system behaviour during transmission line disturbances and failure. This was achieved by simulating short circuits on the line phases and observe the fault voltage and current signals signature, see figure 4.15. Various fault scenarios such as, different fault phases, fault locations and fault inception angles were carried out. In this section, a single phase to ground, phase to phase, double phase to ground, and three phase faults obtained through simulation from the HVLF transmission line were demonstrated. All these fault types were simulated at different locations from the measurement point (B3). The fault inception angle was also taken into consideration in this study. The observed voltage and current signals from the voltage transformers (VTs) and current transformers (CTs) respectively, were used to develop an accurate fault detection and location algorithm.

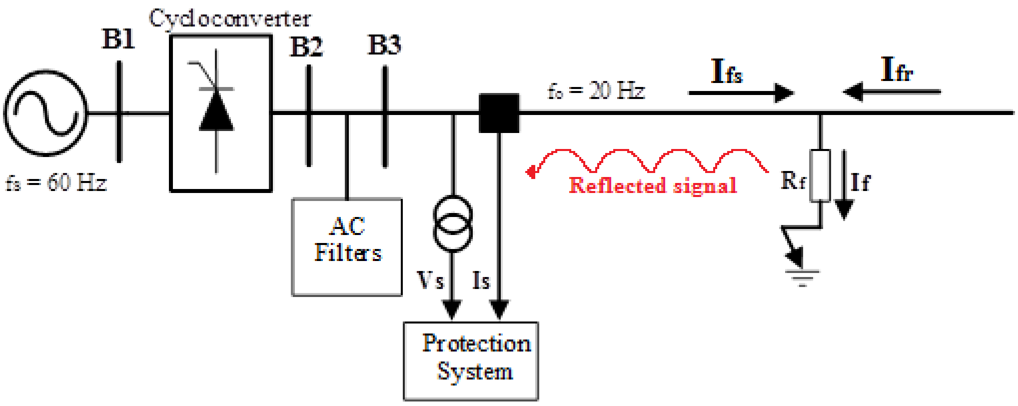

Figure 4.15: Single line diagram of HVLF system under line fault conditions.

Initially, a study on the effect of the line faults on the harmonic spectrum was carried out. A comparison between the pre-fault and post-fault harmonics distribution is achieved by investigating the corresponding frequency spectra with the FFT analysis.

4.4.1 Single-Line to Ground Fault (LG)

The proposed HVLF system uses a three-phase line for power transfer, in which a single line to ground fault is the most common fault type. This assumption is based on the most common type of fault occurring on the conventional HVAC system. Over 70% of line failures are involving a single phase to ground and the other two phases will remain healthy [59]. Figure 4.16 shows the three phase current signals of the HVLF system when a phase to ground fault (LG) occurs at time 0.3s and cleared at 0.45s, i.e. three cycles of 20 Hz frequency. The fault is simulated at locations 20, 60, 120, 180 km away from the sending end and the measurement point at Bus3. In this case, the fault resistance was set to 5Ω and ground resistance to 1 Ω. A low fault resistance was chosen based on the assumption of subsea cable conductor interruption given in [90] . The waveforms show clearly that, after the fault incident the magnitude of the faulty phase (phase-A) voltage drops and the phase-A current rises. This result is expected as the resistance reduces between the faulty phase and the ground.

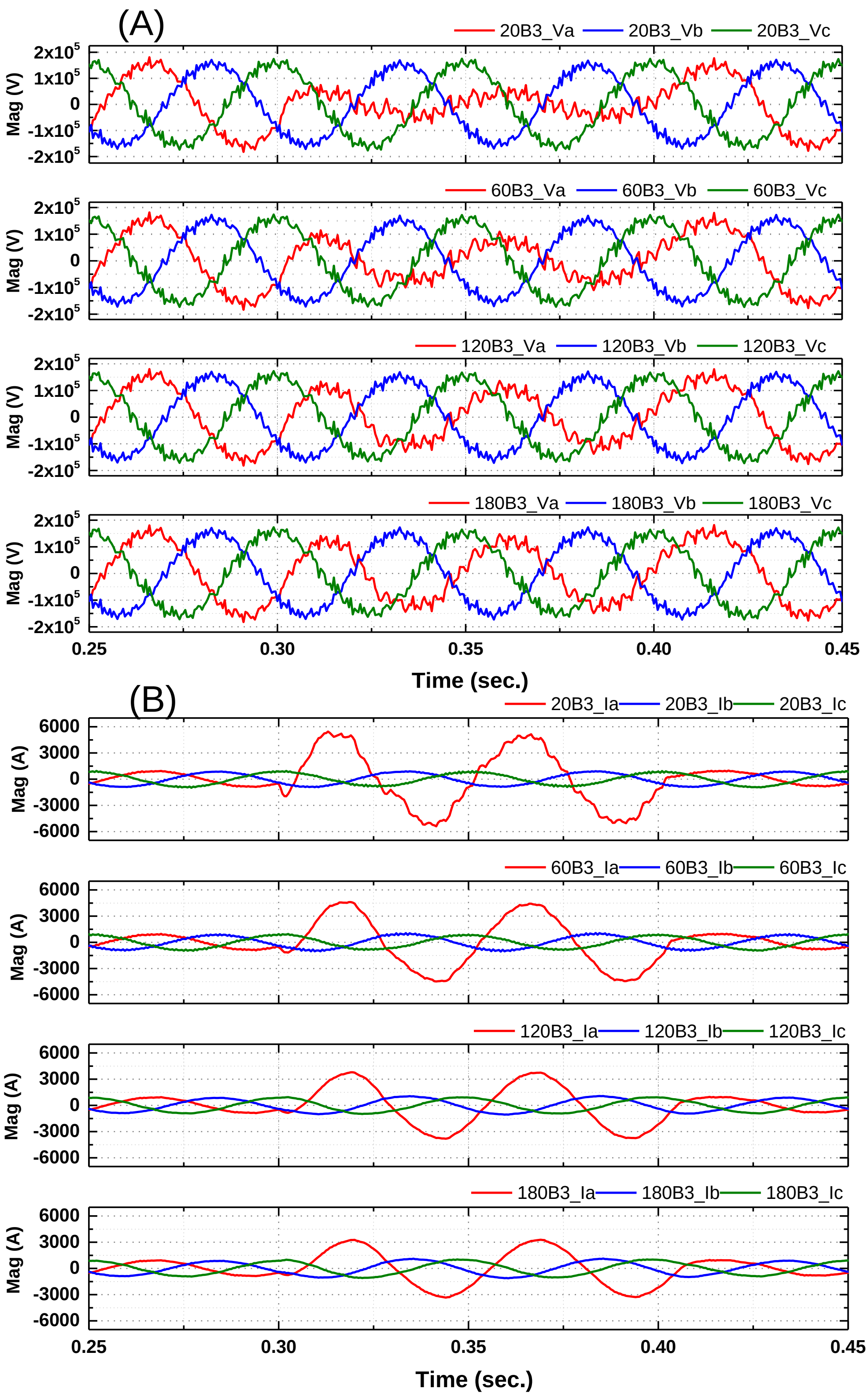

Figure 4.16: The captured waveform at B3 when an LG fault occurs (a) voltage (b) current.

The waveforms given in figure 4.16 show that the faulted phase current signal has a higher magnitude when the fault occurs at a distance closer to the measurement point located at the sending end. In addition, the magnitude of the high frequency (ripple) transients when the fault distance increases. Therefore, the FFT analysis was carried out for only two fault locations, in which one of them was at very close location to the source and the other at the extreme end of the line, i.e. 20 km and 180 km. This was done in order to investigate the maximum and the minimum fault generated transients that could be captured at the measurement point. The results from the FFT show that the magnitude of the harmonics generated due to the fault has decreased with increasing fault location, see figure 4.18. Also, the total harmonic distortion (THD) is reduced from about 16% to 13% at distances 20, 180 km respectively. This behaviour is expected, because with distance, increasing the transmission line parameters (R, L and C) will form a passive filter suppressing the high frequency transients. However, the presence of odd and even harmonics with a higher magnitude for both locations is noticeable compared to those harmonics obtained at the normal condition. The highlighted harmonics given in figure 4.17 have a magnitude of over 3% of the fundamental frequency (20 Hz). These harmonics were presented after the fault occurred, and need to be captured with its time signature in order to be used for fault diagnosis. An accurate analysis tool is required in order to utilise these features for developing new protection scheme. This tool should have the ability to obtain these transient and its time of existence precisely. Note that similar trends were also observed in the simulation of the other two phases faults, i.e. BG and CG faults as given in appendix B.1.

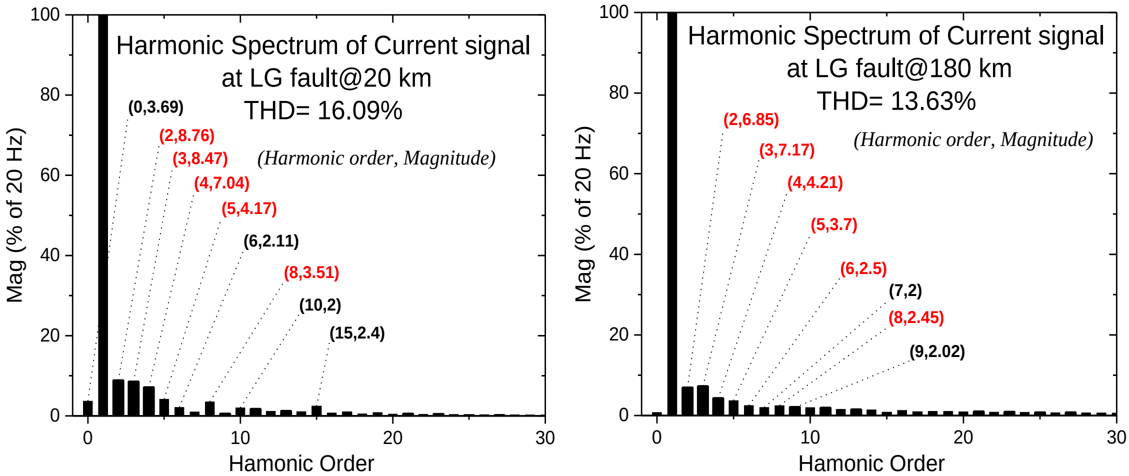

Figure 4.17: Harmonic spectrum of the faulty phase current signal for an LG fault at 20 km and 180 km distances.

4.4.2 Line to Line Fault (LL)

Similar scenarios of the line to ground fault were carried out on a line to line fault. In this type of fault, the two phases are shorted without being connected to the ground. The voltage and current waveforms for a phase A to phase B fault (AB fault) are shown in figure 4.18. The fault position was also varied to 20, 60, 120 and 180 km away from the sending end and the measurement point at busbar 3. It is observed that the magnitude of faulty phase currents rise while the healthy phase remains unchanged at all locations. The current waveforms of the faulty phases show a higher magnitude at a closer fault location in comparison with the extreme far location. Also, the voltage magnitude of two faulty phases drops at closer locations. But, with increasing distance it shows an unbalanced voltage. This is a result of the fault is being supplied from the receiving end and the unbalance load distribution on the cycloconverter switches. This unbalanced load on the cycloconverter output has resulted in loosing voltage synchronisation on its control system. Similar results were also obtained from the simulation of the other line to line faults, i.e. BC and AC faults, as given in appendix B.2.

FFT analysis of the two faulty phase current waveforms was also carried out at the selected two fault locations at 20 km and 180 km from the sending end. The results from the FFT show that the magnitude of the harmonics generated due to the fault is decreased with the fault location being increased, see figure 4.19. The total harmonic distortion (THD) is reduced from about 16% to 8% at distances 20, 180 km respectively. This behaviour is very similar to the line to ground fault analysis obtained previously. Taking into account, the remaining healthy phase has a lower THD with a low harmonic magnitude.

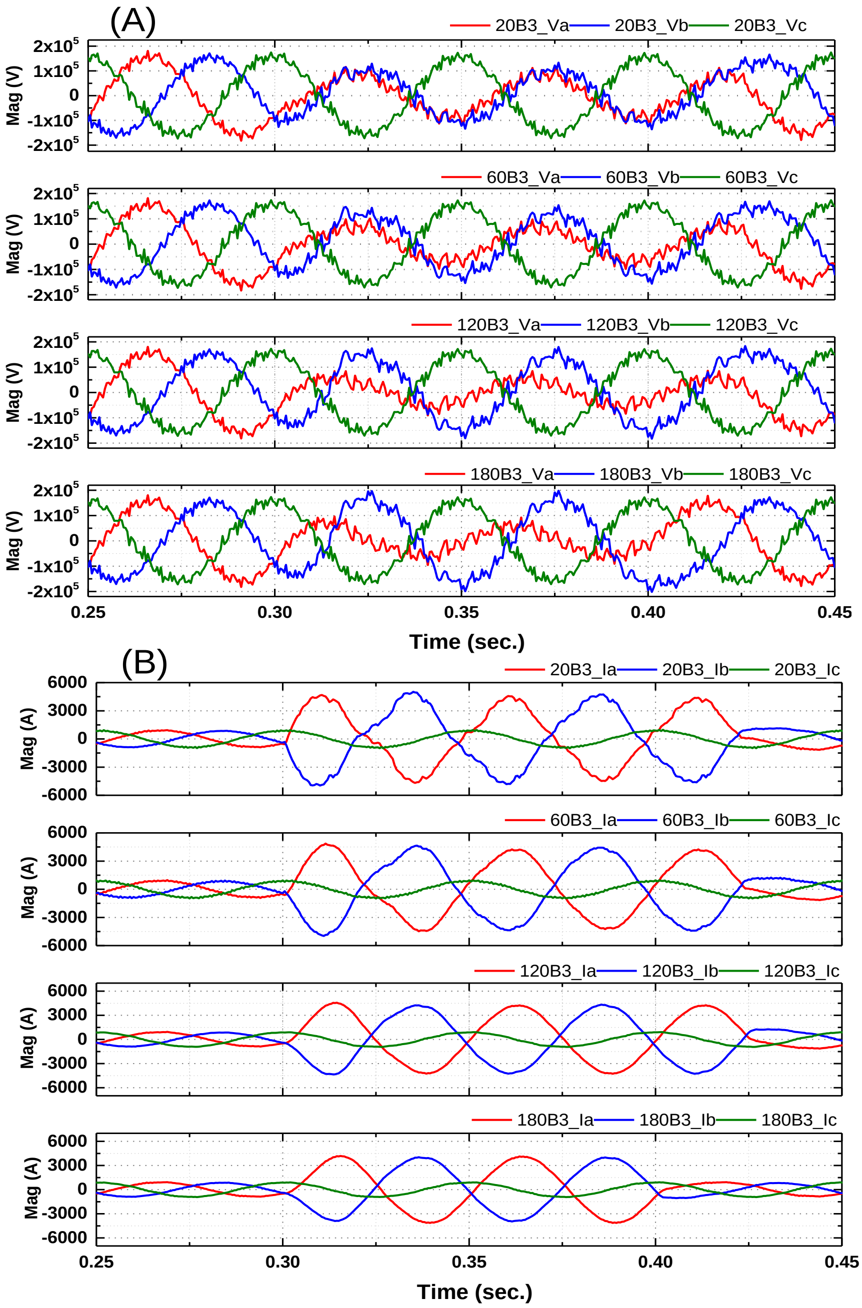

Figure 4.18: The captured waveform at B3 when an AB fault occurs (a) voltage (b) current.

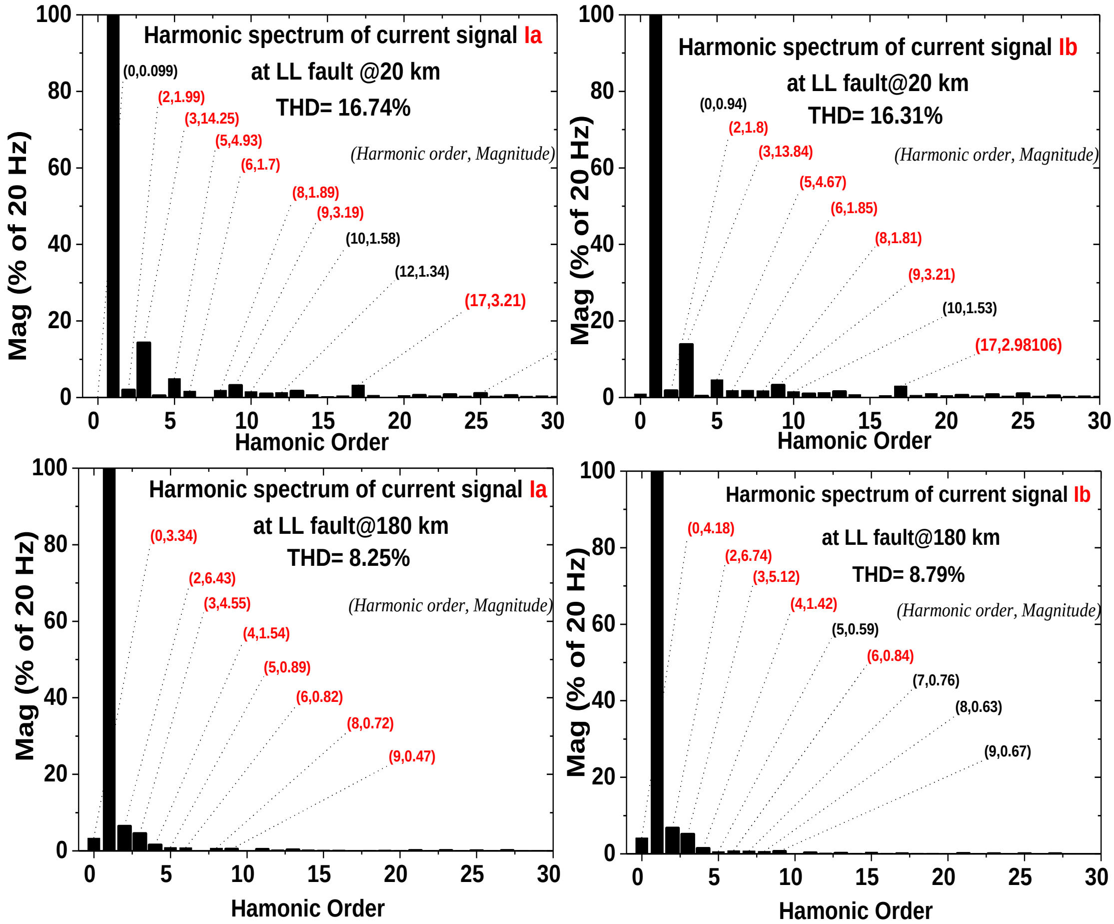

Figure 4.19: Harmonic spectrum of the faulty phases (Ia and Ib) signals of an LL fault, at 20 km and 180 km distances.

4.4.3 Double Line to Ground Fault (LLG)

In this type of fault, the two phases are shorted and connected to the ground. The voltage and current waveforms for a phase A and phase B to ground fault (ABG fault) are shown in figure 4.20. These waveforms are also obtained by changing the fault location to 20, 60, 120 and 180 km away from the sending end and the measurement point at busbar 3. It is observed that the magnitude of the faulty phase currents rise while the healthy phase remains unchanged at all locations.

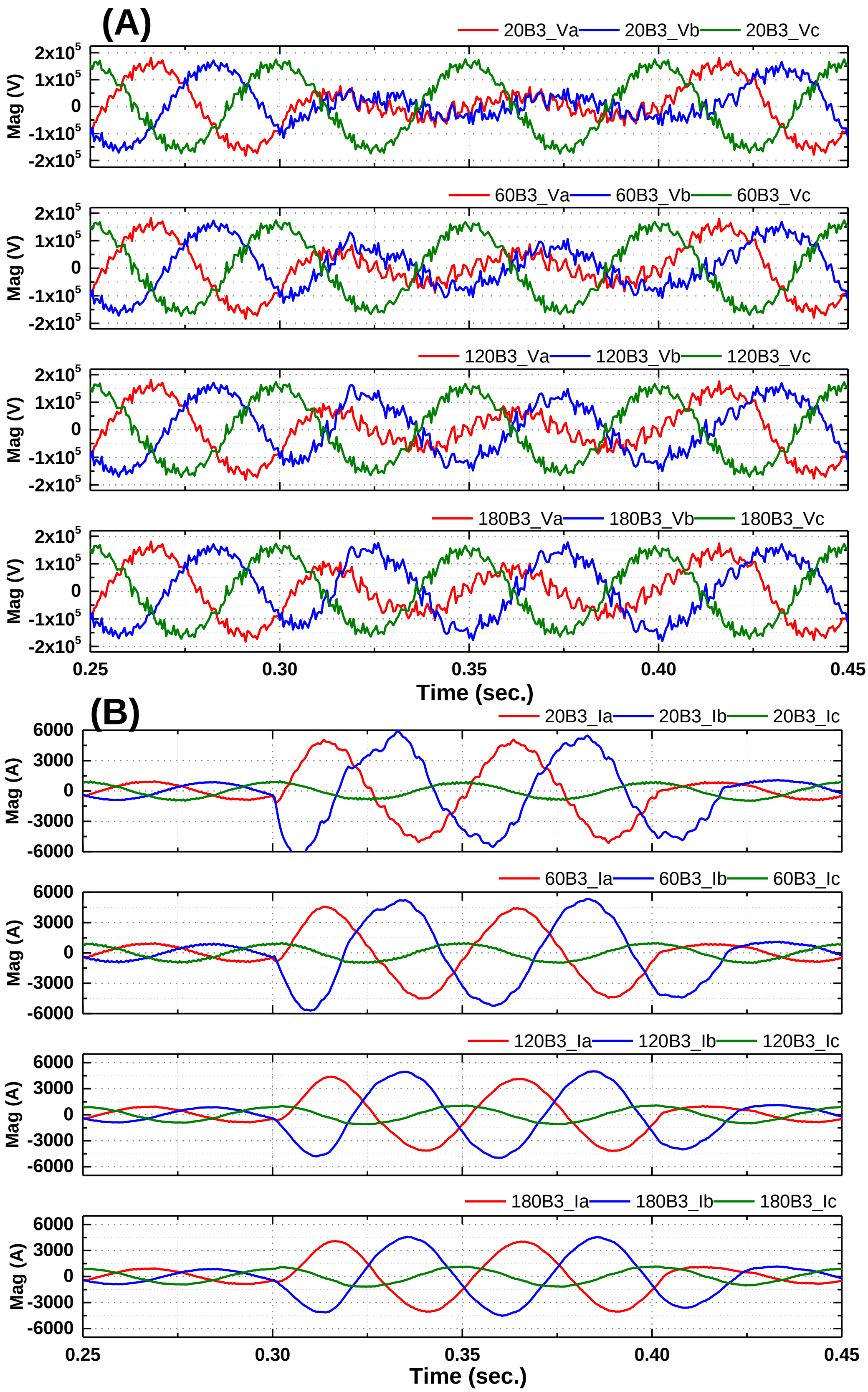

Figure 4.20: The captured waveform at B3 when an ABG fault occurs (a) voltage (b) current

The results of the FFT analysis show a similar trend with phase to phase fault obtained previously, see figure 4.21. The only difference is one of the faulty phases has a higher distortion on the current waveform, in this case phase b shown in figure 4.20(b). This is due to the timing of the fault occurrence with respect to the cycloconverter switching control. However, still the presence of odd and even harmonics during under post-fault condition with a higher magnitude is clear.

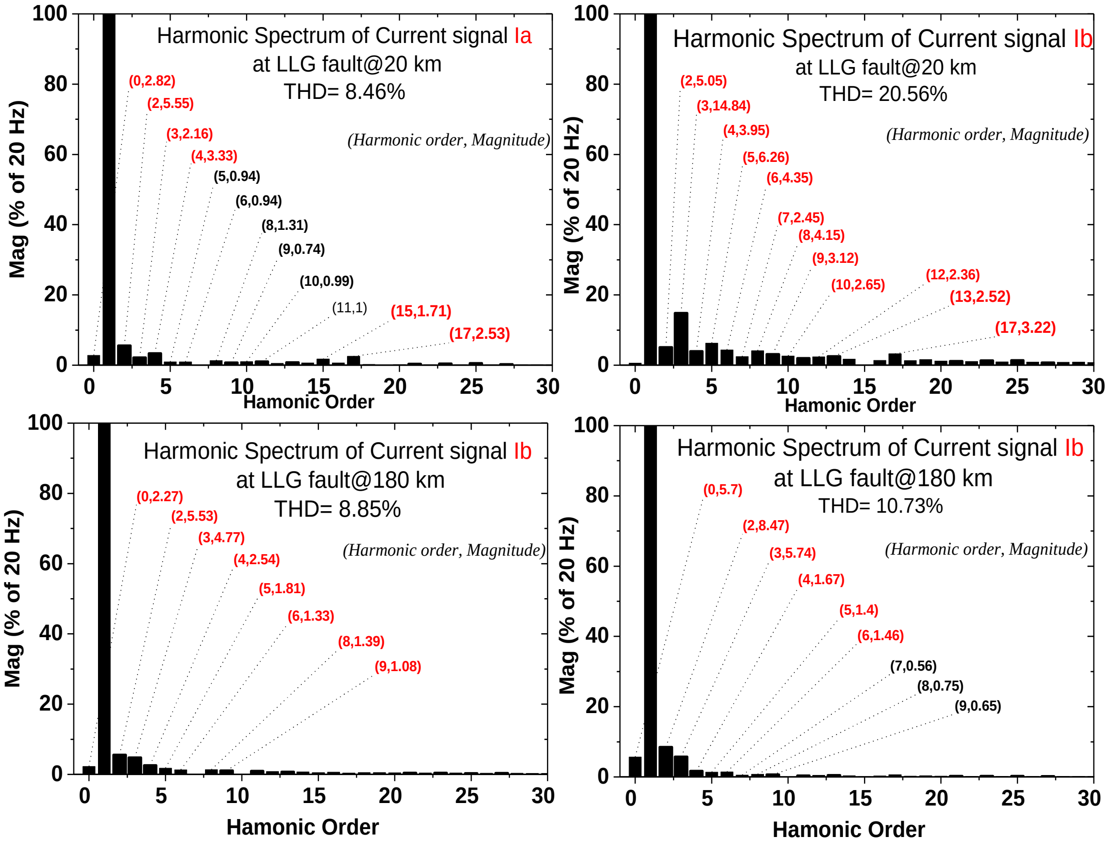

Figure 4.21: Harmonic spectrum of the faulty phases (Ia and Ib) signals of an LLG fault, at 20 km and 180 km distances.

4.4.4 Three-Lines Fault (LLL)

The three line fault is simulated by applying a short circuit on the three phases (ABC) of the line and without any connection to the ground. The voltage and current waveforms for a phase A and phase B to phase C fault (ABG fault) are shown in figure 4.22.

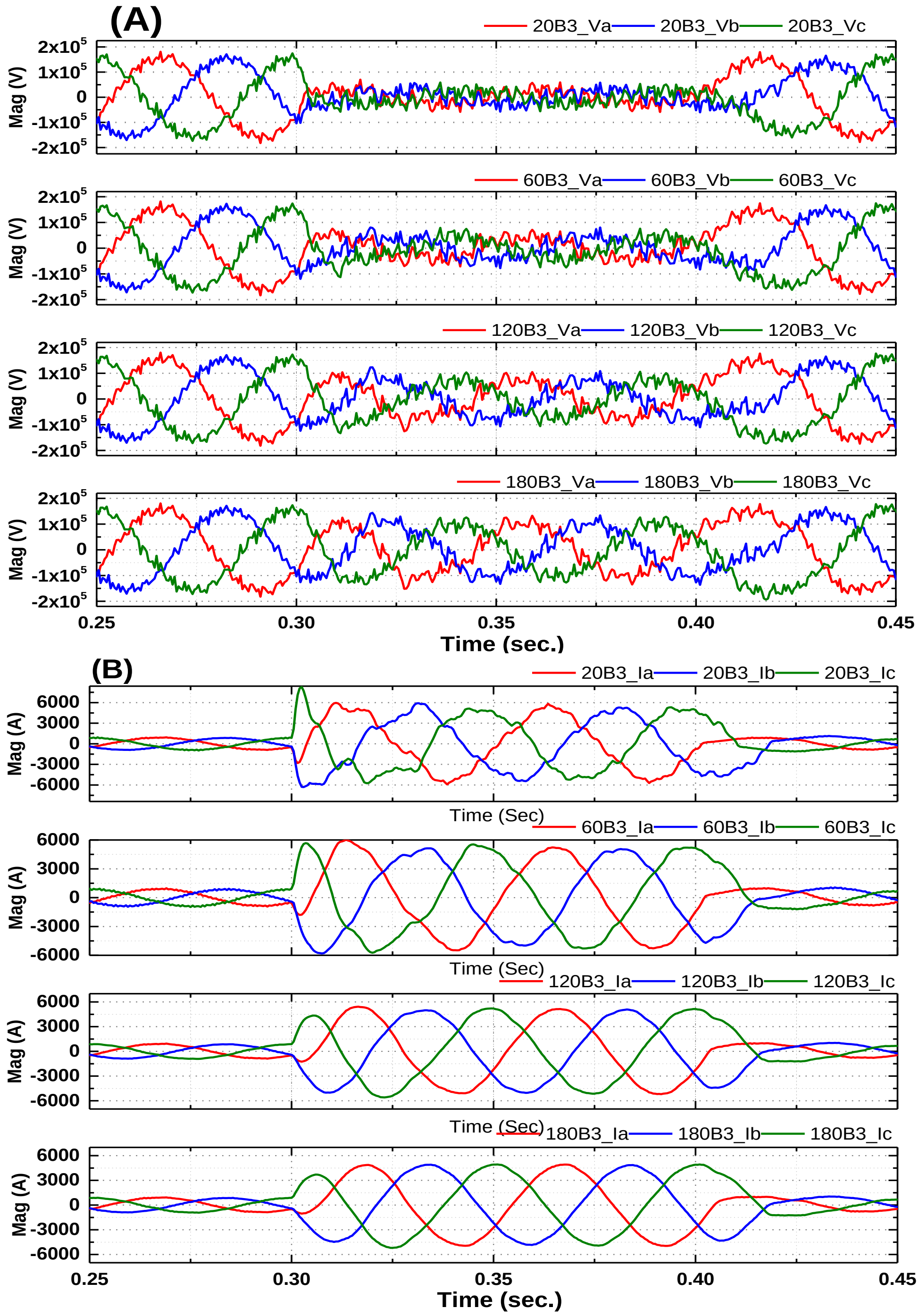

Figure 4.22: The captured waveform at B3 when a ABC fault occurs (a) voltage (b) current.

The captured waveforms demonstrate that there is a high voltage drop with an increase in the current magnitude of all phases after the fault occurred. However, the closest distance fault shows a higher level of high frequency transients in comparison with the fault at further locations. As given earlier with other fault types, the harmonic spectra of the faulty phases was investigated by applying an FFT analysis to the current waveforms. This analysis was performed on the fault waveforms obtained at the selected two locations of 20 km and 180 km from the sending end.

The harmonic spectra of the LLL fault current waveforms clarify that the magnitude of the highlighted harmonics has decreased with the distance of fault being increased, see figure 4.23. The time of fault occurrence with respect to the phase of the current signal has a significant effect on the magnitude of the harmonics generated. In figure 4.24, phase C shows a higher THD because the fault occurs when the magnitude of the current signal was at a peak value, see figure 4.22. Therefore, an investigation will be carried out (in chapter 6) in order to clarify the effect of the fault inception angle on the harmonic distribution.

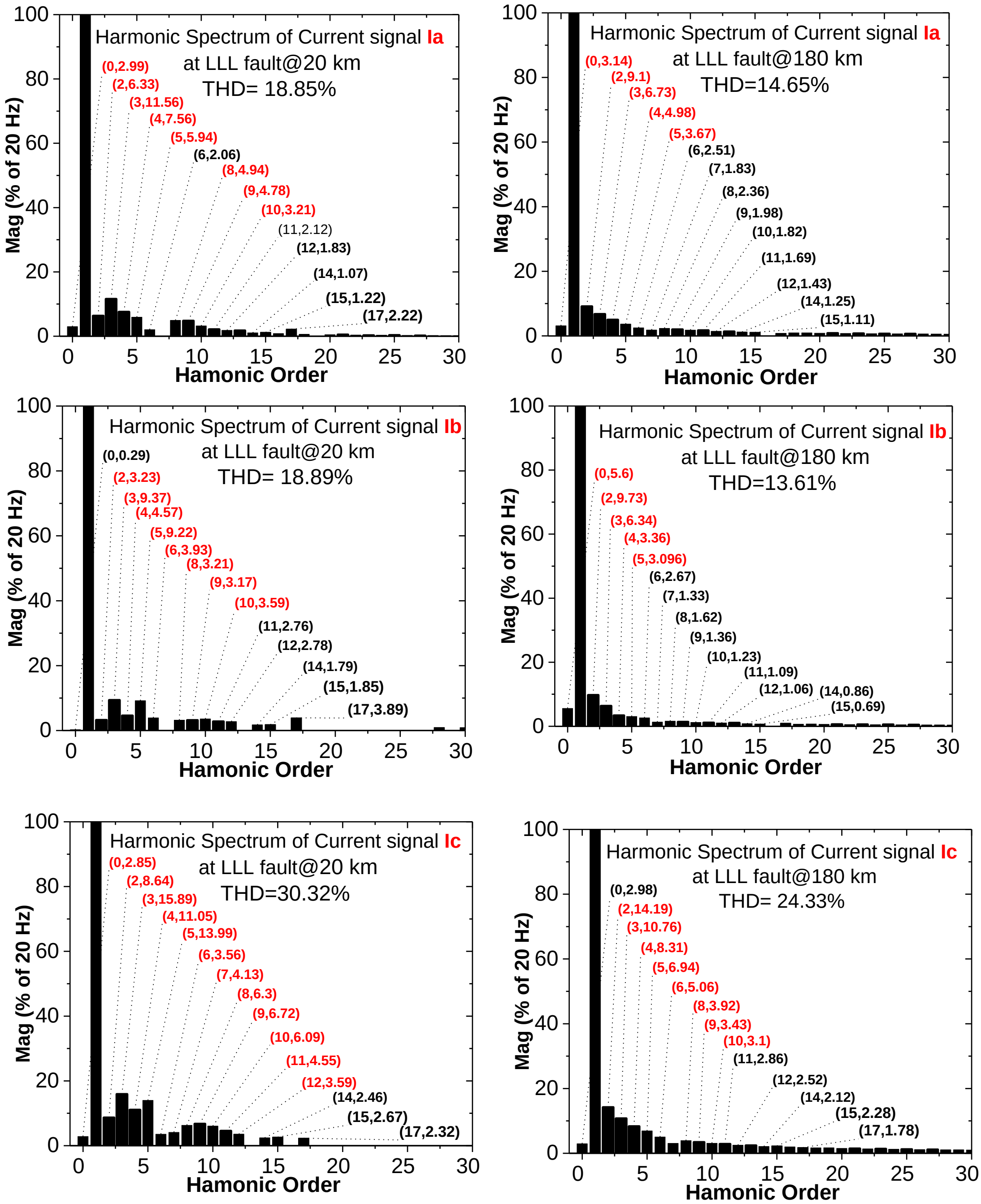

Figure 4.23: Harmonic spectrum of the faulty phases (Ia, Ib and Ic) signals of an LLL fault, at 20 km and 180 km distances.

4.4.5 Three-Phase to Ground Fault (ABCG)

The three lines to ground fault is the worst fault scenario occurring on the transmission line, in which a short circuit of all three phases (ABC) to ground takes place. Figure 4.24 demonstrates the voltage and current waveforms obtained at the sending end (busbar 3) when an LLLG fault is conducted. The waveforms show a very similar system behaviour between an LLLG fault and the LLL fault given in figure 4.23. The harmonic spectra of the LLLG current waveforms illustrates high frequency transients after the fault occurs, see figure 4.25. The post fault harmonics that exist are very close in magnitude to those obtained for an LLL fault. As mentioned previously, the harmonic magnitude decreases with increasing the fault distance. All the highlighted harmonics show a magnitude of over 3% of the fundamental frequency (20 Hz). However, the FFT analysis has provided the frequency range of those harmonics but without time information. The time signature of those transients is required in order to be used for fault diagnosis.

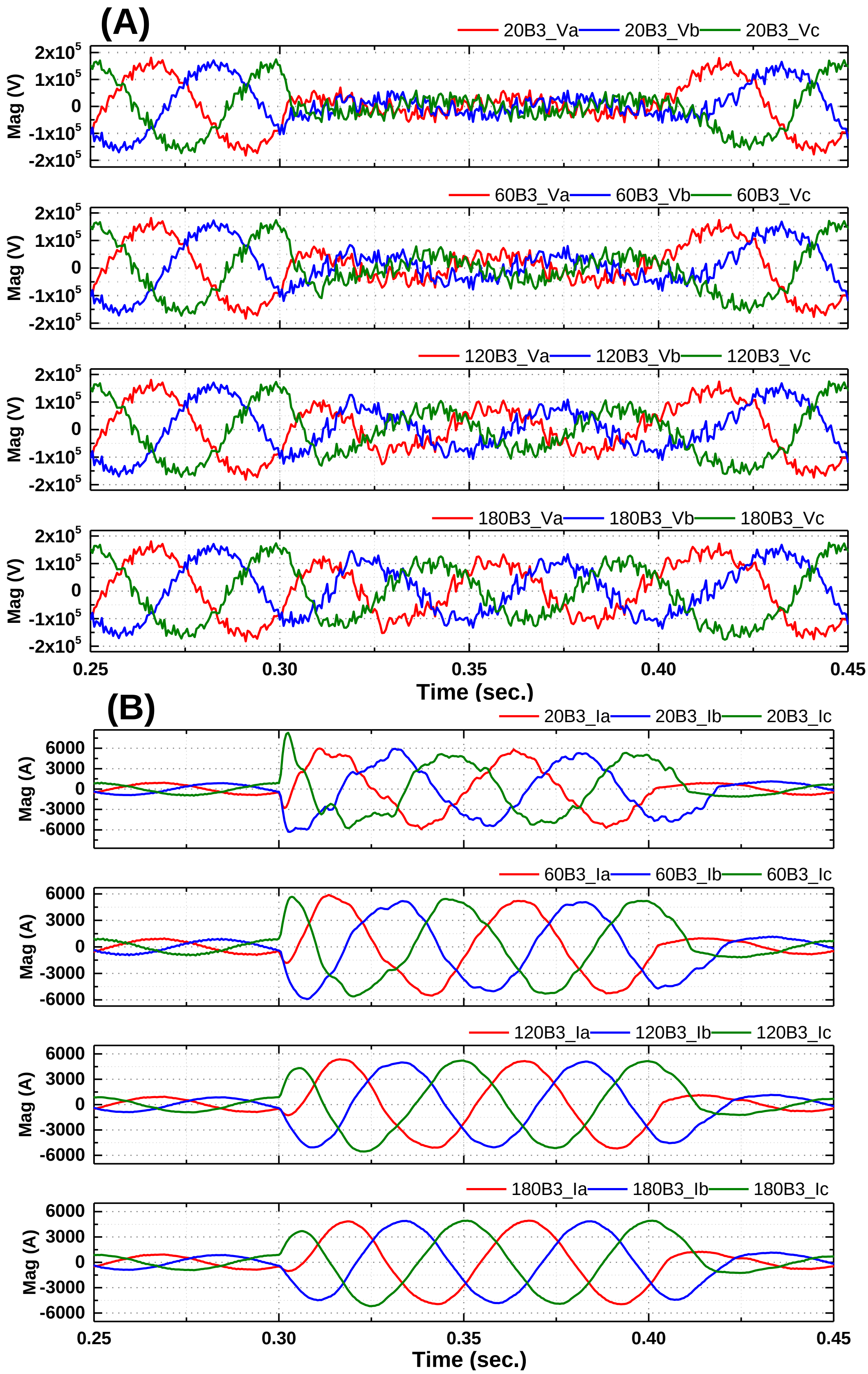

Figure 4.24: The captured waveform at B3 when an ABCG fault occurs (a) voltage (b) current.

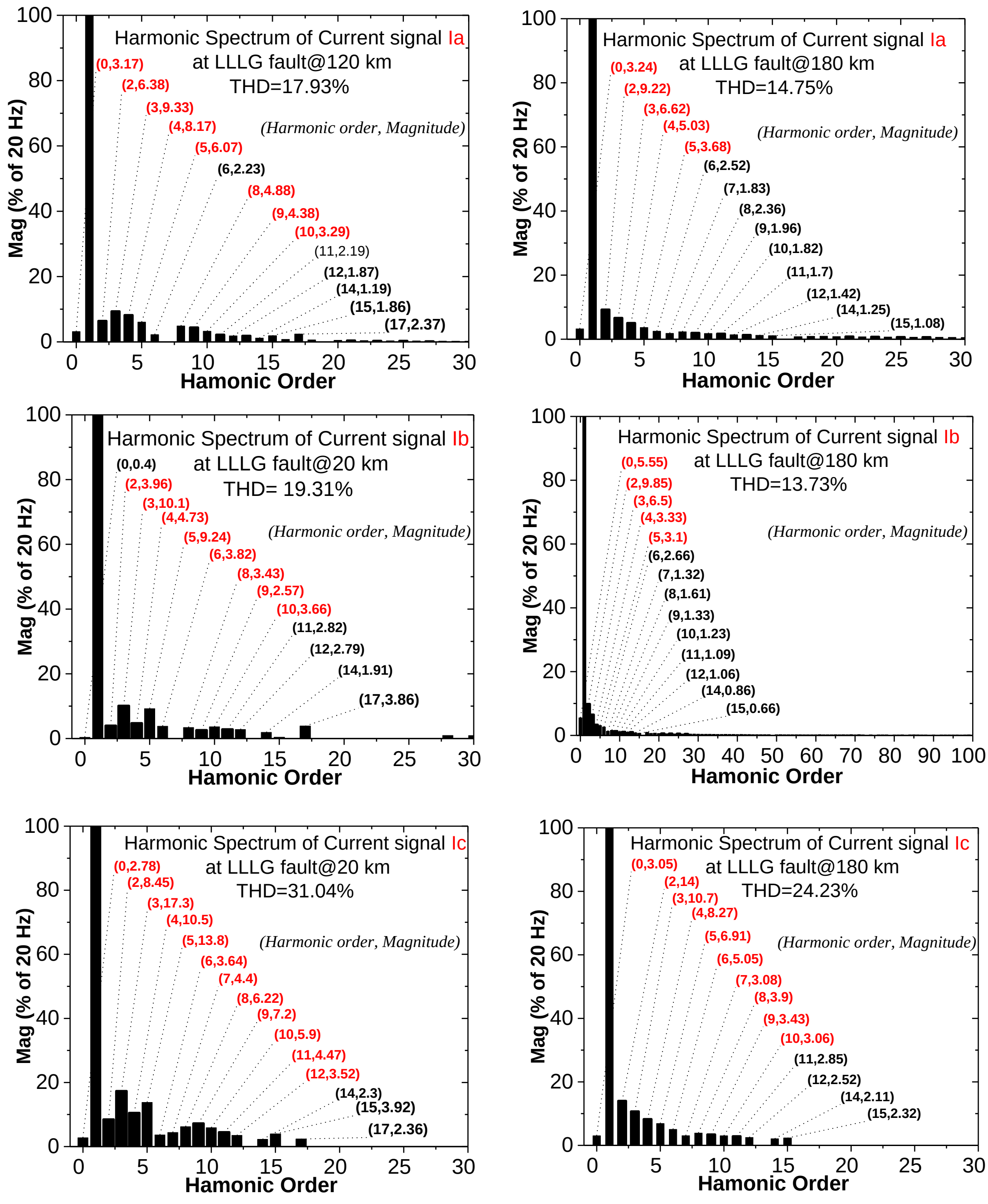

Figure 4.25: Harmonic spectrum of the faulty phases (Ia, Ib and Ic) signals of an LLLG fault, at 20 km and 180 km distances.

4.5 FFT Results Analysis

In this chapter the simulation of the HVLF system with Matlab-Simulink is presented. The system's components were modelled using practical data that was taken from the manufacturer's database. Since the HVLF system is a proposal, the Matlab model could be considered as a benchmark for an HVLF offshore wind power transmission system. In this research, the model was used to investigate the system behaviour under the transmission line failure. Hence, a comparative analysis was done between all possible transmission line fault scenarios. These scenarios were performed over different fault locations. Then, the three phase current waveforms captured at the sending end of the line were analysed with the Fast Fourier Transform (FFT). The analysis was done in order to investigate the harmonics generated after the fault occurred. The effect of the fault location on the magnitude of the post-fault harmonics was also investigated. This was achieved by comparing the harmonic spectra of the two fault signals initiated at close and remote distances from the sending end, i.e. 20 and 180 km.

It was observed that for a fault located closer to the measurement point at the sending end the harmonics magnitudes were higher than those of a remote fault. Nevertheless, the analysis has illustrated the presence of even and odd harmonics on the captured post-fault waveforms. Taking into account that these harmonics did not exist during normal conditions, see figure 4.14. The main objective of the FFT analysis was to clarify the frequencies of the post-fault generated transients. These frequencies were highlighted in the harmonic spectra obtained under different fault conditions, as given above. It was found that as the system operates on a low frequency (20 Hz), the transients generated after the fault occurred have frequencies up to 350 Hz (17^{th} order harmonics). Thus, the required protection system should have the ability to identify these transients accurately.

However, as discussed previously, the FFT has a limitation on providing a time stamp for the captured transients. As a result, another analysis tool is required in order to detect these transient and their time of existence. The next chapter will address the design of a new protection system based on Wavelet Transforms (WT). The Wavelet Transform has been chosen because it has the ability to provide better details for a noisy signals. This characteristic is due to the fact that the mother wavelet behave as a bandpass filter. However, the filters of the wavelet transform need to be tuned in order to capture the frequency transients highlighted previously. This will lead to an improvement in the accuracy of the proposed protection system. To date, there has been no study that has been conducted on developing a protection scheme for the proposed HVLF transmission system.

Chapter 5
The HVLF Transmission Line Protection System

5.1 Overview

This chapter aims to contribute to the utilisation of the post-fault transients of the HVLF transmission line for fault identification and location. The previous chapter has shown that the HVLF system faults introduces additional transient components to the spectrum of the power frequency and the pre-fault cycloconverter harmonics. These transients were identified using the FFT analysis of the three-phase current signals. It was shown that these transients range from DC to high frequency of up to 350 Hz are distributed throughout the three-phase current signals spectrum. However, the FFT analysis has provided the frequency information of these transients but without time information. The time information of the captured transients is essential to determine the instant in which the fault was initiated. Therefore, a frequency extraction tool is required to determine the frequency composition and the time details in order to identify and locate faults.

The conventional protection algorithms applied to the HVAC or HVDC systems have been proven to be of great reliability in practice. Nevertheless, it was shown, through FFT analysis of faulty phase current waveforms, that for an HVLF system the fault generated transients have a different frequencies range. Therefore, in this research the realisation of a compatible HVLF protection algorithm has been addressed. This protection algorithm is required to accurately differentiate between post-fault generated transients and pre-fault frequencies generated by the cycloconverter.

In this chapter the utilisation of the Wavelet Packets Transform (WPT) to analyse the three-phase current signals under all possible fault scenarios of the HVLF transmission line is demonstrated. This was achieved by the simulation of different fault scenarios on an HVLF transmission line. This chapter illustrates the impact of different fault scenarios, such as fault type, and the fault location, on the sensitivity and reliability of the proposed protection system.

5.2 Wavelet and Packet Wavelet Transform

It is described in the research literature that the Wavelet Transform has been utilised for the protection of HVAC and HVDC transmission systems. Numerous studies have proved it is a fast and efficient tool to analyse transients of the voltage and current signals. Unlike the Fourier Transform, the Wavelet Transform decomposes a signal into divisions of the frequency domain by using a short window wavelet function for high frequencies and a longer one for lower frequency analysis. This process called the multi-resolution analysis (MRA), in which the input signal is processed with a set of highpass (HPF) and lowpass filters (LPF) at multiple levels, as discussed in chapter 3. The lowpass filter represents the mother wavelet function, while the highpass filter is the scaling function derived from the wavelet function. The high frequency details (d1) is obtained from the HPF and an approximation of the original signal is obtained from the LPF (A1), see figure 5.1. A further analysis level is introduced in order to extract another band of high frequencies that still exist in the signal. The process is repeated until nearly all the high frequency information is extracted. Note that at each level of the analysis the output signal is down sampled by a factor of 2 to avoid redundancy, as shown in chapter 3.

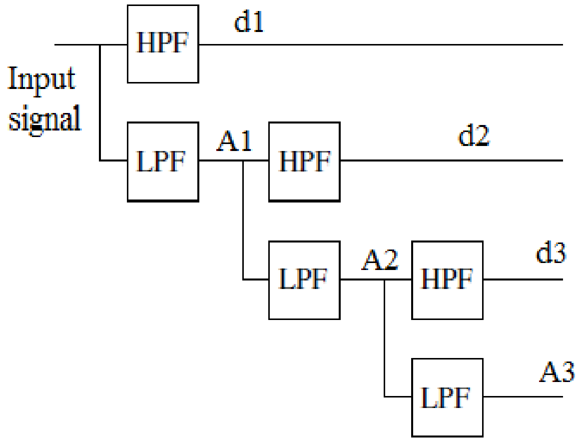

Figure 5.1: A three level wavelet transform MRA.

In this research, the Wavelet Transform is proposed to extract the frequency information from the fault signal of the HVLF system. As was shown in the previous chapter, the fault signal has transients with frequencies ranging up to 350 Hz contributed along the frequency spectrum. It is clear in figure 5.1 that in the first level of analysis the frequencies contained in the signal are divided into two halves. This makes all higher frequencies extracted in one frequency band (d1). In the next analysis level, the lower half of the frequency band (the approximation coefficient) is then subdivided into another low and high frequency components. Hence the wavelet MRA provides less detail on the high frequency resolution of the analysed signal. Taking into consideration that the frequency resolution of the analysis filter might also result in losing some of the necessary information contained in the signal. Therefore, applying the wavelet MRA could result in losing certain important information that is located in the higher frequency components.

The solution to this limitation is achieved by processing the detailed and the approximation coefficients of the first analysis level by another set of highpass on lowpass filters. This method of analysis is called the Wavelet Packets Transform (WPT). The WPT is a generalisation of the wavelet MRA, in which a better high frequency detail is obtained from the analysed signal. Figure 5.2 shows that at the first level of analysis, the frequency contents of the input signal is divided into high and low frequencies represented by detail and approximation coefficients respectively. Unlike the wavelet MRA, in the second level of analysis the detail coefficient is also divided into low and high frequency coefficients, and the process is repeated for further levels. As a result, the information of the high frequencies contained in the signal are extracted with higher resolution. Therefore, this research adopts the utilisation of the WPT analysis to extract frequency features from the HVLF fault signals. This was done to obtain all high frequency information from the fault signal.

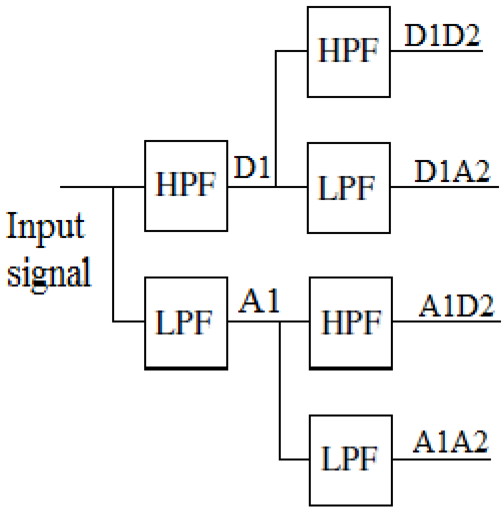

Figure 5.2: One level analysis of the Wavelet Packets Transform (WPT).

The wavelet toolbox provided by Matlab-Simulink provides signal processing with different mother wavelet functions with a friendly user interface [26]. The toolbox includes algorithms for the Continuous Wavelet Transform (CWT), Discrete Wavelet Transform (DWT) as well as the Wavelet Packets Transform (WPT). All the resulting analysis coefficients can also be displayed visually. The visual display shows how the frequency content of the analysed signal changes over time. This is presented by multiple signals or coefficients each one refers to a particular frequency band. In this chapter, the captured fault signals from the simulations of the HVLF system model, given in chapter 4, are processed with the WPT analysis.

5.3 Selection of the Mother Wavelet Function for Fault Algorithm

It can be seen in the research literature that many mother wavelet functions have been applied to the analysis of power system transients, such as Haar, Daubechies and Morlet. In this section, the selection of the most appropriate mother wavelet function applied to the analysis of HVLF system transients is addressed. A DWT analysis was carried out to examine the variation between the different mother wavelet functions and the effect of the wavelet order. The comparison was achieved by applying Haar and different orders of Daubechies mother wavelets to analyse a fault signal obtained from the HVLF system, see figure 5.3. However, other types of mother wavelet applied for fault transient analysis was described in subsection 3.4.3. In this section, the Haar mother wavelet function was chosen because it is the simplest mother wavelet. This mother wavelet is a step function taking values 1 and -1, on (0 to 0.5) and (0.5 to 1), respectively. The Daubechies mother wavelet function of the first order (db1) is the same as the Haar function. A higher order mother wavelet such as, db2 and bd4 have a higher number of samples based on the following equation [91]:

$$Number\ of\ samples = 2\ \times order\ of\ the\ mother\ wavelet \tag{5.1}$$

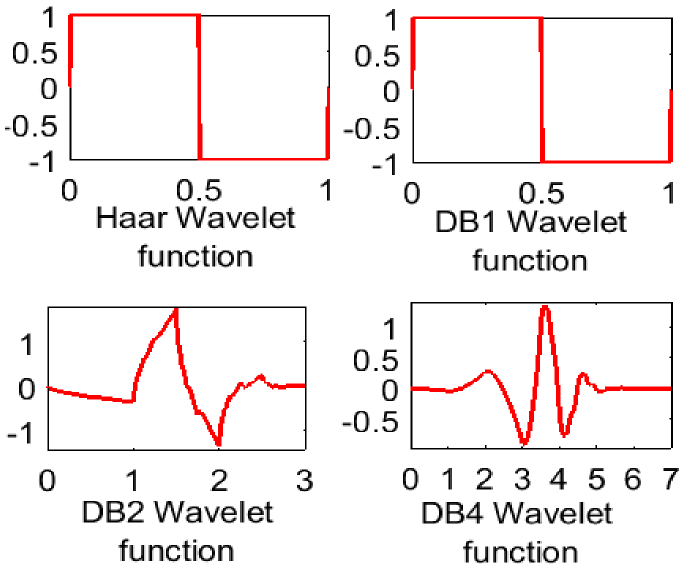

Figure 5.3: Haar, Daubechie's 1, 2 and 3 mother wavelet functions.

The window shape of the mother wavelet function determines the filter characterises in the wavelet transform analysis. Therefore, for fast transients and an oscillating signal the rectangular shape of these functions does not provide an accurate detail for high frequencies. Hence, a higher order oscillating mother wavelet functions such as, db2 or db4 were also selected for the analysis of these signals. In this study, the selected mother wavelet functions were tested to extract transients from a line to ground fault signal. The faulty phase current signal was captured at busbar 3 of the simulated HVLF system shown in figure 4.12. The results of the three levels DWT analysis are illustrated in figure 5.4. These results show the approximation and the detailed coefficients obtained using Haar, db1, db2, and db4 mother wavelets respectively. The approximation coefficient represents the original input signal after all high frequencies were removed. The detail coefficients represents the high frequencies removed at the last stage of the analysis. The results demonstrate the variation in the accuracy of the different mother wavelet functions for identification of different frequency details within the signal.

The results show clearly that a rectangular form waveform of the input signal after the high frequency contents were extracted using Haar and db1 mother wavelets. However, db2 and db4 mother wavelets provided a better high frequency contents extraction of the analysed signal. However, it can be noted that when db2 is applied, some high frequency contents still exist in the signal at the last level of analysis, see figure 5.4. This means that db2 mother wavelet required a further analysis level to extract all the high frequency content from the signal. Whereas, db4 mother wavelet shows at the third level of analysis that all high frequency content is removed and a smoother version of the input signal is obtained. This means that the db4 mother wavelet has the ability to extract high frequency content within a shorter analysis level. Nevertheless, selecting a higher order mother wavelet such as db5 or higher will increase the number of samples and consequently the processing time. Hence, the db4 mother wavelet was selected in this research due to its ability to detect the variations in frequency content more precisely.

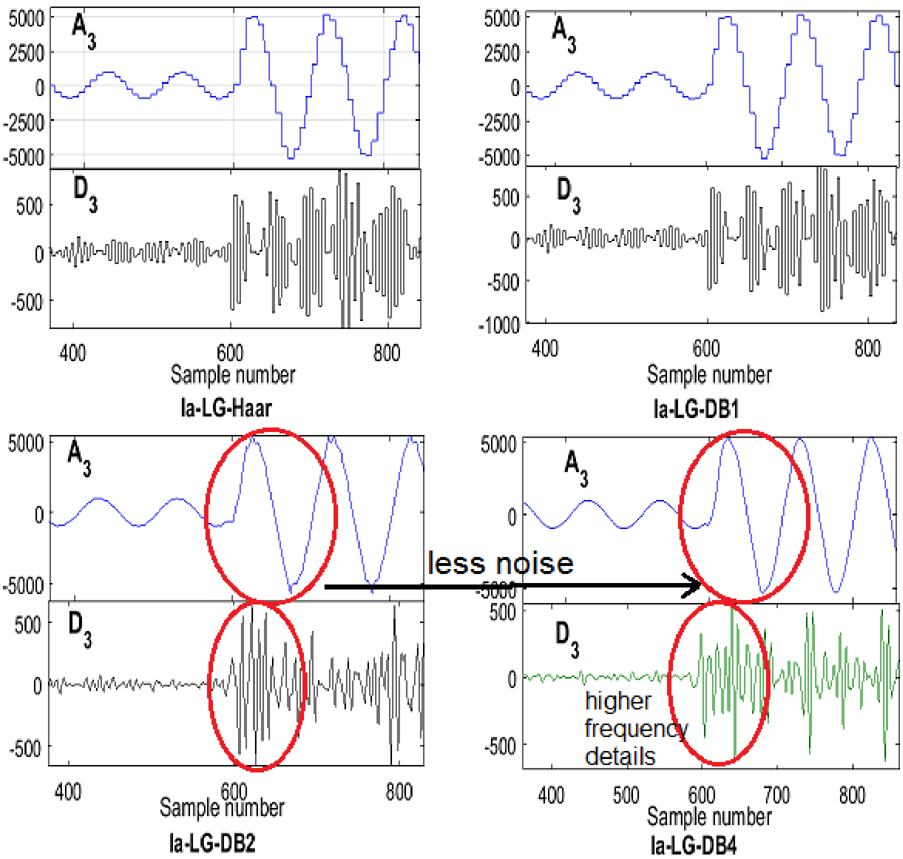

Figure 5.4: Faulty phase signal analysed with wavelet transform using Haar, db1, db2, and db4 mother wavelets respectively.

5.4 Modelling of the Wavelet Packets Transform

In this research, the Wavelet Packets Transform (WPT) has been used due to the ability to decompose a signal from low frequency to high frequency at high resolution, and without losing the time domain information. Additionally, the WPT provides extraction of the frequency features within a shorter analysis level, allowing high speed of fault detection. Therefore, this technique was used to enhance the ability of the proposed protection system to differentiate between the system harmonics and the fault generated transients.

In this work, a three level WPT analysis with the db4 mother wavelet has been applied to extract the fault signature. Figure 5.5 (a) shows the distribution of the lowpass and the highpass filters to obtain the approximation (A) and the detailed (D) coefficients respectively. The number associated with each coefficient refers to the analysis level. Figure 5.5 (b) illustrates the number of coefficients obtained at each level of the WPT. It is clear that at level 1 of the analysis only two coefficients (A1, D1) were obtained, while four coefficients are obtained at the next analysis level. It is clear that the number of coefficients obtained at each level is equal to 2^j, where j refers to the level number. Hence, the number of samples in the input signal should not be less than 2^j.

In this study, the input signal to the WPT was obtained from the CTs in the HVLF system at a sampling rate of 2 kHz. This sampling frequency was chosen based on the range of the fault transients obtained from the FFT analysis in chapter 4, and therefore, only three levels of analysis was applied.

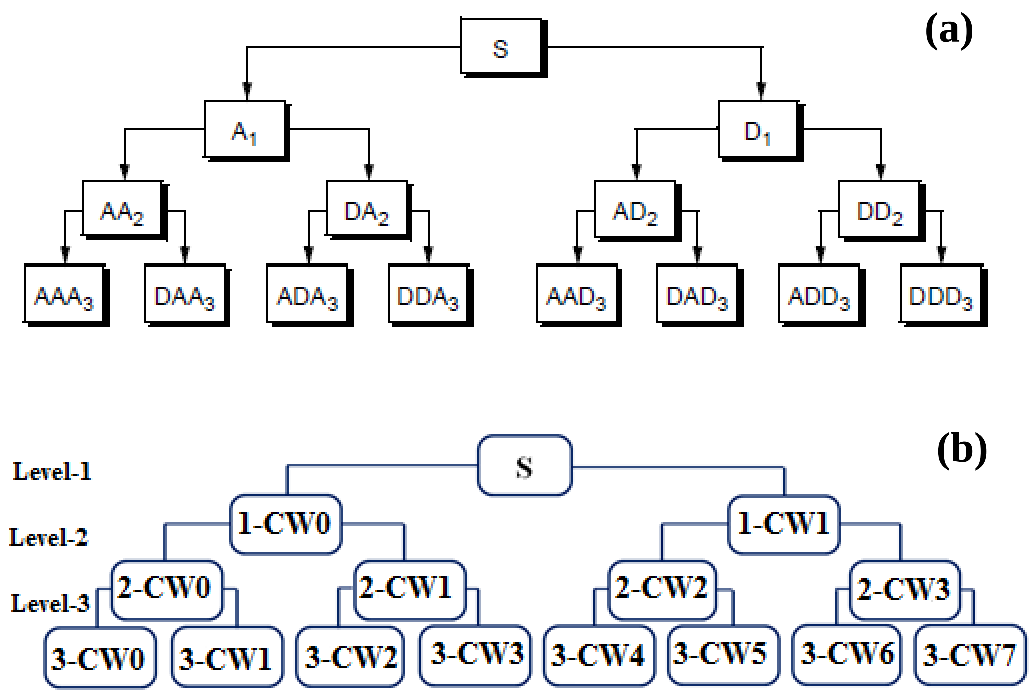

Figure 5.5: Wavelet packet transform tree (a) filters distribution (b) coefficients.

The coefficients obtained from the WPT represents the frequency details contained in the input signal. Each coefficient indicates how a specific frequency band is distributed over a time scale. Table 5-1 illustrates the frequency range of each coefficient obtained at the third level of the WPT tree shown in figure 5.5. Taking into account that the sampling frequency of the input signal was set to 2 kHz, then the highest frequency detail can be determined is 1 kHz according to Nyquist's sampling theorem [51]. In table 5.1 it can be noted that the power frequency is contained in the WPT coefficient CW0. Hence, this coefficient represents the lowest frequency band contained in the signal. Correspondingly, the higher frequency details are distributed in the other coefficients. Therefore, for high frequency transients detection the coefficient CW0 will be neglected. In this study, the WPT was designed for only three analysis levels and the bandwidth of each coefficient obtained was set to 125 Hz, i.e. about 6^{th} harmonic of the 20 Hz power frequency. A lower sampling rate was not chosen because this would have resulted in losing details of the higher frequencies contained in the input signal.

Table 5.1: frequency range of the WPT coefficients obtained at the third analysis level.

Coefficients at level 3	Frequency range
CW0	0 Hz – 125 Hz
CW1	125 Hz –250 Hz
CW2	250 Hz – 375 Hz
CW3	375 Hz – 500 Hz
CW4	500 Hz – 625 Hz
CW5	625 Hz – 750 Hz
CW6	750 Hz – 875 Hz
CW7	875 Hz – 1 kHz

The WPT tree shown in figure 5.5 was implemented with the wavelet toolbox provided by Matlab-Simulink, see figure 5.6. In this model, the three-phase current signals obtained from the CTs at busbar B3 of the HVLF model were processed with WPT filter banks. Each WPT filter bank consists of sets of lowpass and highpass filters that are distributed to form the wavelet tree shown in figure 5.5. In this block the mother wavelet was specified to db4 and the number of analysis levels to 3. The input signals were pre-processed using Matlab buffer blocks in order to convert the signal input from array format to frame based format. The input frame size to the wavelet block should have a number of samples that is a multiple of 2^n, where n is the number of levels. The number of levels was set to 3, thus, each block has 8 ports in the output representing the WPT coefficients. Later, the obtained coefficients were processed for spectral energy calculations.

The WPT model was initially tested by simulating a transmission line fault on the HVLF model given in chapter 4. A single line to ground fault (AG) at distance of 60 km from the sending end at time 0.3 second was demonstrated as an example. The captured three-phase current signals at the measurement point was fed to the WPT model shown in figure 5.6.

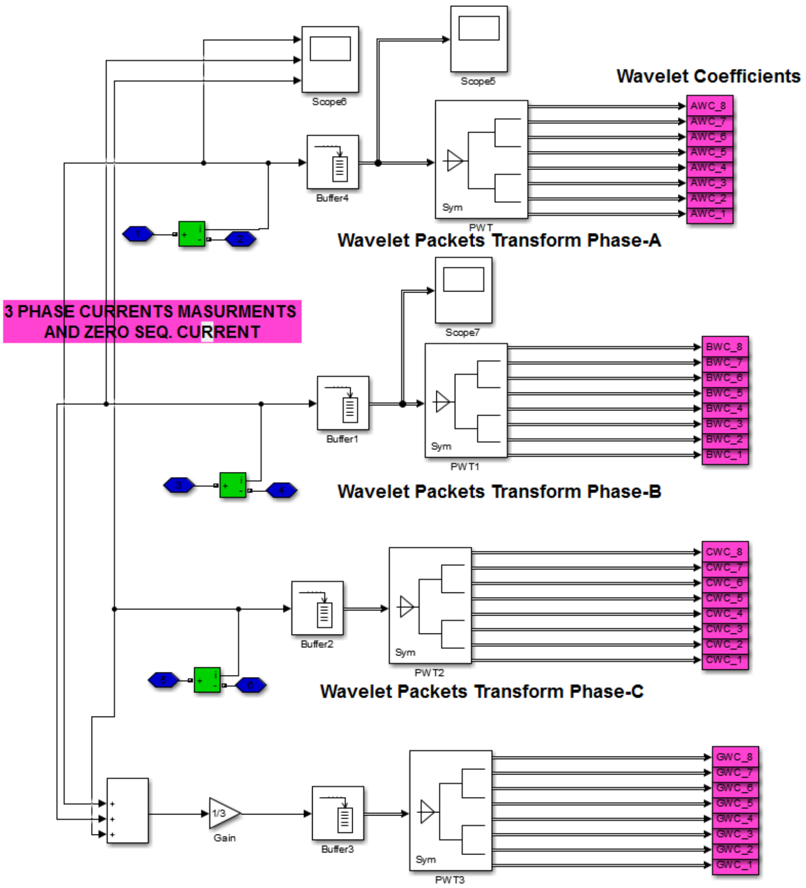

Figure 5.6: Wavelet Packets Transform with Matlab-Simulink.

The WPT analysis results from the faulty phase signal (phase A) are shown in figure 5.7. The results obtained shows the WPT coefficients behaviour over the selected time scale. Each coefficient represents a specific frequency band given in table 5-1. The coefficient CW0 refers to the lowest frequency band including the power frequency, i.e. 20 Hz. Therefore, this coefficient represents the original input signal after most of the high frequency contents have been extracted. The results show that there is a significant change in each coefficient after the fault occurrence at time 0.3 sec. The two detailed coefficients CW1, CW3 at level three of the analysis provides the high frequency details extracted from the approximation and the detailed coefficients of level 2 respectively, see figure 5.5(a). Hence, these two coefficients have very distinctive features with the highest obtained magnitude. Although coefficient CW2 shows a considerable change after the fault occurrence, but it is representing only the lower frequency band of the detailed coefficient obtained at level 2.

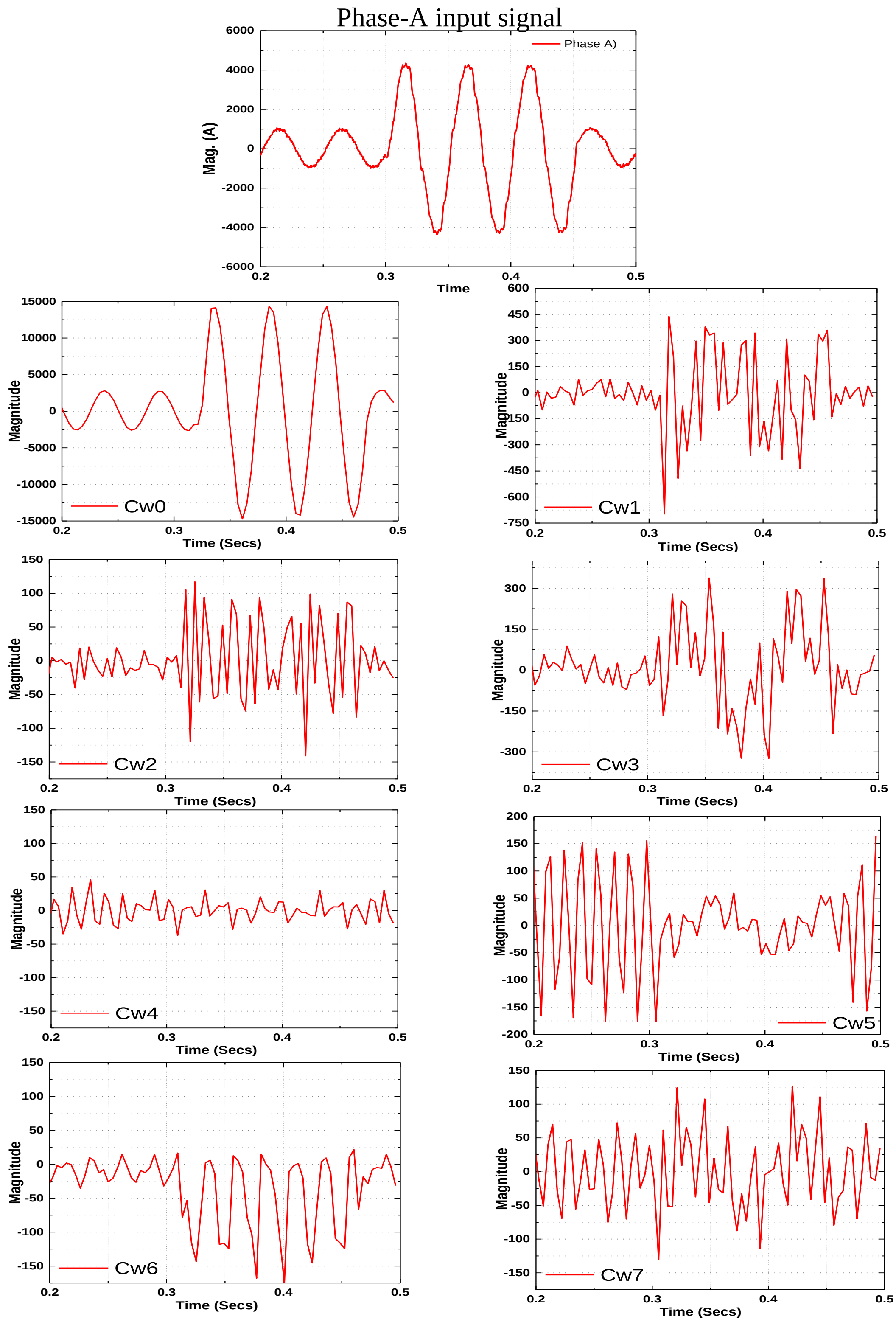

Figure 5.7: The WPT analysis of phase-A current signal when an AG fault occurs at 60 km.

Also, coefficients CW4, CW5 were extracted from the approximation coefficient of the detailed signal at level 2 given in figure 5.5(a). These two coefficients have not shown a significant change as their magnitudes are still low in comparison with CW1 and CW3. As was shown previously in chapter 4, the FFT analysis has demonstrated that some of the high frequencies were filtered by the transmission line after the fault occurrence. Hence, coefficient CW5 shows a lower magnitude after the fault occurrence. Finally, the highest frequency band exist in the input signal is contained in coefficient CW7, showing negligible change with insignificant increase in magnitude.

The results have demonstrated that the WPT analysis is capable of capturing all the frequency details contained in the faulty phase current signal. Hence, the proposed fault detection algorithm applied to the HVLF system utilises the WPT analysis for fault diagnosis. A simulation of different transmission line fault types at various locations of the HVLF transmission line was carried out. The next section represents the results obtained from the WPT analysis of the three-phase current signals under all possible fault scenarios.

5.5 HVLF Fault Signals Analysis using WPT

In this section, the ability of the designed WPT to extract the high frequency information from the HVLF current signals was tested thoroughly. Simulation of different fault types at various locations of the transmission line was carried out. Then, the three-phase current signals measured with the CTs at the sending end were processed using the WPT. The results of the WPT analysis were studied in order to obtain the characteristics of the fault transients. These characteristics are used for extracting the fault features applied to the protection system. As shown above, the fault type and location information are preserved in the high frequency details.

These features were obtained by evaluating the spectral energy of the WPT coefficients obtained at the third analysis level. The spectral energy is obtained as follows:

$$\mathrm{SE}_{d(3,CWx)} = \sum_{k=0}^{n} \left| I_{d(3,CWx)} \right|^2 \qquad (5.2)$$

where $|I|$ is the magnitude of the sample k at the corresponding analysis coefficient, n is the maximum sample number, and CWx is the order of the WPT coefficient at the third analysis level.

The spectral energy of all WPT tree coefficients were obtained by simulating various fault types such as, line to ground (LG), double line to Ground (LLG), three lines (LLL) and three lines to ground (LLLG) faults. Therefore, a total of 11 fault types were simulated at four locations of the transmission line. The arbitrary selected locations were at distances of 20, 60, 120, 180 km from the measurement point at the sending end. Under all fault conditions, the fault resistance and the ground resistance were set to 5Ω and 1 Ω, respectively. A low fault resistance was chosen based on the assumption of subsea cable conductor interruption given in [90]. The effect of the fault inception angle on the proposed protection system is also investigated thoroughly in next chapter. In this chapter, for all fault scenarios the fault was simulated to occur at 0.3 sec, and the measured current signals were sampled at 2 kHz. The WPT analysis of the three-phase current signals was carried out as previously discussed in Section 5.4.

In order to determine a reliable fault detection decision, the spectral energy of all the WPT coefficients vs. time stamp plot was obtained. Then, the spectral energy plot of the WPT coefficients was used to determine whether the corresponding phase was involved in the fault or not. The phase selection criteria is based on two main requirements:

1) The faulty phase with a maximum spectral energy obtained from certain coefficients appears at fault incident due to the fault generated high frequency transients.
2) The selected coefficient or coefficients for fault identification must provide a substantial response under all fault conditions, such as fault type and location.

Based on these criteria, a comparison of the spectral energies of the resulted WPT coefficients for different fault types and locations have been investigated, and the results are presented in detail in the following subsections.

5.5.1 Single Line to Ground Fault (LG)

In order to evaluate the performance of the designed WPT based protection system, a single line to ground fault on the HVLF transmission line was initially simulated using Matlab-Simulink. Then, the measured three-phase current signals were processed with the modelled WPT. Note that, the waveform of these signals was previously shown in figure 4.17. The fault resistance was set to 5Ω and ground resistance to 1 Ω, and the fault was simulated to take place at time 0.3 seconds. The fault resistance was chosen according to the . The WPT analysis results of phase-A to ground fault at locations of 20, 60, 120 and 180 km from the sending end are given in figures 5.8 to 5.11. Since, coefficient CW0 represents the input signal with most of the high frequencies are filtered out, then the results given in this chapter illustrate the remaining 7 coefficients obtained at the third level analysis. These coefficients show the existence of the corresponding frequency band given in table 5-1 over the specified time scale.

In figure 5.8, it can be noted that under pre-fault condition all coefficients of the three phases A, B and C have a relatively low spectral energy amplitude. The low energy amplitude in these coefficients is due to the presence of the cycloconverter generated harmonics. However, high energy spikes produced in the coefficients such as CW1, CW2, CW3 and CW6 of the faulty phase signal when a phase-A to ground fault occurs at time 0.3 seconds. Note that, for other healthy phases B and C the energy amplitude remains low after the fault incident. Other WPT coefficients such as CW4, CW5 and CW7 shows an oscillatory behaviour with low energy amplitude. The energy content of each coefficient is highly dependent on the frequency of the post-fault generated transients. Therefore, the highest energy amplitude was obtained for coefficients CW1 and CW3 as they represent the high frequency components of the analysed signal. Taking into account, these coefficients are the output of the high-pass filters at the previous analysis level, see figure 5.5.

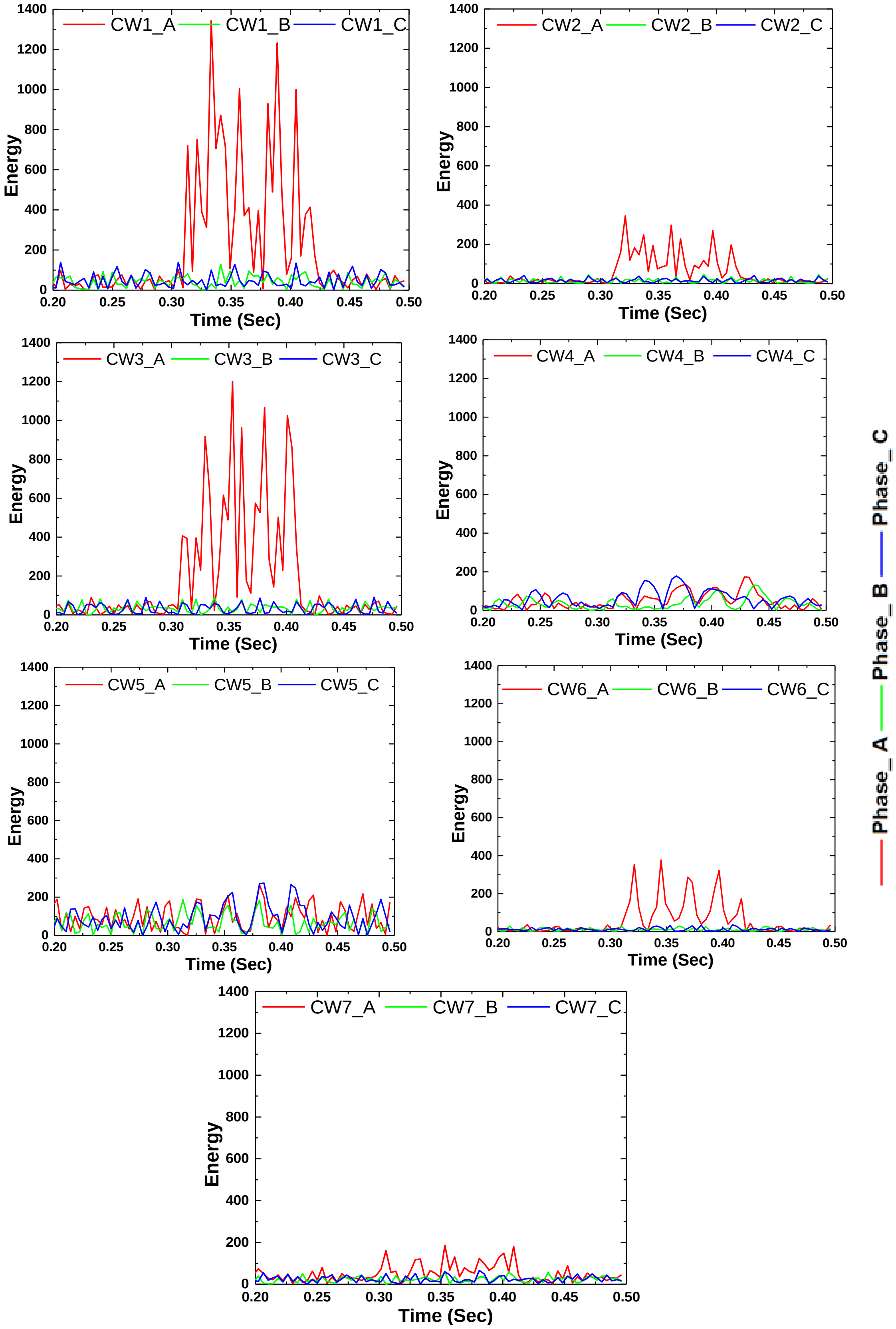

Figure 5.8: Wavelet Coefficients of the three-phase current signals of an LG fault at 20 km from sending end.

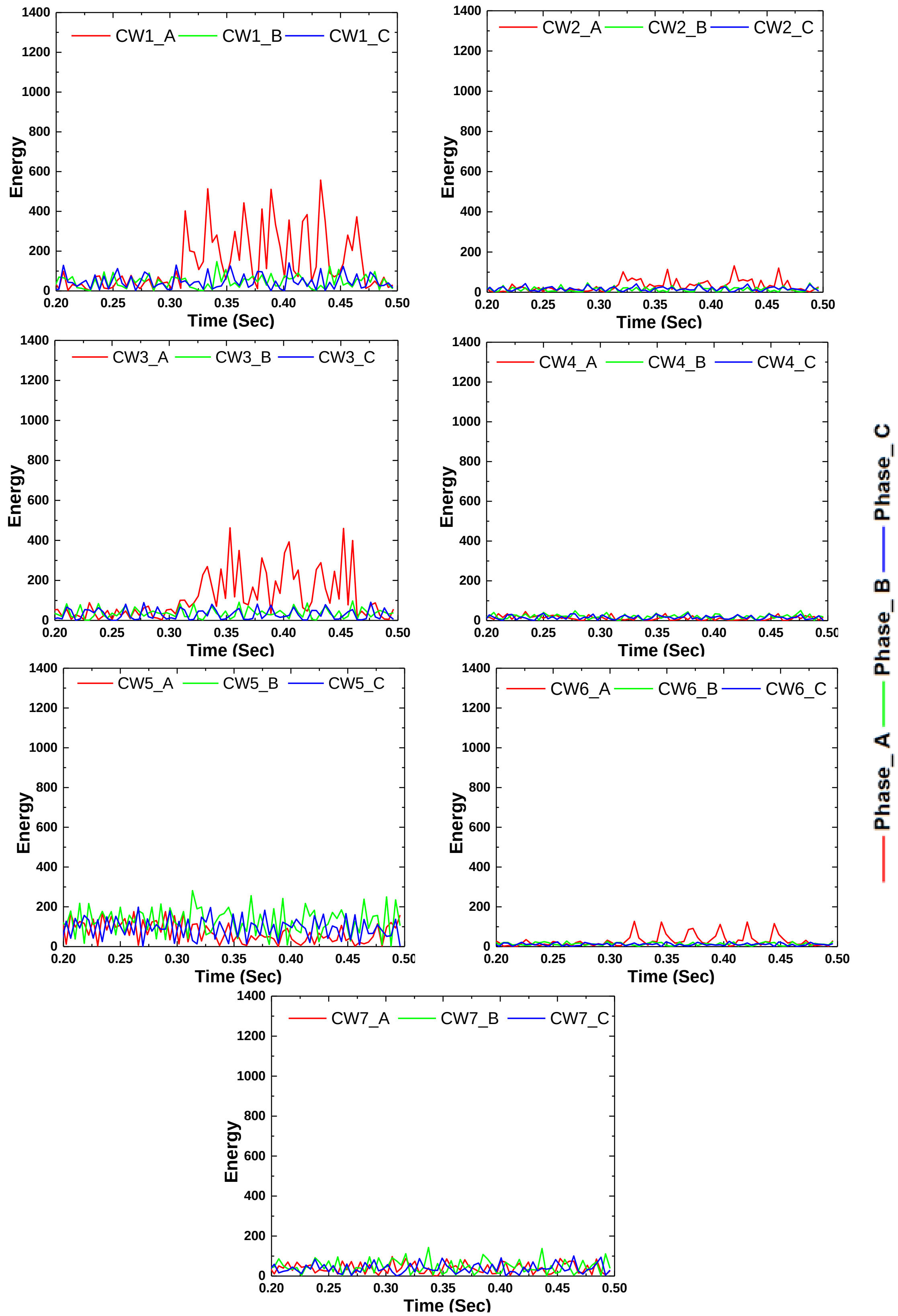

Figure 5.9: Wavelet Coefficients obtained from the three-phase current signals of an LG fault at 60 km from sending end.

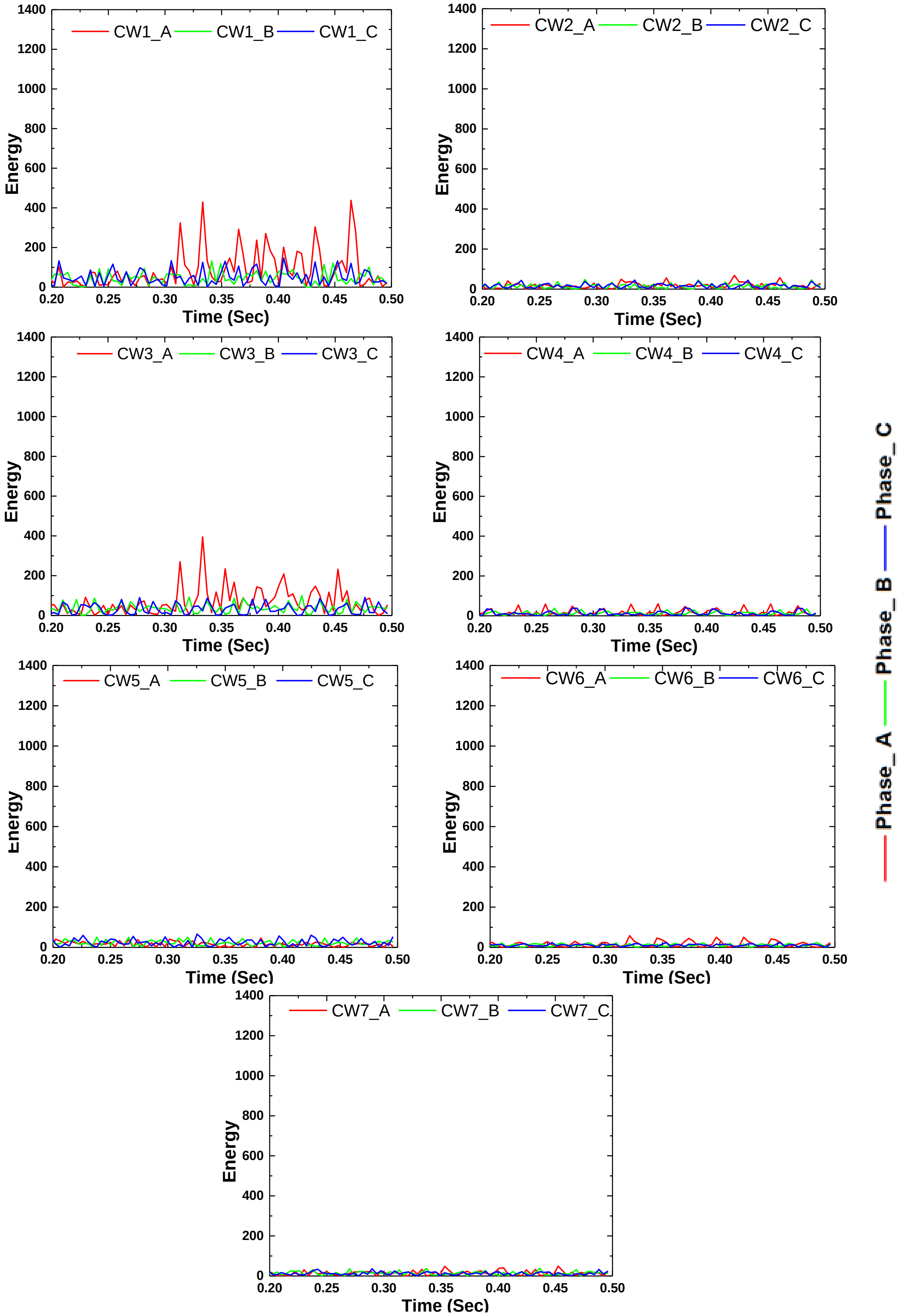

Figure 5.10: Wavelet Coefficients obtained from the three-phase current signals of an LG fault at 120 km from sending end.

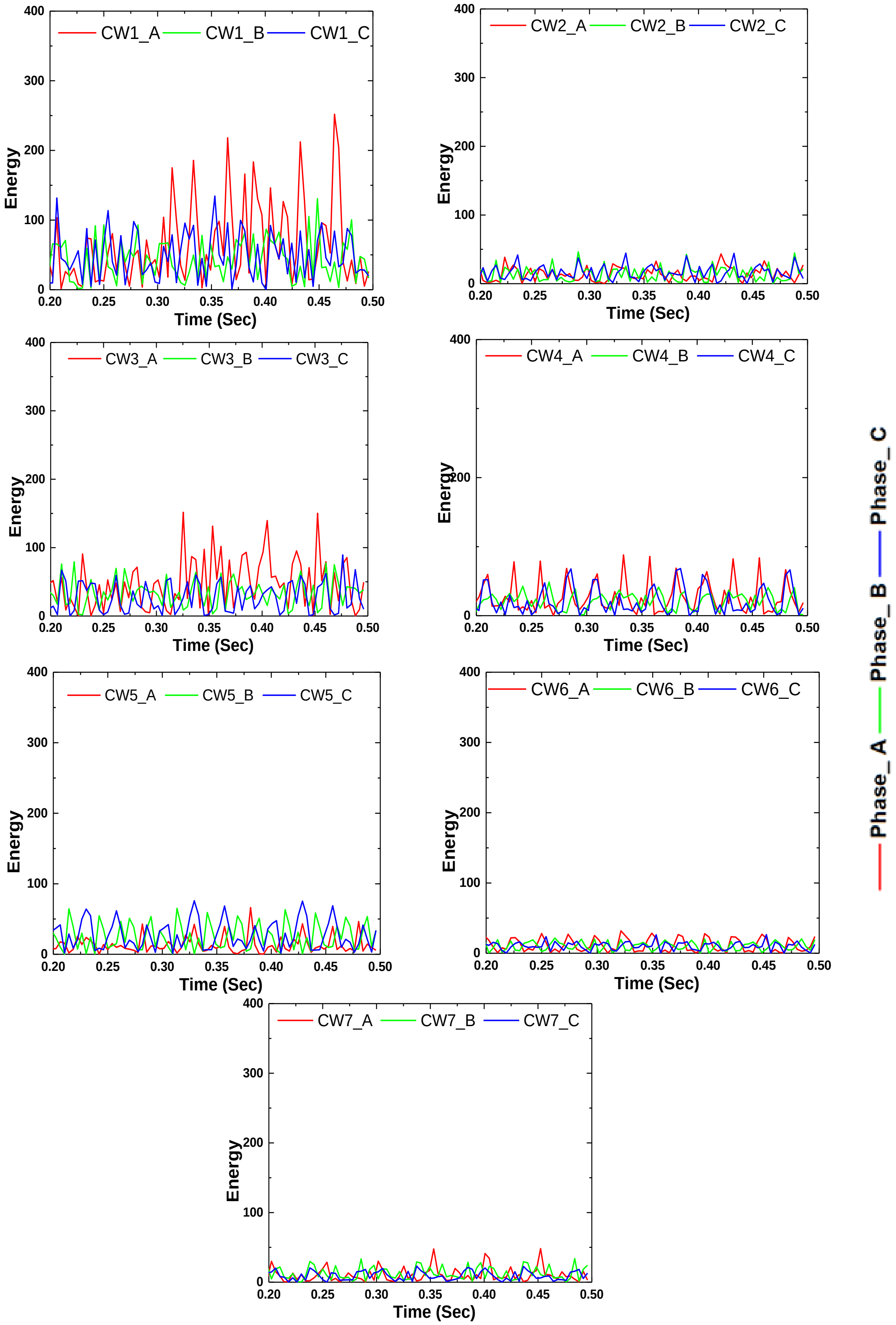

Figure 5.11: Wavelet Coefficients obtained from the three-phase current signals of an LG fault at 180 km from sending end.

Figures 5.9 to 5.11 show the phase-A to ground fault at further distances from the measurement point. It can be observed that the energy amplitude of coefficients CW1, CW2, CW3 and CW6 decease when the fault distance increases. Also, it is clear that at extreme remote fault distances such as 120 and 180 km, coefficients CW2 and CW6 obtained from the faulty phase-A signal have an insignificant change in the energy amplitude after the fault occurs. This is because the transmission line segment between the fault point and the measurement point increases and consequently the line impedance increases too. The additional line impedance forms a passive filter in which the frequencies within the frequency band of these coefficients are suppressed.

Other WPT coefficients (CW4, CW5 and CW7) have shown negligible change in the energy content after the fault incident at all simulated distances. This confirms that the fault generated transients are not in the range of these coefficients frequency band. In addition, the energy amplitude of the WPT coefficients of the non-faulty phases B and C remain relatively low at all tested distances. Finally, it was recommended that the frequency components obtained from the two WPT coefficients CW1 and CW3 are a useful choice to the protection algorithm.

5.5.2 Line to Line Fault (LL)

A double line fault with similar fault scenarios to the previous LG fault simulations was carried out. Figures 5.12 to 5.15 demonstrate the WPT analysis results of the three-phase current waveforms for a phase-A to phase-B fault occurring at time 0.3 secs. In this case, the fault resistance was set to 5Ω.The spectral energy obtained from the WPT coefficients shows high magnitude spikes in the analysed faulty phases A and B signals after the fault occurrence. This high spectral energy is clearly visible on the WPT coefficients CW1, CW2, CW3, CW6 and CW7 when the fault occurs at 20 km distance. However, the spectral energy magnitude of those phases decreases when the fault distance increases, see figures 5.13 to 5.15.

It can also be noticed that coefficients CW2, CW6, CW7 obtained from the faulty phases signals show unimportant change at extreme fault locations such as 120 and 180 km. Also, coefficients CW4 and CW5 have shown negligible change in the obtained spectral energy under all conditions. Keeping in mind, the spectral energy obtained from the WPT of phase-C signal keeps at a low level during pre- and post-fault conditions. It was found that the fault generated transients of the double line fault can be consistently captured with the WPT coefficients CW1 and CW3 at all tested distances.

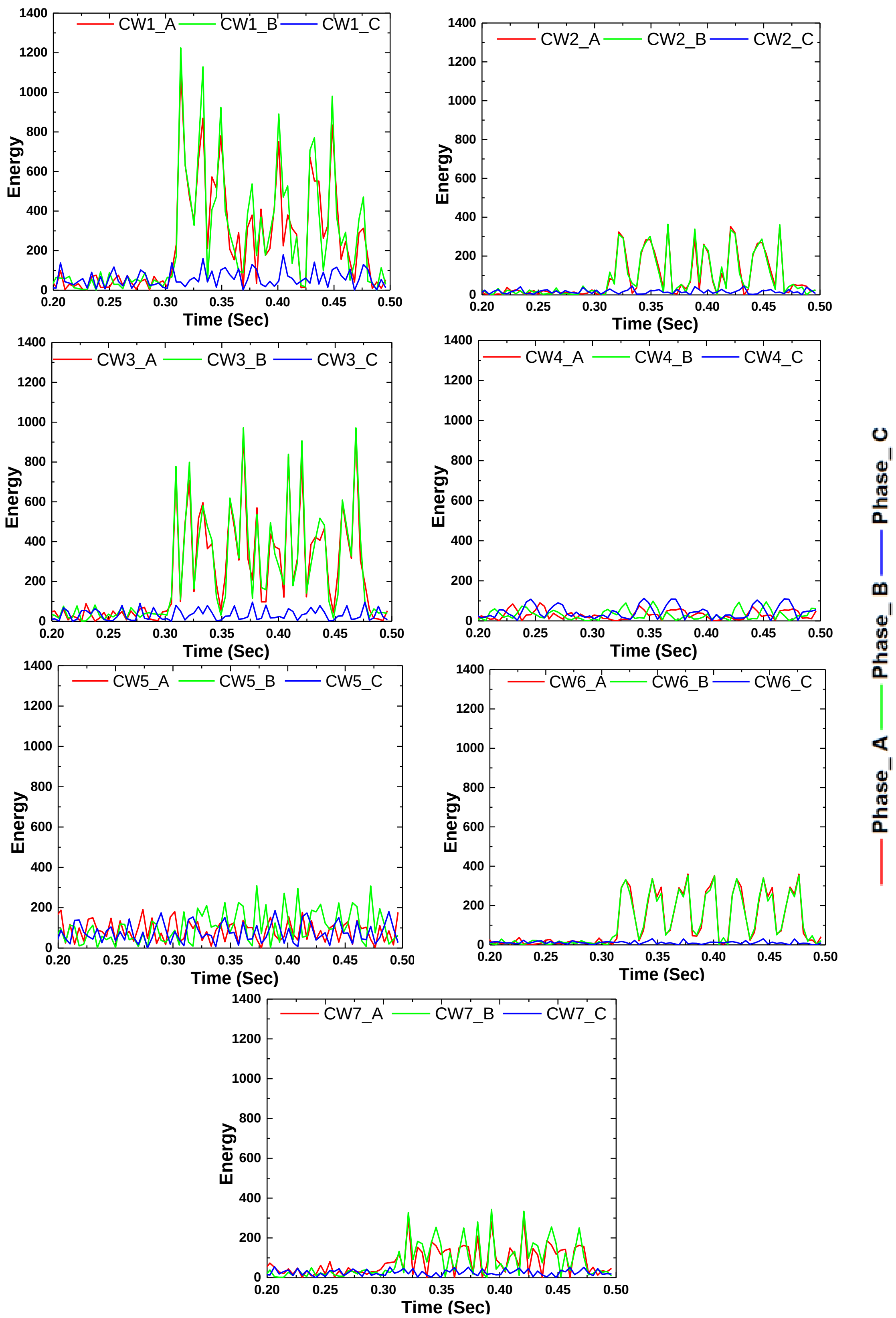

Figure 5.12: Wavelet Coefficients obtained from the three-phase current signals of an LL fault at 20 km from sending end.

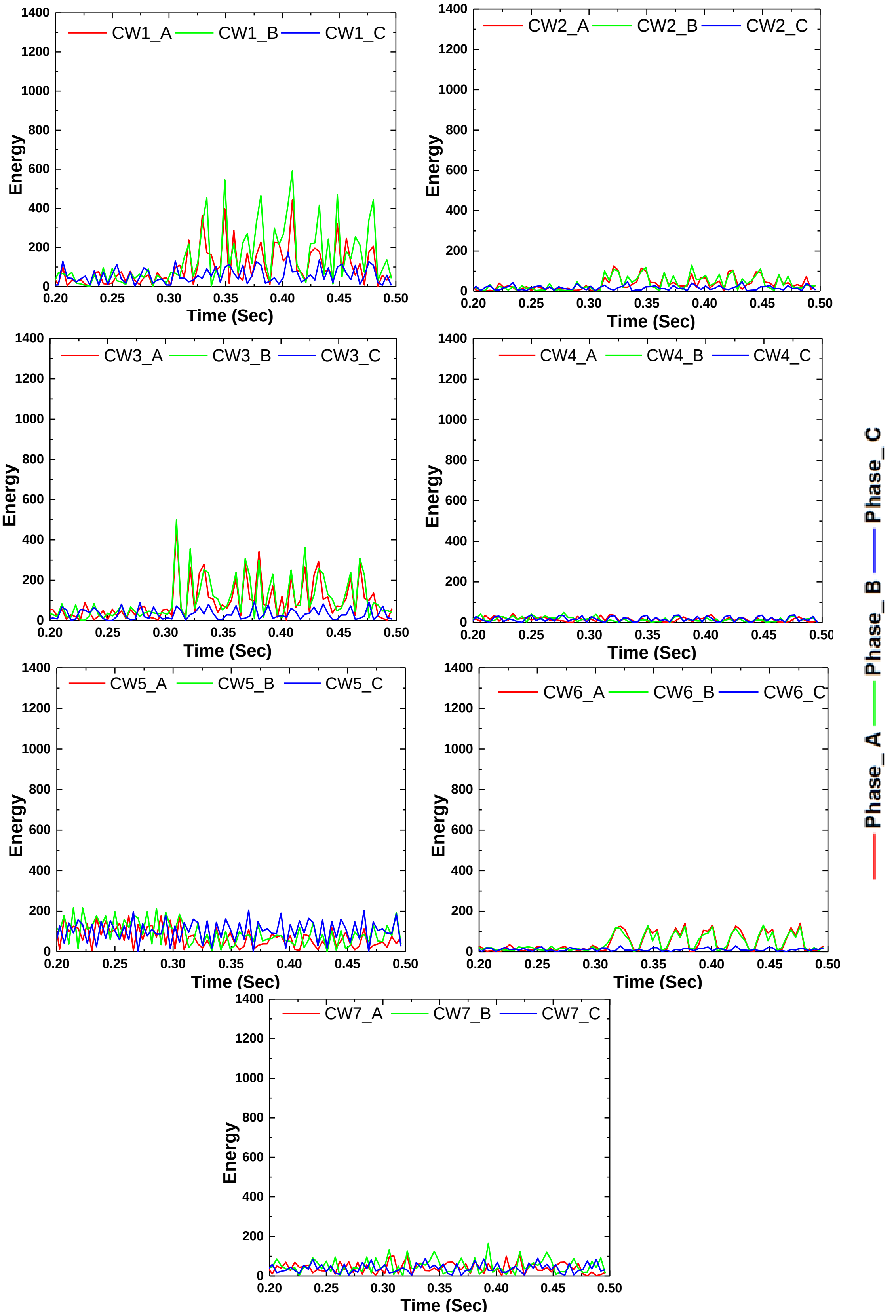

Figure 5.13: Wavelet Coefficients obtained from the three-phase current signals of an LL fault at 60 km from sending end.

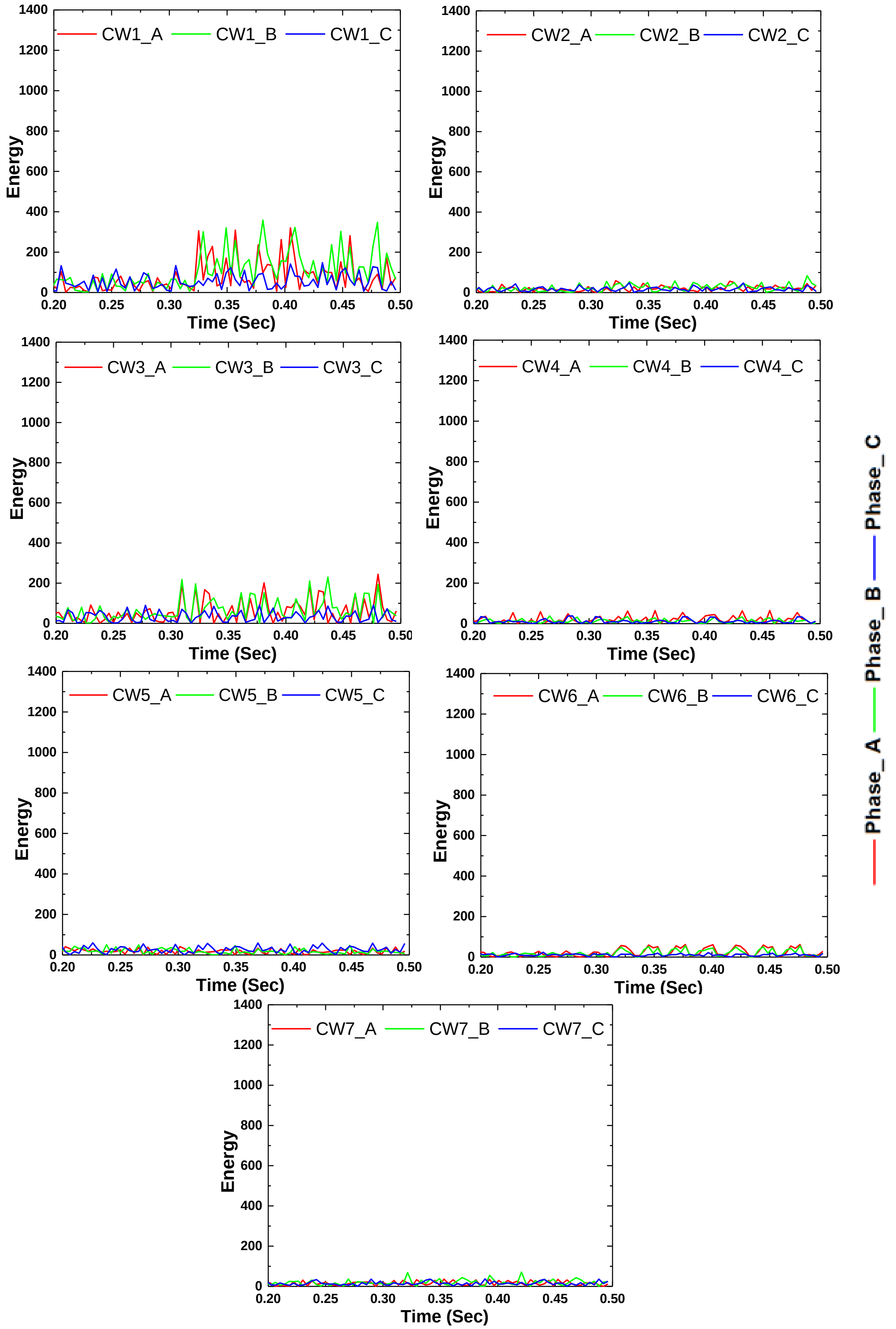

Figure 5.14: Wavelet Coefficients obtained from the three-phase current signals of an LL fault at 120 km from sending end.

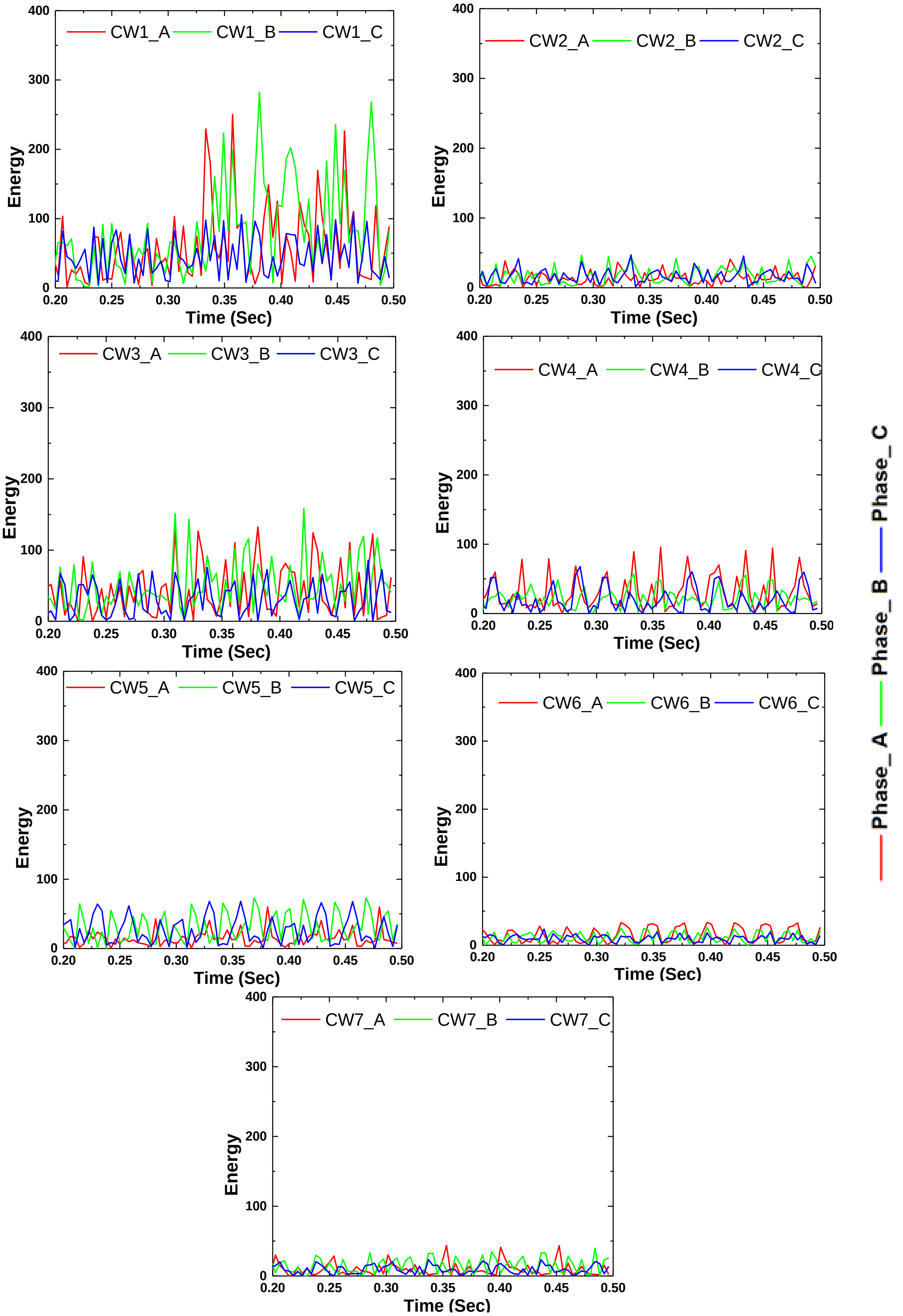

Figure 5.15: Wavelet Coefficients obtained from the three-phase current signals of an LL fault at 180 km from sending end.

5.5.3 Double Line to Ground Fault (LLG)

The performance of the WPT was tested when a double line to ground fault occurs on the HVLF system. This type of fault was simulated with similar to the previously carried out fault parameters and locations. In this case, the fault resistance was set to 5Ω and ground resistance to 1 Ω. The WPT analysis results of the three phases current signals obtained from double phases (phase A and Phase B) to ground fault are given in figures 5.16 to 5.19. The obtained spectral energy of all three phases of all WPT coefficients is relatively low before the occurrence of the fault. Then, the results show that a high spectral energy is obtained from the faulty phases A and B when the fault occurs at time 0.3 sec. Also, in terms of the coefficients behaviour during pre- and post-fault conditions, a similar observation to the double line fault can be noted. The WPT coefficients CW1 and CW3 have shown a consistent behaviour when the fault occurs at all locations. The spectral energy of those coefficients of the faulty phases rises immediately after the fault incident. All other coefficients have shown uneven behaviour when the fault distance changes.

In this type of fault, the only difference noted was the magnitude of the spectral energy of the coefficients is slightly higher compared to those of the double line fault. This is due to the ground return path and hence less electromagnetic coupling between phases. Therefore, for the detection of ground involvement in the fault, the zero sequence component of the three-phase current was utilised. The zero sequence component is obtained by summing up the three phase currents, and then analysed with the WPT model, see figure 5.6. The detailed results obtained from this analysis are given in subsection 5.5.6 later. It is also clear, the magnitude of the spectral energy of coefficients CW1 and CW3 decreases when the fault distance increases. However, the spectral energy of WPT coefficients obtained from the healthy phase (phase-C) signals remain low during all times.

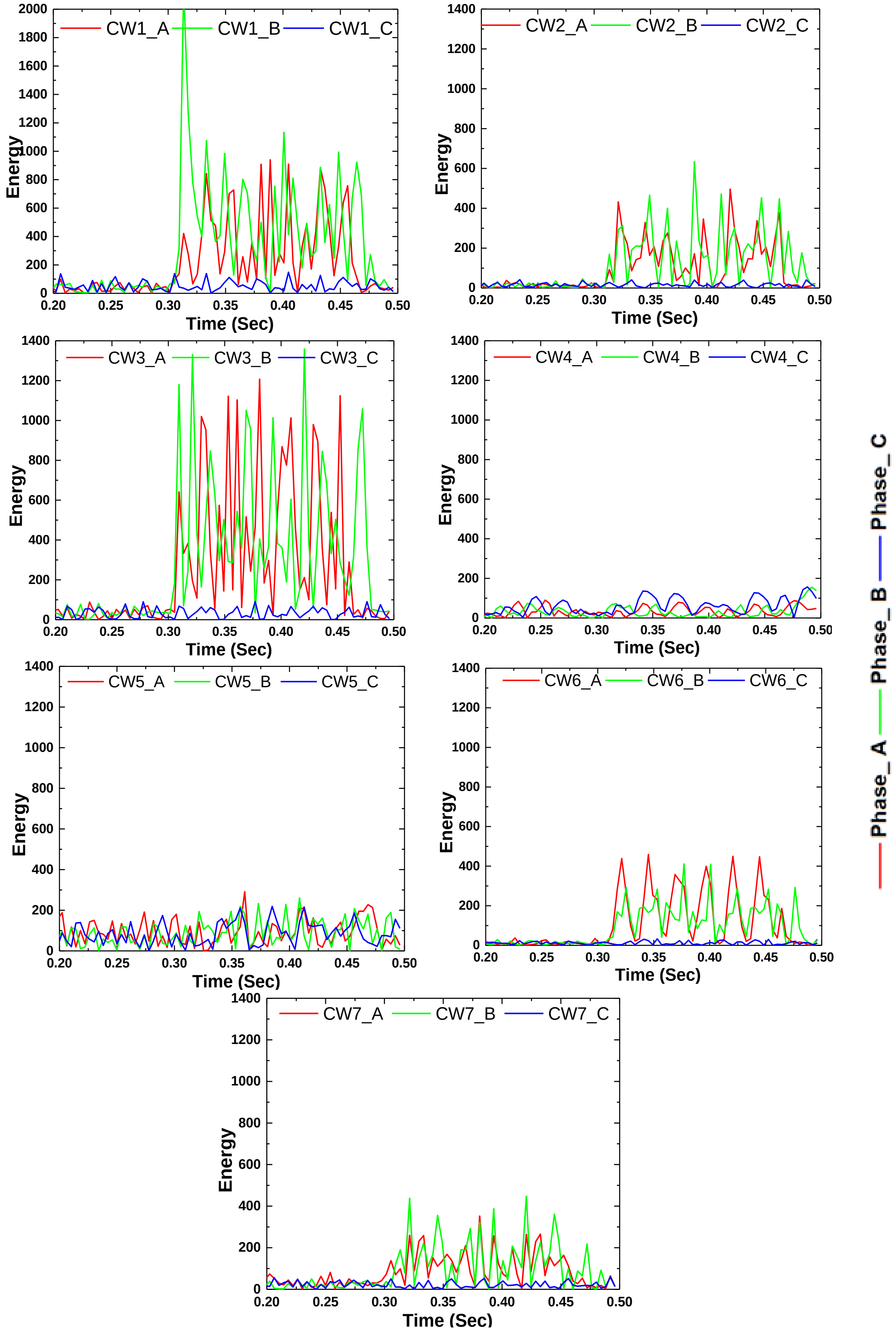

Figure 5.16: Wavelet Coefficients obtained from the three-phase current signals of an LLG fault at 20 km from sending end.

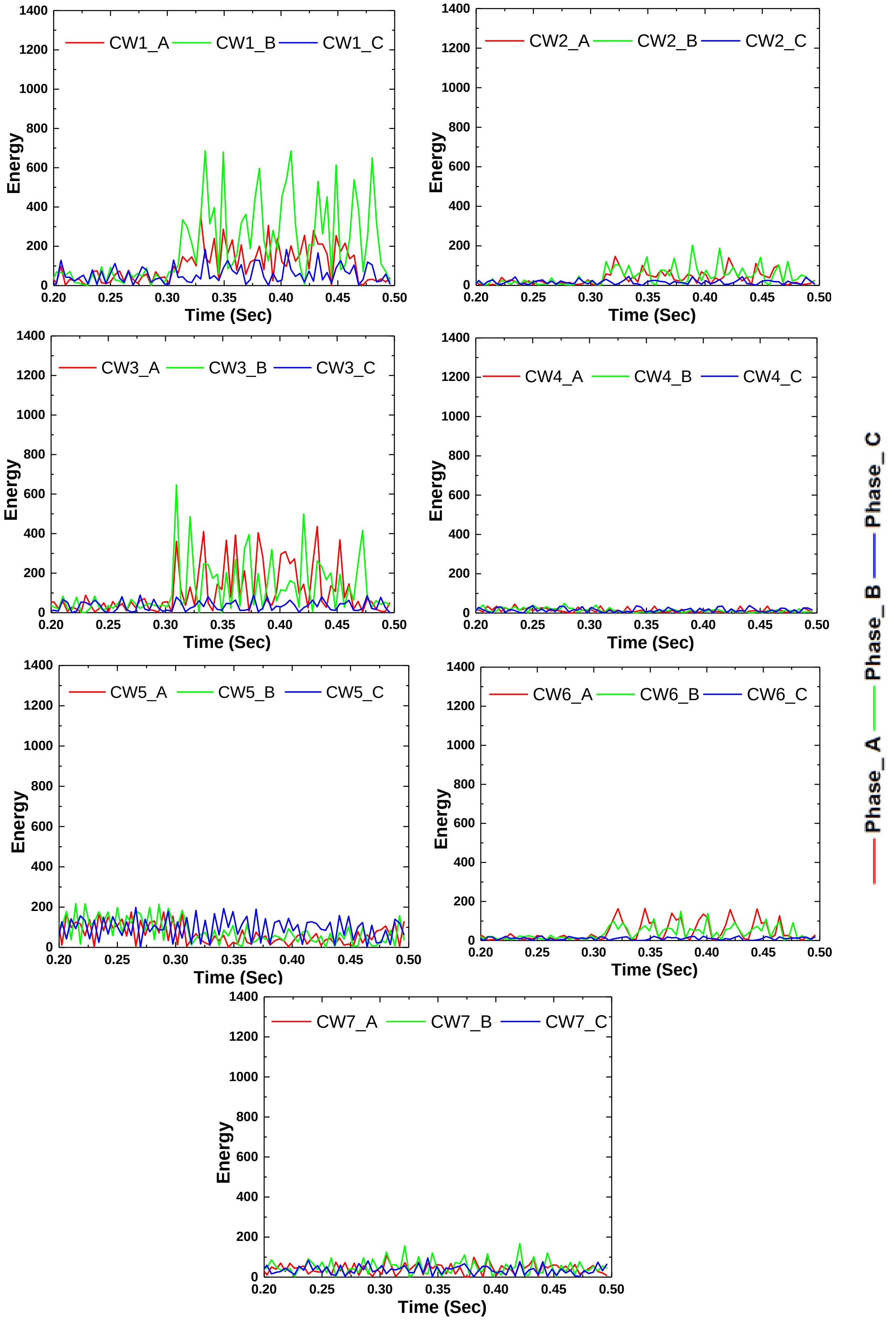

Figure 5.17: Wavelet Coefficients obtained from the three-phase current signals of an LLG fault at 60 km from sending end.

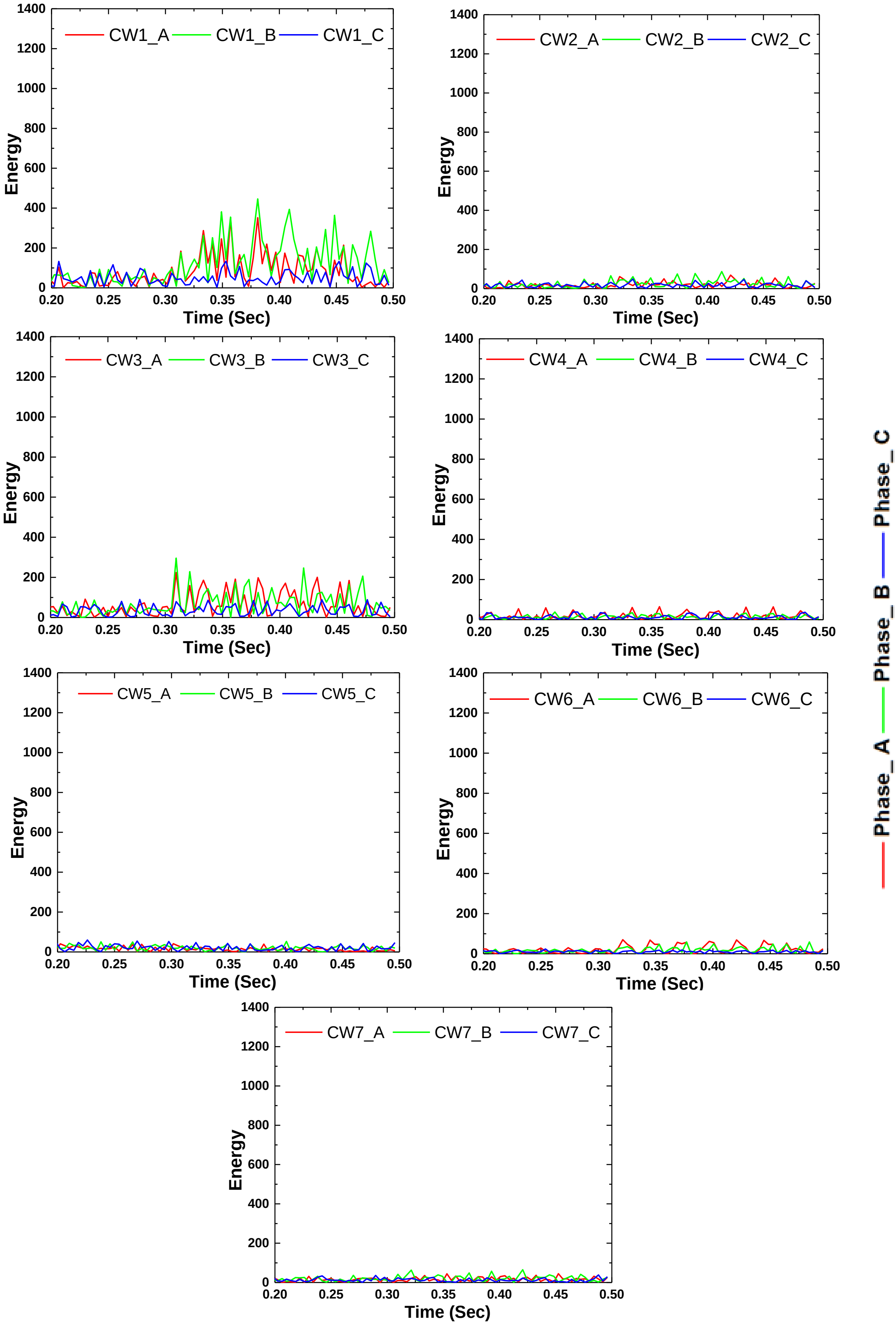

Figure 5.18: Wavelet Coefficients obtained from the three-phase current signals of an LLG fault at 120 km from sending end.

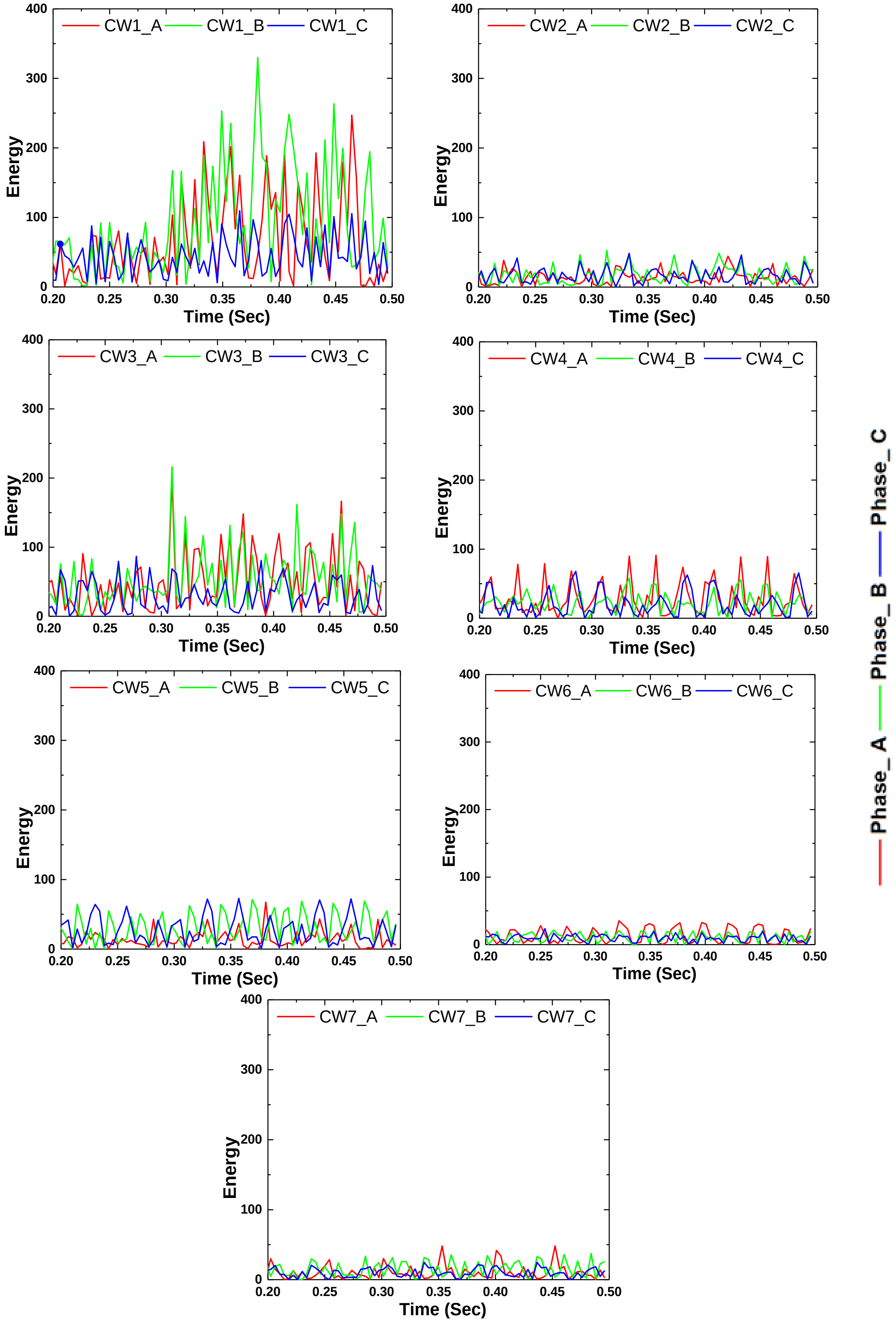

Figure 5.19: Wavelet Coefficients obtained from the three-phase current signals of an LLG fault at 180 km from sending end.

5.5.4 Three Lines Fault (LLL)

Although this type of fault is less frequent to occur, but it is considered as the worst fault case on the transmission system. Therefore, the three phase fault current signals were processed with the designed WPT in order to test performance of the protection system. In this work, a simulation of a short circuit on the three phases A, B and C of the HVLF transmission line was carried out. The fault parameters and locations applied in this test were the same as the previously simulated LG and LL faults. Therefore, the fault resistance was set to 5Ω and ground resistance to 1 **Ω**. The WPT coefficients obtained from the analysis of the captured current signals are given in figures 5.20 to 5.23. The results show clearly that for some coefficients the spectral energy rises immediately after the fault occurrence. The frequency distribution of the fault generated transients almost agrees with those obtained when a double line fault occurs. Where, at close locations coefficients CW1, CW2, CW3, CW6 and CW7 of all the three phases A, B and C show significant increase in the energy after the fault occurrence. However, at extreme remote locations, i.e. 120 and 180 km, only CW1 and CW3 have shown clearly the presence of the fault transients. In addition, it is important to notice that the magnitude of the spectral energy of the two coefficients CW1 and CW3 decreases with the fault distance being increased.

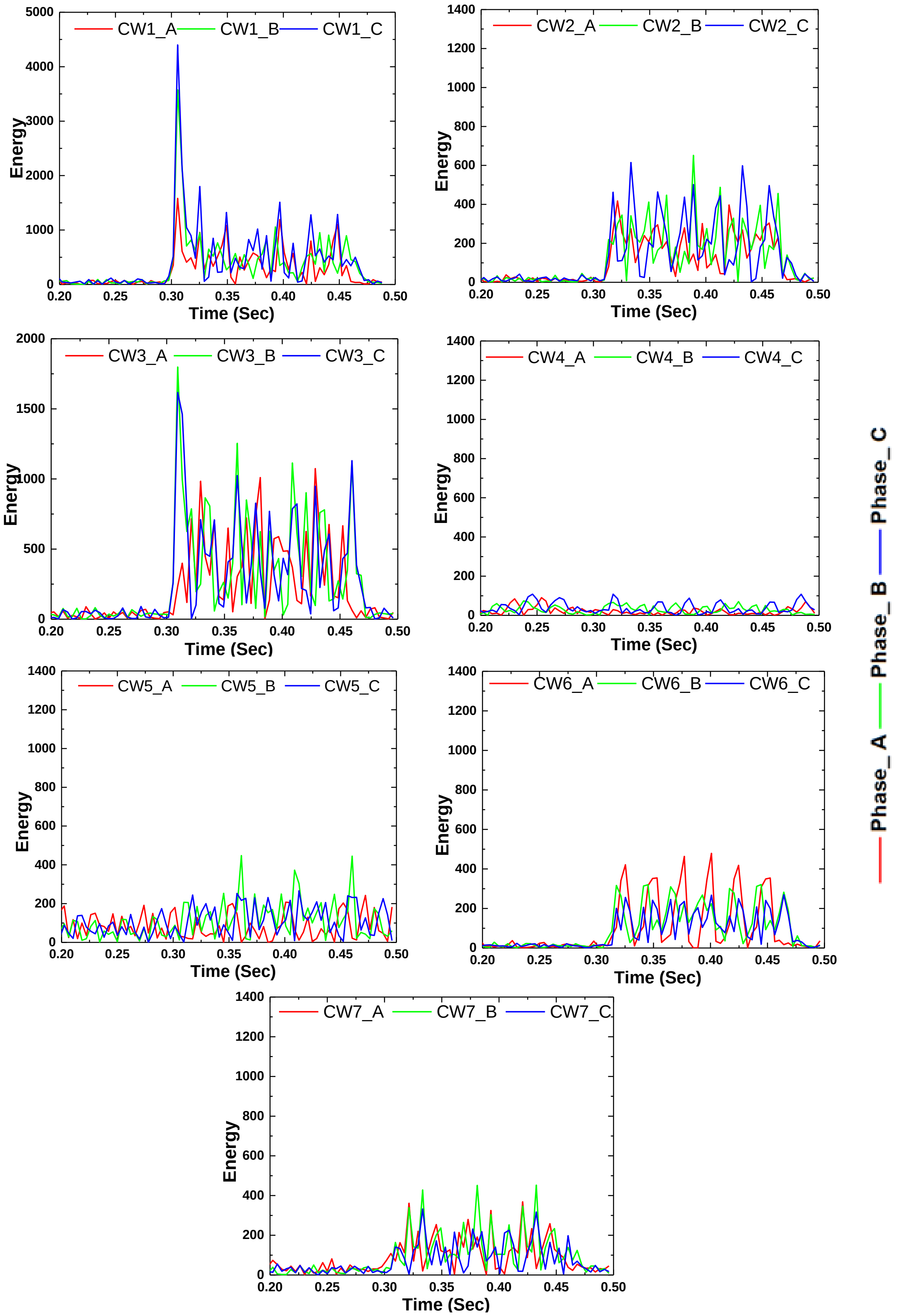

Figure 5.20: Wavelet Coefficients obtained from the three-phase current signals of an LLL fault at 20 km from sending end.

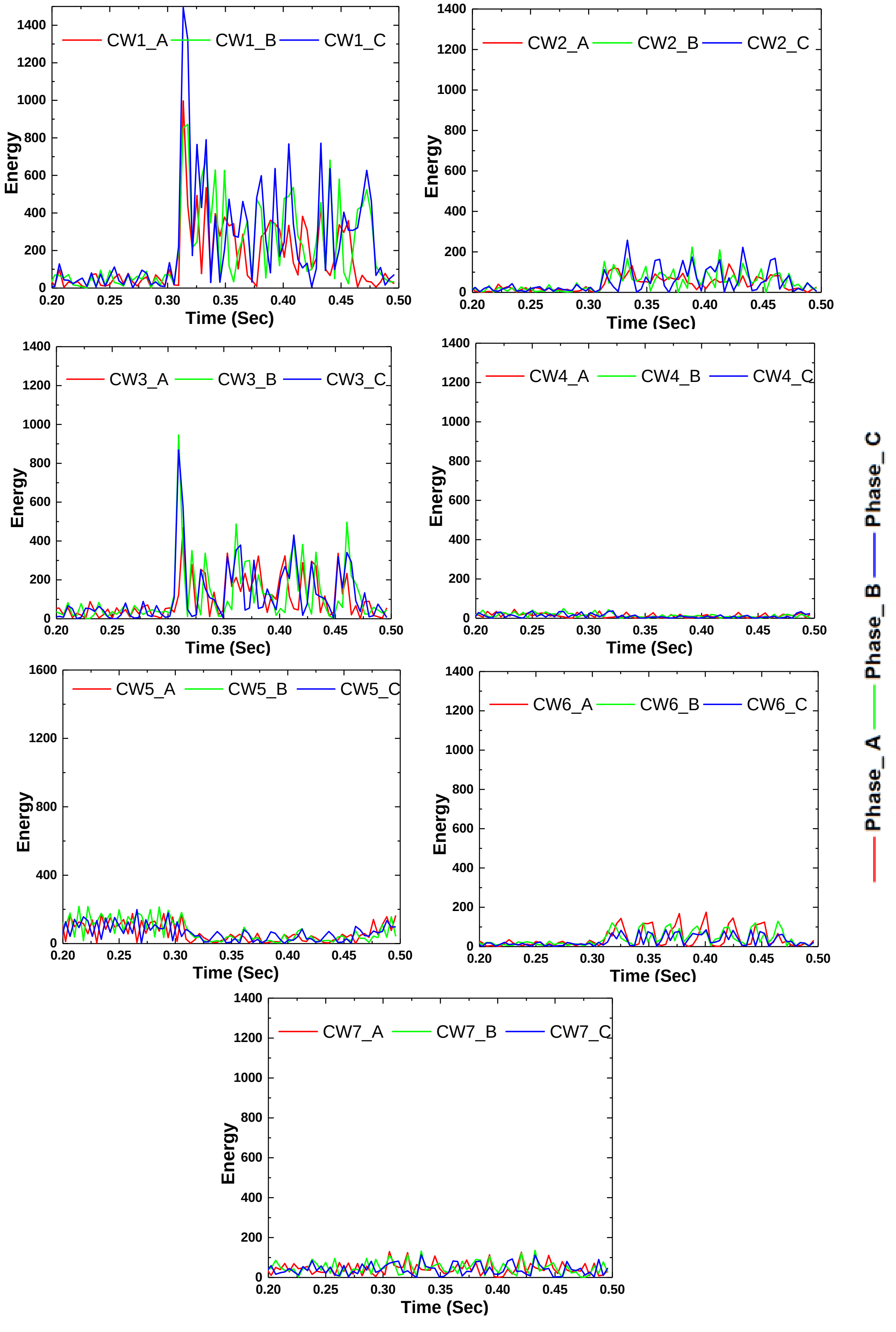

Figure 5.21: Wavelet Coefficients obtained from the three-phase current signals of an LLL fault at 60 km from sending end.

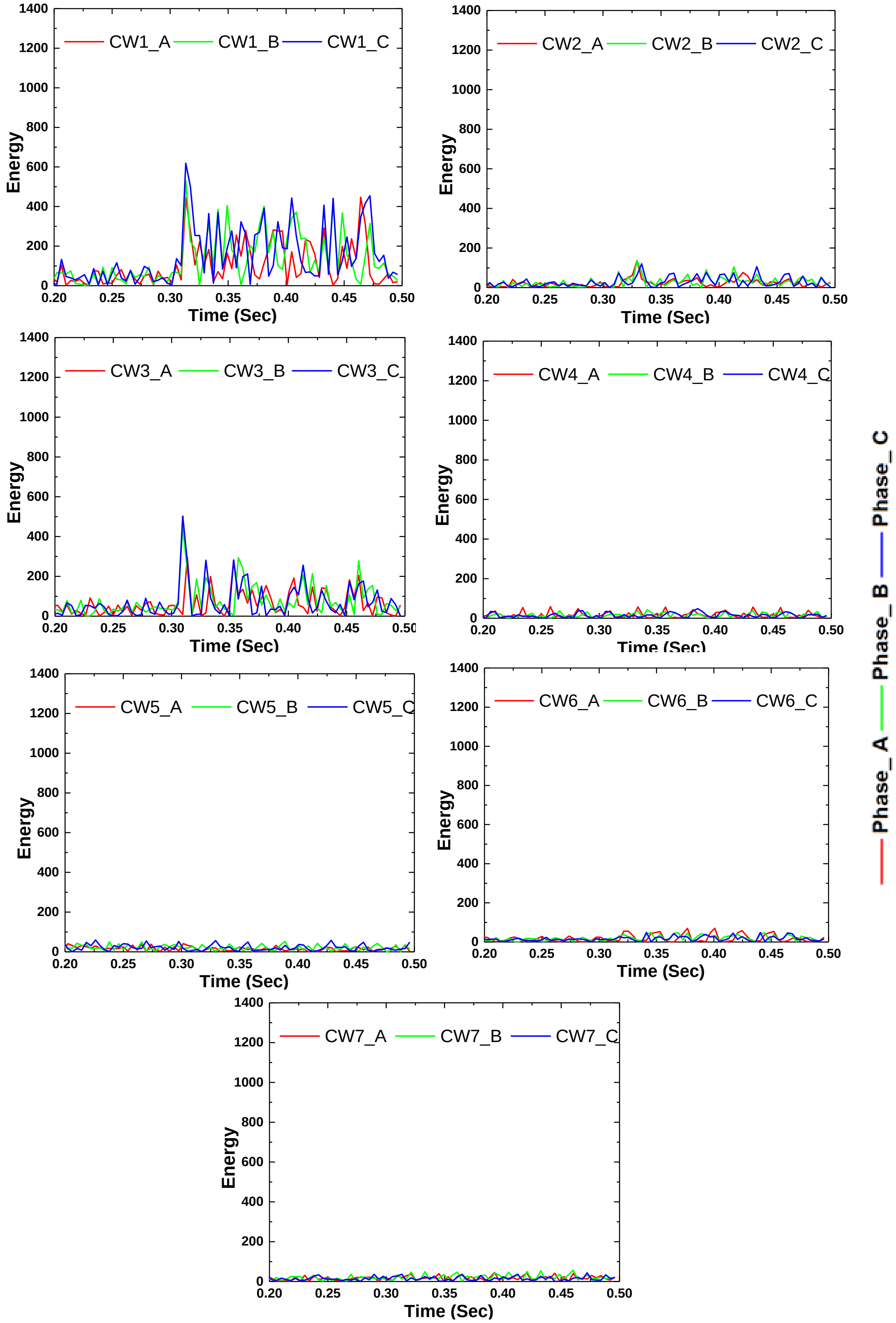

Figure 5.22: Wavelet Coefficients obtained from the three-phase current signals of an LLL fault at 120 km from sending end.

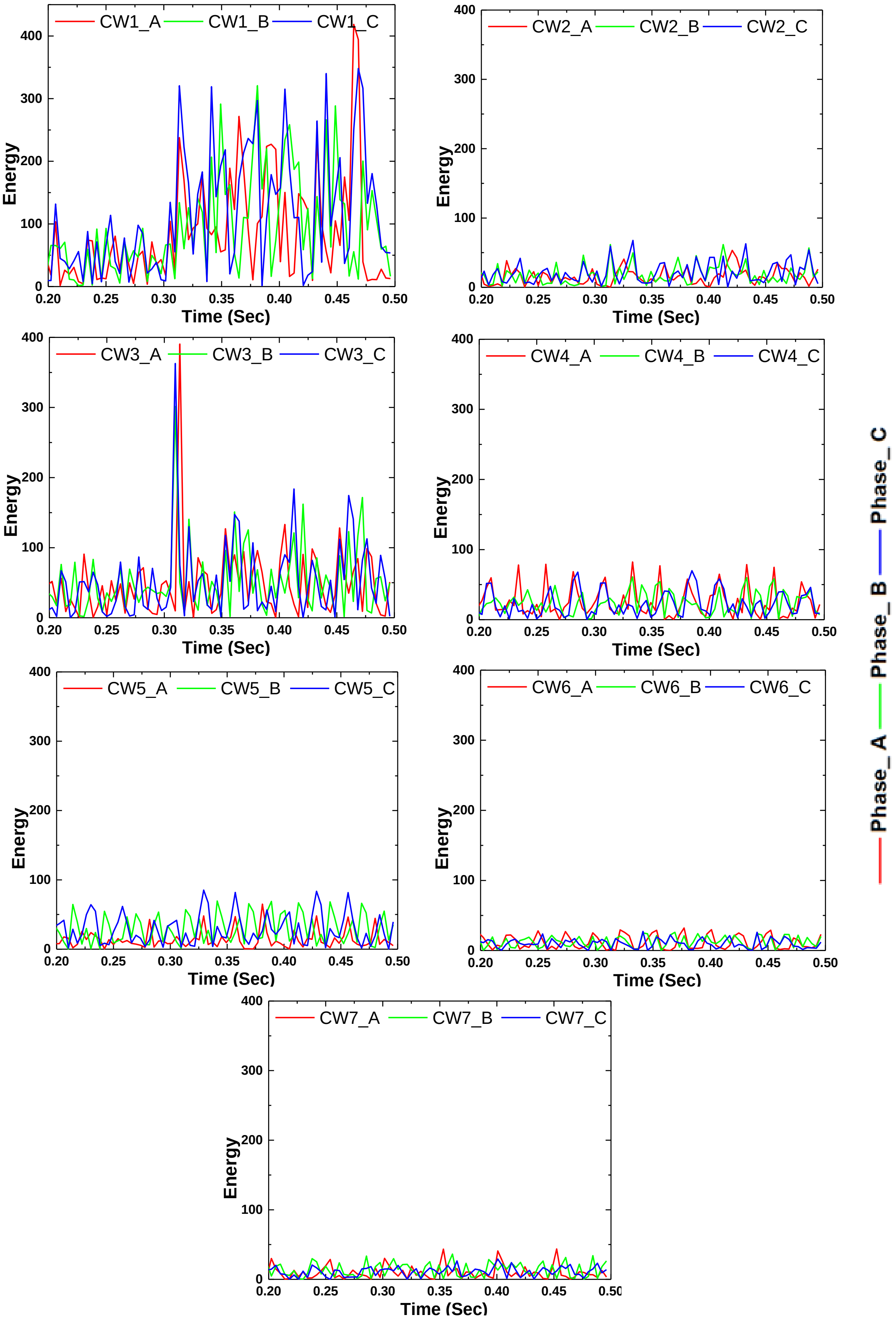

Figure 5.23: Wavelet Coefficients obtained from the three-phase current signals of an LLL fault at 180 km from sending end.

5.5.5 Three Lines to Ground Fault (LLLG)

The ability of the WPT to differentiate between the three lines and three lines to ground fault was investigated in this section. A three lines to ground fault was simulated by applying a short circuit to the three phases A, B and C and ground. The fault resistance was set to 5Ω and ground resistance to 1 Ω. As mentioned earlier in the double line to ground fault, for ground involvement the three phase current zero sequence components were utilised. The waveform of the zero sequence component was then processed with the WPT, and the results of the WPT analysis are given in detail in section 5.5.6.

In this section, the results of the WPT analysis of the current signals obtained when a three phases to ground fault are given in figures 5.24 to 5.27. The WPT coefficients of the three phases show very similar trends with those obtained from the LLL faults. Correspondingly, only coefficients CW1 and CW3 have shown a significant increase in the spectral energy at all fault locations. Also, when the fault distance increases the magnitude of the spectral energy of those coefficients decreases.

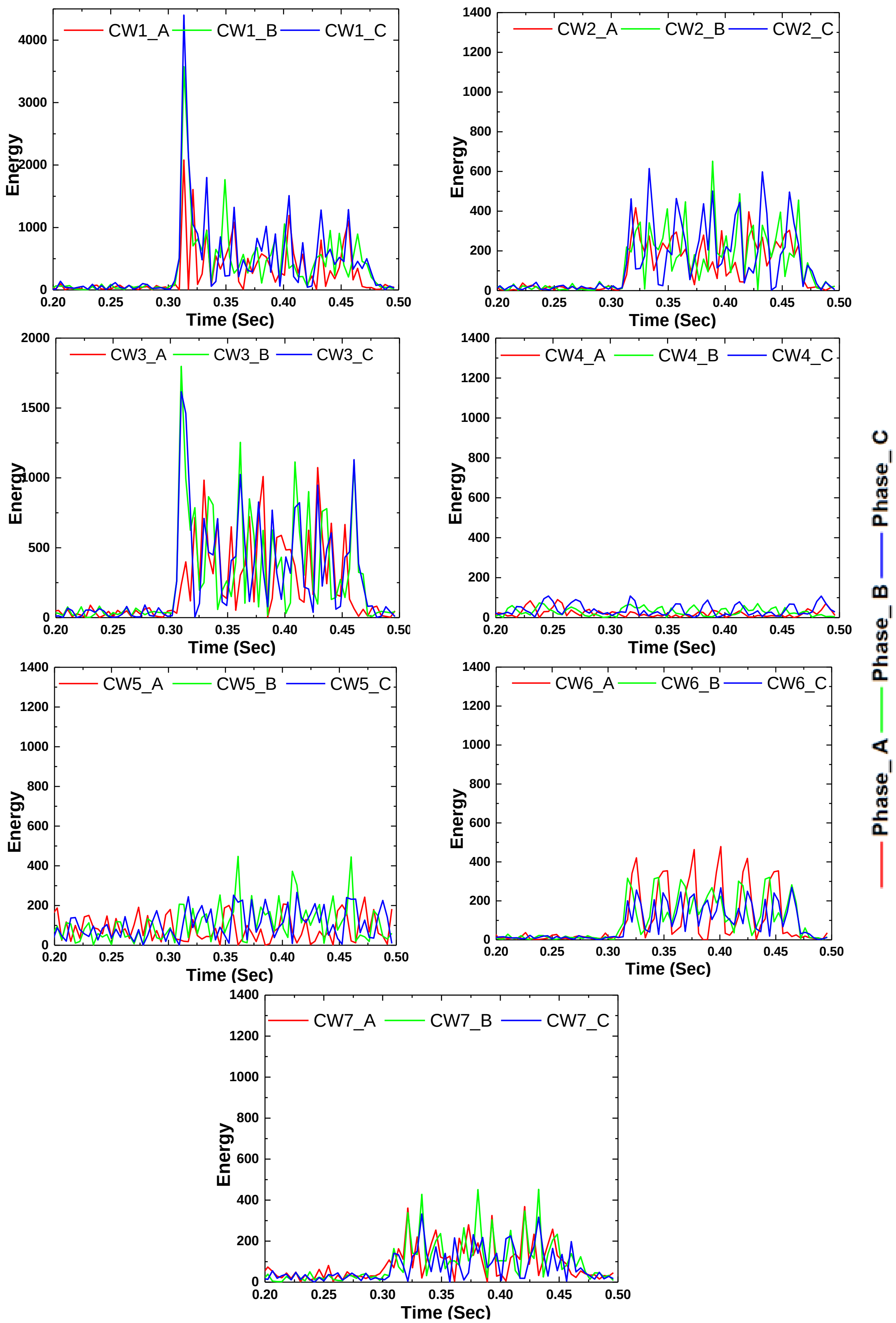

Figure 5.24: Wavelet Coefficients obtained from the three-phase current signals of an LLLG fault at 20 km from sending end.

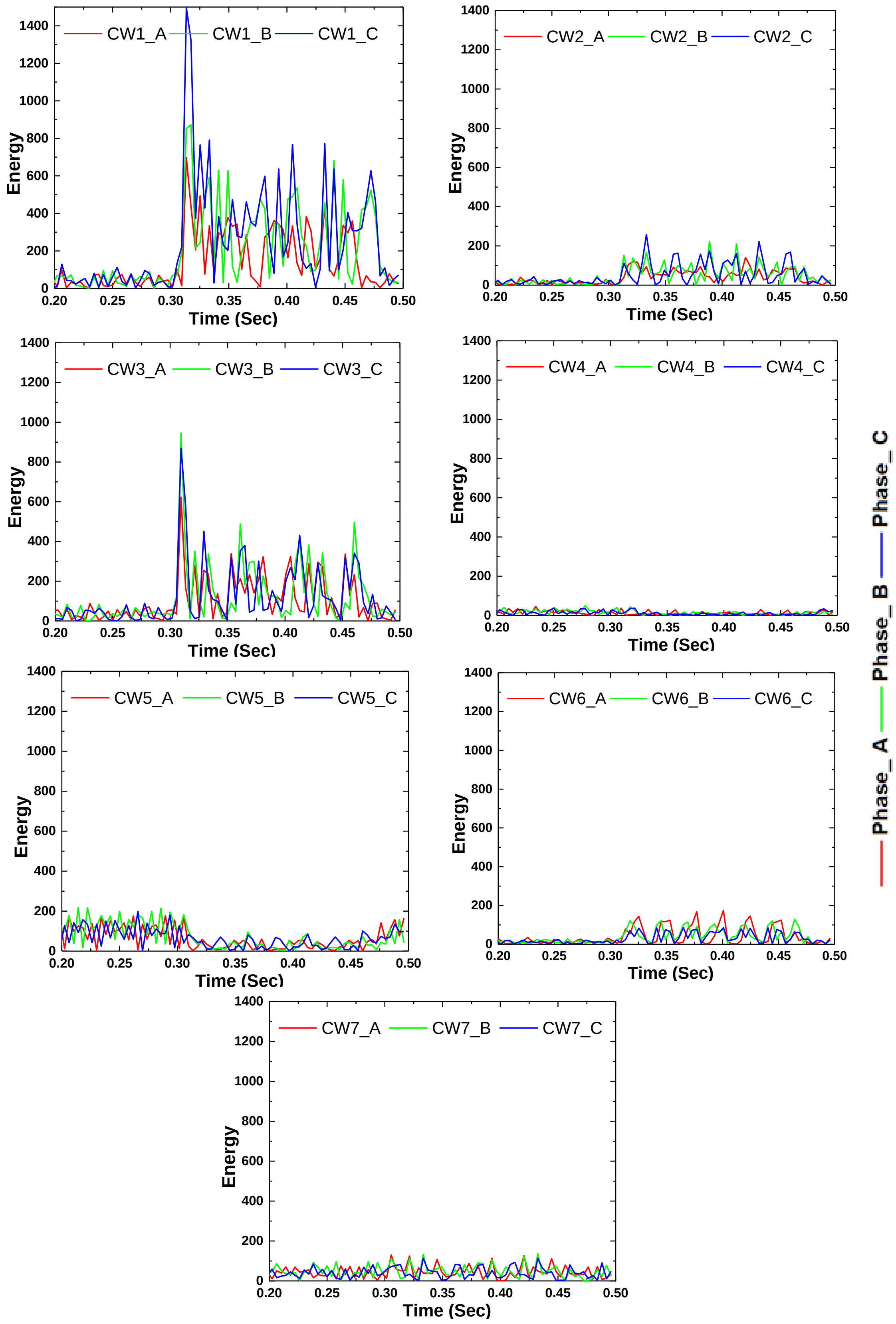

Figure 5.25: Wavelet Coefficients obtained from the three-phase current signals of an LLLG fault at 60 km from sending end.

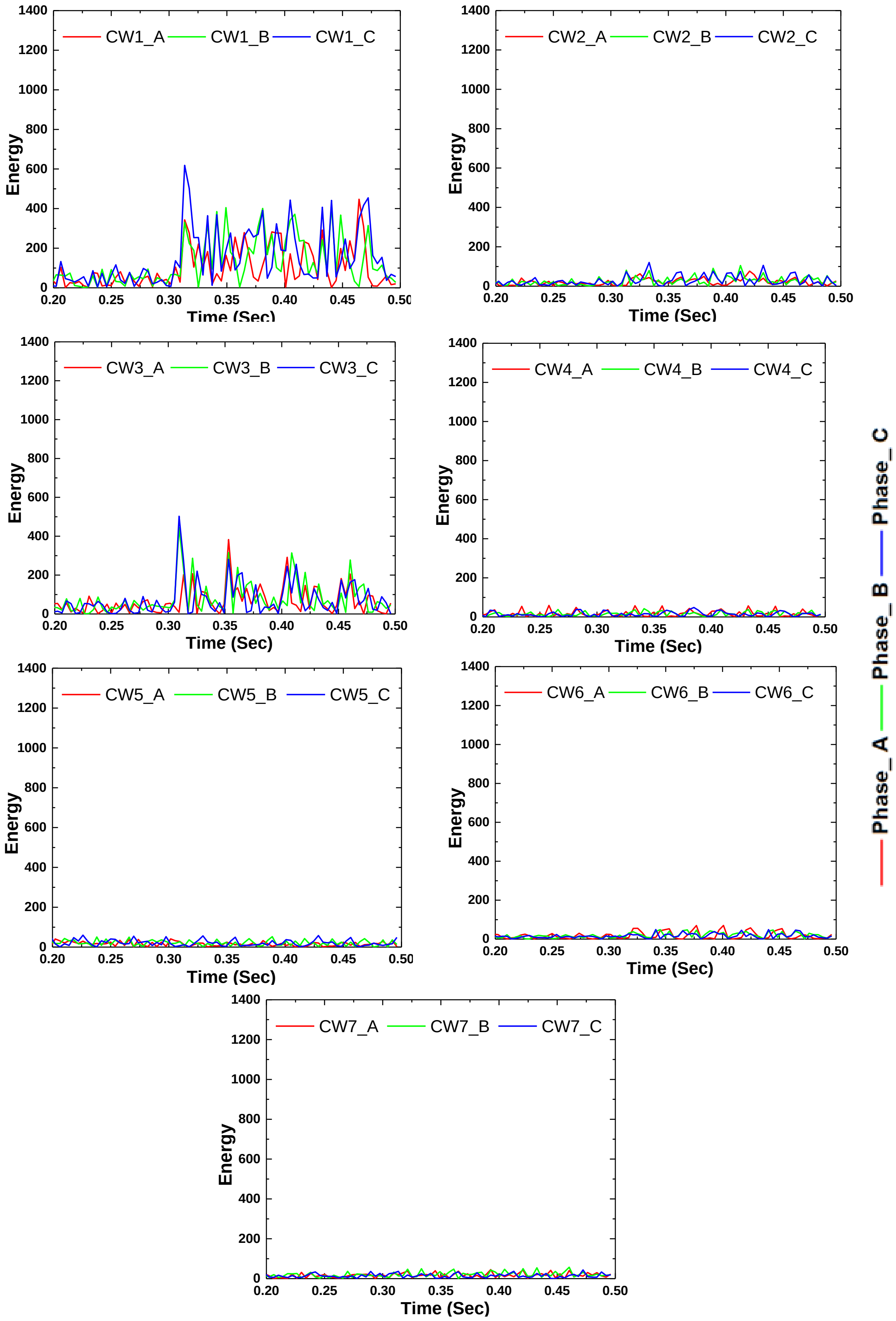

Figure 5.26: Wavelet Coefficients obtained from the three-phase current signals of an LLLG fault at 120 km from sending end.

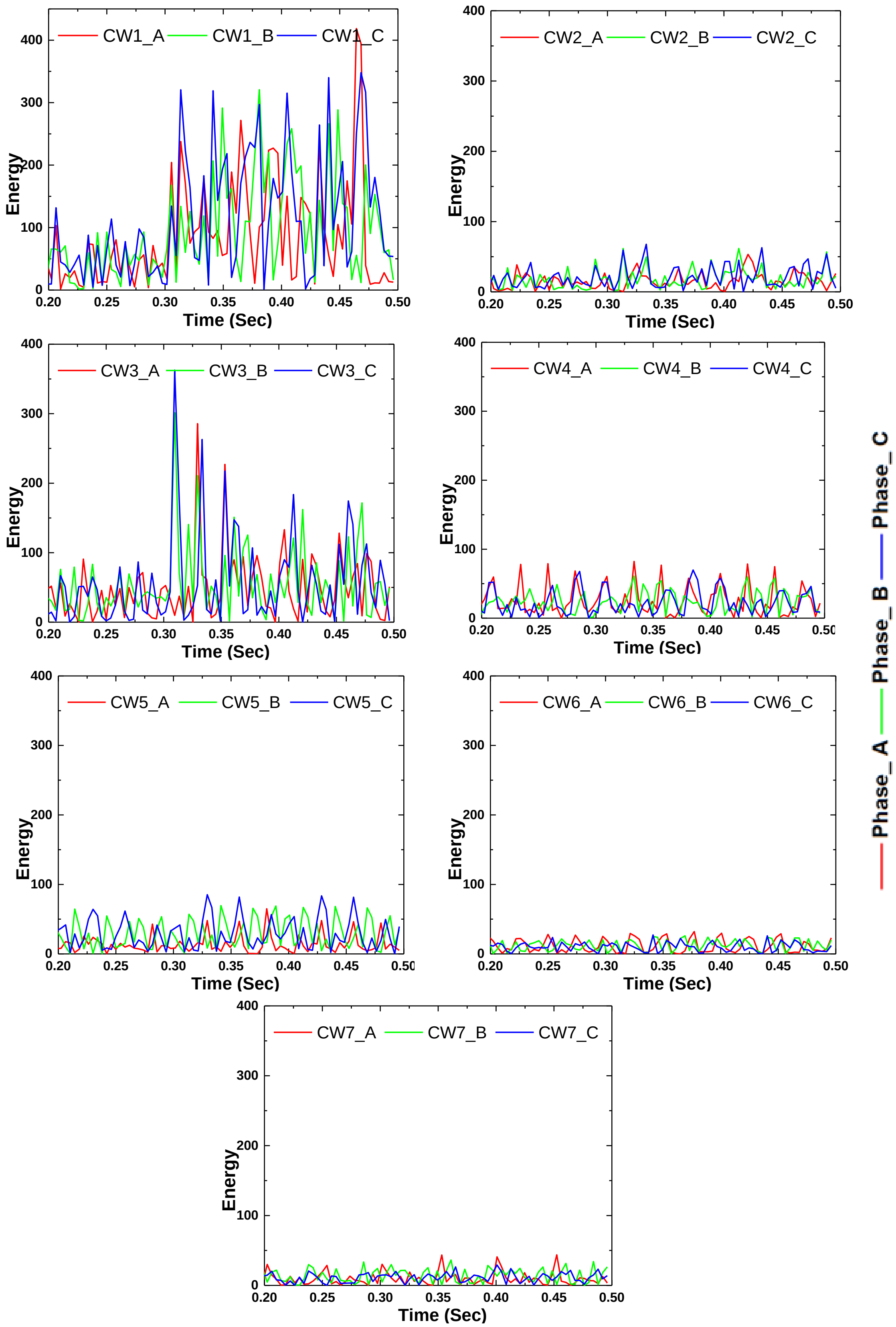

Figure 5.27: Wavelet Coefficients obtained from the three-phase current signals of an LLLG fault at 180 km from sending end.

5.6 Selection of WPT coefficients for fault Algorithms

In the previous section, it was shown that the WPT analysis is used to decompose each input signal to its frequency detail. The obtained WPT coinfections were monitored during various transmission line fault types such as, single-phase to ground faults, phase-to-phase faults, double-phase to ground faults and three-phase to ground faults occurred at various locations of the line. The results from the WPT analysis have showed that this information was visible within the two coefficients CW1 and CW3. These two coefficients represents two separate frequency bands of a lower and higher frequencies details respectively, see table 5-1. However, the frequency band of those two coefficients agrees with the frequencies of the fault generated transients obtained using FFT analysis in the previous chapter, see section 4.4. A lower and higher frequency bands were selected to enhance the robustness of the protection algorithm. This is because the power system transients are highly affected by fault conditions as well as other system disturbances such as switching and lightning. In these case a wrong decision can produced by the fault detection algorithm if only one higher frequency coefficient is utilised. Therefore, these two coefficients were selected to obtain fault identification features applied to the protection system.

5.7 Ground Faults

As previously discussed, in order to investigate whether the ground involved in the fault or not, the three phase zero sequence component was utilised. At all fault conditions the three phase zero sequence component was obtained by summing up the three-phase current obtained by the CTs at the measurement point, and the captured waveform was processed with the WPT, see figure 5.6. The zero sequence component was obtained as follows [92]:

$$I_0 = \frac{1}{3}\left(I_a + I_b + I_c\right) \qquad (5.4)$$

Where, I_0 is the zero sequence current, $I_{a,b,c}$ represents phase A, B and C currents. The zero sequence current is the current flowing to the ground through the system neutral connection. Therefore, when the ground is not involved in the fault such as LL or LLL faults, then the zero sequence current is equal to zero.

Figures 5.28 and 5.29 show the WPT coefficients CW1 and CW3 obtained from a double line (LL) and double line to ground (LLG) faults respectively. The fault parameters and locations were kept the same as the previously carried out scenarios. A comparison study between the two coefficients at all tested distances of the two fault types was carried out. The results show that when the ground is involved in the fault, the spectral energy of the two coefficients obtained from the zero sequence current increases immediately after the fault occurrence, see figure 5.29. Whereas, the spectral energy of the two coefficients obtained from the zero sequence current of non-ground fault remains relatively low, see figure 5.28. The low energy exist in the zero sequence current for a non-ground fault such as LL fault or at normal condition is a result of the cycloconverter generated harmonics contained in the three-phase current signals. A similar result was obtained from a comparative study between three-phase and three-phase to ground faults, and the analysis of the results is given in appendix C.

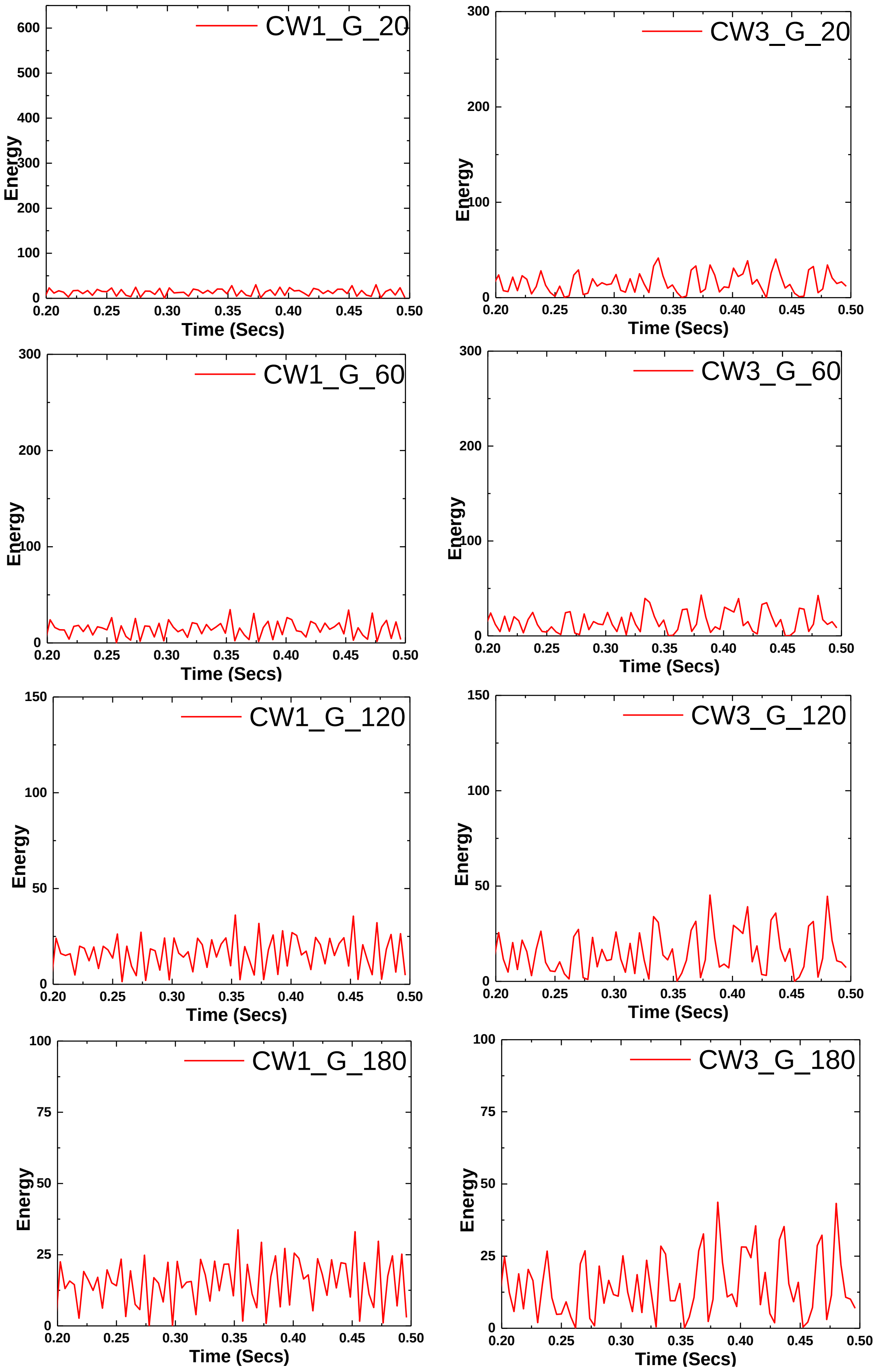

Figure 5.28: WPT coefficients CW1 and CW3 of the zero sequence current of an LL fault at distances 20, 60, 120, and 180 km from the sending end of the HVLF transmission line.

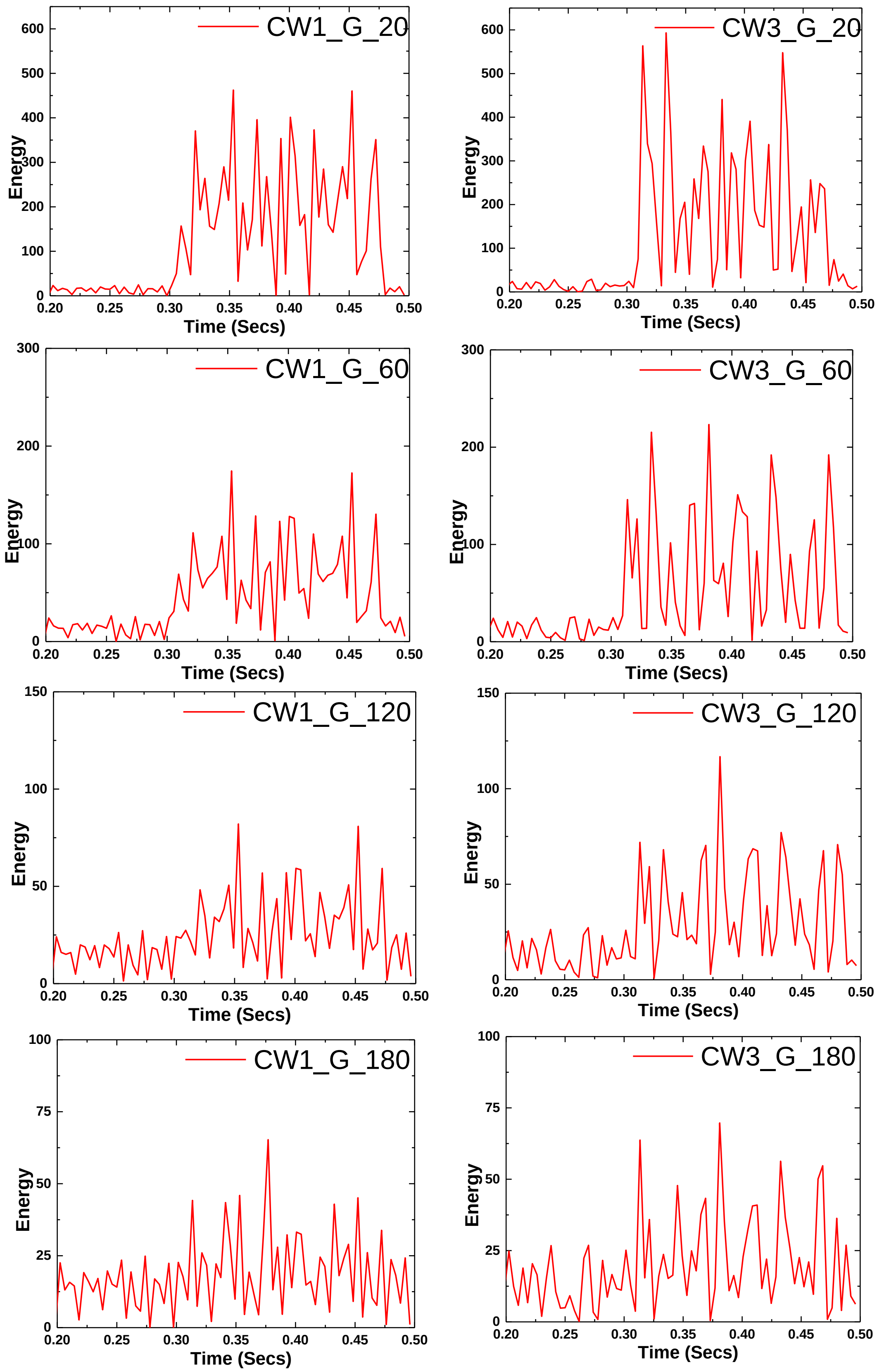

Figure 5.29: WPT coefficients CW1 and CW3 obtained from the zero sequence current of an LLG fault at distances 20, 60, 120, and 180 km from the sending end of the HVLF line.

5.8 Design of the Protection Algorithm

5.8.1 Fault Detection

It is evident from the foregoing results that the WPT provides accurate fault detection from the analysis of the HVLF current signals. In this study, the proposed fault identification algorithm uses the three phase current signals measured at sending end of the line only. The fault was detected by observing the two WPT coefficients CW1 and CW3 obtained at the third analysis level. An extensive series of test results demonstrated the capability of the WPT based protection to identify the correct faulty phase as well as the ground faults. The analysis of the zero sequence current signal has shown promising results to discriminate between double line and double line to ground fault, as well as three lines and three lines to ground faults. A close observation reveals that the WPT based protection system offers a high performance and robustness at all tested fault locations. It has been clearly demonstrated that the features extracted from the WPT coefficients CW1 and CW3 have a more distinct and informative property than other coefficients. These coefficients have shown a clear localisation of the fault generated transients within a good time scale; thus in this work the utilisation of the WPT based fault classification and location algorithm on the HVLF transmission system is proposed.

Figure 5.30 illustrates the fault detection process of the proposed HVLF transmission protection scheme. Firstly, the three-phase current signals were measured at the sending end of the HVLF system by CTs. Then, the three-phase measured current signals are sampled at a 2 kHz sampling rate. This sampling based on the Nyquist’s criteria in order to ensure the detection of the requisite fault transients. The selection of higher sampling frequency will increase the processing time of the digital microprocessor. At this stage, the zero-sequence current is obtained by adding up the three phase current values.

Through the signal pre-processing stage, the signals data is processed to fit the input requirements of designed WPT.

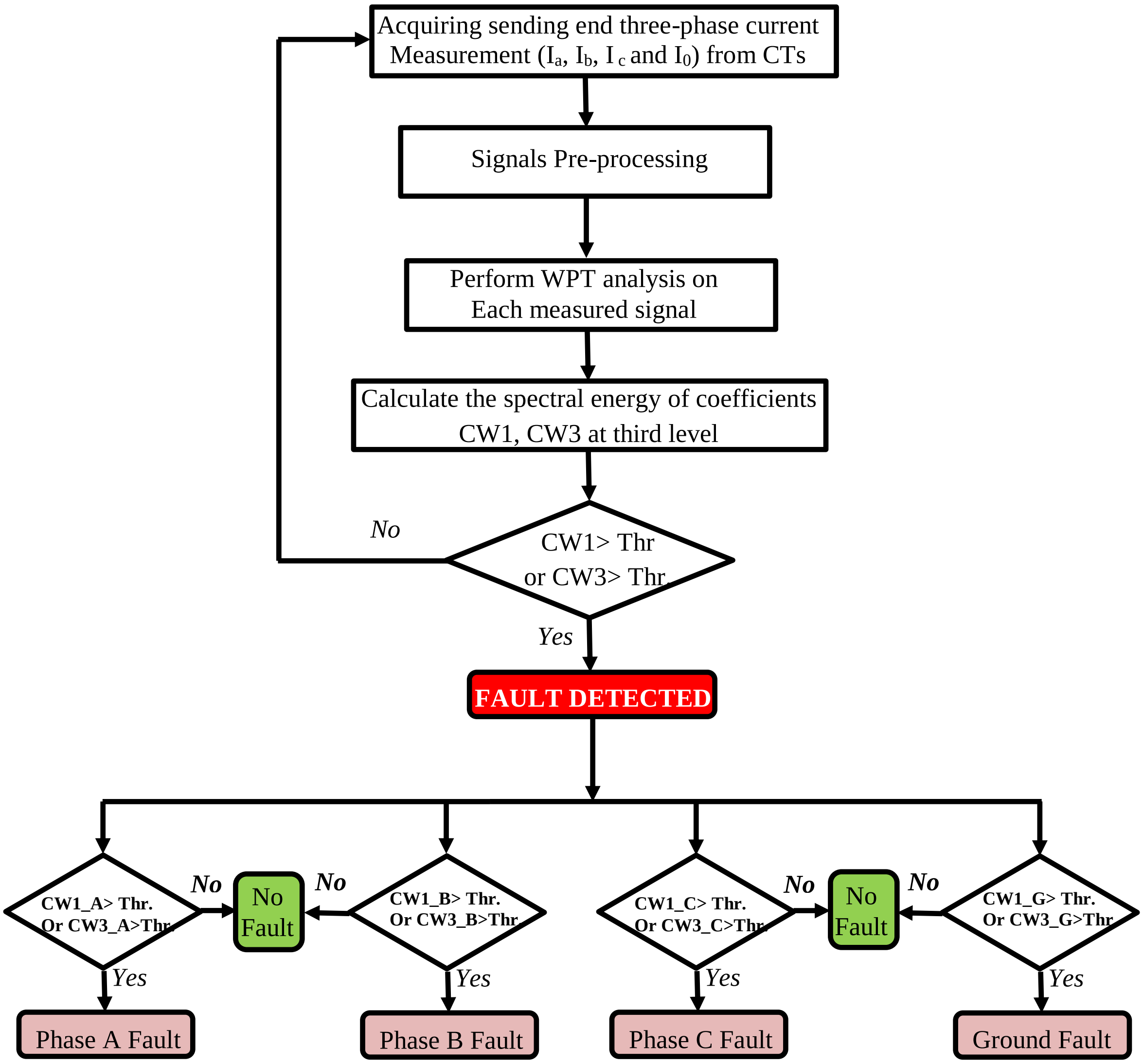

Figure 5.30: flow chart of the proposed protection algorithm

The WPT analysis is used to decompose each input signal to its frequency detail. As shown previously, the most appropriate fault transients are captured by the WPT coefficients CW1 and CW3. Therefore, the complete tree of the complete WPT is not necessarily implemented, but only the filters required to obtain those coefficients. The proposed fault identification is based on the calculation of the selected WPT coefficients, and the associated spectral energy is then chosen as identification features. For the selection of the faulty phase, extensive studies were carried out by simulating several fault types such as, single-phase to ground faults, phase-to-phase faults, double-phase to ground faults and three-phase to ground faults at various locations of the line. Under all fault conditions, the fault resistance and the ground resistance were set to 5Ω and 1 Ω, respectively. Further, the magnitude of spectral energy of the selected coefficients was calculated for each fault scenario. This procedure was carried out to find the minimum and maximum spectral energy in each case, and then set thresholds for fault detection. In the HVLF system these thresholds are set to have a magnitude higher than the pre-fault cycloconverter generated harmonics in order to prevent the protection system from wrongful fault identification. Also, this setting helps in avoiding wrongful fault detection decision in case of lightning transients or any other system short time transients. Therefore, the proposed protection system utilises two WPT coefficients of different frequency bands to accurately obtain the fault detection. The spectral energy of those coefficients is compared with the predefined thresholds, and if the defined condition of any phase is met then the fault detection and classification system is activated. For fault classification, the WPT coefficients of each phase current signals are compared individually with the predefined threshold. If one of the phase’s coefficient has met the pre-set condition then a trip signal will be sent to the corresponding circuit breaker for fault isolation.

Figure 5.31 shows that the WPT coefficients CW1 and CW3 samples are at a low energy level before the fault occurrence i.e. before 0.3 sec. When a line to ground fault occurs, the energy level of phase-A increases to a magnitude above the predefined threshold. This test is carried out for two extreme locations, in which one is very close to the sending end while the second one at the other line end, i.e. 20 and 180 km from the measurement point, see figure 5.31 (a) and (b). These two locations are chosen in order to find out the highest and lowest energy level those two coefficients can reach after the fault incident. The energy levels from these locations are used to accurately define the fault detection thresholds. The results clearly illustrate that the spectral energy of the faulty phase can be detected within a few samples after the fault occurrence. In this study, it was set that the fault decision can only be made when the WPT analysis output continues to satisfying the threshold for approximately 10 msec, i.e. within four obtained samples. This condition is applied for the two obtained WPT coefficients CW1 and CW3. Although this might cause a delay for the fault detection but also to increase the robustness of the protection algorithm and avoid decision making errors.

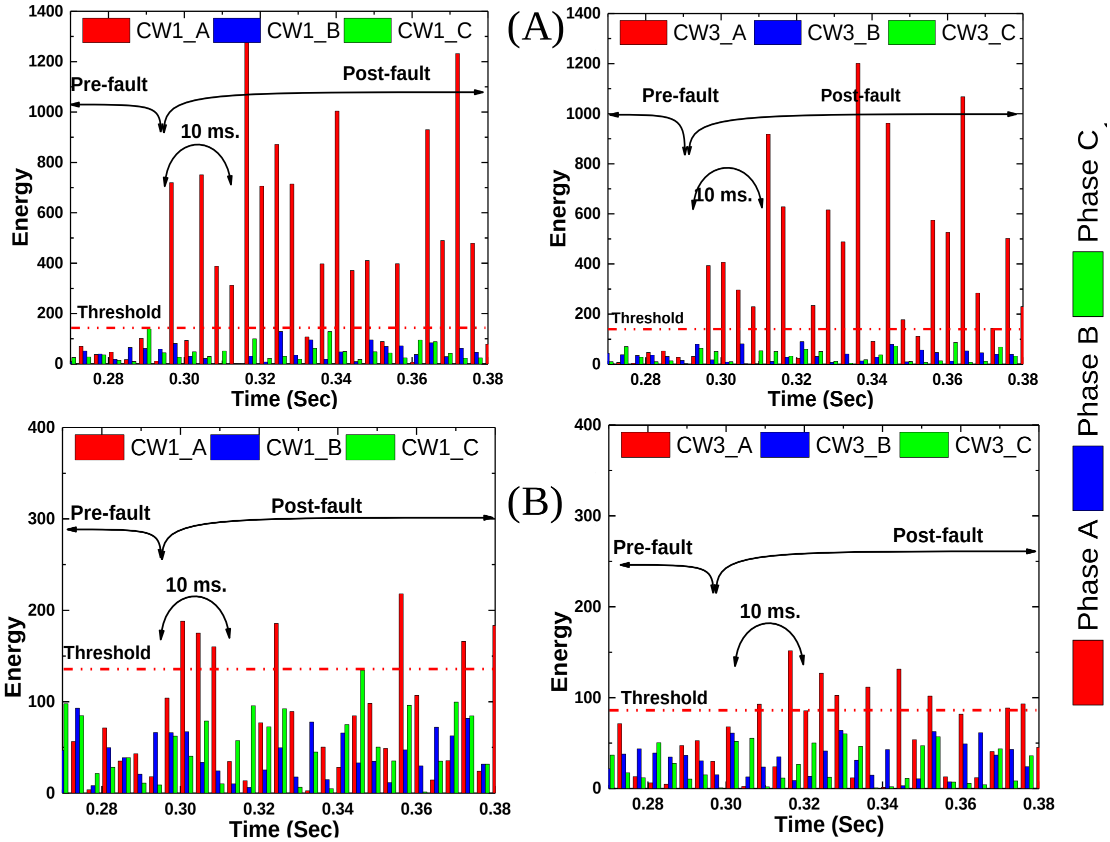

Figure 5.31: Samples of the WPT coefficients CW1 and CW3 obtained from the three-phase current signals when an **LG** fault occurs at distances of (a) 20 km (b) 180 km.

The previous test was also carried out for a phase to phase (LL) fault and for three phases faults (LLL) and the results are given in figures 5.32 and 5.33 respectively. These figures show a sampled form of WPT coefficients CW1 and CW3 obtained from three-phase current signals. Two locations were selected at 20 and 180 km away from the measurement point at sending end in order to investigate the effects of fault location and type have on the post-fault energy calculations of the WPT coefficients. Additionally, these experiments were carried out to determine accurate fault detection thresholds.

The results show that the components of the spectral energy of the faulty phases exceed the predefined thresholds after the fault occurs at time 0.3 sec. Furthermore, it was observed that the fault decision also can be made within approximately 10 msec after the fault occurrence i.e. within 4 samples of the determined WPT coefficients. The results obtained show that the protection algorithm is accurately predicting the fault occurrence time as well as the fault type.

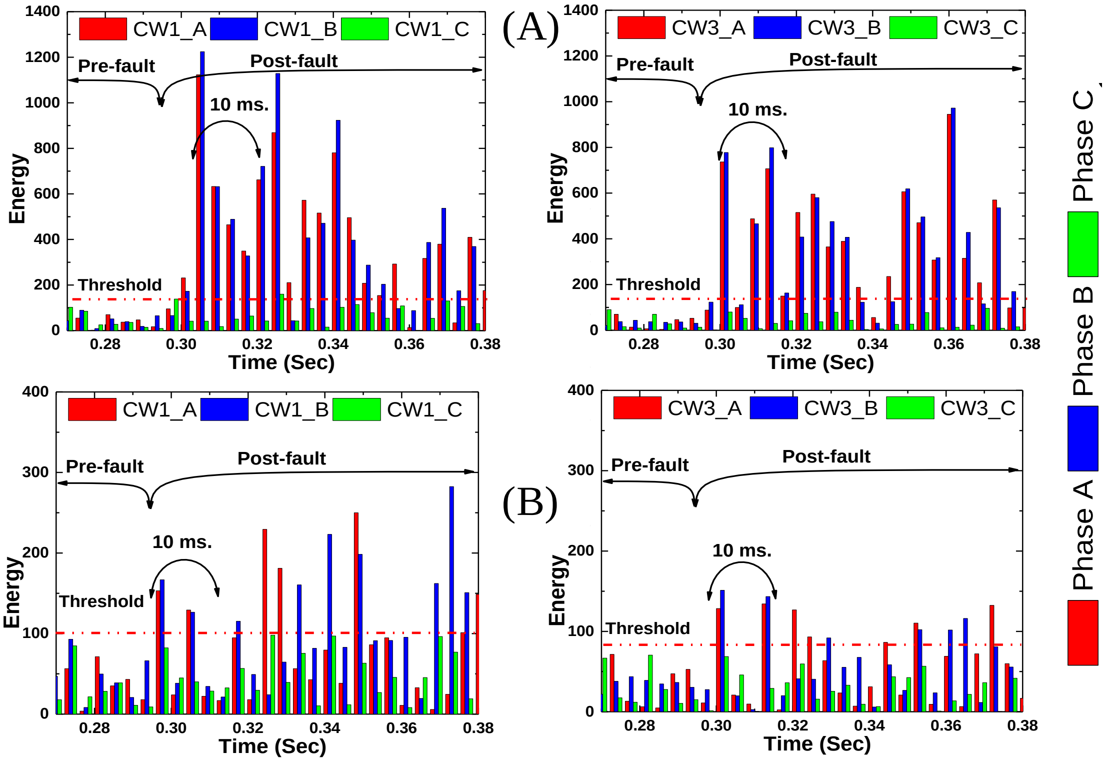

Figure 5.32: Samples of the WPT coefficients CW1 and CW3 obtained from the three-phase current signals when an **LL** fault occurs at distances of (a) 20 km (b) 180 km.

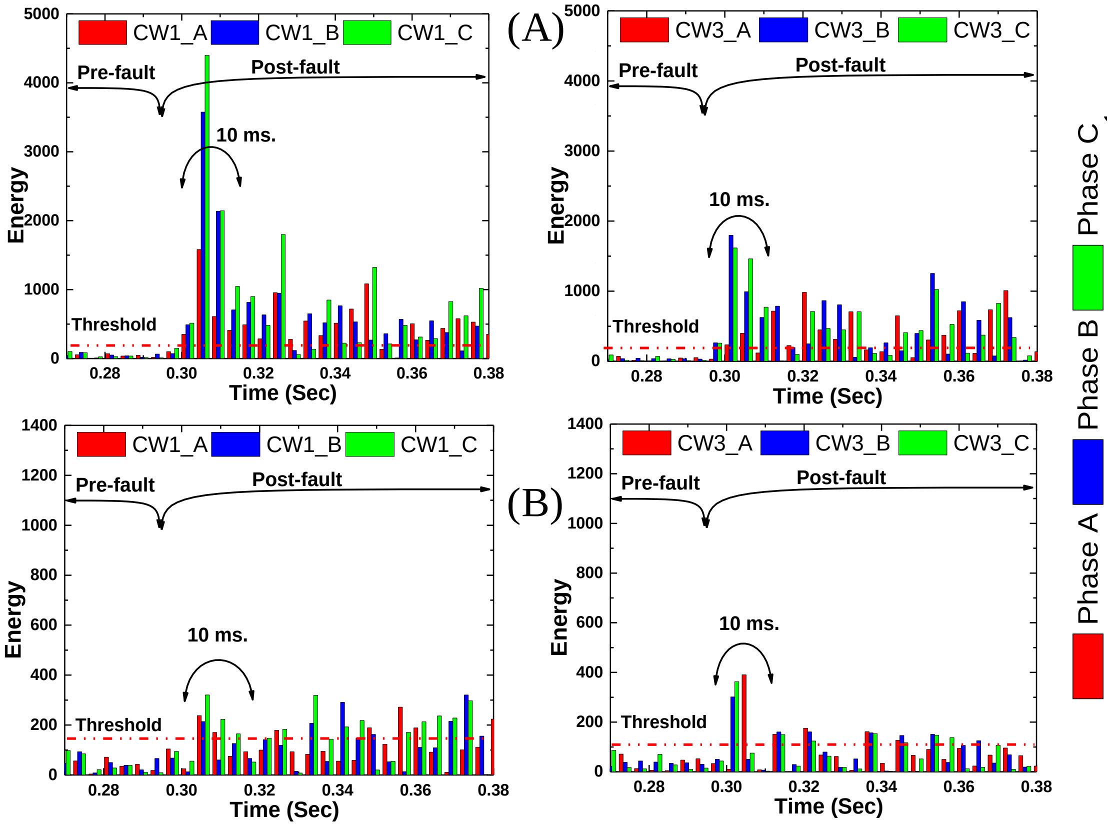

Figure 5.33: Samples of the WPT coefficients CW1 and CW3 obtained from the three-phase current signals when a **LLL** fault occurs at distances of (a) 20 km (b) 180 km.

However, the results show that the minimum spectral energy of the selected coefficients under all fault types, were obtained when the fault occurs at the other end of the line, i.e. 180 km. Therefore, adaptive thresholds can be set using an artificial intelligence tool such as neural network. This neural network can be integrated with the protection algorithm for decision making [82]. This will result in enhancing the fault detection robustness and sensitivity.

5.8.2 Fault Location

Once the fault detection algorithm has identified the fault occurrence and a trip signal is sent to the circuit breaker, then the offline data obtained from the WPT analysis can be used to determine the fault location. As previously demonstrated, the WPT coefficients CW1 and CW3 have shown a significant change in the magnitude of the spectral energy with changes in the fault location of the line. In this section, an algorithm is described for calculating the fault location using the WPT coefficients of the three-phase current signals measured at the sending end of the line. The concept that forms the basis of the proposed location algorithm is that the spectral energy of a specific coefficient is affected by the length of the line segment between the fault point and the measurement point. This is because the traveling wave between the fault point and the measurement point will lose energy in accordance with changes in the transmission line parameters (R, L and C), see figure 4.16. Thus, the proposed algorithm was designed to calculate energy contained in each phase current signal over a time window of 10 msec (4 samples). The location algorithm determines the summation of each four samples in sequence obtained from the wavelet coefficients CW1 and CW3. Though, any of the coefficients can be used for calculating the fault location, only one coefficient (CW1) has been utilised for simplicity.

Various fault type tests were carried out in order to validate the fault location algorithm. Different fault types such as single line to ground (LG), double line (LLG) and three phases (LLL) faults were considered, and in each test the fault resistance and the ground resistance were set to 5Ω and 1Ω, respectively. The fault location was varied in steps of 40 km from 20 to 180 km from the measurement point at the system sending end. Therefore, for location calculations the faults were initiated at five points of the line specifically 20, 60, 100, 140 and 180 km from the sending end. Table 5.2 shows the pre- and post-fault calculated energy samples of the WPT coefficient CW1 when a line to ground (LG) fault occurs at the selected locations. Four pre-fault samples ($X1$ to $X4$) and eight post-fault samples ($X5$ to $X12$) for each phase were selected for fault location calculations. Each set of four samples represent a time window of 10 msec. The algorithm is designed to calculate location features (FL) by summing up each of the four samples in sequence, as follows:

$$\text{Fault Location feature (FL)} = X_n + X_{n+1} + X_{n+2} + X_{n+3} \qquad (5.5)$$

Where n is the sample number of the spectral energy calculated from the WPT coefficient CW1 of each phase. The results given in table 5.2 shows that the location feature of the faulty phase (Phase-A) obtained under healthy conditions is relatively low compared to those obtained after the fault incident. Also, for other healthy phases the location features (FL) obtained from pre- and post-fault conditions remains approximately constant. It is clearly observed that the magnitude of the obtained location feature decreases with the fault location being increased. Thus the transmission line can be divided into four fault zones used for fault location estimation. Figure 5.34 shows the fault location features (FL) of the faulty phase (phase-A) obtained at various locations of the line. It is clearly shown that the magnitude of calculated fault location features decrease with the increase in the fault distance. Thus, pre-set thresholds can be used to break the transmission line into several zones. These thresholds can be optimised by simulating several fault types at various locations of the line. It is important to note that for remote fault locations such as 140 and 180 km the calculated features have marginal decrease in magnitude, see figure 5.34. Thus, any fault located with a distance of over 140 km is considered with one fault zone (zone-4).

Table 5.2: The frequency features of the WPT coefficient CW1 obtained from the three-phase current signals when an **LG** fault occurs.

Distance	Phase	Pre-Fault				Post-Fault								Pre-Fault	Post-Fault	
		X1	*X2*	*X3*	*X4*	*X5*	*X6*	*X7*	*X8*	*X9*	*X10*	*X11*	*X12*	Location feature (Sum)	Location feature (Sum)	Location feature (Sum)
20	a	47.0	17.0	91.4	11.5	719.3	92.9	750.7	387.7	312.2	1343.0	705.8	871.7	166.9	1950.7	3232.8
	b	18.5	45.4	51.8	39.1	81.3	30.5	21.7	0.5	1.9	31.1	8.0	128.8	154.8	134.0	169.8
	c	14.8	9.6	88.6	44.2	26.8	48.2	29.1	51.3	0.5	99.6	22.0	30.3	157.2	155.5	152.5
60	a	44.5	17.7	89.9	13.0	402.3	201.8	195.2	107.5	147.0	514.0	244.5	281.4	165.1	906.8	1186.9
	b	16.9	40.4	56.5	46.2	73.6	29.7	16.9	3.1	1.5	35.2	5.2	147.4	160.0	123.3	189.4
	c	8.1	7.7	101.8	43.0	50.9	26.1	44.5	47.6	9.0	91.4	9.8	20.5	160.6	169.2	130.7
100	a	42.2	20.5	34.0	16.8	201.4	119.9	108.8	125.5	117.0	319.5	155.6	105.3	113.5	555.6	697.5
	b	19.9	37.7	49.7	39.4	63.7	61.6	38.7	1.2	13.5	6.3	9.2	40.2	146.7	165.2	69.2
	c	11.6	4.5	29.0	43.7	35.2	47.8	47.1	16.5	41.1	58.1	7.1	44.0	88.7	146.6	150.3
140	a	42.7	17.9	33.3	17.2	194.1	108.6	161.2	0.3	90.7	233.6	115.3	23.0	111.1	464.2	462.7
	b	20.3	36.8	36.1	64.1	52.7	10.3	13.1	5.2	17.5	45.9	15.5	115.2	157.3	81.3	194.0
	c	10.6	8.5	32.4	43.2	61.7	5.4	49.9	61.2	7.8	127.3	2.2	37.8	94.6	178.1	175.1
180	a	43.1	18.0	39.0	18.1	175.1	120.2	34.7	13.6	127.0	185.6	59.3	2.6	172.3	343.6	374.6
	b	20.7	58.3	48.2	54.2	47.6	34.4	60.2	6.3	25.4	49.7	13.6	103.8	181.4	148.4	192.5
	c	11.0	9.0	50.4	40.4	40.4	10.2	37.5	65.6	12.6	102.3	6.4	45.0	110.8	153.8	166.3

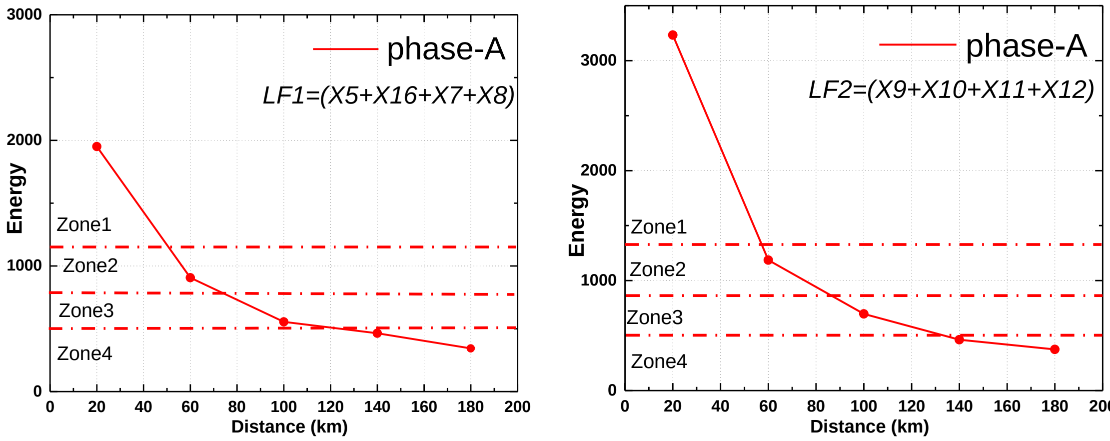

Figure 5.34: The calculated fault location features of **LG** faults distributed over the transmission line.

The results shown in figure 5.34 demonstrates that the fault location can be estimated within 10 to 20 msec. after the fault occurrence, i.e. 4 to 8 samples of the WPT coefficient. This scheme allows a delay in the trip signal that was initiated by the fault identification algorithm that enhances the reliability of the protection system as well as allowing a better fault location estimation. As the HVLF transmission system adapts 20 Hz as power frequency (one cycle period of 50 msec.), then the algorithm is able to detect and locate the fault within approximately less than half a cycle after the fault incident. This provides sufficient time for the trip signal to be initiated and the circuit breaker to operate on the next zero crossing current.

The fault location algorithm was also tested for other fault types such as line to line fault (LL) and three lines fault (LLL). The algorithm was tested by simulating these fault types at the same previously carried out fault locations and time. Tables 5.3 and 5.4 shows the frequency features of the WPT coefficient CW1 obtained from the three-phase current signals when an LL and LLL faults occurs, respectively. Then, the fault location features (FL) were obtained from the pre- and post-fault frequency features marked as ($X1$ to $X12$). As previously given, the location features were obtained by summing each four samples in sequence, in which four samples were selected for the pre-fault and eight samples for the post-fault conditions. The results show that the faulty phases have a higher magnitude of the location features in comparison with the healthy phase(s) for both fault types. However, it was found that the magnitude of these features decreases with the increase in the fault distance. It is clearly demonstrated in figures 5.35 and 5.36 that the fault location can be estimated from the assigned location features. Then, the total length of the line was divided into fault zones by defining fault location thresholds. These thresholds were set in accordance with the calculated location features in each fault scenario.

It is important to mention that the calculated location feature (FL1) in the case of a three phase fault (LLL) has a higher magnitude when the fault occurs at 20 km distance, see figure 5.36. This is because this type of fault involves all the three phases that leads to high disturbances on the system as well as on the cycloconverter terminals. Hence, high transients are captured from the first four samples of coefficient CW1.

Table 5.3: Frequency features obtained from the WPT coefficient from the three-phase current signals when a **LL** fault.

Distance	Phase	Pre-Fault				Post-Fault								Pre-Fault	Post-Fault	
		X1	*X2*	*X3*	*X4*	*X5*	*X6*	*X7*	*X8*	*X9*	*X10*	*X11*	*X12*	Location feature (Sum)	Location feature (Sum)	Location feature (Sum)
20	a	47.0	17.0	95.5	14.3	231.3	1123.2	632.7	464.5	349.4	662.2	869.3	210.9	173.8	2451.7	2091.7
	b	18.5	65.4	66.1	19.1	172.7	1224.6	632.1	488.9	327.9	720.9	1128.6	43.5	169.1	2518.2	2220.9
	c	14.8	9.6	78.9	49.5	41.6	41.7	17.6	50.7	44.0	42.6	59.3	22.5	152.9	151.6	168.4
60	a	44.5	11.7	97.5	14.6	236.9	110.8	103.9	263.9	173.4	161.1	283.8	100.9	168.3	715.5	719.3
	b	16.9	70.4	68.0	32.1	216.8	52.4	122.6	318.5	452.8	2.8	281.8	49.7	187.4	710.2	787.1
	c	8.1	7.7	79.8	42.8	23.6	32.4	55.2	41.2	160.8	52.5	103.8	21.9	138.3	152.5	188.5
100	a	42.2	20.5	52.5	51.2	227.5	67.6	6.4	113.2	98.4	113.8	225.4	15.7	166.4	414.8	453.3
	b	19.9	67.7	64.8	6.2	211.4	49.2	40.8	140.0	138.3	167.4	70.7	95.7	158.6	441.3	472.0
	c	11.6	4.5	35.2	48.2	38.5	30.5	35.6	56.9	38.3	68.6	45.0	30.2	99.4	161.5	182.1
140	a	41.1	18.4	56.9	40.7	162.7	67.1	46.1	89.2	131.2	37.3	89.0	82.4	157.1	365.1	339.9
	b	21.3	70.3	47.9	6.3	172.3	41.0	72.4	94.8	179.8	86.3	38.0	85.6	145.8	380.6	389.8
	c	9.5	12.8	57.3	43.2	40.7	28.2	38.2	45.4	38.0	62.2	43.0	29.7	122.8	152.5	172.9
180	a	46.9	74.7	18.0	19.4	153.2	23.9	22.8	79.6	38.4	120.0	36.1	64.7	159.0	279.4	259.3
	b	21.3	75.3	49.2	24.1	166.8	18.4	21.8	73.2	72.9	158.4	41.3	21.4	169.9	280.1	294.0
	c	18.6	6.7	79.6	58.0	82.3	25.0	10.3	47.0	11.6	63.3	26.9	45.6	163.0	164.7	147.4

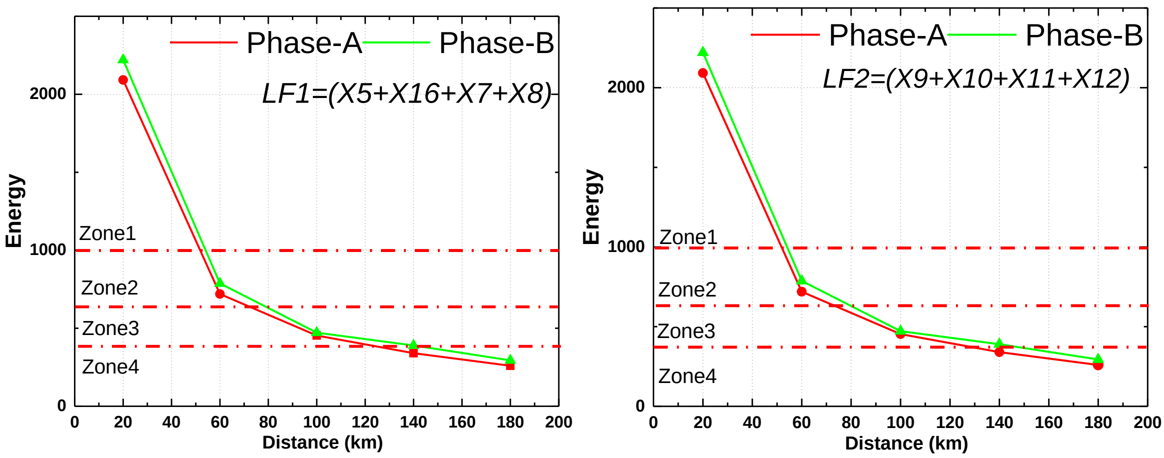

Figure 5.35: The calculated fault location features of LL faults distributed over the transmission line.

Table 5.4: WPT features of coefficient CW1 from the three-phase current signals when a **LLL** fault.

Distance	Phase	Pre-Fault				Post-Fault								Pre-Fault	Post-Fault	
		X1	*X2*	*X3*	*X4*	*X5*	*X6*	*X7*	*X8*	*X9*	*X10*	*X11*	*X12*	Location feature (Sum)	Location feature (Sum)	Location feature (Sum)
20	a	44.0	20.0	91.1	37.1	351.9	1981.2	809.4	408.8	489.3	285.6	957.1	1279.1	192.2	3551.3	3011.0
	b	17.9	61.7	72.4	29.5	491.3	3575.2	2138.2	705.6	815.6	634.4	948.0	717.5	181.5	6910.3	3115.5
	c	13.6	7.6	80.5	26.1	513.6	4400.1	2143.7	1047.6	899.9	483.0	1799.9	58.4	127.9	8105.0	3241.3
60	a	44.5	11.7	100.3	17.1	697.2	438.0	205.9	493.1	476.8	334.6	677.8	496.4	173.6	1834.2	1985.6
	b	16.9	70.4	70.9	23.3	852.4	872.0	215.5	245.0	487.8	591.6	237.6	628.9	181.5	2184.9	1945.9
	c	11.1	8.7	135.5	18.8	994.5	323.7	173.2	765.0	628.5	790.5	129.1	383.4	174.0	2256.4	1931.5
100	a	42.2	20.5	84.4	32.5	388.2	323.7	126.5	296.3	396.2	208.6	14.8	428.1	179.5	1134.8	1047.7
	b	19.9	67.7	66.7	24.3	466.8	350.0	213.9	48.6	223.1	381.7	110.4	454.9	178.5	1079.2	1170.2
	c	11.6	4.5	138.9	27.0	693.8	275.6	144.7	385.6	152.3	449.5	22.7	390.5	181.9	1499.7	1015.0
140	a	42.7	17.9	64.6	26.5	313.0	239.6	88.3	164.6	210.0	382.8	55.2	112.1	151.7	805.6	760.2
	b	20.3	66.8	68.2	39.5	220.9	179.1	164.8	137.5	198.0	229.0	43.9	309.2	194.8	702.2	780.1
	c	10.6	8.5	135.0	22.3	281.2	176.3	214.9	157.4	113.1	281.7	3.7	353.0	176.4	829.7	751.5
180	a	43.1	18.0	104.2	24.9	137.8	170.4	75.0	93.2	100.0	179.0	93.1	82.8	190.3	476.5	454.9
	b	20.7	66.3	67.8	12.6	233.9	60.4	125.9	66.2	141.3	118.8	14.8	206.7	167.4	486.3	481.6
	c	11.0	9.0	94.4	55.4	190.5	123.1	164.8	51.9	147.5	183.0	8.0	119.0	169.8	530.3	457.5

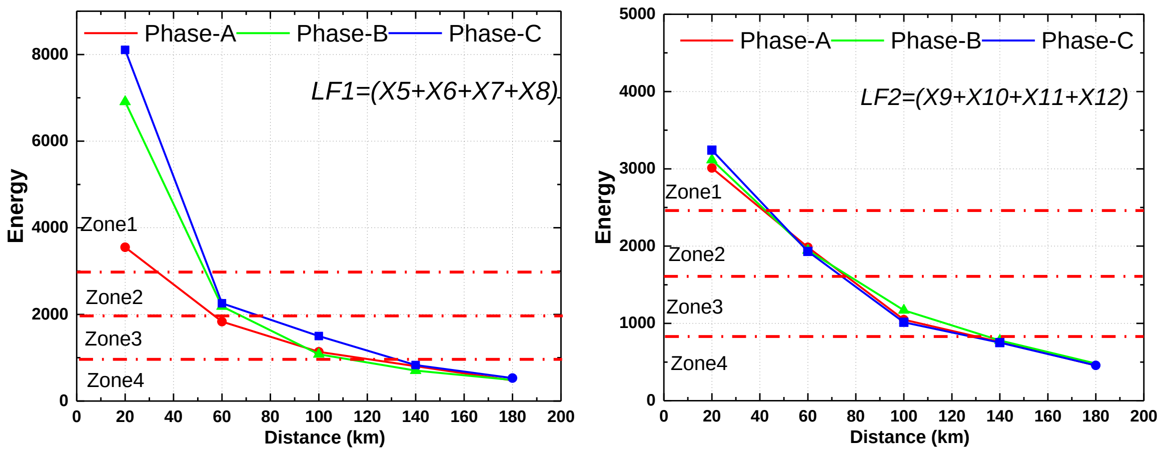

Figure 5.36: The calculated fault location features of LLL faults distributed over the transmission line.

From Tables 5.3 and 5.4, it can be observed that the location algorithm is not affected by the cycloconverter generated harmonics. Hence, the magnitude of the fault location features obtained during pre-fault conditions were relatively low. It was found that the post-fault location features are dependent on the fault characteristics such as fault location and type. However, for all fault types the obtained fault features from the WPT coefficient were less sensitive when the fault occurs at remote locations, i.e. 140km to 180km form the measurement point. Therefore, the location algorithm is sensitive to about 70% of the total line length. For precise fault location, the current signal at the receiving end can be also processed with the location algorithm using a communication link between the sending and receiving points.

Other fault characteristics such as the fault resistance and fault inception angle impact on the detection and location algorithms has been investigated thoroughly in chapter 6 of this thesis. Additionally, the presence of the cycloconverter and the corresponding harmonics was also addressed. The proposed algorithms were applied to an HVLF transmission system supplied with 20 Hz pure sine wave voltage source. The detailed simulation and results are given in chapter 6 of this thesis later.

In the proposed HVLF system, it was found that the fault information is typically contained in the low frequency details. Unlike conventional protection systems that only operate effectively when high frequency transients of up to 1 kHz are detected in the current or voltage measured signals [67]. However, it was proven that for the HVLF system more low frequency details, which contain other useful fault features, need to be considered. Thus, the protection algorithm applied to the HVLF system has shown its ability to identify the transmission fault type and location reliably.

5.9 Advantages of the Proposed Protection Algorithm

In chapters 4 and 5 the principles and results of the protection algorithm proposed to the HVLF transmission system were demonstrated. This section discusses the advantages of this scheme, as follows:

1. The proposed protection algorithm uses a single-end measurement of the three phase current signals to detect and locate faults. In this proposal, the protection principles are based on the detection of transients contained in the reflected current signal from the fault point. Hence, this scheme does not require to exchange information between two measurement points for decision making. Also there will not be any communication

delays to effect the operating time of the tripping signal. Taking into consideration, the protection reliability will not depend on the reliability of the communication link as in the case of protection schemes based on two-end measurements.

2. It is not affected by the cycloconverter generated harmonics. The results have shown that the fault generated transients were clearly identified by the use of the suitable wavelet analysis and the selected mother wavelet. The fault generated transients were detected by monitoring specific wavelet coefficients, such as CW1 and CW3 as illustrated in this study. These coefficients have the ability to detect the fault generated transients of frequencies located within its filter frequency band. The wavelet analysis has shown the ability to provide a time-frequency representation of those transients. The results demonstrate the feasibility and reliability of the proposed protection scheme. Thus, the proposed scheme can be realised for practical implementation to the HVLF transmission system protection.

3. The transmission line faults were detected within less than half a cycle of the power frequency. The total time required by the protection system to detect a fault was about 10 to 20 msec. This time comprises the time required to identify the fault type as well. It was found that the fault classification algorithm performs effectively for all tested faults type at various locations on the line.
4. The proposed location algorithm is capable of locating various types of fault, for various locations along the HVLF transmission line. It is capable of locating faults using the offline data obtained from the WPT coefficient CW1 only. Nevertheless, since the location algorithm uses offline data obtained from the WPT analysis, other coefficients such as CW3 can still be used to support the location decision. Hence, this will enhance the flexibility and reliability of the proposed algorithm.

5. The algorithm described in this chapter takes the electrical behaviour of the HVLF system into account. This includes the power frequency of the line and the resulting transients due to the fault occurrence, as well as the presence of harmonics due to the utilisation of the cycloconverter at the sending end. Unlike the conventional HVAC protection systems that usually rely on the fault generated high frequency transients of up to 1 kHz [54, 56, 60, 61, 67, 93, 94].
6. The protection and location algorithm can be implemented with an artificial intelligent (AI) tool such as Artificial Neural Networks (ANN) or Fuzzy Logic for decision making. As shown in chapter 2, numerous studies have been conducted in the last few decades addressing the advantages of the combination of signal processing techniques and artificial intelligent systems applied to power system protection. At an early stage of this research, an evaluation study has been presented on the combination of wavelet analysis with Modular Neural Networks (MNNs) applied to the conventional 50 Hz HVAC transmission line protection [82]. Although, neural networks were not presented in this thesis, it is possible to apply the same previous proposal to the designed HVLF protection algorithms. The Neural networks proposed by the author of this thesis in [82] were utilised as fault type and location classifiers only. The input to these networks was fed from the WPT analysis. Hence, with the modification of the WPT applied to the HVLF system in this research, the input to these networks can still be maintained.

Chapter 6
Impact of the Fault Parameters and System Structure on the Protection Algorithm

6.1 Overview

The robustness of the new protection algorithm has been further evaluated by investigating the impact of the HVLF system parameters, namely the fault inception angle and the switching and control of the cycloconverter. In this chapter, the fault inception angle effects the magnitude of the fault generated transients that were obtained by means of the WPT coefficients energy analysis. Therefore, the fault inception angle was varied, and the energy of the WPT coefficients obtained from the three-phase current signals was observed under various fault types and locations.

Recently several HVLF transmission systems of different configurations have been proposed in the literature [15, 20-22, 24, 33, 34, 95]. Some of these topologies proposed includes power generation at a lower frequency, such as 20 or 16.7 Hz. Therefore, in order to provide an overview of the generality of the proposed protection algorithms, this chapter discusses the possible factors affecting the performance of the protection system. This study focused on the impact of the cycloconverter utilisation at the sending end. In chapter 4 and 5, the spectral analysis of the pre- and post-fault three-phase current signals obtained from the cycloconverter based HVLF system was given in detail. Therefore, a comparative study has been conducted to determine the effects of the cycloconverter and its corresponding harmonics on the proposed protection algorithm. Hence, the cycloconverter was replaced by its internal reactance, and the HVLF system was supplied with a 20 Hz pure sine wave source. Simulations of various fault scenarios were carried out, and harmonic spectra of the current waveforms were analysed. The results have been compared with those obtained for the cycloconverter based HVLF system.

6.2 Impact of the Fault Inception Angle

The post-fault generated transients are affected by the point where the fault takes place during the phase current cycle [48]. In this study the phase-A current signal was taken as the reference signal in which the fault inception angle was determined. Thus, the phase-A fault inception angle has been varied in order to evaluate its impact on the fault induced transients. The HVLF system described in chapter 4 has been used to simulate several fault types at various locations on the line, and in each case the fault angle was changed in a step of 45°. Thus, the selected fault inception angles for this study were 0°, 45°, 90°, 135° and 225°. The transmission line faults where firstly initiated when the voltage of phase-A at minimum (fault inception angle = 0). Then the fault timing where changed accordingly in order to obtain other fault inception angles (45°, 90°, 135° and 225°). At all tested short circuit faults (LL, LLL. etc.) the phase-A voltage signal was taken as reference. As given in chapter 5, the WPT analysis for fault detection was carried out for two fault location points. The selected locations were 20, and 180 km from the sending end. These locations were chosen in order to find out the highest and lowest energy levels of the WPT coefficients that can be obtained after the fault incident at a given fault angle. Therefore, these two locations were selected in this test, and the fault angle was varied accordingly. Figures 6.1 and 6.2 show the three-phase current signals when an LG fault occurs at locations of 20 km and 180 km, respectively. The figures clearly show that the angle at which the fault occurs was set to 0°, 45°, 90°, 135° and 225° in subplots (a), (b), (c), (d) and (e), respectively. Although the waveforms plot does not clearly show the transients, high frequency transients were produced after the fault occurrence. It was also noted that after one cycle of the fault incident, the cycloconverter tries to synchronise the fault current to a 20 Hz power frequency. Therefore, the following cycles were of higher magnitude and approximately uniform. This is because the cycloconverter control uses the cosine crossing method, in which the output is synchronised to a reference control signal, as described in chapter 3.

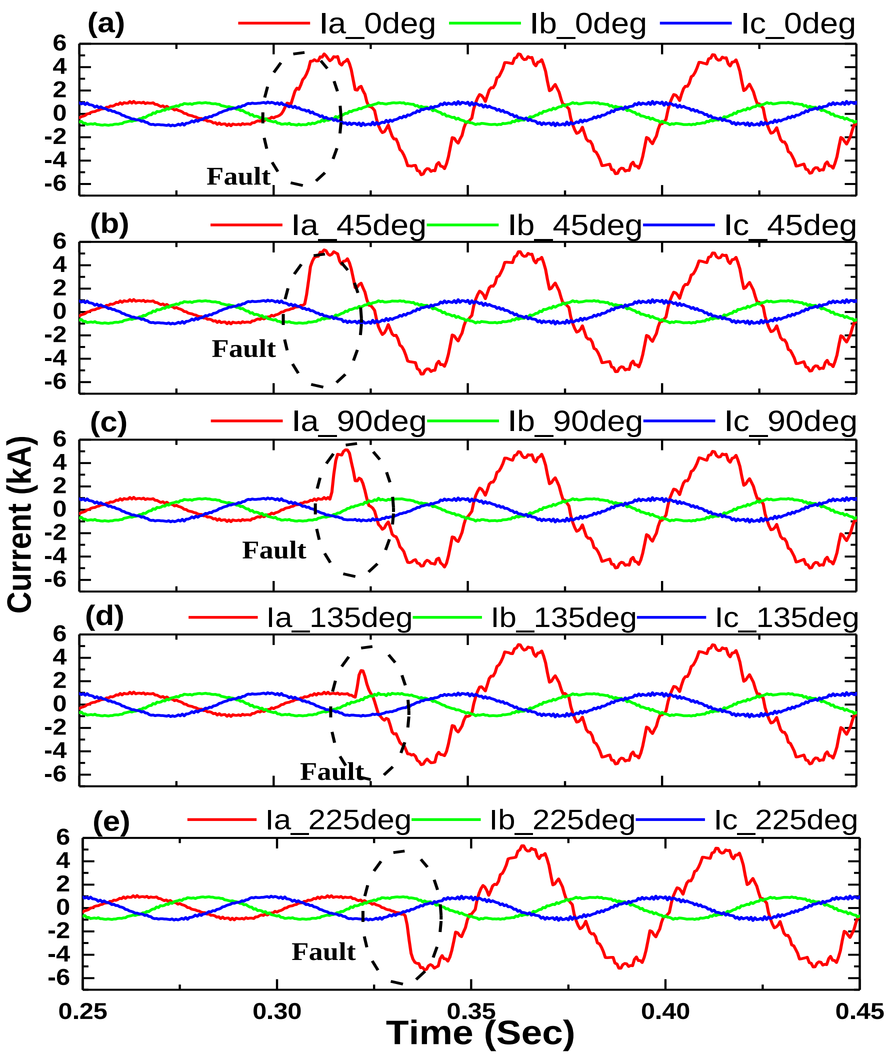

Figure 6.1: The three-phase current signals when an LG fault occurs at 20 km with fault inception angle = (a) 0, (b) 45, (c) 90, (d) 135 and (e) 225

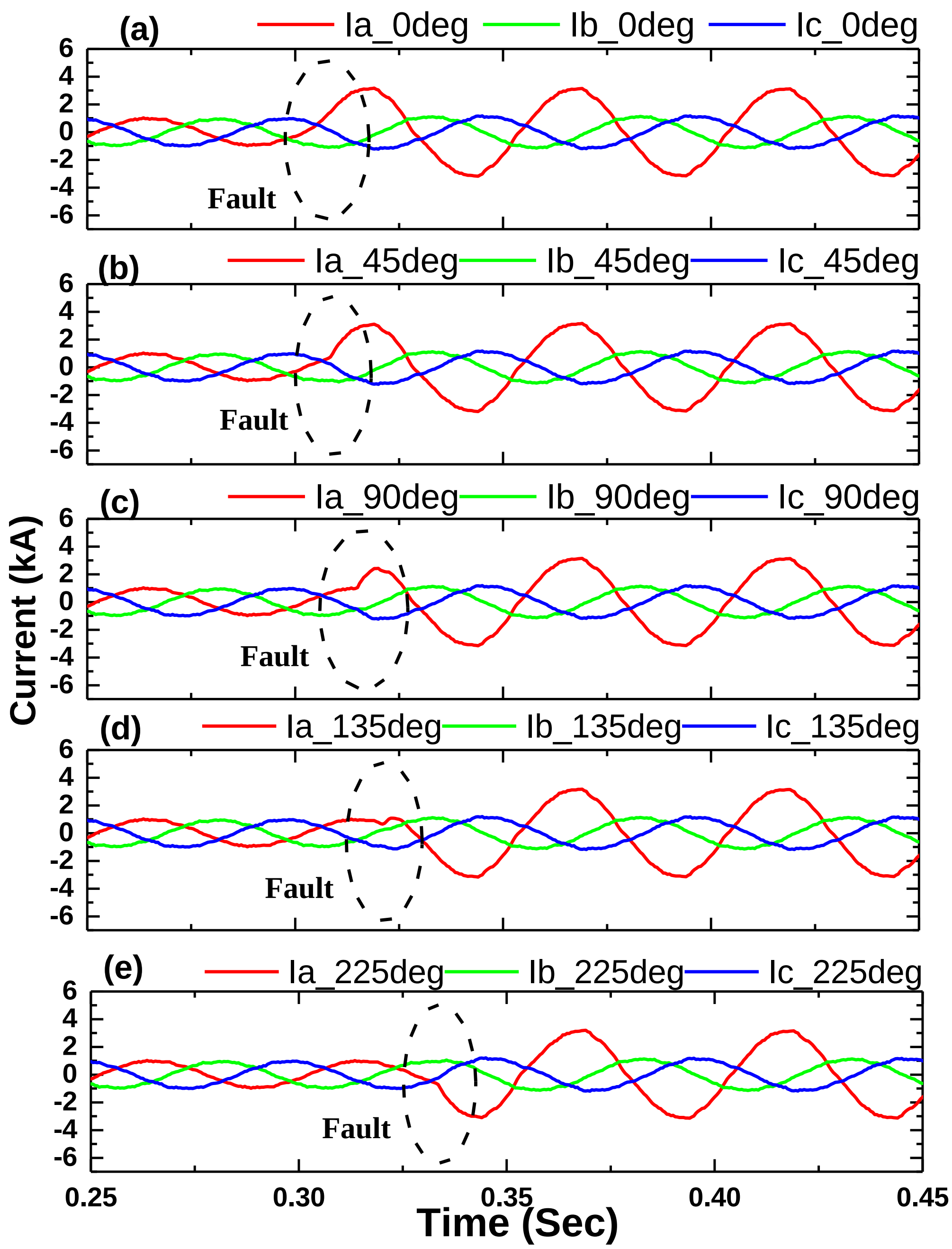

Figure 6.2: The three-phase current signals when an LG fault occurs at 180 km with fault inception angle = (a) 0, (b) 45, (c) 90, (d) 135 and (e) 225.

It is also noticeable that some of the high frequency fault generated transients are suppressed in the line when the fault occurs at a remote location such as 180 km, see figure 6.2. Therefore, the frequency content of the three phase current signals obtained under all tested inception angles was investigated by means of the WPT analysis.

The WPT analysis to the captured current waveforms shown in figures 6.1 and 6.2 was carried out, and the resulted coefficients CW1 and CW3 are given in figures 6.3 and 6.4, respectively. These coefficients were selected for the fault detection and location algorithms given in chapter 5. These results depicts the spectral energy of the selected coefficients under the corresponding fault inception angle. Figure 6.3 clearly shows that the spectral energy of the WPT coefficients CW1 and CW2 varies with changes in the fault inception angle. This is because the magnitude of the captured transients is affected by the magnitude of the faulty phase current signal at the fault occurrence instant. Although the magnitude of the spectral energy varies, the results demonstrated that both coefficients have significant increase in the energy level after the fault incident at all tested inception angles. Also, at both fault locations the energy magnitude exceeds the predefined fault thresholds, and the detection algorithm was accurately able to detect the fault within 10 mesc. i.e. (4 samples) after the fault occurrence. This test proves that the method proposed earlier for fault detection using the selected WPT coefficients works independently of the fault inception angle.

By observing the reduction in the magnitude of the spectral energy shown in figures 6.3 and 6.4, it is obvious that the selected coefficients can be utilised for fault location as proposed in chapter 5. The results of both tested fault locations illustrate that the spectral energy reduces with the increase in fault distance, and the fault inception angle has not shown any effect. It can be stated that the proposed detection and location algorithms are independent of the fault inception angle. However, for further validation, tests were carried out to investigate the effect of the inception angle on the protection algorithm in case of other fault types such as, line to line fault (LL) and three lines fault (LLL).

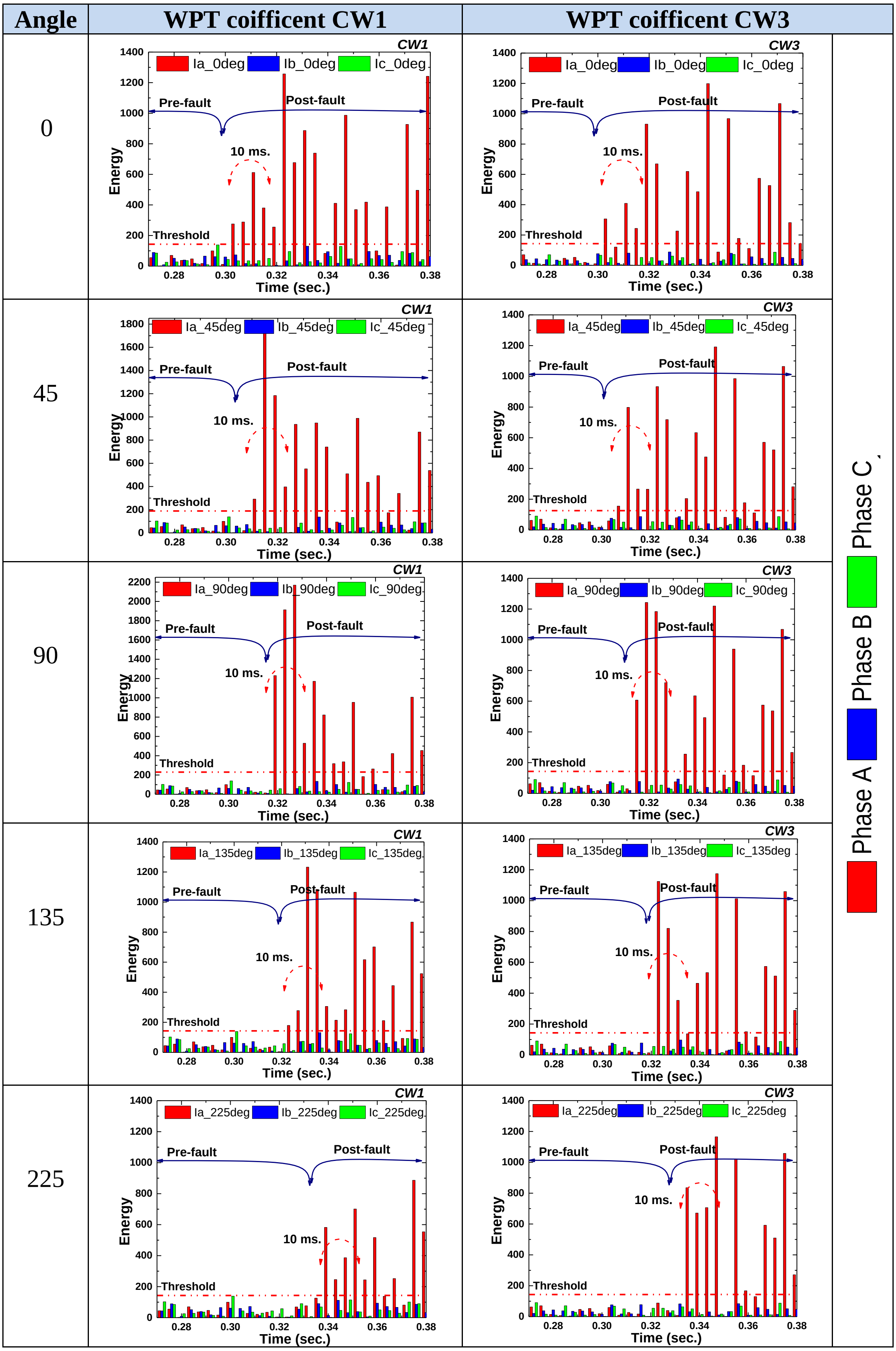

Figure 6.3: The WPT coefficients obtained from an **LG** fault of different fault inception angle at location of **20** km.

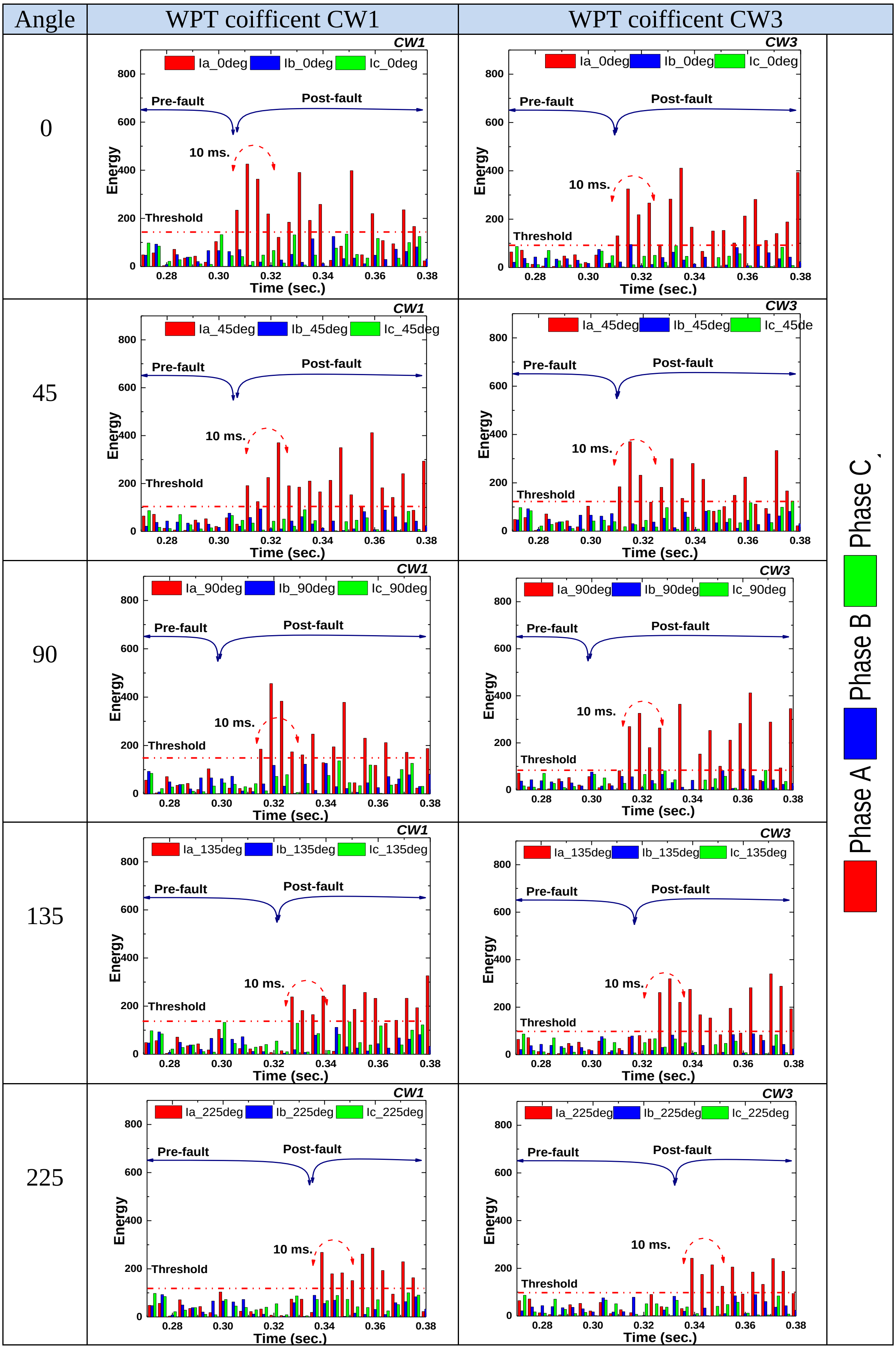

Figure 6.4: The WPT coefficients obtained from an **LG** fault of different fault inception angle at location of **180** km.

Therefore, the effect of the inception angle on the fault detection scheme was also examined under different fault types. For each type of fault, the same procedure was carried out, and the fault was initiated at fault inception angles of 0°, 45°, 90°, 135° and 225°. Taking into consideration that the fault inception angle is correspond to the fault inception angle of phase-A. Figures 6.5 to 6.12 illustrate the waveforms and the WPT coefficients in the case of a line to line (LL) fault and three lines fault (LLL) at locations of 20 and 180 km from the sending end. For each fault scenario the WPT coefficients CW1 and CW3 are given in the following figures. The results shows that similar trends were obtained for both fault types at all examined inception angles. It is clearly demonstrated that the fault can be detected within approximately 10 msec after its occurrence. Also, the magnitude of the spectral energy of the analysed faulty phases show a significant decrease with the increase in fault distance. All results show that faults occurs at various inception angles, types and locations were correctly detected. This means that the fault detection and location schemes have shown their ability to detect and locate line faults despite fault types or parameters.

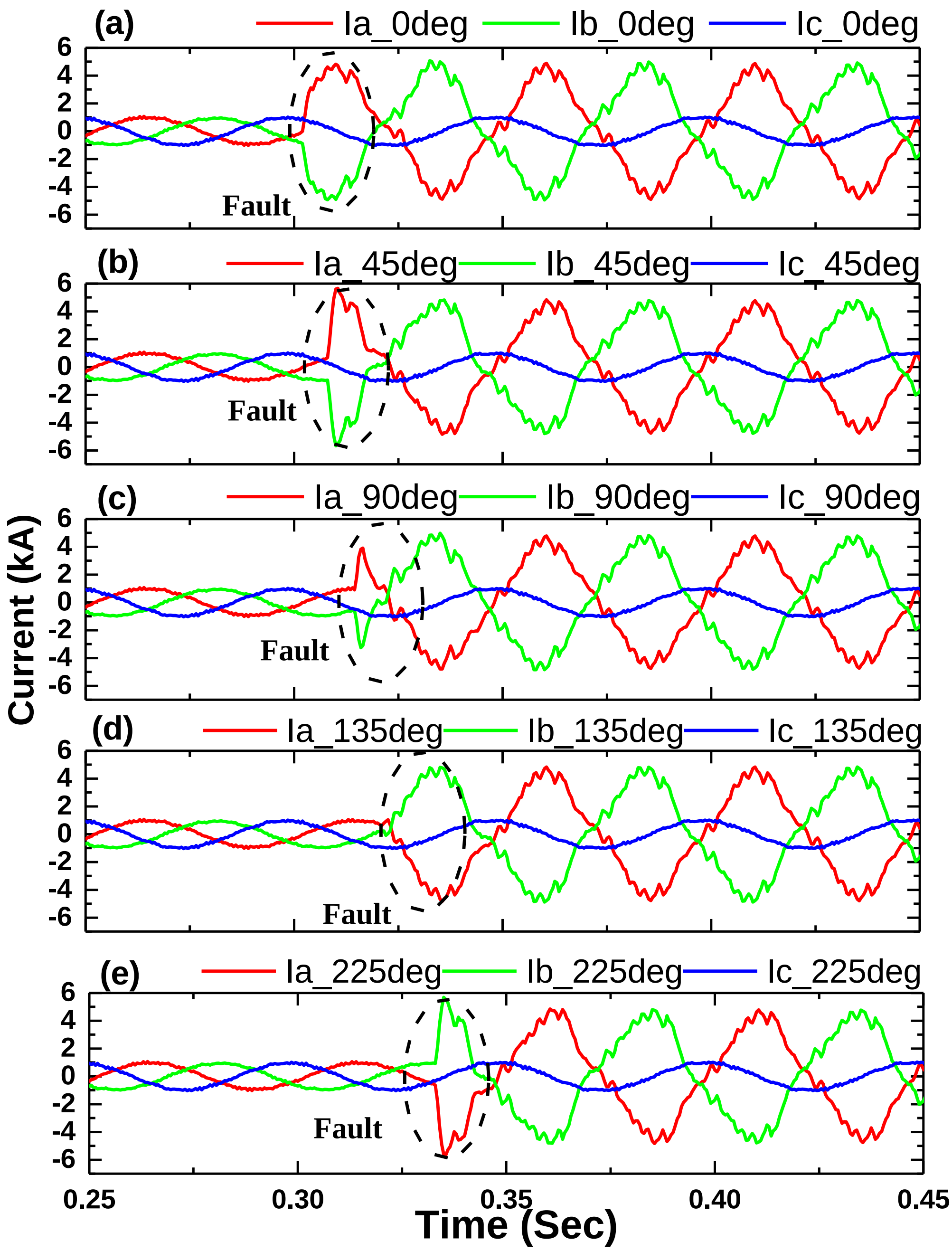

Figure 6.5: The three-phase current signals when an LL fault occurs at 20 km with fault inception angle = (a) 0, (b) 45, (c) 90, (d) 135 and (e) 225.

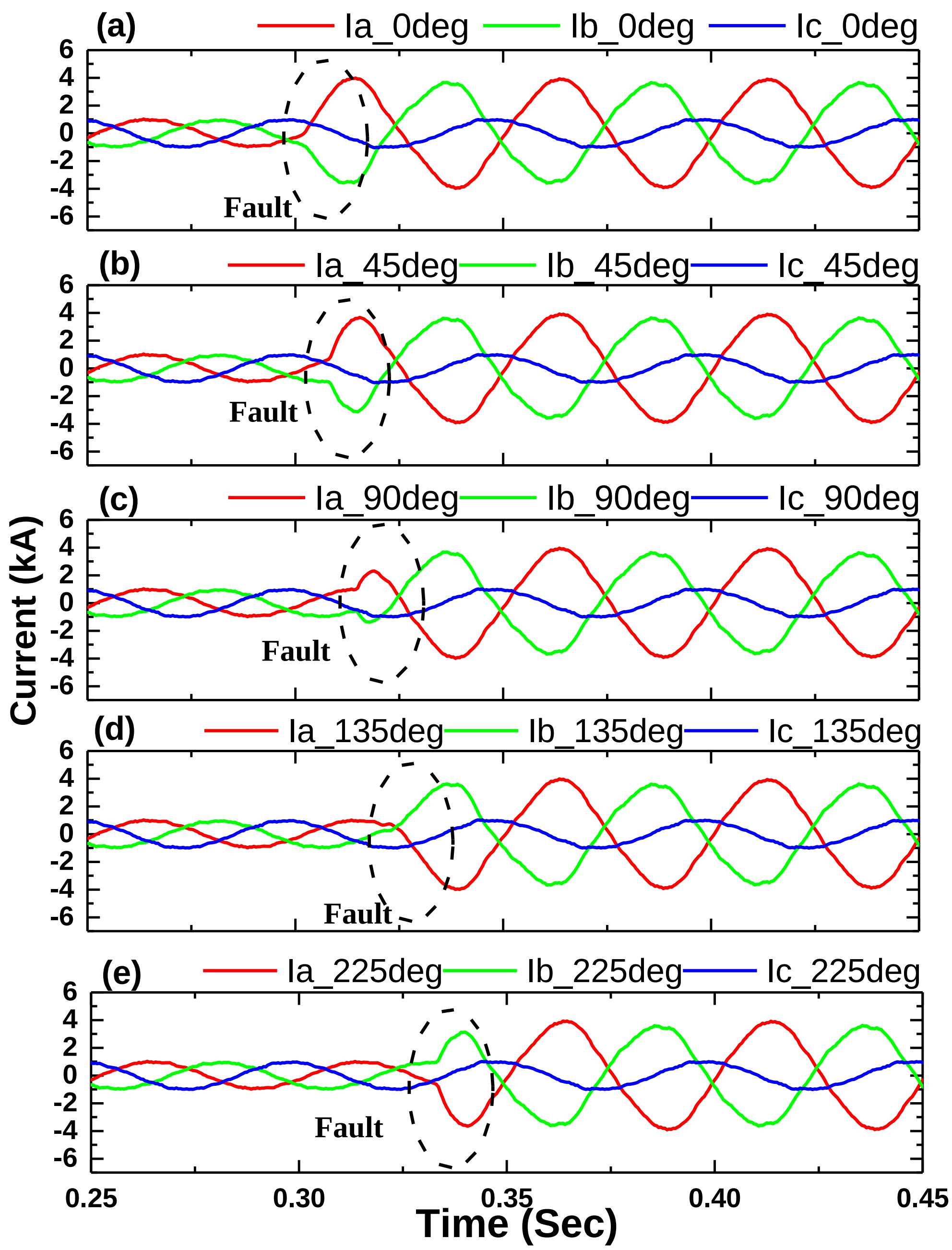

Figure 6.6: The three-phase current signals when an LL fault occurs at 180 km with fault inception angle = (a) 0, (b) 45, (c) 90, (d) 135 and (e) 225.

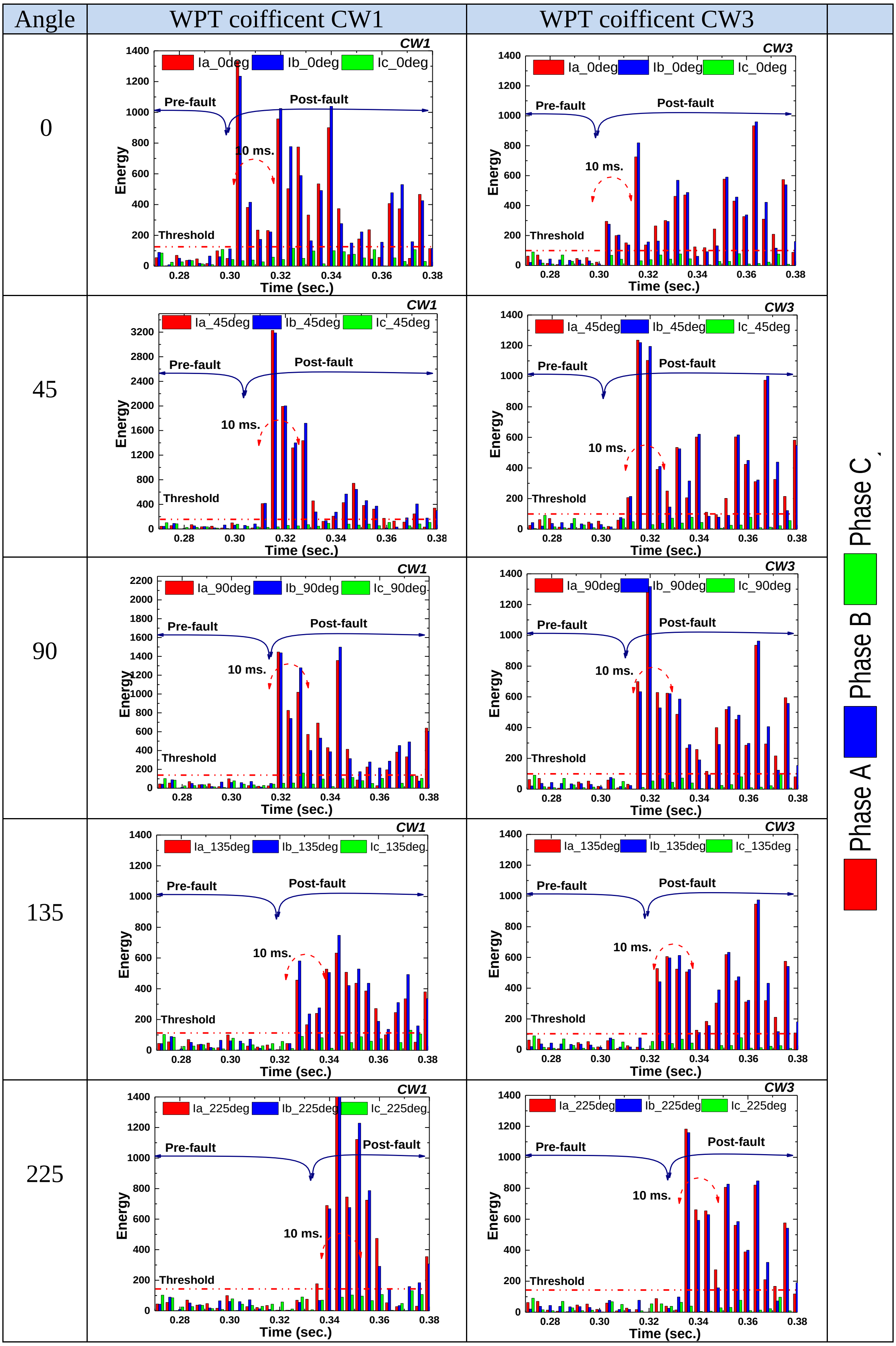

Figure 6.7: The WPT coefficients obtained from an **LL** fault of different fault inception angle at location of **20** km.

<table>
<tr><th>Angle</th><th>WPT coifficent CW1</th><th>WPT coifficent CW3</th><th></th></tr>
<tr><td>0</td><td>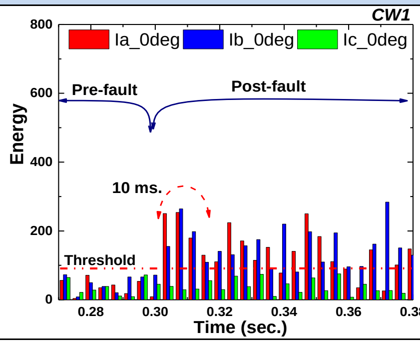
</td><td>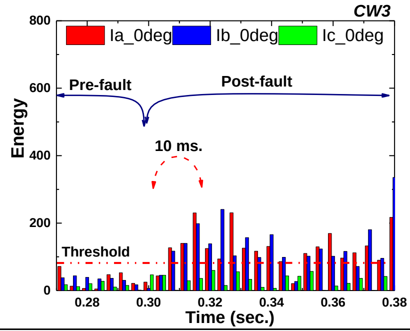
</td><td rowspan="5">
</td></tr>
<tr><td>45</td><td>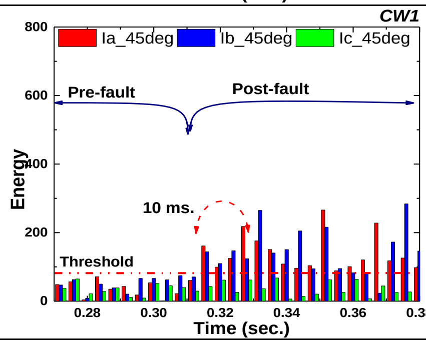
</td><td>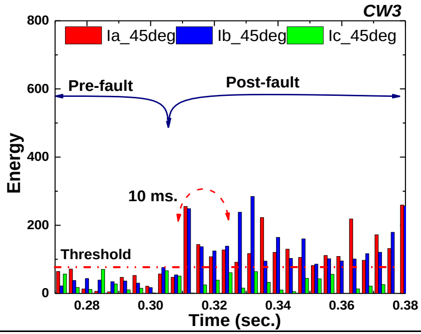
</td></tr>
<tr><td>90</td><td>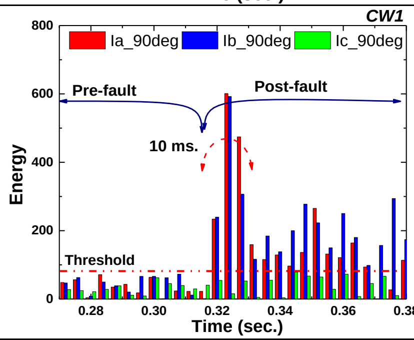
</td><td>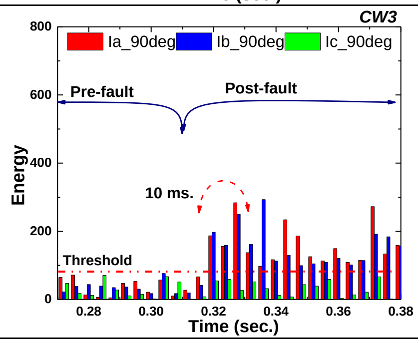
</td></tr>
<tr><td>135</td><td>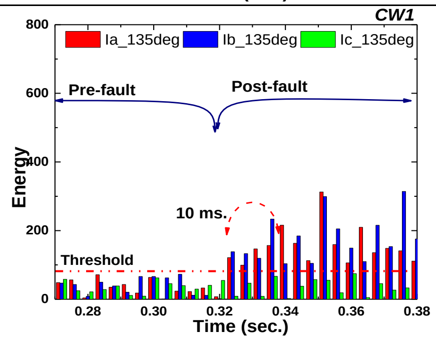
</td><td>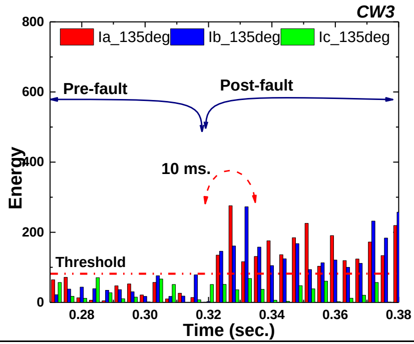
</td></tr>
<tr><td>225</td><td>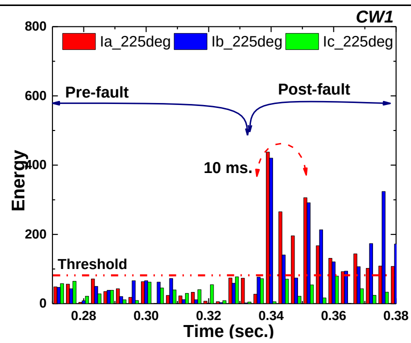
</td><td>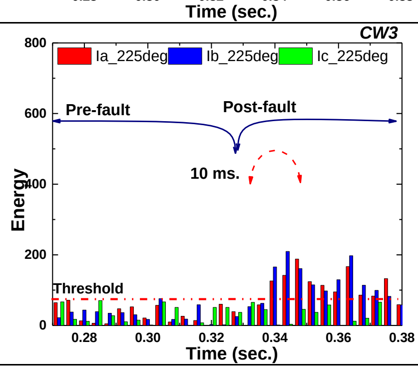
</td></tr>
</table>

Figure 6.8: The WPT coefficients obtained from an **LL** fault of different fault inception angle at location of **180** km.

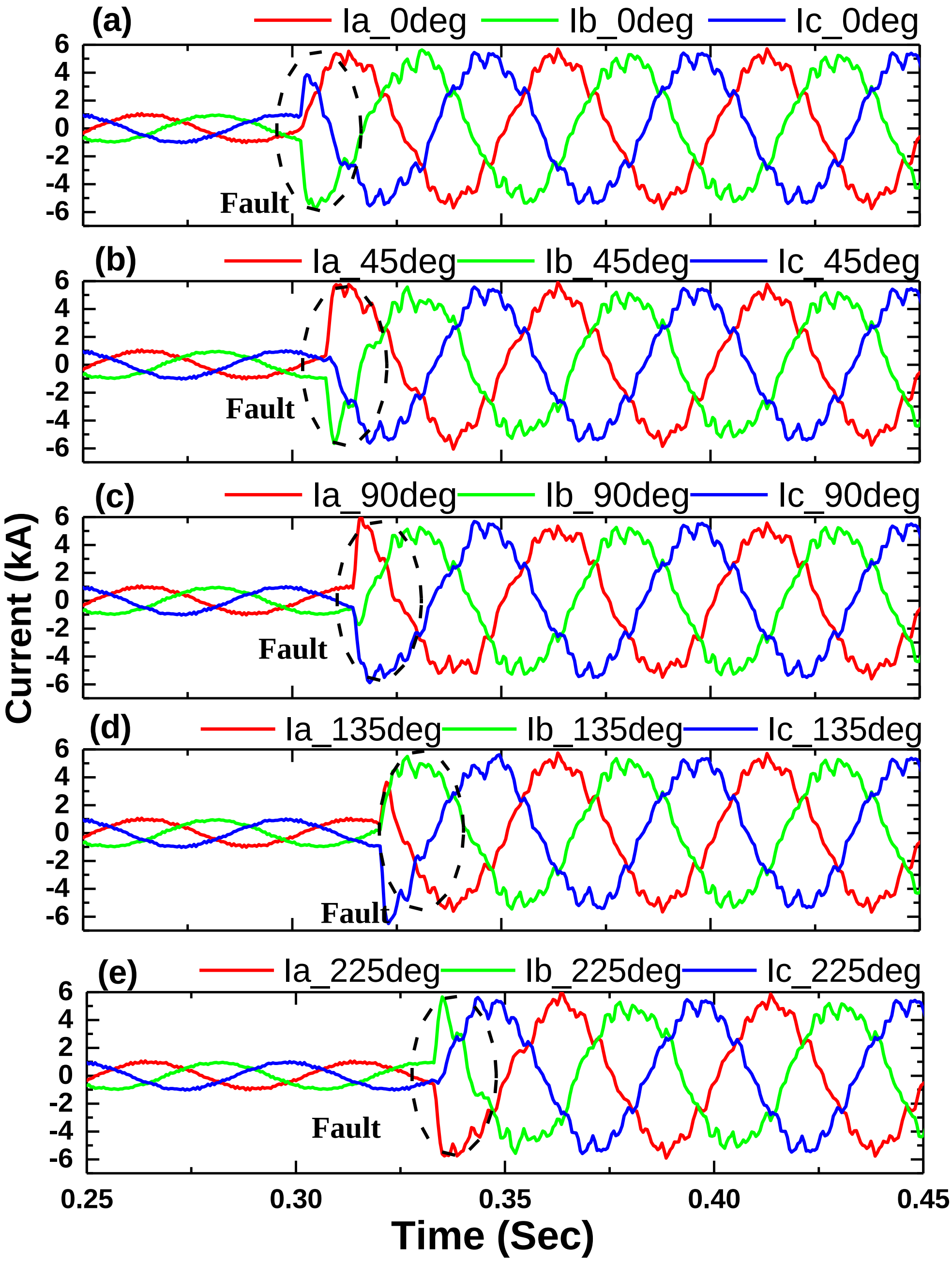

Figure 6.9: The three-phase current signals when an LLL fault occurs at 20 km with fault inception angle = (a) 0, (b) 45, (c) 90, (d) 135 and (e) 225

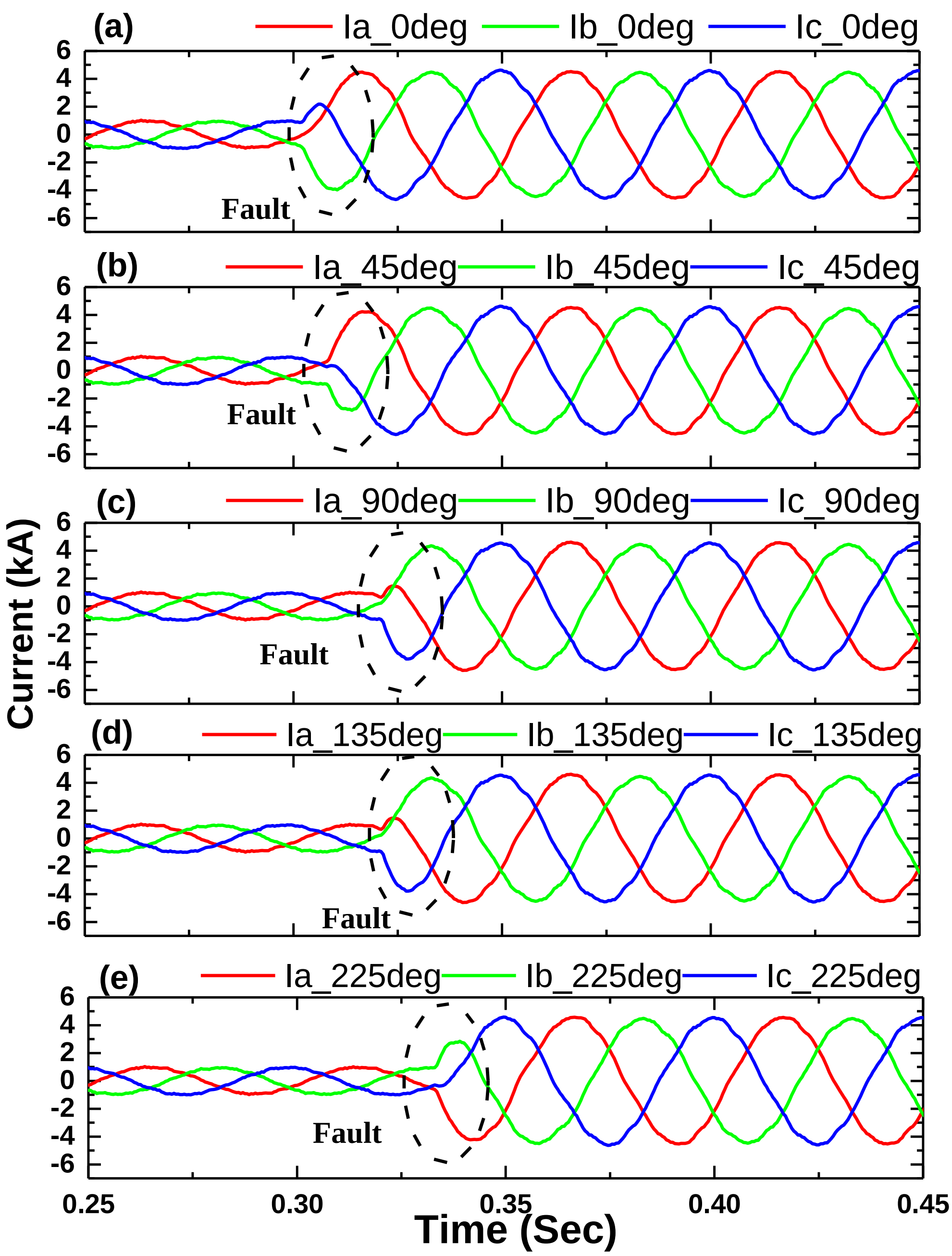

Figure 6.10: The three-phase current signals when an LLL fault occurs at 180 km with fault inception angle = (a) 0, (b) 45, (c) 90, (d) 135 and (e) 225.

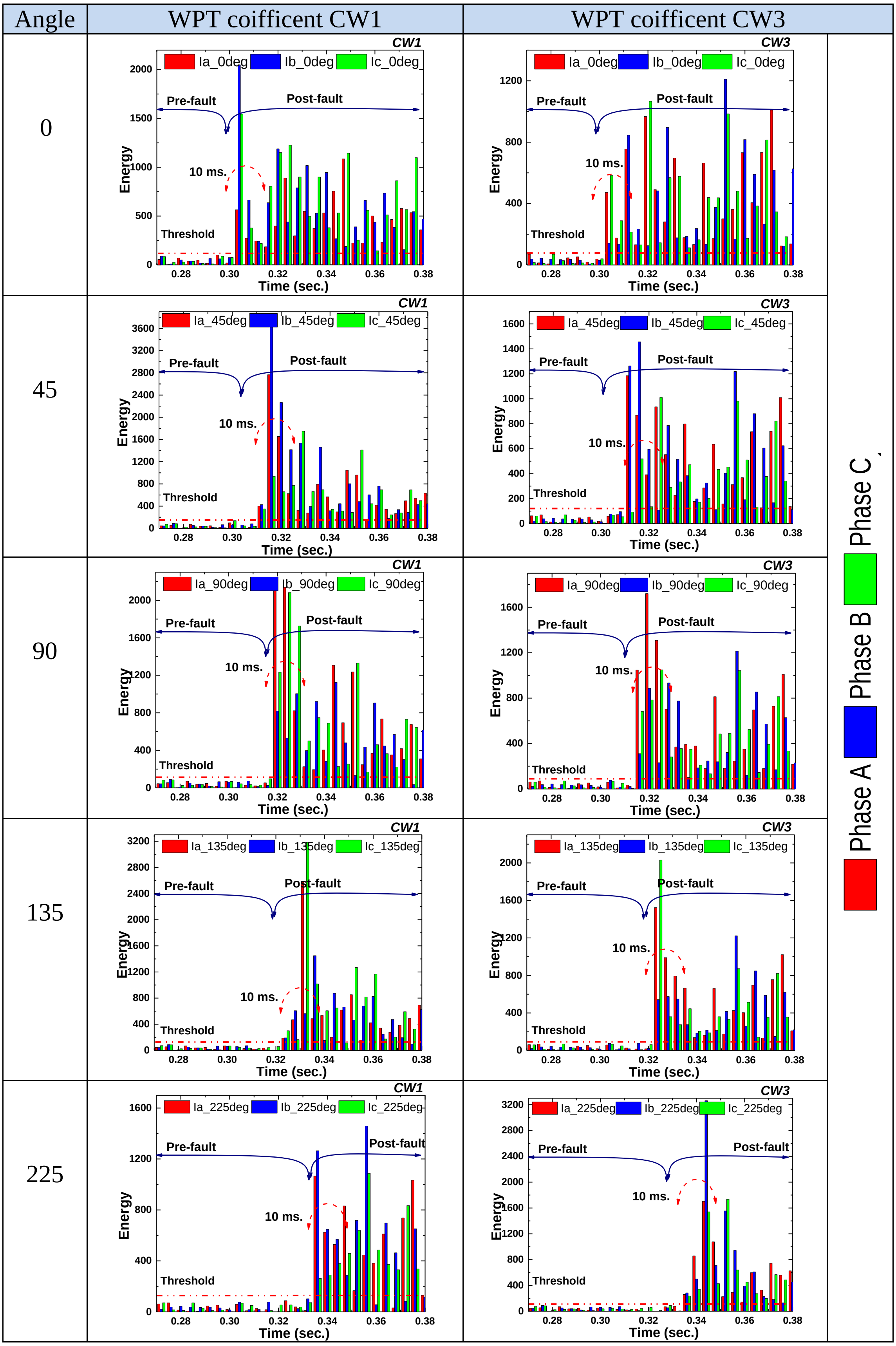

Figure 6.11: The WPT coefficients obtained from an **LLL** fault of different fault inception angle at location of **20** km.

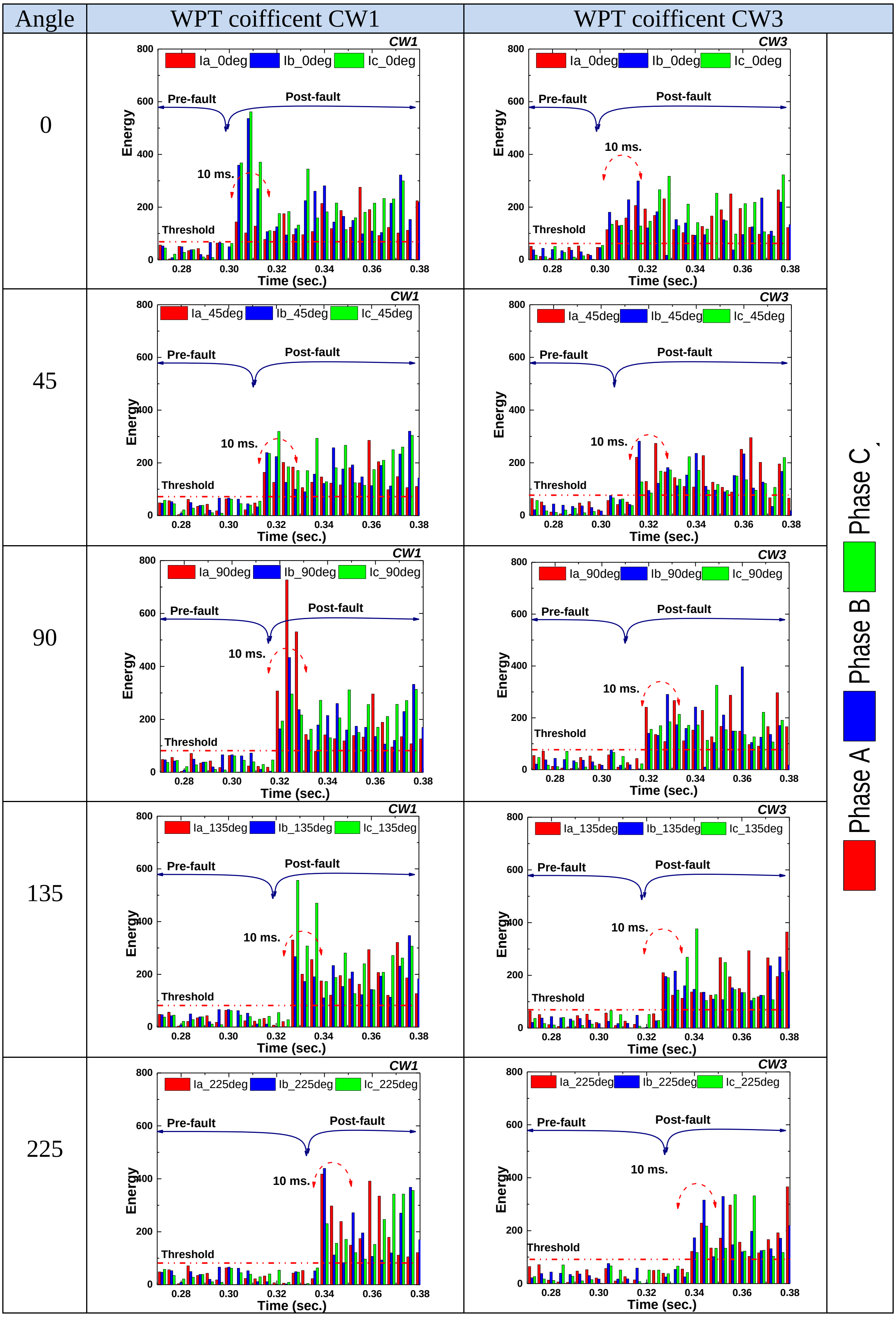

Figure 6.12: The WPT coefficients obtained from an **LLL** fault of different fault inception angle at location of **180** km.

6.3 Impact of Cycloconverter Utilisation

In the previous chapters, the proposed protection scheme has been evaluated based on the adopted HVLF system configuration. This topology of the HVLF system implements a cycloconverter at the offshore station as a frequency changer, taking into consideration that the offshore wind power is generated and collected at the conventional 50/60 Hz. The results of this configuration have shown the presence of harmonics generated by the cycloconverter are injected into the transmission line. Therefore, filter banks were implemented to suppress these harmonics and to improve transmission system efficiency. However, it was shown in the previous chapters that these harmonics interfere with the fault generated transients. This results in difficulties for the protection system to differentiate between these harmonics and the fault generated transients. In this study, it was shown that the designed protection algorithms have the ability to detect faults despite changes to the fault or system parameters. Nevertheless, a further test was undertaken in order to validate the protection algorithm's performance under different HVLF system topologies. The aim of this experiment was to illustrate the effects of cycloconverter harmonics and control on the transmission line fault signature.

In this section, an evaluation of the cycloconverter influence on the fault generated transients was carried out. This was achieved by replacing the cycloconverter in the Matlab model given in chapter 4 (figure 4.12) with its inter-group reactance, see figure 6.13. The system was supplied with a 20 Hz sine wave voltage source, and the transmission line parameters (R, L and C), as well as the receiving end load are kept the same. Figure 6.13 shows the simulated model in Matlab-Simulink.

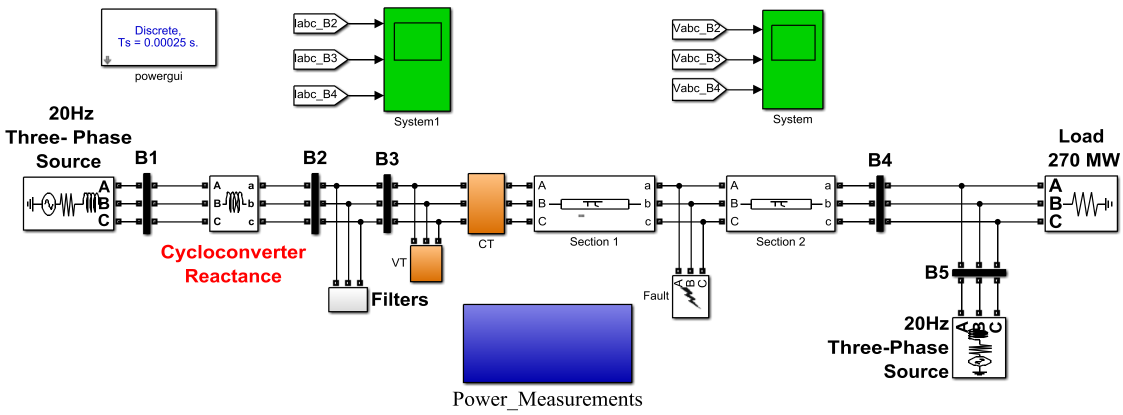

Figure 6.13: Matlab model of the HVLF system supplied with 20 Hz voltage source.

Then, the same fault scenarios in the previous tests of transmission line fault were carried out. In this section, a single line to ground fault (LG) was initiated at locations 20, 60, 120 and 180 km from the measurement point at the line sending end was taken as a case study. The three-phase current waveforms obtained at the measurement point are shown in figure 6.14. The waveforms show that there are high frequency transients present after the fault occurrence at time 0.3 sec.

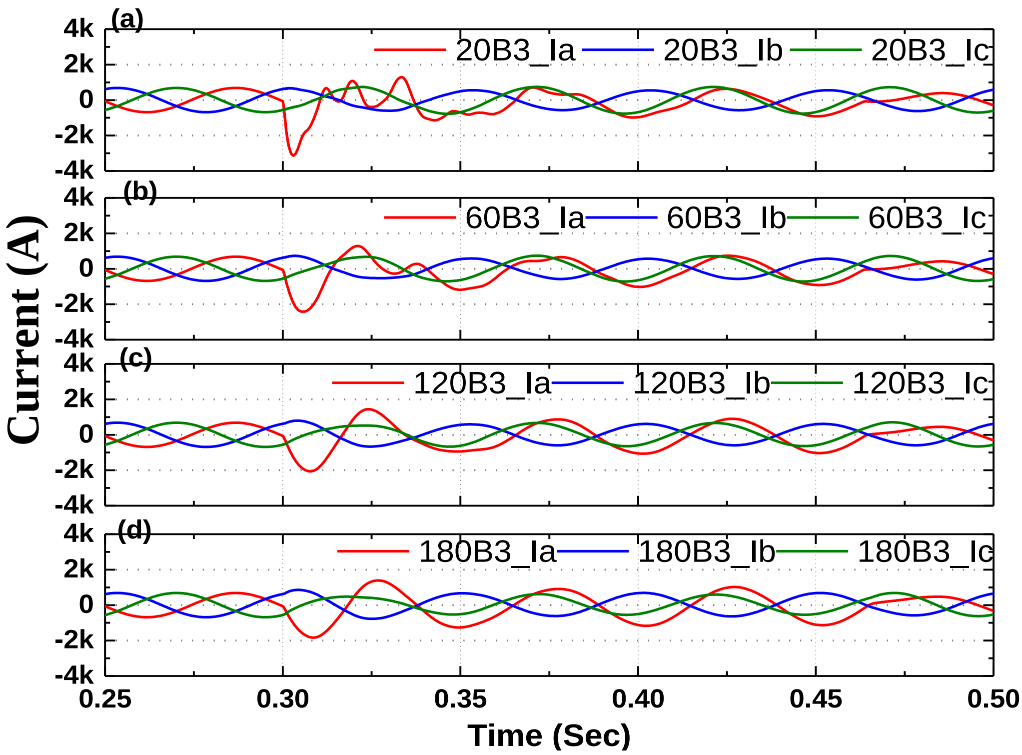

Figure 6.14: The three-phase current waveforms for an LG fault at 20, 60, 120 and 180 km, with the cycloconverter replaced.

Initially, the frequency spectra of the simulated line to ground (LG) fault at locations 20 and 180 km was investigated using FFT analysis, and the results are displayed in figure 6.15. These results show the presence of even harmonics in addition to odd harmonics. In comparison to the harmonic spectrum of the same fault scenario given in chapter 4, it is clear that due to the cycloconverter switching and control the transients of the post fault current are significantly attenuated. Thus, the magnitudes of the post-fault current harmonics are higher as shown in figure 6.15.

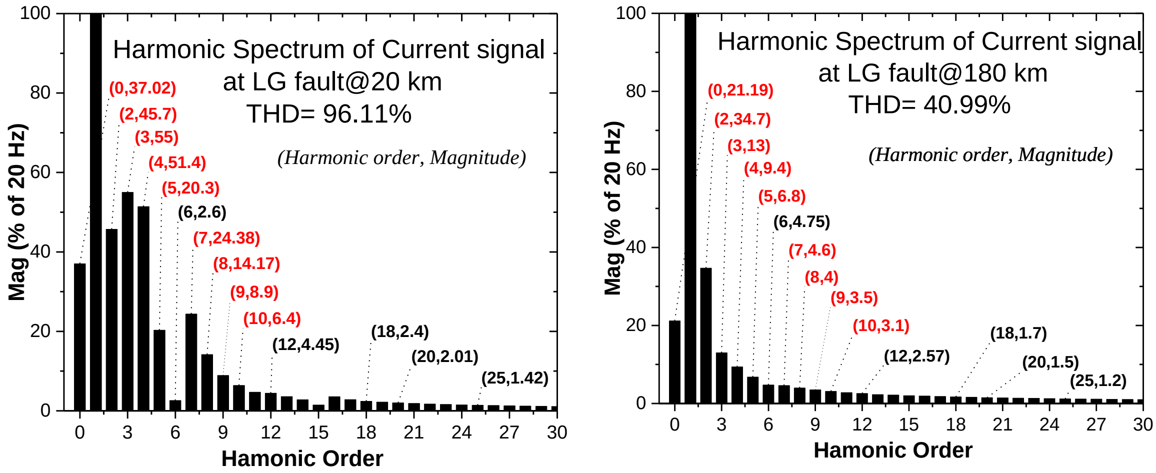

Figure 6.15: Harmonic spectrum of the current signal when an LG fault occurs at 20, 180 km locations on the HVLF transmission line supplied by a 20 Hz sine wave voltage source.

Moreover, some harmonics were attenuated in the line when the fault occurred at the location of 180 km, and thus the total harmonic distortion (THD) reduced from about 96% to 40%. However, in order to test the performance of the proposed protection algorithm, the WPT analysis of the three-phase current signals was carried out. Figure 6.16- a and b shows the WPT coefficients CW1 and CW3 obtained for locations at 20 and 180 km, respectively. These coefficients represent the transients contained in the current signals within the corresponding frequency band, as given in table 5.1. The results show that the captured fault generated transients have the same frequency range of those captured from the cycloconverter based system. Yet, unlike the cycloconverter based results, the analysis shows that for all coefficients the obtained pre-fault spectral energy is nearly zero. This is because that the HVLF system is supplied with a 20 Hz pure sine wave, and hence no harmonics exist under the pre-fault condition.

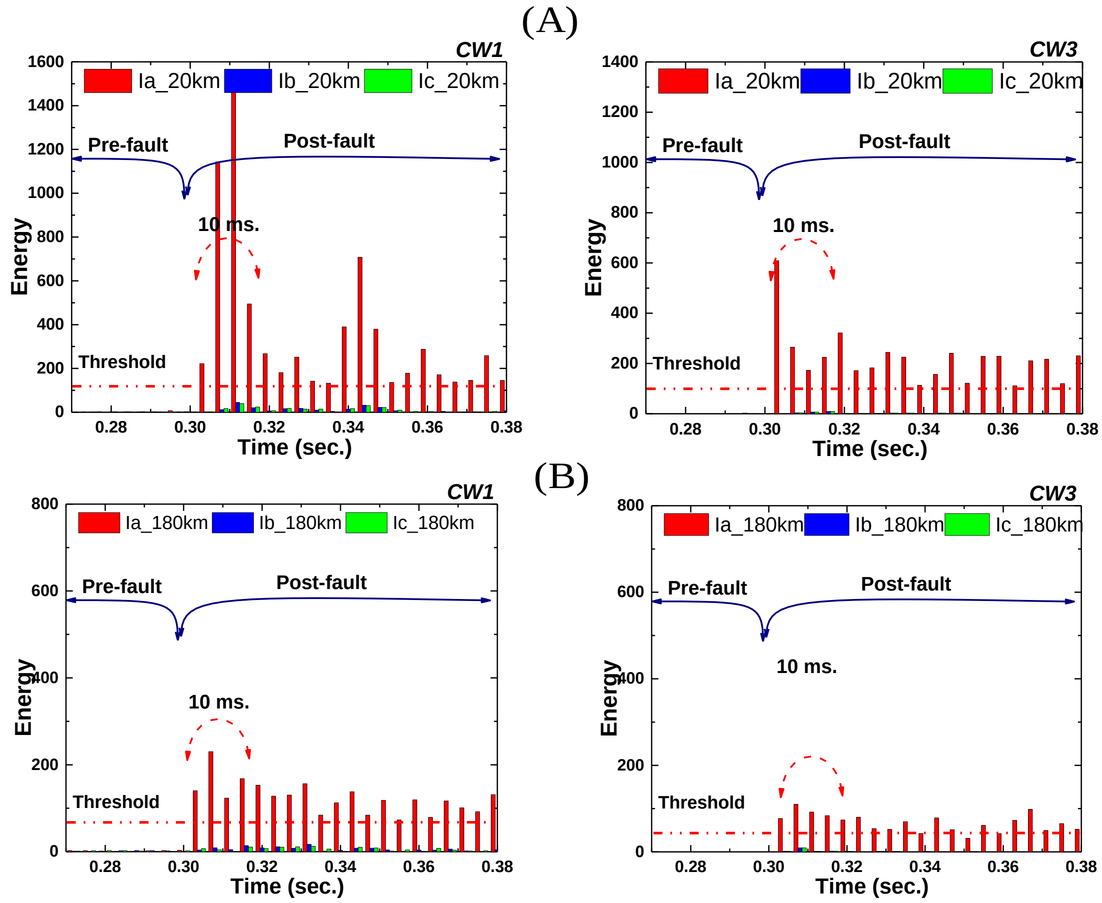

Figure 6.16: Samples of the WPT coefficients CW1 and CW3 obtained from the three-phase current signals when an LG fault occurs at distances of (a) 20 km (b) 180 km, with the cycloconverter replaced.

However, the absence of pre-fault harmonics enhance the protection system sensitivity to any high frequency transients occurring. Nevertheless, at both locations the results demonstrate that the fault was detected within approximately 10 msec of its occurrence. Additionally, by comparing the spectral energy of coefficient CW1 obtained at 20 km and 180 km, it is obvious that there is a significant reduction in its magnitude. Hence, the proposed location algorithm can accurately identify the fault zone. This test proves that the proposed protection algorithm can be applied to an HVLF system of any topology despite of the presence of per-fault harmonics or not.

However, the configuration of an HVLF system, including the low frequency generated power topology, requires a reactive power compensation of any size. Thus, the filters were kept in this simulation as a compensation system. In any electrical power system, this reactive compensation system is also contributes to the post-fault transients. Hence, from practical point of view the implementation of a transmission system without the utilisation of reactive power compensation is not possible. It was shown in this study, the frequency range of the post-fault transients is relative to the fundamental power frequency of the system in spite of the system structure or line parameters. However, the designed protection algorithms have shown high sensitivity to the presence of the post-fault generated transients of the tested HVLF system structures.

Chapter 7
Conclusions and Future Research

7.1 Conclusions

This thesis shows that the HVLF transmission system is a viable alternative to HVAC and HVDC systems for long distance offshore power transmission of distances over 50 km, due to the following factors:

- Reducing the fundamental power frequency results in a reduction in reactive current, and consequently increases the active power transfer capability of the line.
- The mature HVAC circuit breakers technology can be adapted to implement a multi-terminal HVLF grid through minor modifications if necessary.
- The alternating field albeit at a much lower frequency mitigates the space charge accumulation mechanism and thus reduces the aging effects of the XLPE cable. Therefore, the failure rate of the cable is reduced and accordingly increases its service life.

A detailed study on the structure of the HVLF system was presented. It was found that utilising frequency changers at both ends of the transmission line has significant advantages such as:

- Eliminates the need for any wind turbine modification as well as a large low frequency step-up transformer. Thus, this topology retains the conventional wind turbine generators, offshore collection network, and conventional HVAC transformers.

- On the offshore platform only a step-down frequency changer is required.

Therefore, for the HVLF system presented in this thesis, a high power naturally commutated cycloconverter was chosen due to its mature and well developed technology for high power applications. The frequency spectrum analysis has shown that even with the characteristics of tuned AC filters to prevent cycloconverter generated harmonics from being injected into the line, some high frequency harmonics were still present in the line. The Total Harmonic Distortion (THD) of the current and voltage signals during pre-fault condition were 11.5% and 4.5% respectively. Hence, a detailed investigation into the harmonic distribution during post-fault condition and their effects on the protection system was carried out.

It was also concluded in chapter 2, a signal processing tool is required to enable faults to be detected and their distances from a reference point evaluated in the presence of cycloconverter harmonics. In chapter 3, a brief description of the signal processing techniques applied to the power system transient analysis was carried out and the following points were noted:

- The Discrete Fourier Transform (DTF) and the Short-Time Fourier Transform (STFT) have limitations in providing accurate time-frequency representation of the analysed signal.
- Although, the Wavelet Transform has shown a comprehensive time-frequency representation in the analysis of transient signals, it was found that a higher level of analysis was required, but it still yielded poor high frequency resolution.
- The Wavelet Packets Transform has shown higher frequency details within a lower level analysis. Hence, the WPT using Daubechies (db4) mother wavelet was selected for fault feature extraction from the three-phase current waveforms.

In chapter 4, it was established, through FFT analysis of faulty phase current waveforms for various fault types and locations, that the post-fault transients have a frequency range of up to 350 Hz. Thus, the conventional HVAC protection systems are not compatible for the HVLF system because:

- The frequency range of the fault generated transients in the HVLF system is lower than those of in HVAC system.
- The presence of the pre-fault harmonics in the HVLF system need to be considered in order to prevent the protection system from falsely triggering.
- Hence, the lowpass and highpass filters of the WPT analysis are required to be tuned in order to extract the HVLF fault generated transients.

A new fault detection and location algorithm based on the WPT analysis with Daubechies-4 (db4) mother wavelet analysis was developed in this research, as shown in chapter 5. The algorithm was designed to detect the fault generated transients contained in the faulty phase(s) current signals measured at the sending end of the line. The algorithm's performance has been tested for various types of fault at several locations along the line, and the results showed that:

- The fault transients can be detected using the WPT coefficients CW1 and CW3 only.
- The transmission line faults can be detected within 10 to 20 msec. after the fault incident.
- The predefined thresholds set for fault detection have prevented the detection algorithm from reacting to the pre-fault generated harmonics.

- Additionally, the offline data of the WPT analysis were used for fault location estimation. The fault location was estimated using only one of the WPT coefficients (CW1).
- The WPT coefficients and thresholds were set so that the protection system is effective for a fault towards the receiving end.

In chapter 6, the impact of the fault inception angle variation on the response of the protection system was examined by simulating various fault types occurring at different inception angles. The system detected faults in spite of different transient levels due to variation in fault inception angle.

Finally, replacing the cycloconverter by its equivalent inter-group reactance and suppling the system with a 20 Hz sinewave voltage source has revealed the impact of its switching and control on the fault transients. The results showed that the post-fault current harmonics are of a higher magnitude compared to those generated when in the presence of the cycloconverter. However, the protection algorithms have shown higher fault detection sensitivity due to the absence of the cycloconverter pre-fault generated harmonics in the system.

In conclusion, under all tested fault scenarios the designed WPT based protection system has successfully detected and located transmission line faults. This thesis seeks to contribute to both the understanding and applications of transmission technologies in the field of large scale offshore wind power integration to the utility grid. Although, this research did not receive any specific grant from funding agencies in the public, commercial, or not-for-profit sectors, the research has opened up the possibility of developing the next generation of offshore transmission technology to enable a reliable, efficient and high capacity provision of renewable energy.

7.2 Future Work

The following issues were noted during the research, however due to time limitations, were recommended for possible future work.

1. In terms of the HVLF system structure, it was shown in the literature survey, there is ongoing research to introduce high performance power electronic based frequency changers, such as the Hybrid Cycloconverter or Multi-level Matrix Converter (MMC). Additionally, a standard benchmark to the HVLF system structure needs to be introduced, as in the CIGRE HVDC benchmark for example. Introducing a standard benchmark to the HVLF system will provide a better comparison of the various operational, control, and integration to the grid strategies, as well as system behaviour under steady-state and fault conditions.
2. In terms of the protection system, an artificial intelligent (AI) tool such as Artificial Neural Networks (ANN) or Fuzzy Logic can be integrated with the proposed protection algorithm for decision making.
3. One of the requirements for the implementation of large scale HVLF offshore networks in the future is the implementation of reliable and high current interruption performance HVLF circuit breakers. Detailed design and performance tests at realistic voltage and current levels are required.
4. The fault detection and location algorithms were tested through computer simulations of various transmission line fault scenarios using practical system parameters. However, the hardware implementation of the HVLF system including the protection algorithm will provide a better realisation for a practical application.
5. In this work only the sending end cycloconverter generated harmonics effects on the fault transients were considered. However, still another step-up frequency

converter is required at the receiving end. This converter will behave as a nonlinear load that produce harmonics injected into the transmission line. Thus, those harmonics effects on the fault signature need to be considered by the protection algorithm. This can be achieved by readjusting the pre-set fault identification thresholds.

References

[1] Renewable Energy Policy Network. (2017). *Renewables 2017 Global Status Report*. Available: http://www.ren21.net/status-of-renewables/global-status-report/. *accessed on*: (15/07/2107).

[2] European Wind Energy Association. (2014). *Wind in power: 2015 European statistics*. Available: http://www.ewea.org/statistics/. *accessed on*: (12/06/2016).

[3] European Commission-Eurostat. (2017). *Energy Production and Imports*. Available: http://ec.europa.eu/eurostat/statistics-explained/index.php/Energy_production_and_imports. *accessed on*: (05/07/2017).

[4] H. J. Bahirat, B. A. Mork, and H. K. Hoidalen, "Comparison of wind farm topologies for offshore applications," in *Power and Energy Society General Meeting, 2012 IEEE*, 2012, pp. 1-8.

[5] M. Bilgili, A. Yasar, and E. Simsek, "Offshore wind power development in Europe and its comparison with onshore counterpart," *Renewable and Sustainable Energy Reviews*, vol. 15, pp. 905-915, 2011.

[6] Roland Berger, EWEA, BWE. (2013). *Offshore Wind Toward 2020*. Available: http://www.rolandberger.com. *accessed on*: (20/03/2015).

[7] V. K. Sood, *HVDC and FACTS controllers: applications of static converters in power systems*. Boston: Kluwer Academic Publishers, 2004.

[8] J. Suonan, S. Gao, G. Song, Z. Jiao, and X. Kang, "A novel fault-location method for HVDC transmission lines," *Power Delivery, IEEE Transactions on*, vol. 25, pp. 1203-1209, 2010.

[9] Z. Xiao-Dong, T. Neng-Ling, J. S. Thorp, and Y. Guang-Liang, "A transient harmonic current protection scheme for HVDC transmission line," *Power Delivery, IEEE Transactions on*, vol. 27, pp. 2278-2285, 2012.

[10] E. Kontos, R. T. Pinto, S. Rodrigues, and P. Bauer, "Impact of HVDC Transmission System Topology on Multiterminal DC Network Faults," *Power Delivery, IEEE Transactions on*, vol. 30, pp. 844-852, 2015.

[11] C. M. Franck, "HVDC circuit breakers: A review identifying future research needs," *IEEE Transactions on Power Delivery*, vol. 26, pp. 998-1007, 2011.

[12] G. Heger, H. Vermeulen, J. Holtzhausen, and W. Vosloo, "A comparative study of insulator materials exposed to high voltage AC and DC surface discharges," *Dielectrics and Electrical Insulation, IEEE Transactions on*, vol. 17, pp. 513-520, 2010.

[13] W. Lau and G. Chen, "Simultaneous space charge and conduction current measurements in solid dielectrics under high dc electric field," in *International Conference on condition monitoring and diagnosis*, Changwon, South Korea, 2006.

[14] M. Marzinotto and G. Mazzanti, *IEEE Press Series on Power Engineering: Extruded Cables for High-Voltage Direct-Current Transmission : Advances in Research and Development*: Wiley, 2012.

[15] W. Fischer, R. Braun, and I. Erlich, "Low frequency high voltage offshore grid for transmission of renewable power," in *Innovative Smart Grid Technologies (ISGT Europe), 2012 3rd IEEE PES International Conference and Exhibition on*, 2012, pp. 1-6.

[16] W. Xifan, "The fractional frequency transmission system," *IEE Japan Power & Energy. Tokyo, Japan: IEEE*, pp. 53-58, 1994.

[17] X. Wang and X. Wang, "Feasibility study of fractional frequency transmission system," *Power Systems, IEEE Transactions on*, vol. 11, pp. 962-967, 1996.

[18] X. Xiang, M. M. C. Merlin, and T. C. Green. (2016, Cost analysis and comparison of HVAC, LFAC and HVDC for offshore wind power connection. *IET Conference Proceedings*.

[19] A. Papadopoulos, S. Rodrigues, E. Kontos, T. Todorcevic, P. Bauer, and R. T. Pinto, "Collection and transmission losses of offshore wind farms for optimization purposes," in *Energy Conversion Congress and Exposition (ECCE), 2015 IEEE*, 2015, pp. 6724-6732.

[20] M. Carrasco, F. Mancilla-David, G. Venkataramanan, and J. Reed, "Low frequency HVac transmission to increase power transfer capacity," in *T&D Conference and Exposition, 2014 IEEE PES*, 2014, pp. 1-5.

[21] H. Chen, M. H. Johnson, and D. C. Aliprantis, "Low-frequency AC transmission for offshore wind power," *Power Delivery, IEEE Transactions on*, vol. 28, pp. 2236-2244, 2013.

[22] I. Erlich, F. Shewarega, H. Wrede, and W. Fischer, "Low frequency AC for offshore wind power transmission - prospects and challenges," in *AC and DC Power Transmission, 11th IET International Conference on*, 2015, pp. 1-7.

[23] J. Ruddy, R. Meere, and T. O'Donnell, "A comparison of VSC-HVDC with low frequency AC for offshore wind farm design and interconnection," *Energy Procedia*, vol. 80, pp. 185-192, 2015.

[24] A. Canelhas, S. Karamitsos, U. Axelsson, and E. Olsen, "A low frequency power collector alternative system for long cable offshore wind generation," in *AC and DC Power Transmission, 11th IET International Conference on*, 2015, pp. 1-6.

[25] C. N. Mau, K. Rudion, A. Orths, P. Eriksen, H. Abildgaard, and Z. Styczynski, "Grid connection of offshore wind farm based DFIG with low frequency AC transmission system," in *Power and Energy Society General Meeting, 2012 IEEE*, 2012, pp. 1-7.

[26] MathWorks, "MATLAB and Statistics Toolbox Release 2016a, The MathWorks, Inc., Natick, Massachusetts, United States.," 2016a ed, 2016.

[27] R. Perveen, N. Kishor, and S. R. Mohanty, "Off-shore wind farm development: Present status and challenges," *Renewable and Sustainable Energy Reviews*, vol. 29, pp. 780-792, 2014.

[28] P. Bresesti, W. L. Kling, R. L. Hendriks, and R. Vailati, "HVDC connection of offshore wind farms to the transmission system," *Energy Conversion, IEEE Transactions on,* vol. 22, pp. 37-43, 2007.

[29] D. van der Born, "Investigation of space charge injection, conduction and trapping mechanisms in polymeric HVDC mini-cables," MSc Thesis, Delft University of Technology, 2011.

[30] S. Chuangpishit, A. Tabesh, Z. Moradi-Sharbabk, and M. Saeedifard, "Topology design for collector systems of offshore wind farms with pure DC power systems," *Industrial Electronics, IEEE Transactions on*, vol. 61, pp. 320-328, 2014.

[31] C. L. Wadhwa, *Electrical Power Systems*. Kent, GBR: New Academic Science, 2012.

[32] X. Wang, C. Chengjun, and Z. Zhichao, "Experiment on fractional frequency transmission system," *Power Systems, IEEE Transactions on,* vol. 21, pp. 372-377, 2006.

[33] P. B. Wyllie, Y. Tang, L. Ran, T. Yang, and J. Yu, "Low Frequency AC Transmission - Elements of a Design for Wind Farm Connection," in *AC and DC Power Transmission, 11th IET International Conference on*, 2015, pp. 1-5.

[34] N. Qin, S. You, Z. Xu, and V. Akhmatov, "Offshore wind farm connection with low frequency AC transmission technology," in *Power & Energy Society General Meeting, 2009. PES'09. IEEE*, 2009, pp. 1-8.

[35] P. Achara and T. Ise, "Operating phase and frequency selection of low frequency AC transmission system using cycloconverters," in *Power Electronics Conference (IPEC-Hiroshima 2014-ECCE-ASIA), 2014 International*, 2014, pp. 3687-3694.

[36] A. Kalair, N. Abas, and N. Khan, "Comparative study of HVAC and HVDC transmission systems," *Renewable and Sustainable Energy Reviews,* vol. 59, pp. 1653-1675, 2016.

[37] M. Szechtman, T. Wess, and C. Thio, "A benchmark model for HVDC system studies," in *AC and DC Power Transmission, 1991., International Conference on*, 1991, pp. 374-378.

[38] V. Sood, V. Khatri, and H. Jin, "EMTP modelling of CIGRE benchmark based HVDC transmission system operating with weak AC systems," in *Power Electronics, Drives and Energy Systems for Industrial Growth, 1996., Proceedings of the 1996 International Conference on*, 1996, pp. 426-432.

[39] M. H. Rashid, *Power electronics handbook: devices, circuits and applications*: Academic press, 2010.

[40] C. W. Lander, *Power electronics*: McGraw-Hill, Inc., 1987.

[41] B. Wu, J. Pontt, J. Rodríguez, S. Bernet, and S. Kouro, "Current-source converter and cycloconverter topologies for industrial medium-voltage drives," *IEEE Transactions on Industrial Electronics*, vol. 55, pp. 2786-2797, 2008.

[42] B. Pelly, *Thyristor Phase-Controlled Converters*: John Wiley & Sons, New York, 1976.

[43] P. Aravena, L. Moran, R. Burgos, P. Astudillo, C. Olivares, and D. Melo, "High-Power Cycloconverter for Mining Applications: Practical Recommendations for

Operation, Protection, and Compensation," *Industry Applications, IEEE Transactions on,* vol. 51, pp. 82-91, 2015.

[44] T. Xu, C. Klumpner, and J. Clare, "Hybrid cycloconverters: An exploration of benefits," in *Power Electronics and Applications, 2007 European Conference on*, 2007, pp. 1-10.

[45] M. Callavik, A. Blomberg, J. Häfner, and B. Jacobson, "The hybrid HVDC breaker," *ABB Grid Systems Tech. Paper,* 2012.

[46] A. Elhaffar and M. Lehtonen, "Travelling waves based earth fault location in 400 kV transmission network using single end measurement," in *Power Engineering, 2004. LESCOPE-04. 2004 Large Engineering systems Conference on*, 2004, pp. 53-56.

[47] FE Perez, E Orduna, and G. Guidi, "Adaptive wavelets applied to fault classification on transmission lines," *Generation, Transmission & Distribution, IET*, vol. 5, pp. 694-702, 2011.

[48] H. Dommel and J. Michels, "High-speed Relaying Using Traveling Wave Transient Analysis," in *IEEE Transactions on Power Apparatus and Systems*, 1978, pp. 1011-1011.

[49] K. V. Babu, M. Tripathy, and A. K. Singh, "Recent techniques used in transmission line protection: a review," *International Journal of Engineering, Science and Technology,* vol. 3, 2011.

[50] C. H. Kim and R. Aggarwal, "Wavelet transforms in power systems. I. General introduction to the wavelet transforms," *Power Engineering Journal,* vol. 14, pp. 81-87, 2000.

[51] M. Weeks, *Digital Signal Processing Using MATLAB & Wavelets*: Jones & Bartlett Learning, 2010.

[52] R. X. Gao and R. Yan, *Wavelets: Theory and Applications for manufacturing*: Springer, 2010.

[53] D. C. Robertson, O. I. Camps, J. S. Mayer, and W. B. Gish, "Wavelets and electromagnetic power system transients," *Power Delivery, IEEE Transactions on,* vol. 11, pp. 1050-1058, 1996.

[54] X. Dong, S. Luo, S. Shi, B. Wang, S. Wang, L. Ren, *et al.*, "Implementation and Application of Practical Traveling-Wave-Based Directional Protection in UHV Transmission Lines," *IEEE Transactions on Power Delivery,* vol. 31, pp. 294-302, 2016.

[55] R. Goli, A. G. Shaik, and S. S. T. Ram, "Fuzzy-Wavelet Based Double Line Transmission System Protection Scheme in the Presence of SVC," *Journal of The Institution of Engineers (India): Series B,* vol. 96, pp. 131-140, 2015.

[56] J. Barros, R. I. Diego, and M. de Apraiz, "Applications of Wavelet Transform for Analysis of Harmonic Distortion in Power Systems: A Review," *Instrumentation and Measurement, IEEE Transactions on,* vol. 61, pp. 2604-2611, 2012.

[57] P. F. Ribeiro, "Wavelet transform: an advanced tool for analyzing non-stationary harmonic distortions in power systems," in *Proceedings IEEE ICHPS VI*, 1994, pp. 365-369.

[58] J. Upendar, C. Gupta, and G. Singh, "Discrete wavelet transform and probabilistic neural network based algorithm for classification of fault on transmission systems," in *India Conference, 2008. INDICON 2008. Annual IEEE*, 2008, pp. 206-211.

[59] S. A. Gafoor and P. V. R. Rao, "Wavelet Based Fault Detection, Classification and Location in Transmission Lines," in *Power and Energy Conference, 2006. PECon '06. IEEE International*, 2006, pp. 114-118.

[60] K. Lout and R. K. Aggarwal, "A feedforward Artificial Neural Network approach to fault classification and location on a 132kV transmission line using current signals only," in *Universities Power Engineering Conference (UPEC), 2012 47th International*, 2012, pp. 1-6.

[61] F. Perez, R. Aguilar, E. Orduna, and G. G. J Jäger, "High-speed non-unit transmission line protection using single-phase measurements and an adaptive wavelet: zone detection and fault classification," *Generation, Transmission & Distribution, IET,* vol. 6, pp. 593-604, 2012.

[62] S. G. Mallat, "A theory for multiresolution signal decomposition: the wavelet representation," *Pattern Analysis and Machine Intelligence, IEEE Transactions on,* vol. 11, pp. 674-693, 1989.

[63] C. H. Kim and R. Aggarwal, "Wavelet transforms in power systems. Part 2: Examples of application to actual power system transients," *Power Engineering Journal,* vol. 15, pp. 193-202, 2001.

[64] A. H. Osman and O. P. Malik, "Protection of parallel transmission lines using wavelet transform," *Power Delivery, IEEE Transactions on,* vol. 19, pp. 49-55, 2004.

[65] O. P. Malik, "Application of Neural Networks in Transmission Line Protection," in *Power Engineering Society General Meeting, 2007. IEEE*, 2007, pp. 1-6.

[66] F. Martin, J. Aguado, M. Medina, and J. Munoz, "Classification of faults in double circuit lines using Wavelet transforms," in *Industrial Technology, 2008. ICIT 2008. IEEE International Conference on*, 2008, pp. 1-6.

[67] C. Jianyi and R. K. Aggarwal, "A new approach to EHV transmission line fault classification and fault detection based on the wavelet transform and artificial intelligence," in *Power and Energy Society General Meeting, 2012 IEEE*, 2012, pp. 1-8.

[68] A. H. Osman and O. P. Malik, "Transmission line distance protection based on wavelet transform," *Power Delivery, IEEE Transactions on,* vol. 19, pp. 515-523, 2004.

[69] A. I. Megahed, A. M. Moussa, and A. Bayoumy, "Usage of wavelet transform in the protection of series-compensated transmission lines," *IEEE Transactions on Power Delivery,* vol. 21, pp. 1213-1221, 2006.

[70] M. Solanki, Y. Song, S. Potts, and A. Perks, "Transient protection of transmission line using wavelet transform," 2001.

[71] S. Ekici and S. Yildirim, "Fault Location Estimation on Transmission Lines Using Wavelet Transform and Artificial Neural Network," in *IC-AI*, 2006, pp. 181-184.

[72] O. Poisson, P. Rioual, and M. Meunier, "New signal processing tools applied to power quality analysis," *Power Delivery, IEEE Transactions on*, vol. 14, pp. 561-566, 1999.

[73] Z. Nan and M. Kezunovic, "Transmission Line Boundary Protection Using Wavelet Transform and Neural Network," *Power Delivery, IEEE Transactions on*, vol. 22, pp. 859-869, 2007.

[74] P. Dutta, A. Esmaeilian, and M. Kezunovic, "Transmission-line fault analysis using synchronized sampling," *IEEE Transactions on Power Delivery*, vol. 29, pp. 942-950, 2014.

[75] E. B. M. Tayeb and O. A. A. A. Rhim, "Transmission line faults detection, classification and location using artificial neural network," in *Utility Exhibition on Power and Energy Systems: Issues & Prospects for Asia (ICUE), 2011 International Conference and*, 2011, pp. 1-5.

[76] F. Martín and J. A. Aguado, "Wavelet-based ANN approach for transmission line protection," *Power Delivery, IEEE Transactions on*, vol. 18, pp. 1572-1574, 2003.

[77] G. Cardoso, J. G. Rolim, and H. H. Zurn, "Application of neural-network modules to electric power system fault section estimation," *Power Delivery, IEEE Transactions on*, vol. 19, pp. 1034-1041, 2004.

[78] X. Liu, A. Osman, and O. Malik, "Hybrid traveling wave/boundary protection for monopolar HVDC line," *Power Delivery, IEEE Transactions on*, vol. 24, pp. 569-578, 2009.

[79] K. Nanayakkara, A. Rajapakse, and R. Wachal, "Fault location in extra long HVDC transmission lines using continuous wavelet transform," in *International Conference on Power Systems Transients (IPST2011)*, 2011.

[80] O. K. Nanayakkara, A. D. Rajapakse, and R. Wachal, "Location of dc line faults in conventional hvdc systems with segments of cables and overhead lines using terminal measurements," *Power Delivery, IEEE Transactions on*, vol. 27, pp. 279-288, 2012.

[81] J. Barros and R. I. Diego, "Analysis of harmonics in power systems using the wavelet-packet transform," *IEEE Transactions on Instrumentation and Measurement*, vol. 57, pp. 63-69, 2008.

[82] D. Jwad and P. Lefley, "Evaluation studies of combined wavelet and neural network applications in high voltage transmission line protection," in *Developments in Power System Protection (DPSP 2014), 12th IET International Conference on*, 2014, pp. 1-5.

[83] ABB. Submarine Cable Systems: Attachment to XLPE Land Cable Systems-Users Guide [Online]. Available: https://library.e.abb.com/public/2fb0094306e48975c125777c00334767/XLPE%20Submarine%20Cable%20Systems%202GM5007%20rev%205.pdf

[84] B. M. Weedy, B. J. Cory, N. Jenkins, J. B. Ekanayake, and G. Strbac, *Electric power systems*: John Wiley & Sons, 2012.

[85] IEEE, "IEEE Recommended Practice and Requirements for Harmonic Control in Electric Power Systems," *IEEE Std 519-2014 (Revision of IEEE Std 519-1992)*, pp. 1-29, 2014.

[86] P. Peltoniemi, R. Pöllänen, M. Niemelä, and J. Pyrhönen, "Comparison of the Effect of Output Filters on the Total Harmonic Distortion of Line Current in Voltage Source Line Converter–Simulation Study," in *Int. Conference on Renewable Energy and Power Quality, Mallorca*, 2006.

[87] R. Blasco-Gimenez, N. Aparicio, S. Ano-Villalba, and S. Bernal-Perez, "LCC-HVDC connection of offshore wind farms with reduced filter banks," *Industrial Electronics, IEEE Transactions on*, vol. 60, pp. 2372-2380, 2013.

[88] ABB. Power Capacitors and Harmonic Filters [Online]. Available: https://library.e.abb.com/public/7385b4a156d09453c1257bf600227be7/1HSM%209543%2032-00en%20Capacitors%20Buyers%20Guide%20Ed%201.pdf

[89] J. Arrillaga and N. R. Watson, *Power system harmonics*: John Wiley & Sons, 2004.

[90] R. J. Hamidi and H. Livani, "Traveling-wave-based fault-location algorithm for hybrid multiterminal circuits," *IEEE Transactions on Power Delivery*, vol. 32, pp. 135-144, 2017.

[91] O. Rioul and M. Vetterli, "Wavelets and signal processing," *IEEE signal processing magazine*, vol. 8, pp. 14-38, 1991.

[92] L. Hewitson, M. Brown, and R. Balakrishnan, *Practical power system protection*: Elsevier, 2004.

[93] D. Guillen, M. R. A. Paternina, A. Zamora, J. M. Ramirez, and G. Idarraga, "Detection and classification of faults in transmission lines using the maximum wavelet singular value and Euclidean norm," *IET Generation, Transmission & Distribution*, vol. 9, pp. 2294-2302, 2015.

[94] N. Saravanan and A. Rathinam, "A Comparitive Study on ANN Based Fault Location and Classification Technique for Double Circuit Transmission Line," presented at the Proceedings of the 2012 Fourth International Conference on Computational Intelligence and Communication Networks, 2012.

[95] J. Ruddy, R. Meere, and T. O’Donnell, "Low Frequency AC transmission for offshore wind power: A review," *Renewable and Sustainable Energy Reviews*, vol. 56, pp. 75-86, 2016.

Appendices

Appendix-A: Matlab model of the cycloconverter control system.

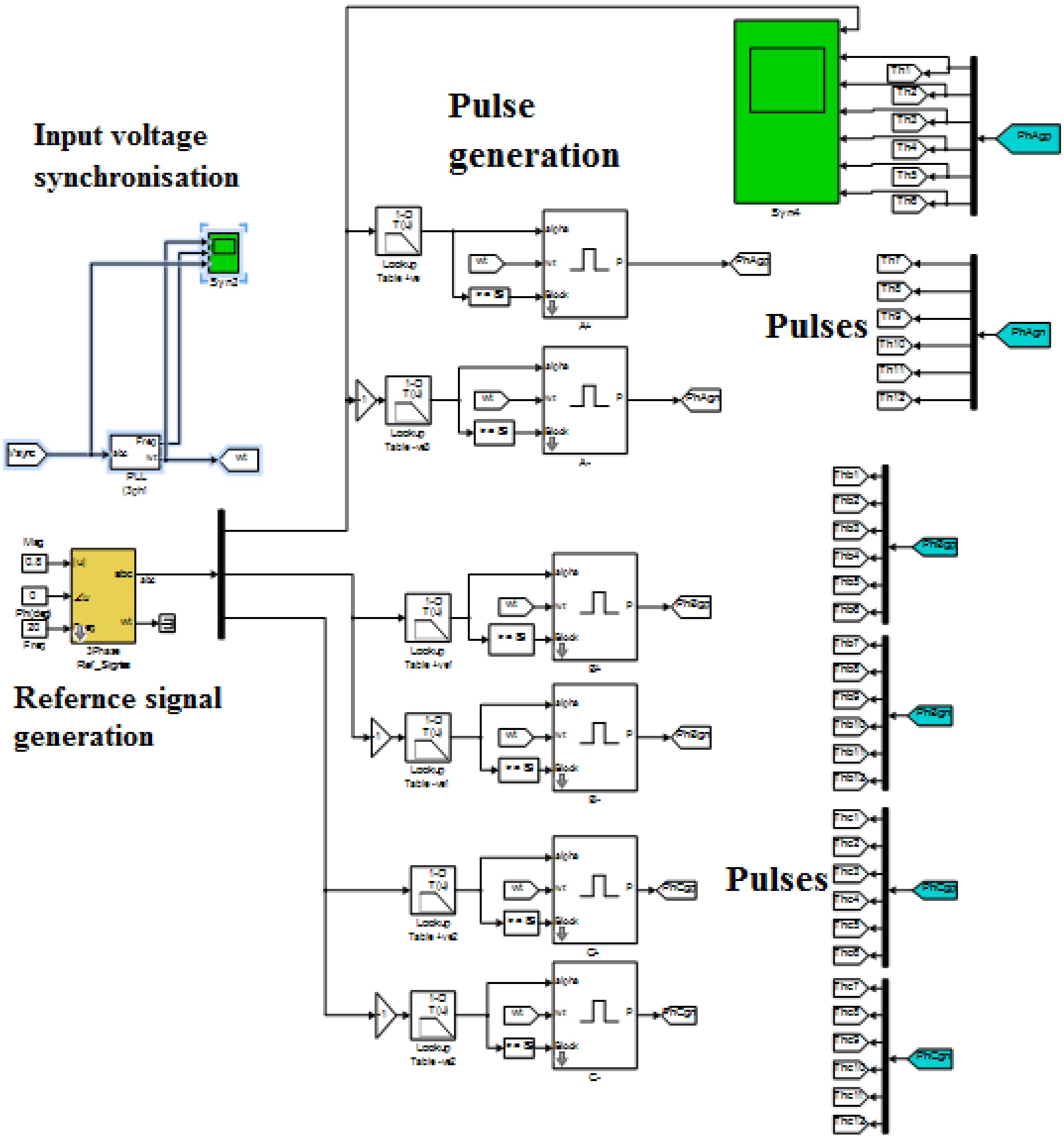

The input voltage signal was synchronised with a cosine reference signal having the desired output frequency. The control method was described in chapter 4, section 4.2.1

Appendix-B: Voltage and Current Waveforms of Different Fault Types

1. The three-phase current waveforms measured at busbar 3 when (a) Phase-B to ground and (b) Phase-C to ground faults occur at various locations of the line.

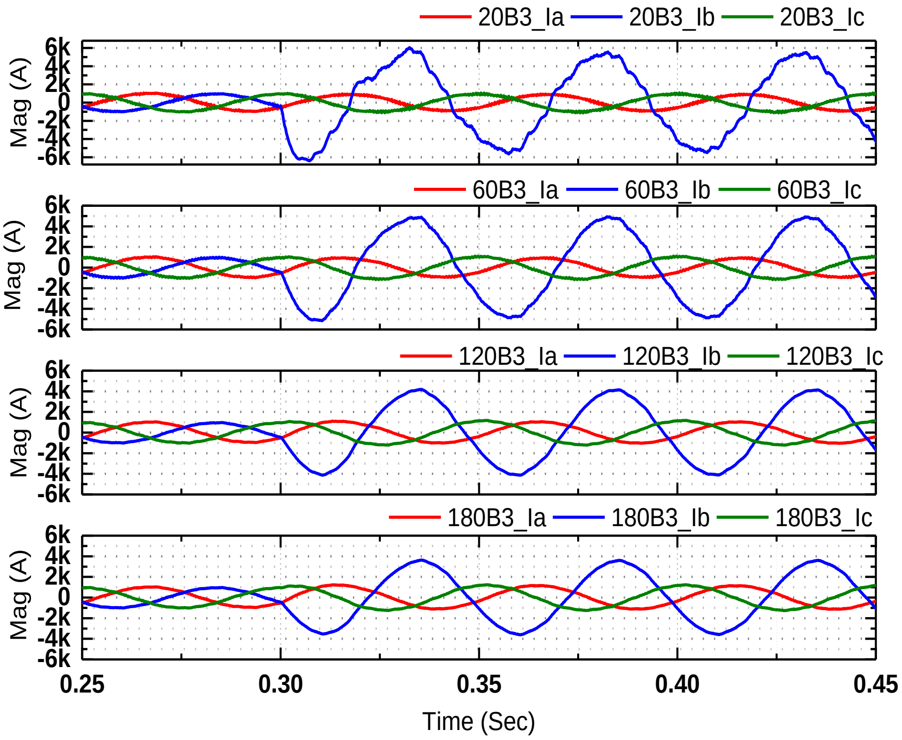

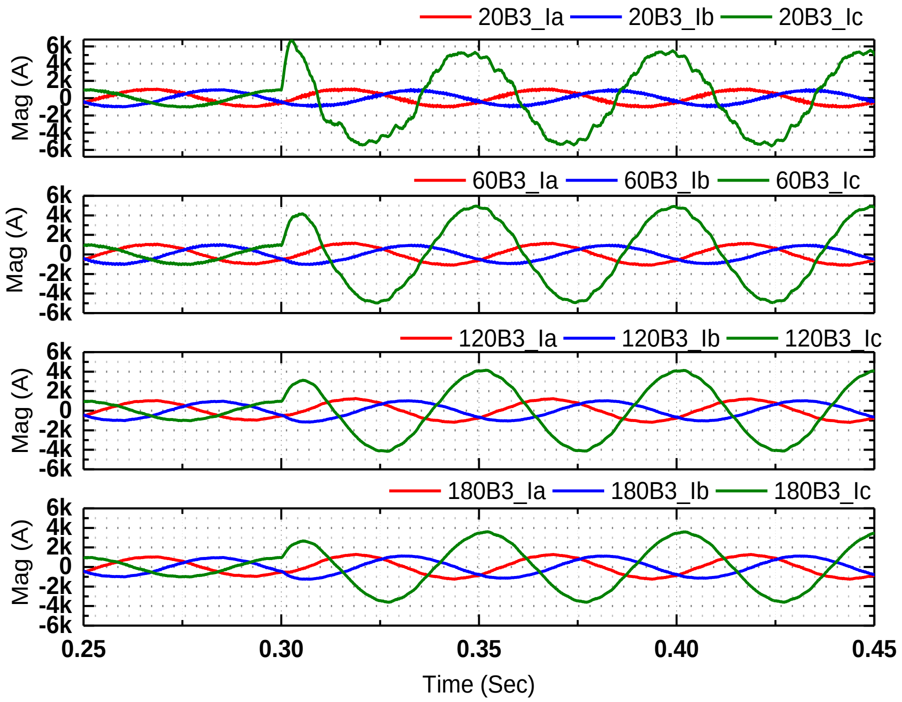

2. The three-phase current waveforms measured at busbar 3 when (a) phase-B to phase-C and (b) Phase-A to phase-C faults occur at various locations of the line.

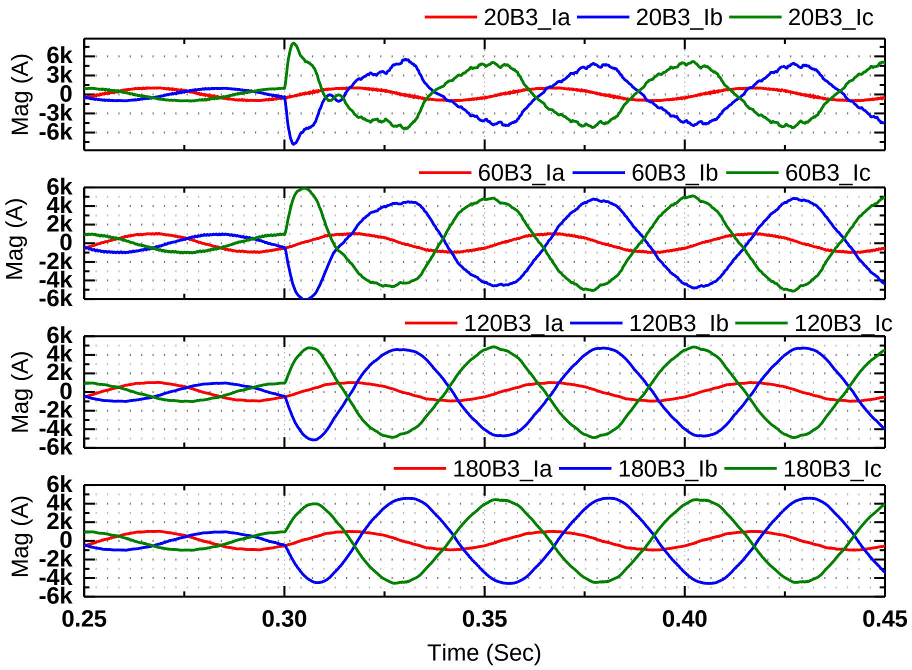

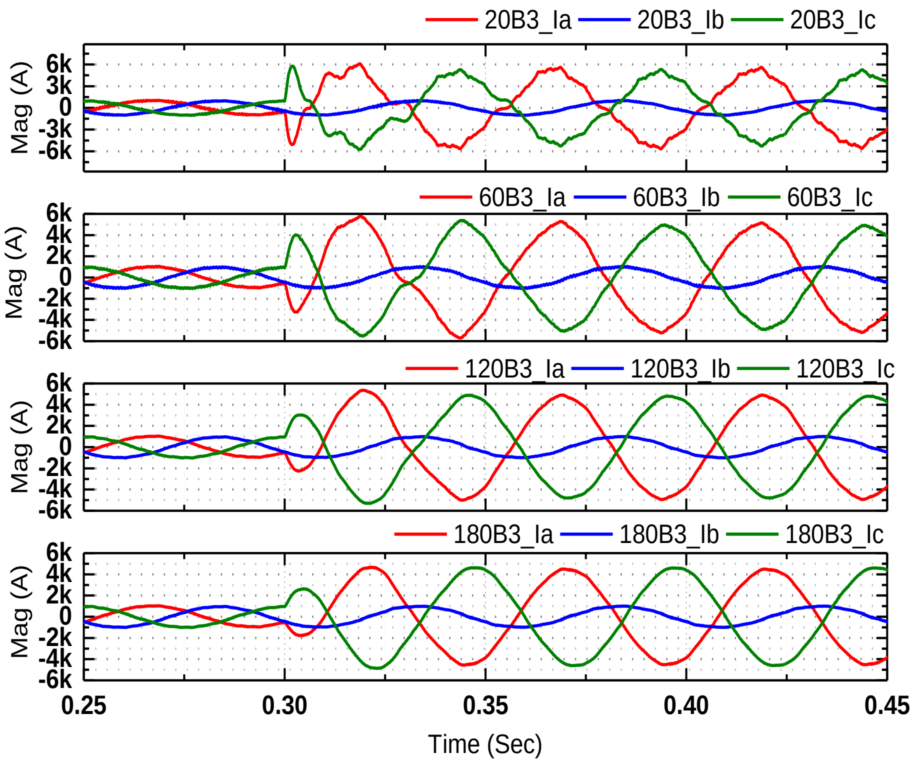

Appendix-C: Ground Fault Calculations

Ground fault detection using the zero sequence current signal analysis with the WPT. The selected WPT coefficients for fault detection were CW1 and CW3 of the third analysis level. A comparison between these coefficients obtained from three phase fault and three phase to ground fault was carried out. These faults were simulated at locations of 20, 60, 120, and 180 km from the sending end.

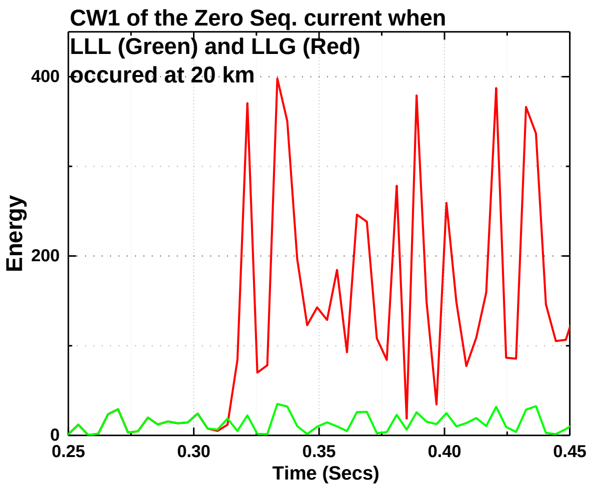

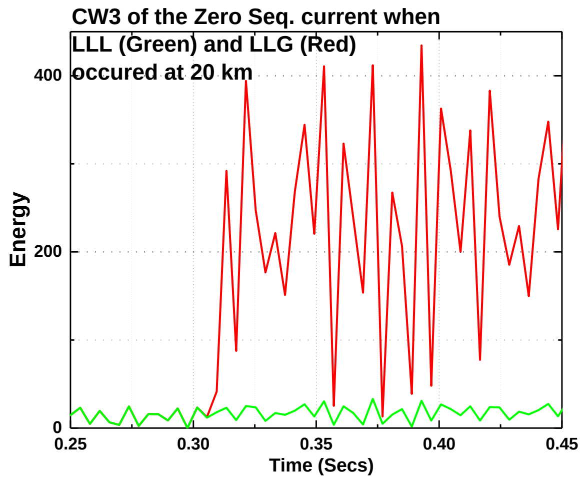

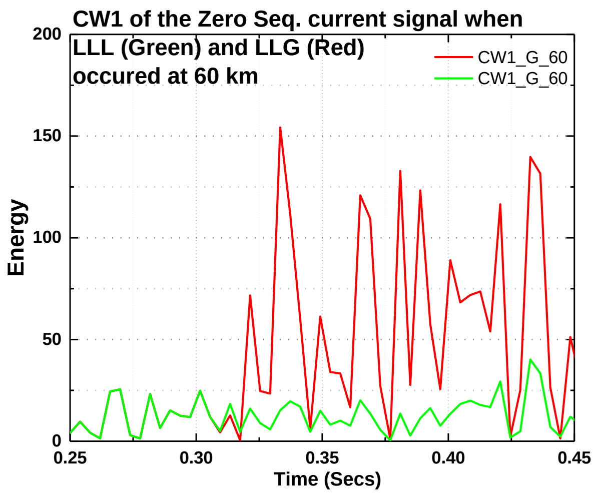

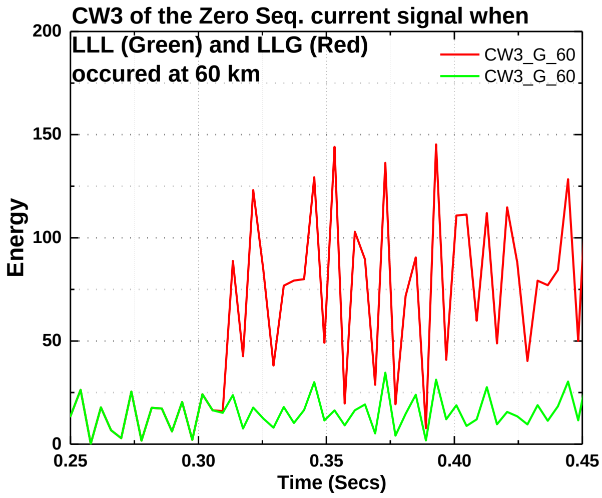

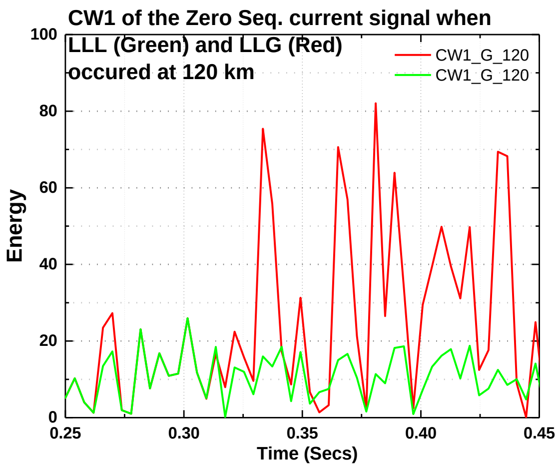
CW1 of the Zero Seq. current signal when
LLL (Green) and LLG (Red)
occured at 120 km
CW1_G_120
CW1_G_120
Energy
Time (Secs)
0
20
40
60
80
100
0.25
0.30
0.35
0.40
0.45

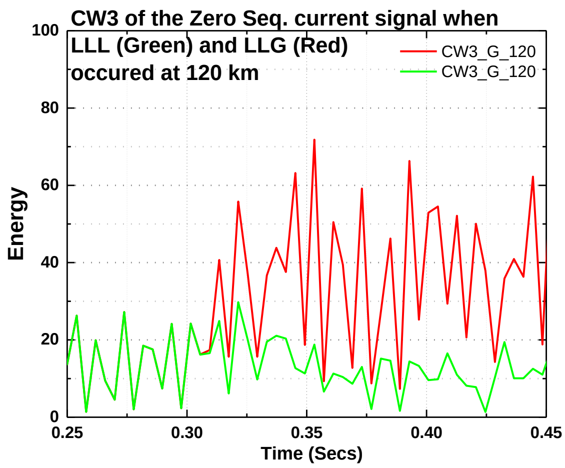
CW3 of the Zero Seq. current signal when
LLL (Green) and LLG (Red)
occured at 120 km
CW3_G_120
CW3_G_120
Energy
Time (Secs)
0
20
40
60
80
100
0.25
0.30
0.35
0.40
0.45

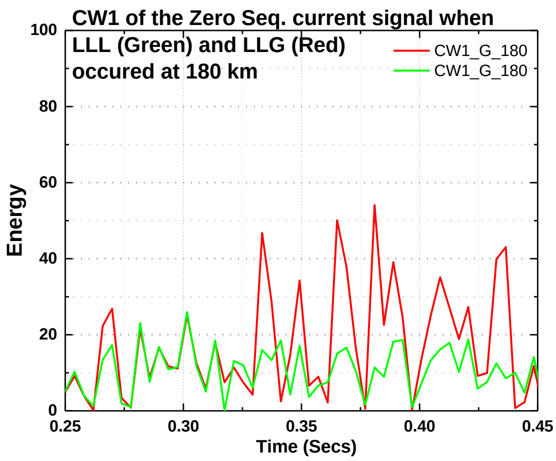
CW1 of the Zero Seq. current signal when
LLL (Green) and LLG (Red)
occured at 180 km
CW1_G_180
CW1_G_180
Energy
Time (Secs)
0
20
40
60
80
100
0.25
0.30
0.35
0.40
0.45

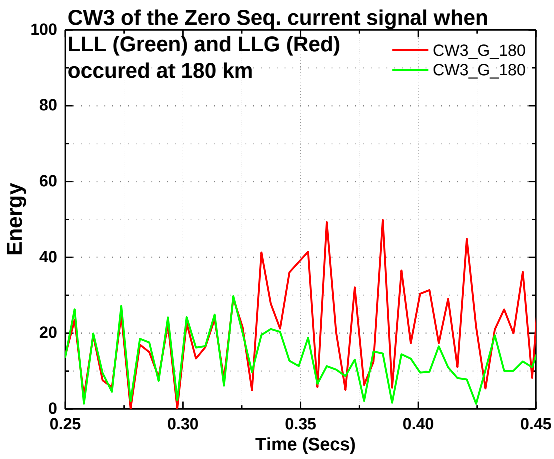
CW3 of the Zero Seq. current signal when
LLL (Green) and LLG (Red)
occured at 180 km
CW3_G_180
CW3_G_180
Energy
Time (Secs)
0
20
40
60
80
100
0.25
0.30
0.35
0.40
0.45